



**HAL**  
open science

# Pérovskites hybrides et ingénierie d'interface pour l'amélioration des dispositifs optoélectroniques

Tao Zhu

► **To cite this version:**

Tao Zhu. Pérovskites hybrides et ingénierie d'interface pour l'amélioration des dispositifs optoélectroniques. Chimie analytique. Université Paris sciences et lettres, 2020. Français. NNT : 2020UPSLC020 . tel-03551362

**HAL Id: tel-03551362**

**<https://pastel.hal.science/tel-03551362>**

Submitted on 1 Feb 2022

**HAL** is a multi-disciplinary open access archive for the deposit and dissemination of scientific research documents, whether they are published or not. The documents may come from teaching and research institutions in France or abroad, or from public or private research centers.

L'archive ouverte pluridisciplinaire **HAL**, est destinée au dépôt et à la diffusion de documents scientifiques de niveau recherche, publiés ou non, émanant des établissements d'enseignement et de recherche français ou étrangers, des laboratoires publics ou privés.

**THÈSE DE DOCTORAT**  
**DE L'UNIVERSITÉ PSL**

Préparée à Chimie ParisTech / École Nationale Supérieure de  
Chimie de Paris (ENSCP)

**Hybrid Perovskites and Interface Engineering for the  
Improvement of Optoelectronic Devices**

Soutenue par

**Tao Zhu**

Le 29 septembre 2020

Ecole doctorale n° 388

**Chimie Physique et Chimie  
Analytique de Paris Centre**

Spécialité

**Chimie Physique**



Composition du jury :

Ilaria, CIOFINI Directrice de Recherche CNRS Chimie ParisTech, ENSCP	<i>Présidente</i>
Fabrice, GOUBARD Professeur, Université de Cergy-Pontoise	<i>Rapporteur</i>
Johann, BOUCLÉ Maître de Conférence, Université de Limoges	<i>Rapporteur</i>
Emmanuelle DELEPORTE Professeur, Ecole Normale Supérieure de Paris-Saclay	<i>Examinatrice</i>
Philip SCHULZ Directeur de Recherche CNRS Institut Photovoltaïque d'Île-de-France	<i>Examineur</i>
Thierry PAUपोर्टÉ Directeur de Recherche CNRS Chimie ParisTech, ENSCP	<i>Directeur de thèse</i>



## Acknowledgments

Time goes fast. I still remember the day I first came to Chimie-ParisTech, as if it were yesterday. The memory in Chimie-ParisTech, in Paris, in France and Europe, is in my mind and my photo album. My PhD career would not be completed without the help of the people around me. I cannot thank them enough for their help.

A special acknowledgment goes out to the China Scholarship Council (CSC) for the opportunity and the financial support during this PhD program. Great thanks to Chimie-ParisTech and CNRS, they supported my communicating abroad and participating in international conferences.

I would like to express my deepest appreciation to my thesis director, Prof. Thierry Pauporté for his guidance and patientless for the last three years of my PhD. I am grateful for his endless support and patience in research investigations, writing articles, and correcting my manuscripts.

I am grateful to our research partners: Prof. Ilaria Ciofini, Dr. Frédéric Labat and Dr. Jun Su for their strong calculation support; Dr. José Alvarez, Dr. Grégory Lefèvre, Dr. Laurent Coolen, Jiawen Liu, Dr. Selina Olthof, Dr. Marie-Noelle Rager, Prof. Bruno Viana, Prof. Gérard Aka for their kind help in doing measurements during my PhD. I am also grateful to Prof. Gilles Wallez, Dr. Odile Majerus, Dr. Pascal Loiseau, Dr. Philippe Vermaut, Dr. Fan Sun for training me on XRD Rietveld, Rama, XRD, SEM measurements, respectively.

I would like to thank Prof. Fabrice Goubard and Dr. Johann, Boulcé for accepting to be my reviewers as well as Prof. Ilaria Ciofini, Prof. Emmanuelle Deleporte, Prof. Philip Schulz, and Dr. Laurent Coolen for being my examiners.

I am deeply grateful for all my colleagues and friends for their help, their support, and all the great times we shared in the laboratory. I would like to thank in particular Dr. Rui Xia, Dr. Maria Ulfa, Dr. Pengjiu Wang, Daming Zheng, Sophie Achigar, Hongli Du, Dr. Zhijin Hou, Changheng Tong, Léa Drget, Hugo Barthelemy, Chabha, Dr. Antonin Leblanc, Fei Cheng, Liam Gollino, Dr. Quentin Morelle and many others.

Finally, best love to my parents (Liqin and Xunge) and sister (Yan), they give me endless love and support. Great thanks to my whole family and friends, they believe in my capability to go further and further on the road of research. Thanks to all teachers that taught me, I would not be a doctor

without their teaching.

In the end, thanks to my dear girlfriend (Yanyi Sun) with full love. She is very kind, smart, beautiful, brave... (many other good adjectives). Besides, she is a doctor and aims to save lives. I am proud of her and I love her. We knew each other in French language course and started a new life together in Paris.

## Table of Contents

<b>General introduction</b> .....	11
<b>Chapter I. Context</b> .....	13
I.1 Semiconductors .....	13
I.1.1 Types of semiconductors .....	14
I.1.2 Two types of current carriers in semiconductors.....	17
I.1.3 Charge generation and recombination.....	21
I.2 Solar Energy .....	24
I.2.1 Photovoltaics for solar energy conversion.....	26
I.2.2 Brief introduction of PV devices .....	27
I.3 Perovskite Solar Cells.....	30
I.3.1 Structures and properties of organic-inorganic hybrid perovskites.....	31
I.3.2 The working principle of perovskite solar cells .....	34
I.3.3 Short overview of perovskite solar cells evolution .....	35
I.4 UV-Photodetectors .....	39
I.4.1 Classification of the UV photodetectors.....	40
I.4.2 Working principle of photovoltaic-type UV photodetectors .....	40
I.4.3 UV photodetector parameters.....	41
I.5 Conclusions .....	42
References.....	43
<b>Chapter II. Response Enhancement of Self-Powered Visible-Blind UV Photodetectors by Nanostructured Heterointerface Engineering</b> .....	47
II.1 Introduction .....	47
II.2 TiO <sub>2</sub> Layers Preparation and Functionalization by SAMs.....	50
II.2.1 Experimental .....	50
II.2.2 Characterizations of the modified TiO <sub>2</sub> surfaces.....	53
II.3 Modelling by Density Functional Theory .....	59
II.3.1 Modelling of the acid adsorption onto TiO <sub>2</sub> .....	59
II.3.2 FTIR by theoretical calculations .....	61
II.3.3 Dipole moment.....	63
II.3.4 Energy band level.....	63

II.4 UV Photodetector Devices .....	66
II.4.1 Experimental .....	66
II.4.2 Characterizations of the UV PDs .....	67
II.5 Conclusions .....	75
References.....	76
<b>Chapter III. Interfacial Engineering through Chloride-Functionalized Self-Assembled Monolayers for High-Performance Perovskite Solar Cells.....</b>	<b>79</b>
III.1 Introduction.....	79
III.2 Experimental .....	82
III.2.1 Preparation of the MAPbI <sub>3</sub> and Cs8FAMA films.....	82
III.2.2 Characterization methods.....	83
III.3 Characterizations of Perovskite Films .....	84
III.3.1 XRD .....	84
III.3.2 SEM .....	84
III.3.3 UV-Vis absorbance and steady-state PL.....	85
III.3.4 Time-resolved photoluminescence and steady-state PL .....	86
III.3.5 UPS and IPES .....	88
III.4 Characterizations of PSCs.....	89
III.4.1 <i>J-V</i> curves and IPCE .....	89
III.4.2 Stability .....	95
III.4.3 Discussion about the effect of SAMs on the PSCs performances .....	97
III.5 Conclusions.....	103
References.....	104
<b>Chapter IV. High Efficiency and Stable Solar Cells Based on MAI Mediated Grown FA<sub>0.94</sub>MA<sub>0.06</sub>PbI<sub>3</sub> Perovskite and 2D Materials Post-Treatment .....</b>	<b>107</b>
IV.1 Introduction.....	107
IV.2 Experimental.....	109
IV.2.1 Preparation of FAMAPbI <sub>3</sub> films.....	109
IV.2.2 Post-treatment method.....	109
IV.2.3 Characterization methods .....	110
IV.2.4 Fitting of the time resolved PL curves.....	110

IV.2.5 Analysis of the impedance spectra .....	111
IV.3 Characterizations of Perovskite Films .....	112
IV.3.1 SEM .....	112
IV.3.2 XRD .....	114
IV.3.3 Perovskite compositions .....	115
IV.3.4 UV-vis absorbance.....	119
IV.3.5 Steady-state PL and TRPL curves .....	119
IV.4 Characterizations of PEAI Treated Perovskite Film .....	121
IV.3.1 SEM .....	121
IV.3.2 XRD.....	121
IV.3.3 Absorbance .....	122
IV.3.4 Steady-state PL and TRPL.....	123
IV.5 Characterizations of PSCs .....	124
IV.5.1 <i>J-V</i> curves .....	124
IV.5.2 EQE curves .....	127
IV.5.3 Ideality factor.....	128
IV.5.4 Stability.....	128
IV.5.5 Impedance spectroscopy study of PSCs .....	132
IV.6 Conclusions.....	138
References.....	139
<b>Chapter V. Stability and Efficiency of Benzylamine Hydroiodide (BEI) Based Mixed-Dimensional Perovskite Solar Cells.....</b>	<b>143</b>
V.1 Introduction.....	143
V.2. Experimental .....	145
V.3 Characterizations of the Perovskite Films .....	146
V.3.1 XRD .....	146
V.3.2 UV-Vis Absorbance.....	147
V.3.3 Steady-state PL spectra .....	148
V.3.4 SEM .....	149
V.4 Characterizations of 2D/3D PSCs.....	150
V.4.1 <i>J-V</i> curves and EQE .....	150

V.4.2 Aging Test.....	152
V.5 Conclusions.....	161
References.....	162
<b>General Conclusion and Perspectives .....</b>	<b>165</b>
Annex II-Chapter II.....	165
Annex III-Chapter III.....	173
Annex IV-Chapter IV .....	176
Annex V-Chapter V .....	184
List of publications and presentations.....	188

## Résumé de la thèse

### **Pérovskites hybrides et ingénierie d'interface pour l'amélioration des dispositifs optoélectroniques**

Au cours des dix dernières années, les cellules solaires à pérovskite (CSP) se sont révélées être la technologie la plus prometteuse en photovoltaïque. Dans cette thèse, nous avons développé des stratégies pour obtenir des cellules solaires très performantes et stables grâce à de l'ingénierie d'interface et à de l'ingénierie sur la composition de la pérovskite. Le chapitre I présente le contexte de cette recherche, développe quels sont les matériaux semiconducteurs et pérovskites ainsi que leur utilisation en optoélectronique et l'énergie solaire. Le chapitre II présente la modification d'interface par des monocouches auto-assemblées (MAA) et leurs applications dans les photo-détecteurs UV. Le chapitre III montre l'application des MAA aux CSP, ce qui a permis d'atteindre un rendement de 21,35 %. Au chapitre IV, nous étudions des pérovskites à bande interdite étroite basées sur le formamidinium (FAPbI<sub>3</sub> stabilisée par le méthyle d'ammonium). Par utilisation d'additifs dans les solutions de précurseur et passivation interfaciale, le dispositif record a atteint un rendement stabilisé de 22,1 %. Dans le chapitre V, nous nous intéressons à l'amélioration de la stabilité des CSP. Des pérovskites 2D/3D à base de benzyle ammonium ont été étudiées. Nous avons obtenu des films et ces cellules solaires remarquablement stables.

La grave pénurie d'énergie et les problèmes de pollution de l'environnement incitent au développement des énergies renouvelables. Les technologies photovoltaïques, qui constituent l'une des stratégies les plus prometteuses, ont suscité un vif intérêt depuis le milieu du XXe siècle. Aujourd'hui, les cellules solaires les plus avancées peuvent produire un rendement de conversion d'énergie (PCE, de l'énergie lumineuse en électricité) supérieur à 40 % mais ces dispositifs souffrent d'une production extrêmement coûteuse. Ce coût élevé empêche la production à grande échelle. Les cellules solaires pérovskites sont à la tête des dispositifs photovoltaïques de la prochaine génération en raison de leurs propriétés photovoltaïques supérieures et de leur faible coût. Les rendements records certifiés pour une CSP à simple jonction et une cellule solaire tandem pérovskite/Si à deux bornes ont déjà atteint 25,5 % et 29,1% respectivement au cours des dix dernières années. Dans cette thèse, nous avons amélioré les propriétés photovoltaïques des CSP en termes de contrôle de l'interface et d'ingénierie de la composition de la pérovskite. Dans le chapitre

I, des connaissances de base sur les semi-conducteurs, telles que le dopage, le niveau de bande d'énergie, les cristaux, etc. ont été données dans un premier temps pour favoriser la compréhension des résultats et la discussion dans la thèse. Ensuite, les principes de fonctionnement des principaux dispositifs photovoltaïques sont illustrés. La théorie fondamentale est l'effet photoélectrique. L'évolution des CSP a été introduite par l'étude des articles classiques. En outre, nous avons également fourni une brève introduction sur les photodétecteurs (PD) à ultraviolets (UV) et expliqué les paramètres importants des PD à UV.

Dans le chapitre II, nous avons d'abord étudié l'effet de la modification des couches de TiO<sub>2</sub> par diverses molécules d'acide organique avec un moment dipolaire variant dans une large gamme. Les modificateurs de surface sélectionnés sont l'acide 4-nitrobenzoïque (NBA), l'acide 4-chlorobenzoïque (CBA), l'acide 4-méthoxybenzoïque (MBA), l'acide 4-nitrobenzoïque et  $\beta$ -alanine ( $\beta$ -ALA). L'adsorption des modificateurs a ensuite été étudiée de manière approfondie par une approche expérimentale et théorique combinée. Ils sont adsorbés à la surface du TiO<sub>2</sub> par leur groupe carboxylate dans un mode bidenté de pontage, comme le montre la figure 1. Les spectres FTIR théoriques trouvés sont en bon accord avec les spectres expérimentaux et montrent la liaison du dipôle moléculaire sur la surface de l'oxyde. Les fonctions de travail de surface (WF) de ces échantillons sont caractérisées par la sonde Kelvin et la spectroscopie photoélectronique UV (UPS).

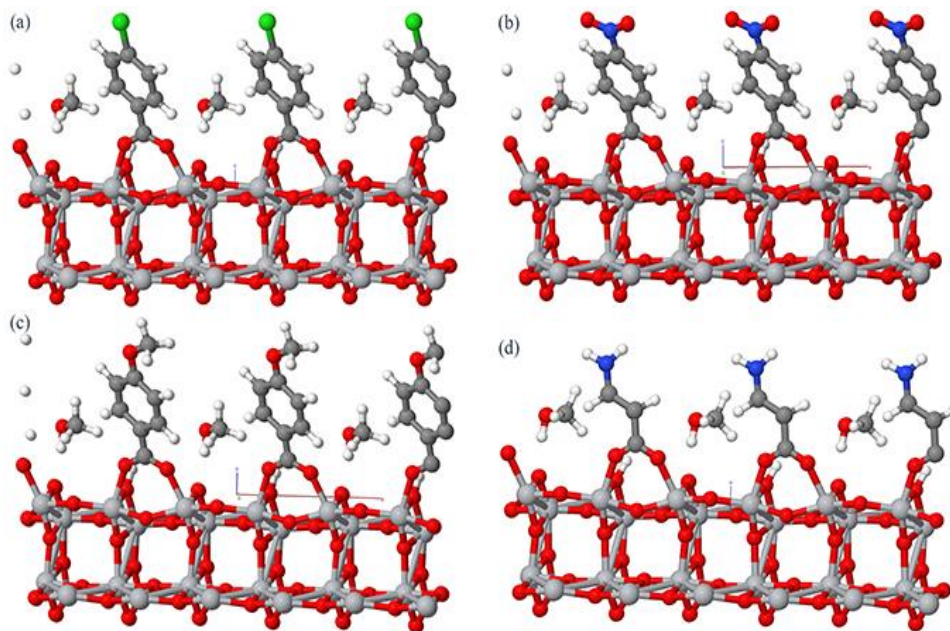


**Figure 1** Structure optimisée des 4 acides adsorbés sur la surface de l'anatase (101). Les atomes de carbone, de titane, d'oxygène, de chlorure et d'azote sont représentés respectivement par des billes grises, argentées, blanches, rouges, vertes et bleues. (a) CBA, (b) NBA, (c) MBA et (d)  $\beta$ -ALA.

Une relation linéaire entre les valeurs de WF et les moments dipolaires des modificateurs adsorbés a été déterminée. De plus, les diagrammes des niveaux d'énergie du TiO<sub>2</sub>, du TiO<sub>2</sub> de surface et aux MAA ont été représentés en fonction des valeurs de niveau de bande d'énergie obtenues.

Nous avons ensuite conçu et fabriqué un photodétecteur UV-A nanostructuré à l'état solide basé sur l'hétérojonction p-n TiO<sub>2</sub>/Spiro-OMeTAD, comme le montre la figure 2. Aucun additif n'a été utilisé dans la couche Spiro-OMeTAD. Le dopage a été réalisé par l'oxydation de la couche dans l'air. Cette approche a permis d'étudier de manière fiable l'effet des acides modificateurs interfaciaux sur la réponse PD. La diode préparée avait un rapport de rectification de 900. Nous avons montré que l'UV-PD pouvait être utilisé en mode auto-alimenté. Nous avons étudié avec soin l'effet des modificateurs interfaciaux sur le fonctionnement et les performances de la DP et nous avons conclu à leur fort impact. Le modificateur NBA a permis d'augmenter la réactivité de l'appareil de 70% par rapport à la jonction p-n vierge. La sensibilité a été mesurée à 69 mA/W à 0 V. Les DP étaient visibles en aveugle en raison de la grande bande interdite (3 eV) du Spiro-OMeTAD et du fait que le rapport de rejet entre les UV-A et la lumière visible était supérieur à deux ordres de grandeur. La sensibilité de l'appareil ( $J_{\text{light}}/J_{\text{dark}}$ ) à 0 V était remarquablement élevée, supérieure à 10<sup>4</sup>. De plus, nous avons constaté que l'allumage et l'extinction de la lumière UV étaient très reproductibles et que leur photo-réaction était stable. Le temps de réponse a été mesuré très rapidement, en dessous de 3 ms. La stabilité à long terme des appareils était importante pour l'application pratique. Le photo-courant d'un UV PD modifié par la NBA est resté pratiquement inchangé après 156 jours de stockage dans des conditions ambiantes.

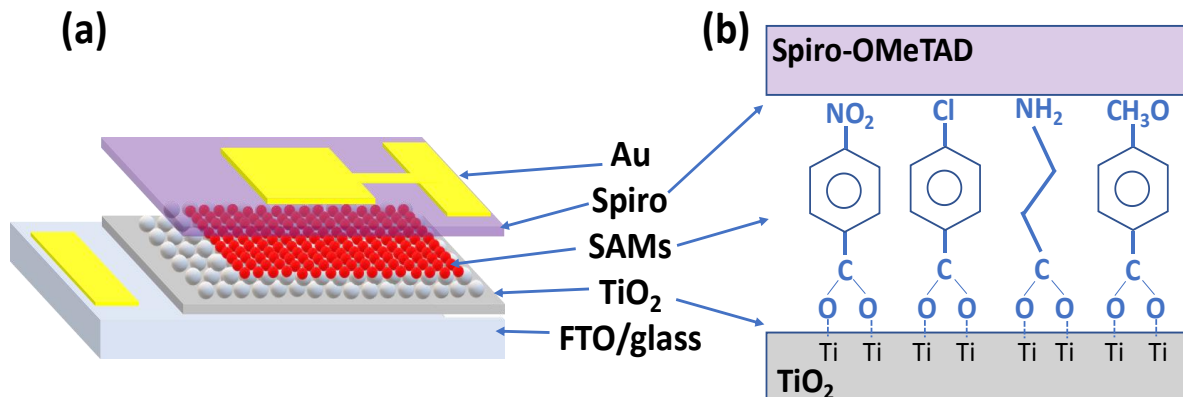


**Figure 2** (a) Vue schématique éclatée du photodétecteur. (b) Schéma de la couche intermédiaire d'acides auto-assemblée entre TiO<sub>2</sub> et Spiro-OMeTAD. De gauche à droite : 4-nitrobenzoate (NBA) ; 4-chlorobenzoate (CBA) ; bêta-alanine (β-ALA) et 4-methoxybenzoate (MBA).

Par l'ingénierie interfaciale, un moment dipolaire a été introduit pour lequel les composantes normales de surface ont été calculées pour les différents acides organiques. Nous avons montré que leur présence induit un pas dans le niveau du vide et que le champ dipolaire formé affecte considérablement le transfert de charge et le photo-courant du dispositif. La plus grande réactivité de la DP modifiée par NBA a alors été expliquée par un meilleur et plus rapide transfert de charge électronique vers le contact électrique sur le  $\text{TiO}_2$ . Pour augmenter la conductivité de la couche Spiro-OMeTAD, des sels de lithium (Li) et de cobalt (Co) ont été ajoutés dans la solution de précurseur. Cependant, l'absorption de la lumière UV a été réduite par le sel de Co et l'interface  $\text{TiO}_2$ /Spiro-OMeTAD a été détruite par le sel de Li, ce qui a perturbé la relation proportionnelle entre les WF de surface et les photo-courants du dispositif.

Au chapitre III, l'effet de la même série de MAA, placées à l'interface  $\text{TiO}_2$ -pérovskite, sur le fonctionnement des cellules solaires basées sur la pérovskite triple-cation  $\text{Cs}_8\text{FAMA}$  a été étudié (figure 3). Nous avons démontré que l'ingénierie de l'interface entre la pérovskite et le titane est importante pour obtenir des CSP très efficaces. En utilisant cette stratégie, nous avons pu préparer des PSC atteignant un PCE de 21,3 % (stabilisé à 20,9 %). Nous avons montré que dans les CSP à triple cation à haute efficacité, la molécule d'acide benzoïque (ACB) fonctionnalisée au chlorure a un effet bénéfique important. Le ACB forme une MAA à la surface du  $\text{TiO}_2$  et est fixée en mode bidenté de pontage. Cette couche intermédiaire n'a pas modifié la morphologie et la cristallinité du film de pérovskite, ce qui a été prouvé par les caractérisations de la microscopie électronique à balayage (MEB) et de la diffusion des rayons X (DRX). Nous avons également montré que son effet ne peut être dû à la gestion du niveau d'énergie de la bande par son moment dipolaire moléculaire, qui est réduit dans une large mesure lorsqu'il est pris en sandwich entre le  $\text{TiO}_2$  et la pérovskite. De plus, une couche de NBA avec un moment dipolaire positif similaire a détruit les propriétés photovoltaïques des dispositifs. Nos recherches expérimentales et théoriques soulignent que l'ACB à l'interface oxyde/pérovskite est bénéfique pour la continuité structurale, la réduction de l'état de piégeage et pour la qualité globale de la pérovskite (figure 3). Nous montrons que la présence d'un substituant halogène sur le ligand (Cl dans le cas de l'ACB) est une condition importante pour établir une liaison stable avec la pérovskite. Nous avons souligné que les interactions chimiques interfaciales sont importantes à considérer pour la conception d'interfaces hautement efficaces et que la conformation relativement fixe du ligand CBA, imposée par sa liaison à la surface de  $\text{TiO}_2$ , a construit une interface CBA- $\text{TiO}_2$  organisée favorablement pour la

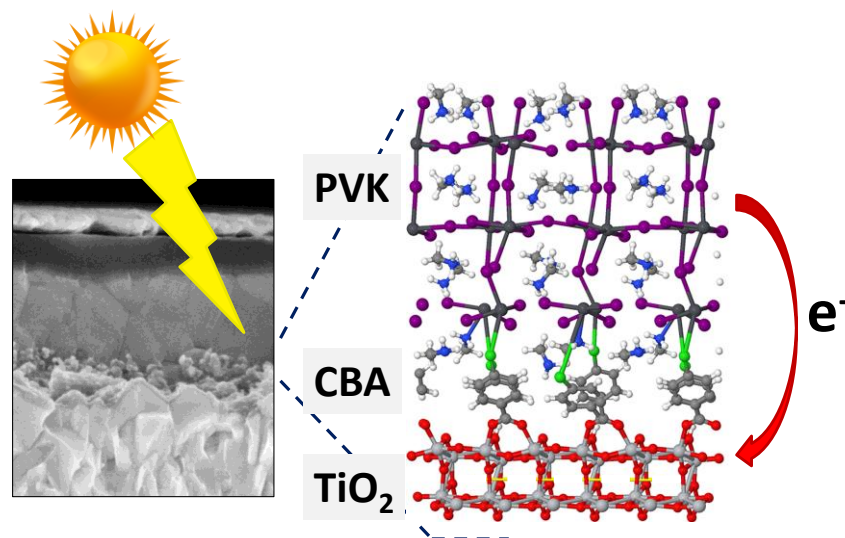


**Figure 3** A gauche : Vue en coupe de la CSP par le MEB. A droite : Modélisation DFT de l'interface.

liaison de la pérovskite. Par modélisation, une injection de charge rapide (24 fs) et un transfert de charge électronique efficace (99,94 %) ont été calculés pour le système TiO<sub>2</sub>/CBA/MAPI. Nous avons également essayé deux autres MAA : l'acide 4-aminobenzoïque (ABA) et l'acide 4-bromobenzoïque (BrBA) dans les CSP. Les résultats montrent que l'ABA peut également améliorer les propriétés photovoltaïques du dispositif malgré que l'ACB reste meilleur.

Un examen plus attentif des courbes d'évolution de l'efficacité montre que l'efficacité de tous les appareils a augmenté au cours des premiers jours. Une période de maturation surprenante est observée au début. Pour élucider ce phénomène d'amélioration des performances, des mesures de photoluminescence (PL) ont été effectuées. L'intensité de la PL est environ dix fois plus élevée après les quelques jours de stockage. Par conséquent, pendant cette étape de maturation, la qualité structurale du film pérovskite est améliorée, les défauts sont recuits / passivés et la recombinaison radiative augmente. Pour étudier l'effet des MAA sur la stabilité de la pérovskite, nous avons élargi l'effet en diminuant l'épaisseur de la couche de pérovskite. Le résultat montre que seules la NBA et  $\beta$ -Alanine peuvent améliorer la stabilité des couches de pérovskite.

Le Cs<sub>8</sub>FAMA et le MAPbI<sub>3</sub> ont une bande interdite de 1,6 eV, ce qui limite le courant photoélectrique à 25 mA/cm<sup>2</sup> maximum, indépendamment des MAA que nous avons utilisés. La bande passante la plus appropriée pour les cellules solaires à simple jonction devrait être proche de 1,3 eV. Dans le prochain chapitre, nous nous concentrerons sur le développement de CSP à

bande interdite plus faible (1,48 eV) basées sur la pérovskite  $\text{FAPbI}_3$ .

Dans le chapitre IV, nous avons développé l'utilisation du chlorure de méthylammonium comme additif dans des solutions de précurseurs de cations organiques mixtes à assez faible concentration. Il est démontré que le  $\text{MACl}$  sert de médiateur pour la croissance des couches. Les films résultants étaient uniformes, compacts, sans trous et constitués de grains de cristaux de pérovskite de taille remarquablement grande. Par cette technique, une petite quantité de cation  $\text{MA}$  a été incorporée dans  $\text{FAPbI}_3$ , stabilisant la phase  $\alpha$  pure. Lorsque les quantités de  $\text{MACl}$  atteignaient 40 % en molaire dans la solution de précurseur, les films de pérovskite obtenus présentaient des pics aux mêmes angles dans les modèles de rayons X. Les courbes UV correspondantes et les courbes PL normalisées en régime permanent se chevauchaient, respectivement. Ces résultats indiquent que la composition finale de la pérovskite pourrait être indépendante de la quantité de  $\text{MACl}$  ( $\geq 40$  mol%) dans la solution de précurseur. La composition exacte a été déterminée par spectroscopie de magnétron nucléaire. Il ne resterait que 6 mol% de cation  $\text{MACl}$  dans le film de pérovskite ( $\text{FA}_{0.94}\text{MA}_{0.06}\text{PbI}_3$ ). L'excès a été éliminé par sublimation et dégradation. La technique de croissance présentée est fiable, robuste et donne des dispositifs efficaces sur une large gamme de concentration d'additifs. La meilleure fraction molaire  $\text{MACl}$  se trouve à 48 mol.%. Pour augmenter encore le PCE des cellules solaires, un traitement avec une solution de  $\text{PEAI}$  a été mis en œuvre. Ce traitement, sans aucune étape de recuit thermique, conduit à la formation spontanée

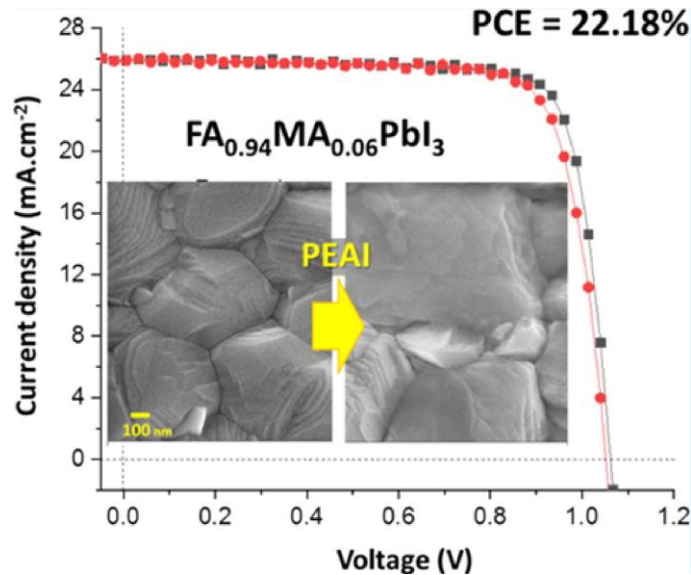


**Figure 4** Courbes  $J-V$  du meilleur dispositif. L'encadré présente les morphologies des films pérovskites  $\text{FA}_{0.94}\text{MA}_{0.06}\text{PbI}_3$  avec et sans traitement  $\text{PEAI}$ .

de pérovskite  $(\text{PEA})_2\text{PbI}_4$  à la surface. La morphologie des films traités au PEAI présentait une couche floue à la surface, qui remplissait les joints de grains et diminuait éventuellement la rugosité de surface. On a également constaté que cette couche tampon favorisait le transfert de charges (les trous vers le HTL) et réduisait la recombinaison causée par les défauts à l'interface pérovskite/HTL. Dans l'ensemble, les dispositifs optimisés avaient un PCE supérieur à 22,1 %. Le rendement élevé était principalement dû à l'amélioration considérable du courant photoélectrique (jusqu'à 26  $\text{mA}/\text{cm}^2$ ), attribuée à la bande interdite plus étroite qui élargit la plage d'absorption de la lumière. La stabilité du dispositif  $\text{FA}_{0.94}\text{MA}_{0.06}\text{PbI}_3$  sous une intensité de 1 soleil a été remarquablement améliorée par rapport aux dispositifs  $\text{MAPbI}_3$  et  $\text{Cs}_8\text{FAMA}$  que nous avons étudiés au chapitre III. Leur stabilité dans des conditions d'humidité élevée a également été testée. Le dispositif  $\text{FA}_{0.94}\text{MA}_{0.06}\text{PbI}_3$  était stable durant 23 h alors qu'une diminution rapide a été observée entre 23 h et 29 h.

Une étude complète des systèmes par spectroscopie d'impédance a été réalisée. La modification des spectres d'impédance dans les premiers jours de stockage du dispositif correspond à une étape de maturation qui implique des réactions à l'interface (ou aux interfaces). La capacité haute fréquence a été indépendante du vieillissement de la CSP et le traitement a été attribué à faible  $V_{\text{appl}}$  à la relaxation diélectrique intrinsèque de la pérovskite. Les résistances haute fréquence  $R_2$  et  $R_4$  ont été analysées comme des résistances de recombinaison et  $C_4$  comme une capacité de recombinaison. De plus, nos résultats indiquent que  $R_2$  et  $C_4$  sont probablement liés à des centres de recombinaison localisés près de l'interface alors que  $R_4$  correspondrait à une résistance de recombinaison interfaciale. Dans l'ensemble, les variations de  $R_2$ ,  $R_4$  et  $1/C_4$  expliquent les variations de FF et de  $V_{\text{OC}}$  des CSP avec le pourcentage molaire de  $\text{MACl}$  et le traitement PEAI. La puissance de sortie des dispositifs produits a été remarquablement stable. Ces CSP se sont avérés résistants aux contraintes électriques, à l'irradiation lumineuse et à l'humidité.

Cependant, la stabilité attendue dans un environnement à forte humidité n'a pas été observée dans ces cellules  $\text{FAMAPbI}_3$ . On peut attribuer le fait que les ions  $\text{MA}^+$  instables étaient facilement libérés de la structure et que la  $\text{FAPbI}_3$  en phase  $\delta$  était plus stable à température ambiante. Pour réaliser la stabilité à long terme contre l'humidité, nous avons développé au chapitre V des matériaux 2D hydrophobes introduits dans la structure 3D de la pérovskite.

Dans le chapitre V, les films pérovskites 2D/3D basés sur BEI et les dispositifs photovoltaïques ont été systématiquement étudiés. Nous avons fabriqué une série de films pérovskites RP avec la formule moléculaire  $BE_2FA_{n-1}Pb_nI_{3n+1}$  ( $n = 1, 2, 3, 5, 9, 20, \text{ et } \infty$ ). Ensuite, les films ont d'abord été caractérisés par DRX, spectroscopie d'absorption UV et spectroscopie PL en régime permanent, afin d'analyser la composition de la phase. Les résultats ont montré que les films pérovskites quasi 2D ( $n \leq 5$ ) étaient composés de phases 2D mixtes, qui appartiennent à  $n = 2, n = 3, n = 4, \dots$  et ainsi de suite. Les phases 2D avec des valeurs  $n$  plus petites ont tendance à se former au bas du film, ce qui fait que la pérovskite 3D ne peut pas être bien protégée. Plus les valeurs  $n$  sont grandes, plus les films pérovskites 2D/3D sont homogènes. La morphologie des films de pérovskite 2D/3D a changé, passant de structures poreuses avec des cristaux dendritiques à des films denses avec des cristaux cubiques à mesure que les valeurs de  $n$  augmentent. Les CSP 2D/3D correspondantes ont été réalisés, et leur efficacité a également augmenté avec les valeurs  $n$ . Après optimisation du processus de fabrication, les PSC quasi-3D et les CSP quasi-2D ont produit les meilleurs rendements de 19,6 % et 17,3 %, respectivement.

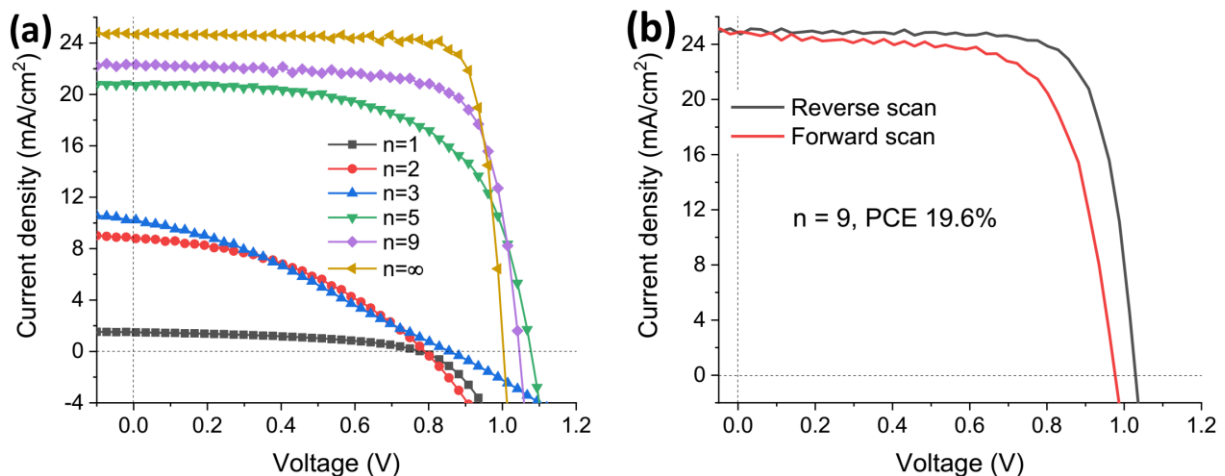


**Figure 5** (a) Courbes  $J$ - $V$  des CSP 2D/3D pour diverses valeurs  $n$  ; (b) Courbes  $J$ - $V$  des balayages avant et arrière pour la meilleure cellule 2D/3D

Les films  $n = 5$  et  $n = 9$  ont été les plus stables de cette série selon le test de stabilité. Les films pérovskites 2D/3D avec des matériaux 2D plus hydrophobes dans la structure n'ont pas présenté une meilleure stabilité, selon le test de vieillissement de ces films en conditions ambiantes. Ce résultat a confirmé notre prévision selon laquelle les phases inférieures de pérovskite 2D/3D avec

des valeurs  $n$  inférieures ne protégeraient pas efficacement les films de pérovskite. Les films pérovskites 2D/3D homogènes avec des valeurs  $n$  appropriées peuvent éventuellement fabriquer des cellules solaires avec une efficacité et une stabilité élevées. Ensuite, la stabilité des dispositifs  $n = 5$  et  $n = 9$  a été testée dans des conditions d'humidité élevées mais également en conditions ambiantes. Le dispositif  $n = 9$  a présenté une meilleure stabilité dans des conditions d'humidité élevée dans les 50 heures, alors qu'il n'a pas montré d'avantages dans un test de stabilité plus long de 27 jours dans les conditions ambiantes. Mais l'aspect du dispositif était plus stable que celui de la pérovskite 3D. Malheureusement, le dispositif  $n = 9$  présentait également une mauvaise stabilité, sous un soleil continu. Nous avons supposé que les parties 2D  $(\text{BE})_2\text{PbI}_4$  dans les films étaient instables. Deux autres phases non-pérovskites ( $\heartsuit$  et  $\clubsuit$ ) liées à la BEI et à la  $\text{PbI}_2$  se sont avérées exister dans les films  $n = 1$ . Le travail est toujours en cours. Ces recherches ont donné lieu à d'autres développements qui conduisent à un brevet en instance.

Au final, une conclusion générale et des perspectives ont été rédigées. Pour les perspectives, nous avons proposé plusieurs stratégies, en termes d'ingénierie des interfaces, d'ingénierie de la composition des pérovskites et de HTM à faible coût, pour améliorer la propriété photovoltaïque et la stabilité des PSC. Pour l'interface  $\text{TiO}_2$ /pérovskite, les acides fluorés pourraient être considérés comme les nouvelles MAA. Le groupe d'ancrage des carboxyles peut être conservé en raison de leur propriété de passivation des défauts sur le  $\text{TiO}_2$ . D'autre part, les pertes d'efficacité à l'interface pérovskite/HTM ont également occupé une grande partie et ont peut-être été réduites. Le post-traitement PEAI pourrait apparemment améliorer l'efficacité des cellules alors qu'il ne permet pas d'améliorer la stabilité du dispositif. Les matériaux 2D fortement hydrophobes, tels que le pentafluorophényléthylammonium (4F-PEAI) et l'iodure de p-méthoxyphényléthylammonium (CH<sub>3</sub>O-PEAI) sont intéressants. Les pérovskites 2D ayant une énergie de formation plus élevée sont considérées comme ayant une meilleure stabilité. Il est également important de concevoir les matériaux de post-traitement sur la base de la structure HTM. Pour l'ingénierie de la composition des pérovskites, la pérovskite  $\text{FAPbI}_3$  a une bande interdite appropriée et une stabilité thermique plus élevée. Il est suggéré de conserver le cation  $\text{FA}^+$  dans la structure. Pour inhiber sa transformation en phase  $\delta$  et améliorer sa stabilité, des cations de métaux alcalins inorganiques, tels que  $\text{K}^+$ ,  $\text{Rb}^+$ ,  $\text{Cs}^+$ , peuvent être envisagés. Pour fabriquer des films de pérovskite de haute qualité, les additifs appropriés dans les solutions de précurseurs sont d'une grande importance, déterminant ainsi les propriétés photovoltaïques des dispositifs. À notre connaissance, l'ion  $\text{Cl}^-$  est

un bon candidat. Quant au HTM à bas prix, le Spiro-OMeTAD et le poly(triarylamine) (PTAA), couramment utilisés, sont assez chers. Leur conductivité dépend de l'ingénierie du dopage, qui sacrifie leur stabilité. Les HTM inorganiques et les HTM polymères sont notables, comme l'oxyde de nickel (NiO), le poly(3-hexylthiophène-2-5-diyle) (P3HT), etc.

## General introduction

Since the first industrial revolution, energy consumption has followed a rapid growth to satisfy the development of modern human society. With the coming exhausted fossil energies, such as oil, gas, and coal, renewables will be indispensable in the future. Solar energy, as a clean and inexhaustible source, attracts extensive attention. For instance, photovoltaic devices are one of the most important applications because they can directly convert light energy into electricity.

Photovoltaic technologies have been developed for decades. The representative product is silicon solar cell, which still dominates the photovoltaic market. However, the need of more efficient and lower-cost solar cells, encourages people to develop new photovoltaic devices. Since about ten years ago, organic-inorganic hybrid perovskite (OIHP) materials have been shown to process excellent photovoltaic properties and they might be the next-generation photovoltaic materials.

In this thesis, we have investigated OIHP solar cells in terms of interface modification and composition engineering. Chapter I is an introduction for our research background. Basic semiconductor knowledge, working principle of photovoltaic devices and a bibliographic review are given. Because our research work also includes light detection, a brief introduction to ultraviolet (UV) photodetectors (PDs) were written at the end of Chapter I.

In Chapter II, we present a novel approach for boosting the performances of self-powered UV photodetectors. A series of dipolar molecules that can form a monolayer on titanium dioxide ( $\text{TiO}_2$ ) have been employed for adjusting the surface work function. Energy band level alignment facilitates the charge injection in the UV PDs. The experimental results have been substantiated by density functional theory (DFT) modeling.

In Chapter III, the monolayers adsorbed onto  $\text{TiO}_2$  films, described in Chapter II, have been used as buffer layers in OIHP solar cells. Triple- and double- cations mixed OIHPs have been employed as the light absorber, respectively. The efficiencies of the solar cells have been boosted by chlorine terminated monolayer. The analysis of the best system has been completed by DFT modeling the entire interface:  $\text{TiO}_2$ , monolayer, and perovskite layer.

In Chapter IV, formamidinium lead tri-iodine ( $\text{FAPbI}_3$ ) has been employed as the OIHP layer because of its narrow bandgap and excellent thermal stability. Methylammonium chloride ( $\text{MACl}$ ) has been used as an additive to improve the quality of the perovskite layer. The obtained perovskite

layers have been treated with 2-Phenylethylamine hydroiodide (PEAI) for reducing the defects and increasing the charge injection. We have obtained highly efficient solar cells with efficiencies greater than 22%. The electric responses for these cells have been studied by impedance spectroscopy analysis.

In Chapter V, we have systematically investigated mixed-dimensional (MD) OIHPs for the light absorber layer due to their excellent stability against moisture. The MD OIHP film stability and cell stability have been discussed separately. Highly efficient and stable perovskite solar cells are presented in this Chapter.

A general conclusion and perspectives are provided at the end of this dissertation.

## Chapter I. Context

Optoelectronics is the combined study of optics and electronics. The applications are everywhere in modern human life, such as photodetectors (PDs), photovoltaics (PVs), optical amplifiers, photonic integrated circuits, lasers, light-emitting diodes (LEDs). They are called optoelectronic devices and are electrical-to-optical or optical-to-electrical transducers. For instance, a photodetector is a key device in the front end of an optical receiver that converts the incoming optical signal into an electrical signal. In this process, semiconductors play an irreplaceable role, which is responsible for harvesting photons and then producing electron-hole pairs.

### I.1 Semiconductors

The discovery of electricity brought new cognitions that metals are good conductors while nonmetals are poor conductors. The latter were called insulators. Metallic conductivity ranges typically between  $10^6$  and  $10^4$  S.cm<sup>-1</sup>, while typical insulators have conductivities less than  $10^{-10}$  S.cm<sup>-1</sup>. Some materials with conductivities ranging between  $10^4$  and  $10^{-10}$  S.cm<sup>-1</sup> are defined as semiconductors. However, real situations are more complex. For example, substances such as alkali-halides whose conductivity is due to electrolytic decomposition must be excluded. Chemically uniform, homogeneous substances are more valuable to discuss their conductivities. Conductivity is just a macro-phenomenon. The fundamental distinction is that semiconductors and insulators have an energy bandgap while metals have no such gap as shown in Figure I.1. In the case of organic semiconductors, the bandgap lies between the highest occupied molecular orbital (HOMO) and lowest unoccupied molecular orbital (LUMO). The conductivity of semiconductors can be high, approaching that of metals in the case of suitable doping. While it can also be low, approaching that of insulators, when the temperature approaches to absolute zero.<sup>1</sup>

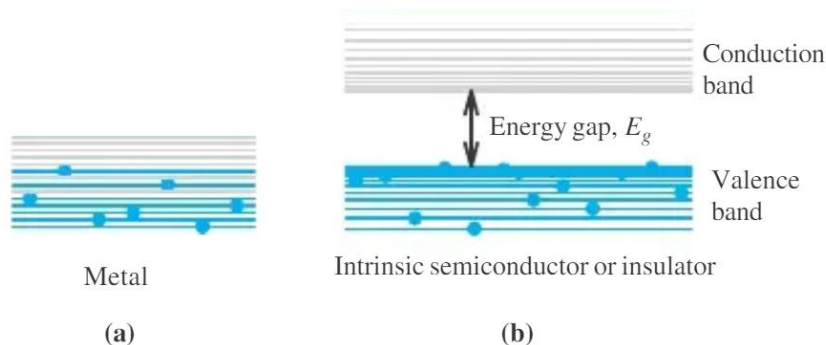


**Figure I. 1** Energy-band diagrams for (a) a metal and (b) an intrinsic semiconductor or an insulator.<sup>2</sup>

## I.1.1 Types of semiconductors

### I.1.1.1 Inorganic semiconductors

Inorganic semiconductors are made from non-carbon-based materials such as silicon, gallium arsenide (GaAs). The 20<sup>th</sup> century has been the golden era for the development of inorganic semiconductors due to the quick development of computer and information technology. Silicon is the most important element semiconductor. It has been studied extensively and widely used in commercial electronic products (Figure I.2c). Another important application is silicon solar cells (Figure I.2a), which has been dominating the photovoltaic markets for decades.

The single silicon crystal has a covalently bonded diamond cubic structure as shown in Figure I.2d. A silicon atom has four covalent bonds that create a tetrahedral organization in the crystal. The unit cell can be imagined as two face-centered cubic (fcc) cells with one cell offset by  $[a/4, a/4, a/4]$ . The offset is more clearly visualized on the top view. Compound semiconductors, typically III-V compounds such as GaAs, indium antimonide (InSb), indium phosphorus (InP), titanium dioxide (TiO<sub>2</sub>) and II-VI compounds such as zinc sulfide (ZnS) or zinc oxide (ZnO), have also met important applications in optoelectronic devices, such as light emitting diodes (LED), photovoltaics (PVs), lasers and so on (Figure I.2b).

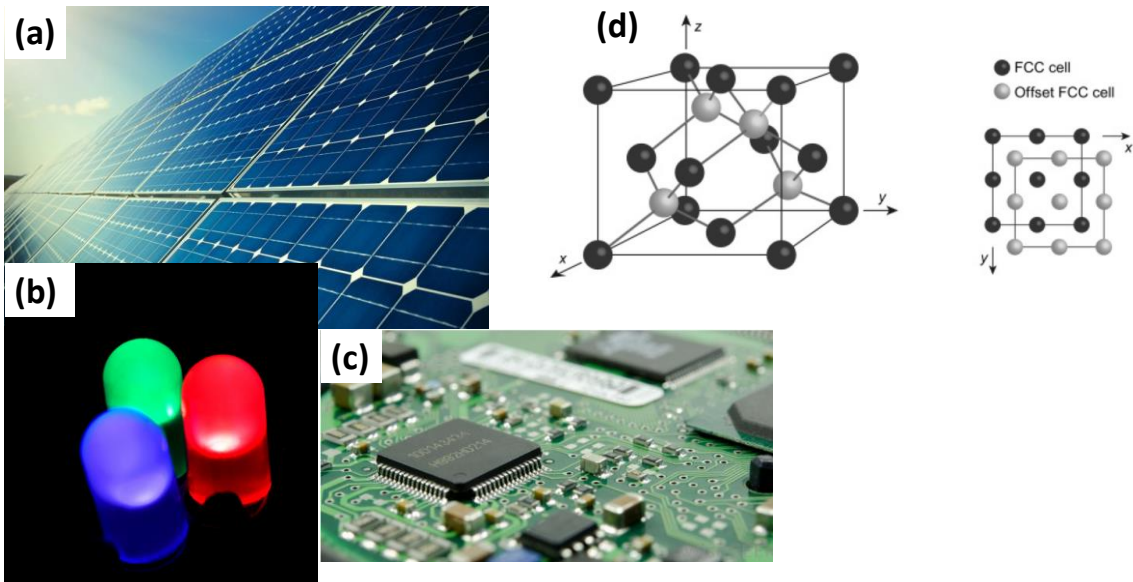


**Figure I. 2** (a) Silicon solar cell, (b) Light emitting diode, (c) Integrated circuit, (d) Diamond crystal structure of silicon.

### 1.1.1.2 Organic semiconductors

Organic semiconductors are a special class of semiconductors that are mainly composed of carbon elements. Because all the organic compounds have bandgaps, they are naturally semiconductors or insulators. The conducting nature of organic semiconductors and inorganic semiconductors can be distinguished (Section I.1.2).

According to the structure of the materials, organic semiconductors can be sorted into amorphous molecular films, molecular crystals, and polymer films (Figure I.3a-c). Amorphous molecular films are generally fabricated through evaporation or spin-coating. Crystallized organic semiconductors are composed of atoms held together by van der Waals interaction. Due to the compact and regular structures of crystallized organic semiconductors, they have higher charge mobilities. Polymer films are defined as a chain of covalently coupled and repeated molecular units (> 100 units). In general, polymer films have large bandgaps and amorphous structures with superior stretchability and thermostability.

Thanks to their versatile properties, organic semiconductors have extensive applications. In optoelectronic devices, for instance, graphene and fullerene derivatives with superior conductivity can be used as electron transfer materials to improve the injection of electrons.<sup>3</sup> Another important application is in flexible devices. For instance, they can be used as the substrates and electrodes in flexible solar cells and photodetectors as shown in Figure I.3a.<sup>3,4</sup>

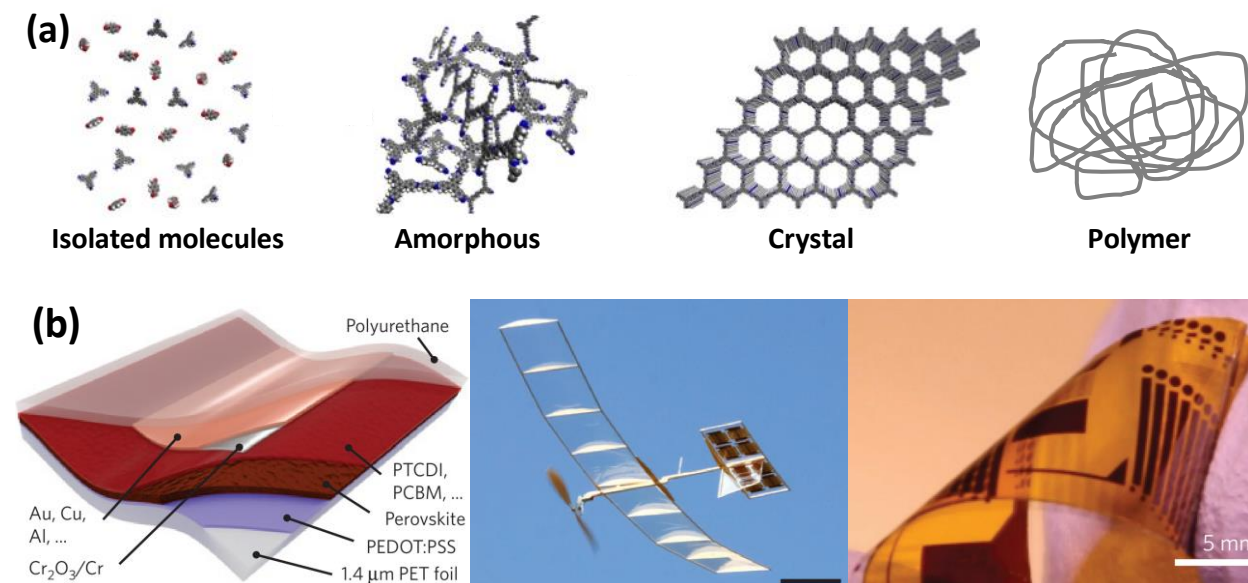


**Figure I. 3** (a) The structures of organic semiconductors. (b) The applications of organic semiconductors: flexible solar cells and photodetectors.<sup>3,4</sup>

### 1.1.1.3 Organic-inorganic hybrid semiconductors

The advantages of organic and inorganic semiconductors can be combined in organic-inorganic hybrid semiconductors (OIHSs). In definition, OIHSs are composed of carbon-based and inorganic elements. Due to the large variety of organic and inorganic materials systems, the number of combinational products OIHSs is extremely enormous. Various properties were found and some of them have already been applied in human life. For instance, Figure I.3b presents a light absorber layer, which is composed of organic-inorganic hybrid perovskites (OIHPs).

In this thesis, we have mainly worked on the latter materials with a 3D structure and  $ABX_3$  as a general formula. Materials with the well-structured periodic placement of atoms are called crystals whether the materials are inorganic, organic, or hybrid organic/inorganic. The smallest assembly of atoms that can be repeated to form the entire crystal is defined as a primitive cell. The primitive cell of 3D OIHPs can be cubic ( $a = b = c$ ), tetragonal ( $a = b \neq c$ ) or orthorhombic ( $a \neq b \neq c$ ). It generally depends on the temperature and ions in the structure (Figure I.4a-c). The detailed information will be provided in Section I.31.

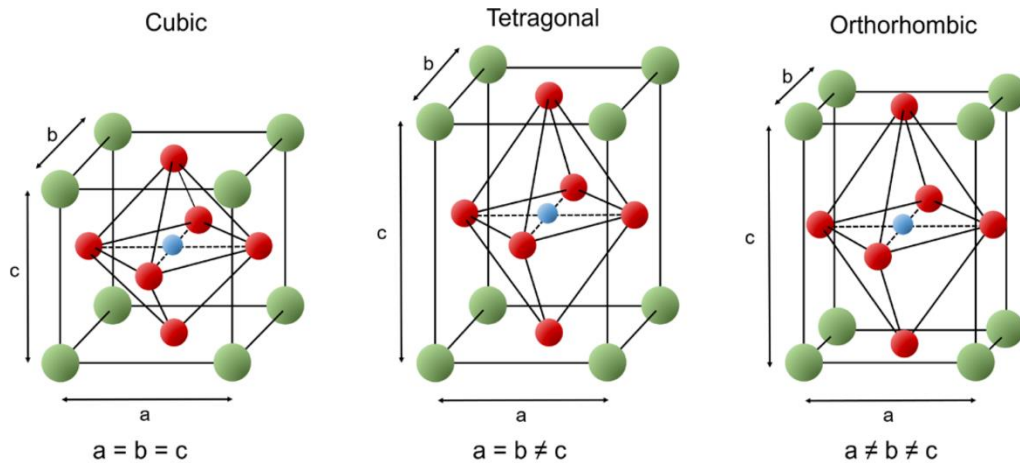


**Figure I. 4** Unit cells of (a) Simple cubic, (b) tetragonal and (c) orthorhombic phases of OIHPs.<sup>5</sup>

To better describe the shape and space position of the crystal, the positions of atoms and different crystallographic planes in terms of lengths of the unit-cell edges,  $a$ ,  $b$ , and  $c$  are recorded in a 3D coordinate system. Any plane in space can be described by the equation:

$$h \frac{x}{a} + k \frac{y}{b} + l \frac{z}{c} = 1 \quad (\text{I.1})$$

where  $a/h$ ,  $b/k$ , and  $c/l$  are intercepts of the  $x$ -,  $y$ - and  $z$ -axes, respectively. Characteristic crystallographic planes are defined by a set of integers,  $(hkl)$ , known as Miller's indices. This will be important for the analysis of the X-ray diffraction (XRD) data. Three main crystallographic planes and directions are presented in Figure I.5.

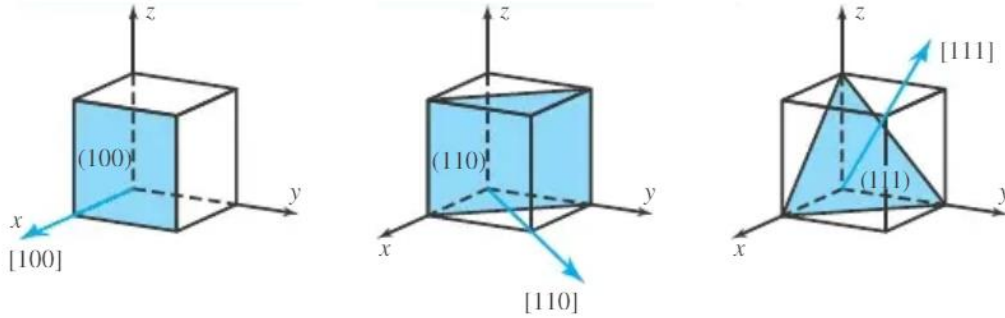


**Figure I. 5** Important directions in cubic crystals.<sup>2</sup>

## I.1.2 Two types of current carriers in semiconductors

### I.1.2.1 Electrons and holes

At a temperature of 0 K, all the electrons are bound through covalent bonds, which is the reason that semiconductors are insulators at 0 K (Figure. I.6a). With increasing temperature, a certain number of covalent bonds can be broken and release electrons to carry the charge away. Meanwhile, positive holes appear at their bonds structure. We call the mobile charged particles the current carriers. The electrical properties of a semiconductor directly depend on the number of current carriers per volume unit or the concentration of carriers. In intrinsic semiconductors, the carrier concentration is  $n_i$ .  $n_i$  is a constant for a given semiconductor at a given temperature. For Si, GaAs, and Ge, the room-temperature  $n_i$  values are  $1.02 \times 10^{10} \text{ cm}^{-3}$ ,  $2.1 \times 10^6 \text{ cm}^{-3}$ , and  $2.4 \times 10^{13} \text{ cm}^{-3}$ , respectively. In addition to temperature, other types of energies, such as pressure, magnetic field, and light, can also break the covalent bonds and release electrons and holes.<sup>2</sup>

For organic semiconductors, the conductivity is extrinsic and results from the injection of charges at electrodes, from intentional and unintentional doping and from the dissociation of photogenerated electron-hole pairs that are bound by their mutual coulomb attraction. This coulomb attraction is significant in organic semiconductors due to their low dielectric constant (typically  $\epsilon_r = 3.5$ ). In the case of inorganic semiconductors, the dielectric constant is larger

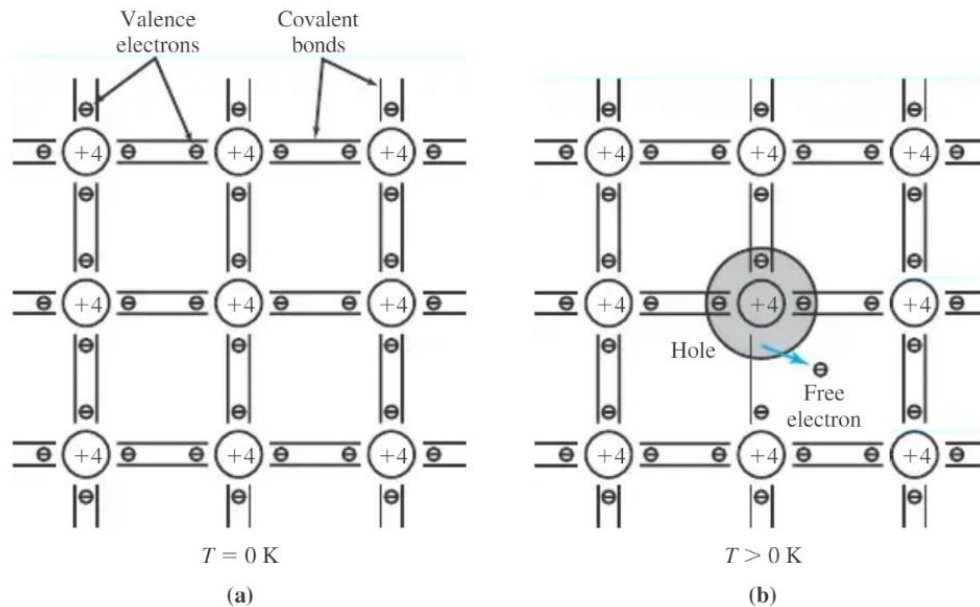


**Figure I. 6** Two dimensional diagrams of Silicon crystals at (a)  $T = 0$  K, all electrons are bounded and (b) for  $T > 0$  K, some covalent bonds are broken and form holes and electrons.<sup>2</sup>

(typically  $\epsilon_r = 11$ ). So coulomb effects between electron and holes are weaker and less important. It results in that light absorption creates free electrons and holes.

$\pi$ -bonds play an essential role in the conductivity of organic semiconductors. It originates from the unique nature of carbon that can form chains, rings, or branches by stable covalent  $\sigma$ - or  $\pi$ -bonds. The  $\sigma$ -bonds are formed by the  $2s$ - $2p$  hybrid orbitals between the adjacent atoms, whereas the  $\pi$ -bonds are formed by the overlap between  $2p$  orbitals of adjacent atoms that do not participate in the formation of  $\sigma$ -bonds (Figure I.7a).

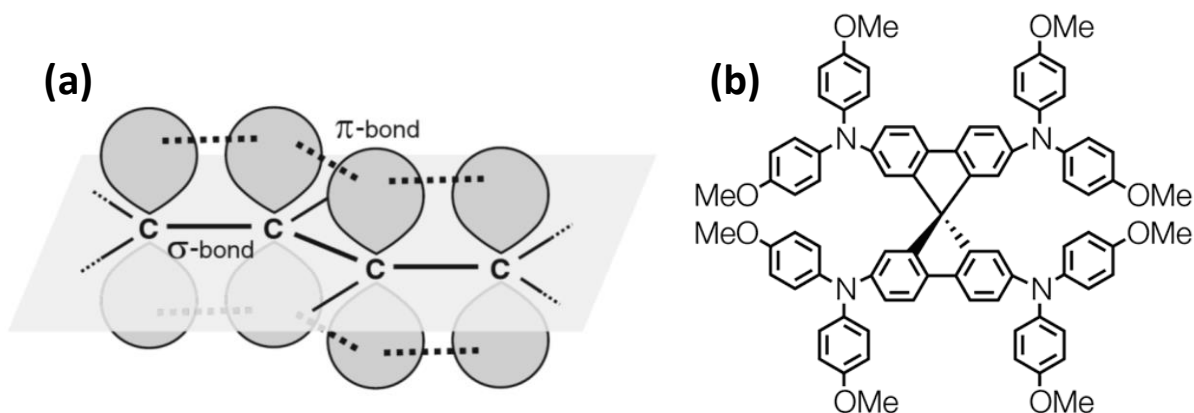


**Figure I. 7** (a) Schematic of a linear chain of carbon connected with  $\sigma$  and  $\pi$  bonds; (b) a molecular structure of Spiro-OMeTAD.

For instance, the molecular structure of Spiro-OMeTAD (2,2',7,7'-Tetrakis[N,N-di(4-methoxyphenyl)amino]-9,9'-spirobifluorene) is presented in Figure I.7b. The numerous benzene rings provide a channel for electron transfer. The amorphous films prepared by spin coating are often used as hole transporting materials in solar cells. In this thesis, it is also used as a light absorber layer in photodetectors.

The conductivities of OIHPs are closer to that of inorganic semiconductors. However, their dielectric constant ( $\epsilon_r = 30-70$ ) is much higher than common inorganic semiconductors, which caused an easy separation of the photogenerated electrons and holes in OIHPs.

### *1.1.2.2 N-type and P-type doping*

Semiconductors with technologically changed concentrations of free electrons or holes are called doped semiconductors. In the process of doping, some silicon atoms are replaced by other types of atoms, which are called impurity atoms or doping atoms. For instance, a silicon atom can be replaced by an atom in the fifth column of the periodic table, such as phosphorus, as shown in Figure I.8a. The phosphorus atom has five electrons in the outer orbit (valence electrons). When phosphorus occupies the Si-site, covalent bonds with the four neighboring silicon atoms are formed. There is no place for the fifth electron. So, it leaves the outer orbit of phosphorus to look for a better position. In other words, the fifth phosphorus electron is easily liberated by thermal energy and becomes a free electron. Therefore, Si replaced by phosphorus increases the concentration of free electrons. This process is called N-type doping. The doping elements are called donors and the concentration of donor ions is denoted by  $N_D$ . To distinguish from holes and electrons in the figure, the immobile ion charges are marked by squares.

P-type doping is formed when some silicon atoms are replaced by atoms from the third column of the periodic table, for instance, boron atoms. A boron atom has three valence electrons, which are taken to form three covalent bonds with the neighboring silicon atoms. To satisfy the fourth covalent bond, every boron atom will capture a thermally generated free electron (generated by breakage of covalent bonds among silicon atoms), hence creating a positive mobile charge named hole as shown in Figure I.8b.

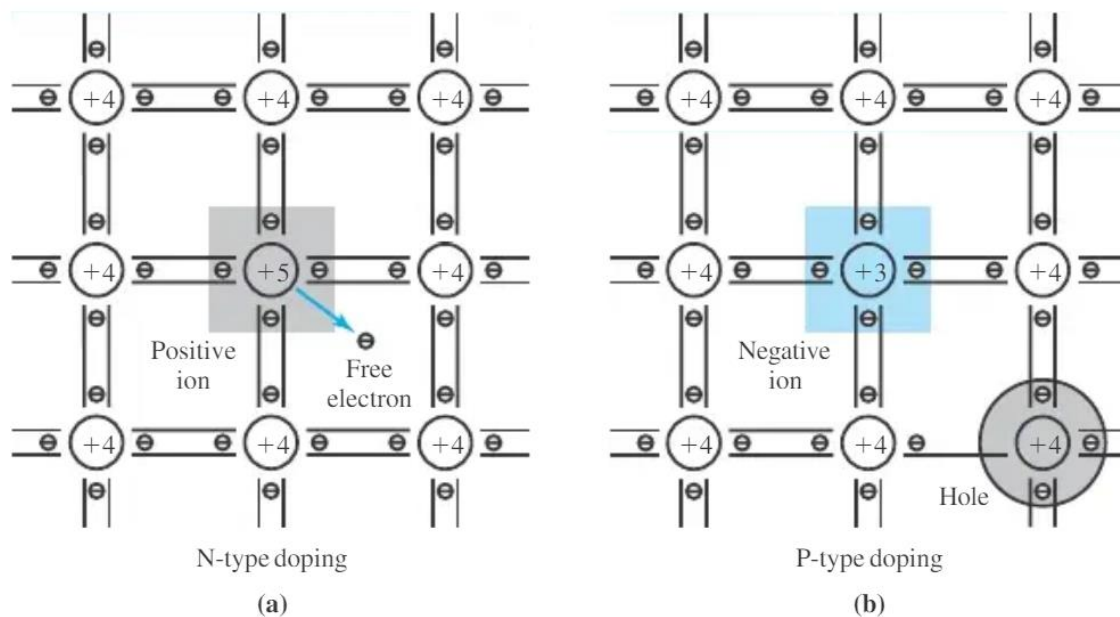


**Figure I. 8** (a) N-type doping and (b) P-type doping. Immobile ion charges are marked with squares.<sup>2</sup>

Controlled doping can be conducted easily in inorganic semiconductors. Yet it encounters serious problems for organic semiconductors. For an intrinsic organic semiconductor, the number of electrons in LUMO (lowest unoccupied molecular orbital) level equals to the number of holes in HOMO (highest occupied molecular orbital) level. P-type doping requires the transfer of an electron from the filled HOMO of the host to the LUMO of the dopant at no or only little energy expense as illustrated in Figure I.9. Correspondingly, the HOMO of the dopant has to be closed to the LUMO of the host to promote n-type doping. This puts serious constraints to the mutual energy levels. In most organic materials, the HOMO is around -5 to -6 eV below the vacuum level, which

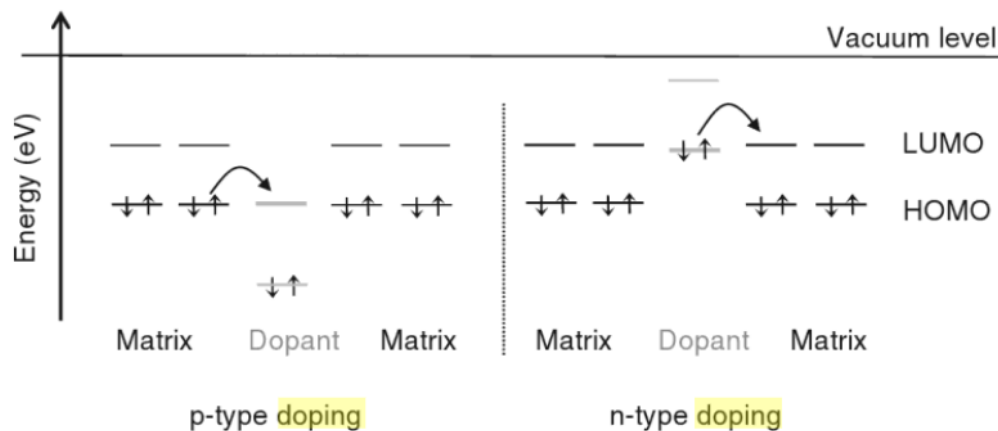


**Figure I. 9** Illustration of the molecular orbital levels for p-type doping and n-type doping.<sup>6</sup>

indicates that the LUMO of the dopants should be at a similar level for p-type doping. Such a strong electron acceptor is not easy to find. For n-type doping, a dopant with very low HOMO (-2.5 to -3.5 eV) is difficult to find.<sup>6</sup>

An efficient way is doping by protons or small metal cations  $\text{Li}^+$  (Lithium). For example, the doping of polyaniline (PAn) by proton is depicted in Figure I.10. The PAn is first protonated then the charges spread to other parts of the molecular chain by intramolecular charge transfer. In this thesis, the Spiro-OMeTAD has been doped by Li-salt.  $\text{Li}^+$  acts as a dopant for the increase of the conductivity.

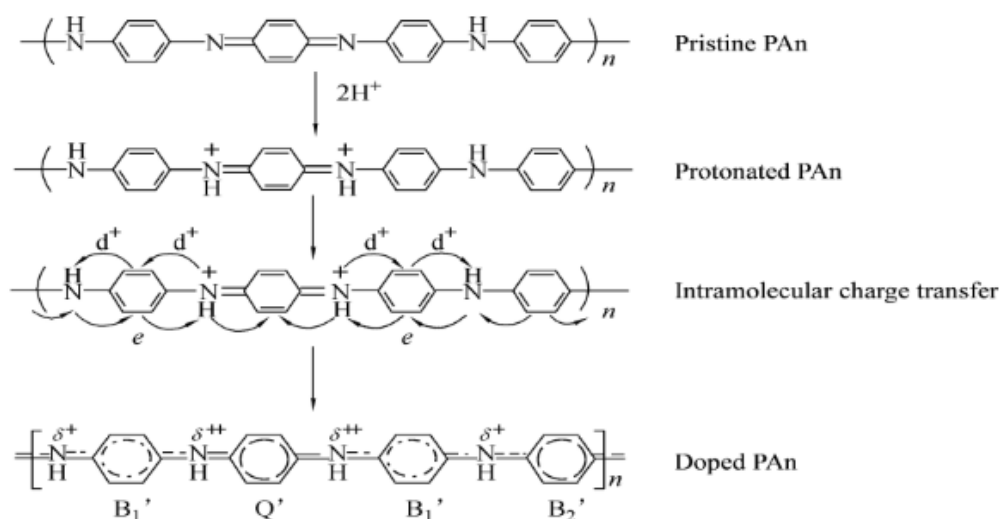


**Figure I. 10** The process of polyaniline (PAn) doping by the proton.

### I.1.3 Charge generation and recombination

Electron-hole generation is a process that creates free electrons and holes. The opposite process of annihilation of free electrons and holes is called charge recombination. In optoelectronic devices, charge generation and recombination are one of the most important steps. The energy band model can help us to understand this process.

#### I.1.3.1 Energy band model

To define charge carriers and introduce some of their fundamental properties, the atomic-bond model has been possibly used alone. However, an electronic device operates not only under the relationship of electric current. The inseparable concept is voltage, which is an electric-potential difference ( $\phi$ ). This electric potential ( $\phi$ ) is directly related to potential energy ( $E$ ) through the

relationship of  $E = -q\phi$ . The simple atomic-bond model does not express the energy state of the current carriers, so it is not sufficient to understand the operation of the semiconductor devices. The energy-band model has been built for the convenient descriptions of the phenomena observed in semiconductor devices. The theory is based on a deep understanding of crystal structure and wave function. For the details, see the book [2].

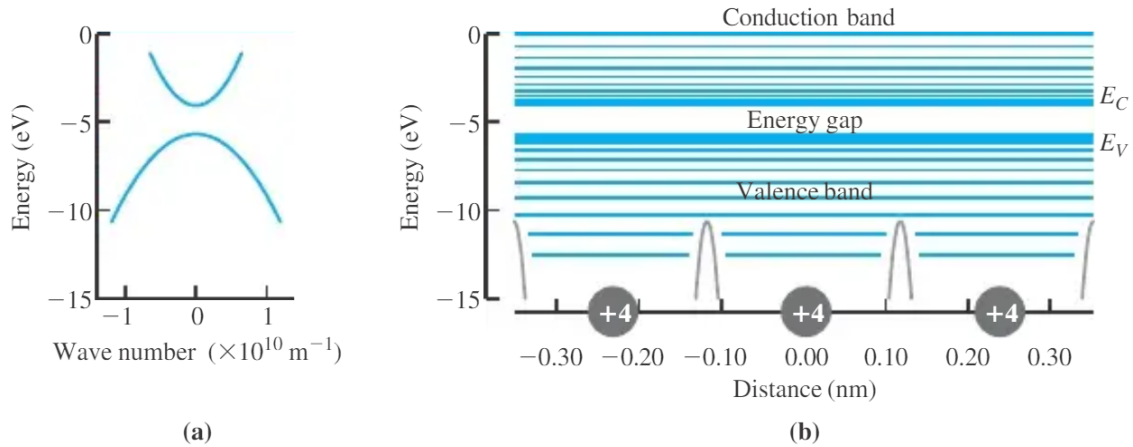


**Figure I. 11** Energy band diagrams of a semiconductor. (a)  $E-k$  (energy-wavenumber) and (b)  $E-x$  diagrams.<sup>2</sup>

The energy band distribution in a semiconductor is illustrated in Figure I.11. The energy band below the gap is called valence band, whereas the energy band above the gap is called conduction band. An electron at the bottom of the conduction band ( $E_C$ ) is a standing wave because of the forward and backward reflections at the crystal-lattice sites. Because such an electron does not move through the crystal, it is convenient to define kinetic energy that is zero for this electron (this means that the potential energy of this and all the other electrons in the conduction band has to be equal to  $E_C$ ). The electrons at higher energy levels in the conduction band will have kinetic energies according to the upper  $E-k$  branch, which can be approximated by a parabola. Electrons with parabolic dependence appear as free electrons. Therefore, the electrons in the conduction band are mobile particles. This is not surprising, given that there are many free levels that the electrons can move on to when their energy is increased by electric field or temperature.<sup>2</sup>

### ***1.1.3.2 Charge generation and recombination***

As mentioned in the last section, the chemical bonds can be broken after absorbing the light energy. Free electrons and holes are released for inorganic semiconductors. Electron-hole pairs are

produced for organic semiconductors. Energy band diagrams can be used to detail this process. As depicted in Figure I.12a, carrier generation due to light absorption occurs if the photon energy is large enough to raise an electron from the valence band into an empty conduction band state, thereby generating one electron-hole pair. A necessary condition is that the energy of the photon,  $E_{ph}$  is larger than the bandgap energy  $E_g$ . If the incoming light is a high-energy beam with an available energy much higher than  $E_g$ , multiple electrons in the valence band can be excited to the conduction band. The electrons stay in the excited state for a short time. They can be transferred to another adjacent electrode by electron transfer or they recover to the ground state by recombination process.

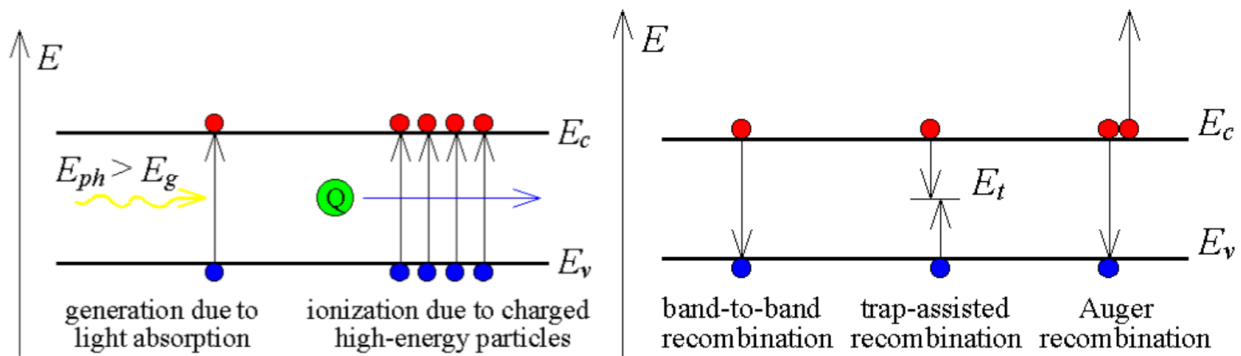


**Figure I. 12** (a) Carrier generation due to light absorption; (b) Carrier recombination mechanisms in semiconductors.<sup>2</sup>

Recombination of electrons and holes is a process by which both carriers annihilate each other: electrons occupy the empty state associated with holes through one or multiple steps. Compared to charge generation, recombination is a process of energy release. In the case of radiative recombination, this energy is emitted in the form of a photon. The band-to-band recombination is typically a radiative transition, where an excited electron moves to the hole in the valence band. In the case of non-radiative recombination, this energy is transferred to one or more phonons. Trap-assisted recombination occurs when an electron falls into a "trap", *i.e.* an energy level within the bandgap caused by the presence of a foreign atom or a structural defect. Once the trap is filled, it cannot accept another electron. The electron occupying the trap, in a second step, moves into an empty valence band state, thereby completing the recombination process. One can envision this process as a two-step transition of an electron from the conduction band to the valence band or as the annihilation of the electron and hole, which meet each other in the trap. We will refer to this

process as Shockley-Read-Hall (SRH) recombination. Recombination at surfaces and interfaces can have a significant impact on the behavior of semiconductor devices. This is because surfaces and interfaces typically contain a large number of recombination centers because of the abrupt termination of the semiconductor crystal, which leaves a large number of electrically active states. Besides, the surfaces and interfaces are more likely to contain impurities than the bulk, since they are exposed during the device fabrication process. This is also a trap-assisted recombination, but the traps are located at the interfaces. In the case of Auger recombination, this energy is passed on to another electron in the form of kinetic energy.

## **I.2 Solar Energy**

Energy is one of the fundamental conditions for human life. Since thousands of years ago, we have gotten energy in various ways, such as food, wood, coals, oil, natural gas, and so on. Today we know that almost all the energies available on earth originate directly or indirectly from the sun. Fossil energies, for instance, coals, were formed by a long-time accumulation, probably up to billion years. Humans cannot wait so long. At the current rate of consumption, the approximate lifetime of the world's petroleum, natural gas, and coal reserves are 50 years, 52.8 years, and 153 years, respectively, according to the prediction of the Statistical Review of World Energy.

Another serious problem is the excessive emission of carbon dioxide ( $\text{CO}_2$ ). As we know,  $\text{CO}_2$  is the main greenhouse gas. Global warming is a truth with more and more  $\text{CO}_2$  emissions, which will possibly cause serious disasters. For instance, the global temperature increasing will cause the sea-level rise due to the thermal expansion of seawater and the melting of the iceberg in Antarctica. When the time comes, the countries at low altitude will be submerged first. The disasters may come earlier with some unknown virus that might be released from the ancient ice and cause plagues to hurt or kill life. Figure I.13 presents global  $\text{CO}_2$  emissions by energy sources from 1990 to 2017. Most  $\text{CO}_2$  emissions are produced through burning coal, oil, natural gas, and these emissions are still increasing with time. In order to mitigate the “greenhouse effect”, we have to reduce our dependence on fossil energy and find new ways to get energy.

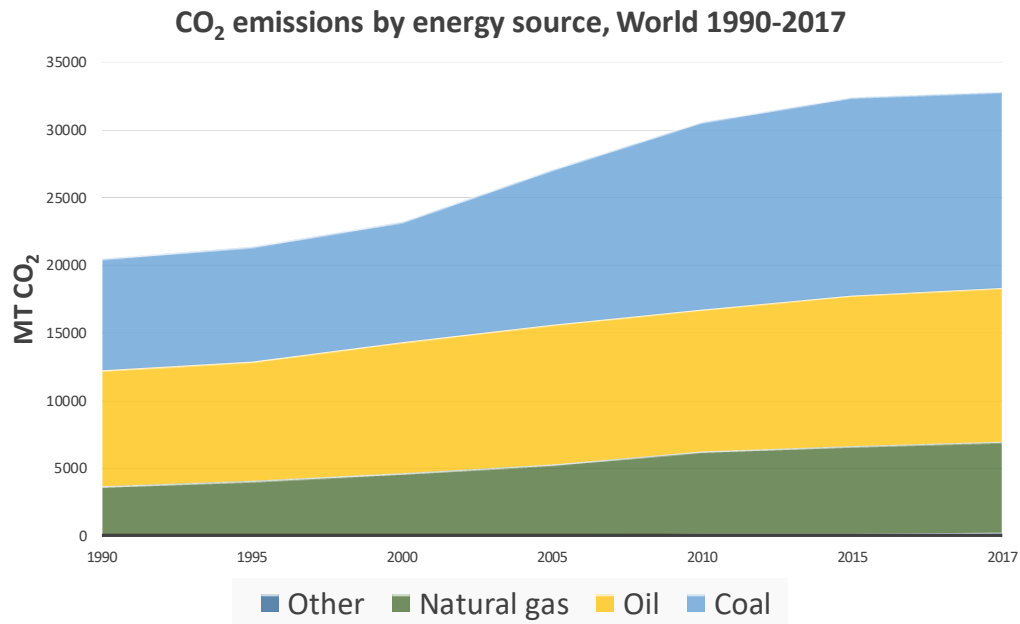


**Figure I. 13** CO<sub>2</sub> emission by energy source, World 1990-2017.

Renewable energies are now considered to replace fossil energy in the future. For instance, wind, solar irradiation, biomass, and so on, are clean, recyclable and inexhaustible energies. However, up to now, they just occupy a small part of the energy mix (Figure I.14), according to the investigation of total world primary energy supply by the source during the 1990-2017 period. There is still a long way to go until replacing fossil energy.

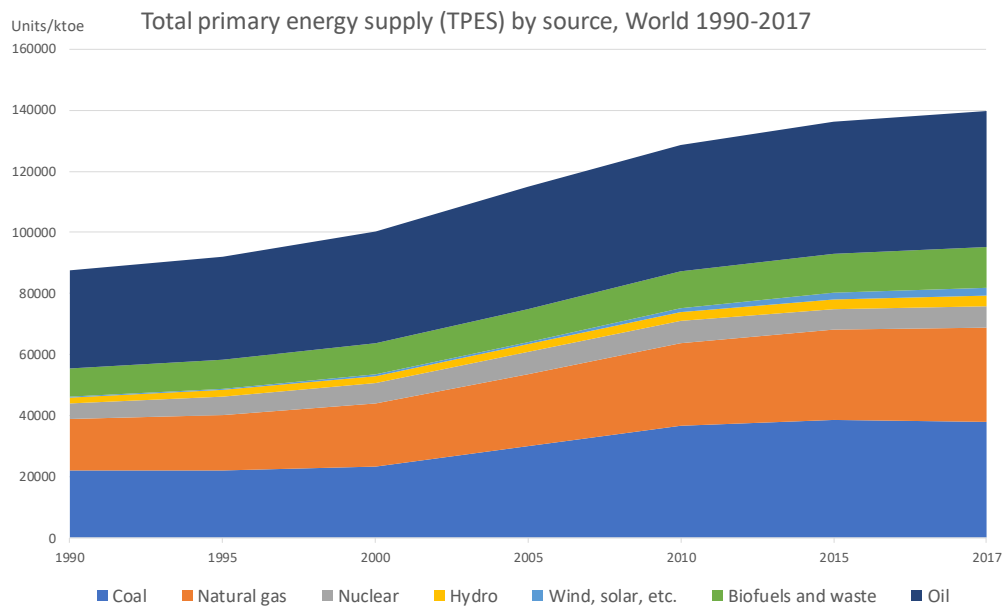


**Figure I. 14** Total primary energy supply (TPES) by source, World 1990-2017.

### I.2.1 Photovoltaics for solar energy conversion

Photovoltaic devices can directly convert solar energy into electricity based on the photoelectric effect. These devices harvest light and convert it to electricity and they are very promising because they are produced with elements that are various and abundant on earth.<sup>7</sup> According to the report of IEA, solar PV has the largest growth rate at 33.91% per year between 1990 and 2018, which means that solar PV has gradually become an important renewable energy resources (Figure I.15). The large-scale application should be ascribed to that the cost of PV devices is decreasing year by year. As shown in Figure I.16, the average auction price of PVs has already been lower than that of wind energy since 2019.

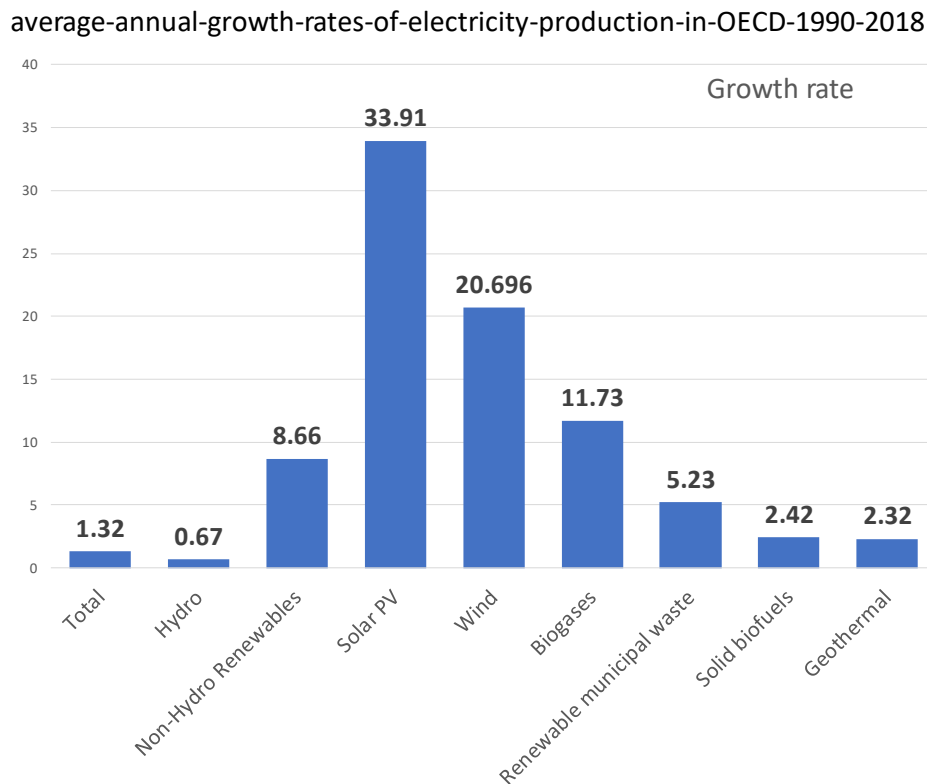


**Figure I. 15** Average annual growth rates of clean energy production in OECD 1990-2018.

Based on different principles or structures, several types of solar PV devices have been developed. We will next briefly introduce the main categories of solar cells: crystallized silicon solar cells, thin-film solar cells, dye-sensitized solar cells, quantum dots solar cells, and PSCs.

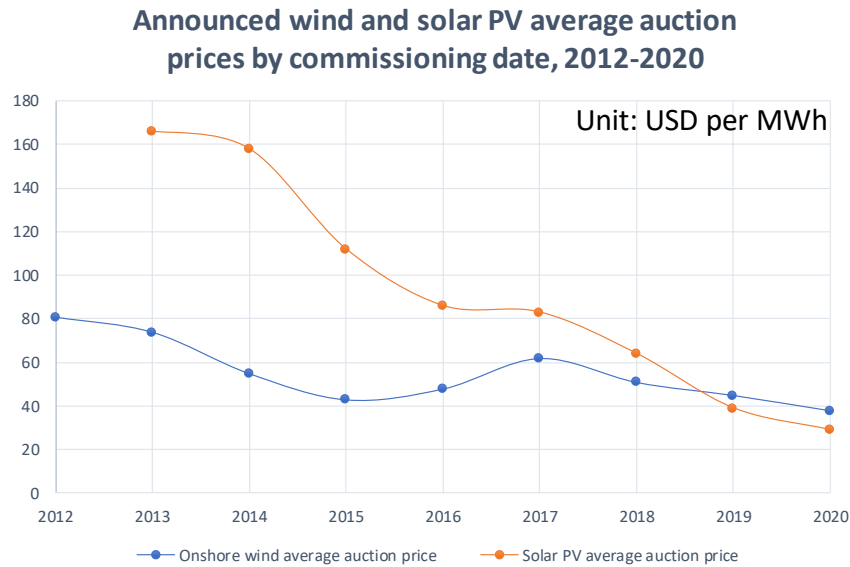


**Figure I. 16** Announced wind and solar PV average auction prices by commissioning date, 2012-2020 (Units: USD per MWh).

## I.2.2 Brief introduction of PV devices

### I.2.2.1 Silicon solar cells

The first silicon solar cell appeared in 1941 and its power conversion efficiency (PCE) was less than 1%.<sup>8</sup> It opened the door of the direct conversion of solar energy into electricity. After 79 years, the best PCE has been improved to a certified record efficiency of 26.1% value for single crystalline silicon solar cells. This device has been dominating the photovoltaic market since the very beginning of 1950. Silicon is stable, non-toxic and abundant on the earth. The raw material ( $\text{SiO}_2$ ) is not lacking but it must be reduced and refined at a high grade to be usable. Except for single crystalline silicon solar cells, researchers and companies have also developed polycrystalline silicon solar cells and amorphous silicon solar cells, which current record PCEs are 22.3% and 14%, respectively.

The fundamental working principle of solar cells is the photoelectric effect in semiconductors. Figure I.17a shows the schematic diagram of a typical single junction crystalline silicon solar cell. The cell consists of a junction between a thin layer of n-type doped Si on thick p-type doped Si. Due to the charge transfer and recombination at the interface, a depleted space charge zone is formed. Since the n-type layer is positively charged and the p-type layer is negatively charged, an electric field (called build-in potential  $V_{bi}$ ) is built in the depleted space charge layer. When the

light shines the cell from the n-type side, the free photogenerated electrons and holes drift to the n-type Si side and the p-type Si side, respectively, under the driving force of the built-in potential.<sup>9</sup>

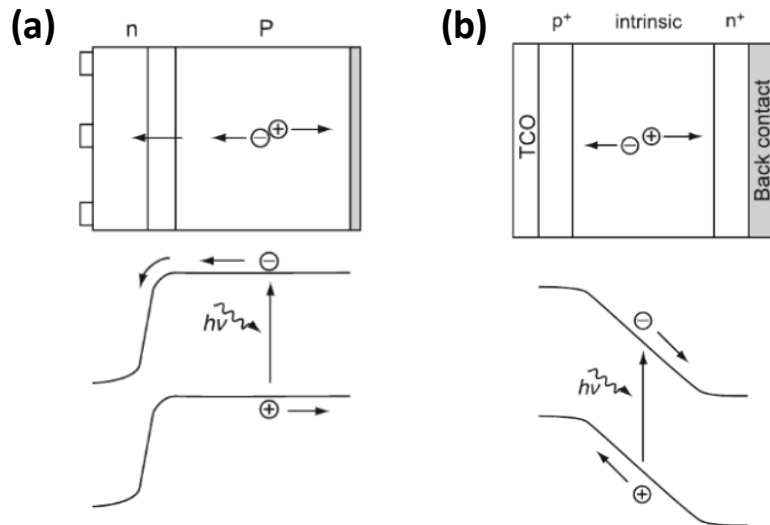


**Figure I.17** The structures of (a) a crystalline silicon solar cell and (b) a typical single-junction amorphous silicon solar cell.<sup>9</sup>

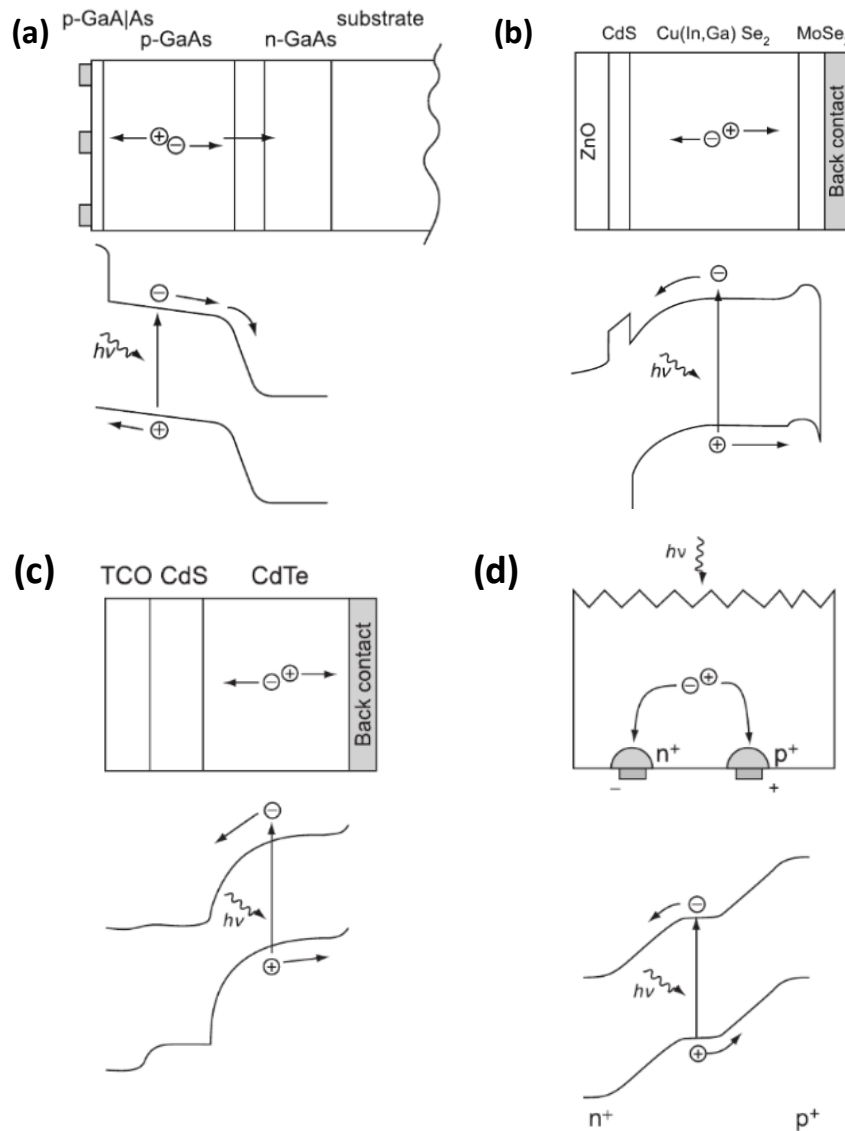
### 1.2.2.2 Thin film solar cells

Figure I.17b shows the working principle of amorphous silicon solar cells. These devices are thin-film solar cells and are based on a p-i-n junction. They contain a layer of intrinsic semiconductor which separates two heavily p-doped and n-doped regions near the contacts. Electrons and holes are generated principally within the space-charge region. Charge separation can be assisted by the built-in potential, thus enhancing the collection efficiency.<sup>9</sup>

The other thin film PV devices are based on gallium-arsenide (GaAs), copper indium gallium diselenide (CuInGaSe) and cadmium telluride (CdTe) semiconductor compounds. Thin film solar cells are also commercialized. These cells usually exhibit high efficiency. They are advantageous because they are less demanding toward the material purity and quality and they employ much less material than the crystalline Si solar cells because the thin films are only several micrometers thick.

Figure I.18a shows the structure of GaAs cells, which is similar to the reverse type of crystalline silicon solar cell, except a thin passivating GaAlAs layer that covers the top surface. The GaAlAs layer prevents electrons from the emitter to reach the surface but transmits most of the incident light into the emitter layer where most of the power is generated. Figure I.18b and 18c show the

structure of CuInGaSe and CdTe cells, respectively. The structure of CuInGaSe is a p-n junction with a passivating thin CdS layer between the transparent electrode (ZnO) and CuInGaSe. The structure of the CdTe cell can be described as substituting CdTe for CuInGaSe and removing the electron blocking layer MoSe<sub>2</sub> in CuInGaSe device structure. The back electrode directly contacts the absorbing layer. Contacts can also be arranged on the same side of solar cells, which is so-called back contact solar cells. The principle is much simpler as shown in Figure I.18d. Photogenerated electrons and holes are collected on the same side. Efficient light absorption is aided here by light trapping: a textured top surface and a reflecting back surface. The absorbing layer can be perovskite too.<sup>10</sup>



**Figure I. 18** The structures of (a) a typical GaAs solar cell, (b) a typical CuInGaSe solar cell, (c) a typical CdTe solar cell and (d) a back contact solar cell.<sup>9</sup>

### 1.2.2.3 Dye-sensitized solar cells and organic solar cells

In 1991, Dr. Michael Grätzel first reported a cheap dye-sensitized solar cell, which was mainly composed of a dye-coated titanium dioxide ( $\text{TiO}_2$ ) mesoporous layer, a liquid redox electrolyte and transparent conducting oxide electrodes.<sup>11</sup> The working principle of this cell is shown in Figure I.19a. Light is absorbed by an organic or organic-metal dye molecule, transferring an electron from the ground state to an excited state (rather than that from the valence band to the conduction band in the semiconductors). The excited state recovers to the ground state by transferring electrons to an electron transfer layer ( $\text{TiO}_2$ ) or trap states. The holes in the HOMO level transfer to a redox electrolyte. In organic solar cells, electron and hole transport layers are both organics and are called electron acceptors and electron donors as shown in Figure I.19b. Light is absorbed in the electron donor layer and the photogenerated electrons are transferred to the electron acceptor layer. Organic solar cells have the advantages of low-cost and can be prepared as lightweight flexible devices, which is an advantage for an application as wearable devices.<sup>12</sup>

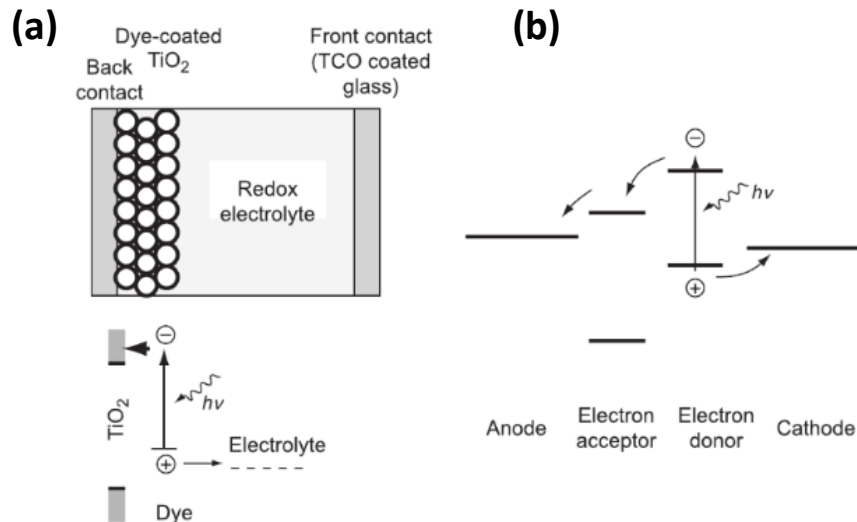


**Figure I. 19** The structures of (a) a dye-sensitized solar cell and (b) an organic solar cell.<sup>9</sup>

### I.3 Perovskite Solar Cells

Recently, perovskite solar cells have attracted great attention due to its distinguished photovoltaic properties. What is the perovskite solar cells? Why perovskites have brilliant photovoltaic properties? What is the outlook of this new technology? The answer will be given in the following sections.

### I.3.1 Structures and properties of organic-inorganic hybrid perovskites

Hybrid perovskites are materials with a general formula of  $ABX_3$ , where A is a monovalent cation (classically  $Cs^+$ ,  $Rb^+$ ,  $CH_3NH_3^+$  (noted  $MA^+$ ) or  $HC(NH_2)_2^+$  (noted  $FA^+$ )), B is a bivalent metal cation such as  $Pb^{2+}$ ,  $Sn^{2+}$  or  $Ge^{2+}$ , and X is a halide anion (typically  $Cl^-$ ,  $Br^-$ ,  $I^-$  or their mixtures).<sup>13</sup> The cations can be mixed to get high photovoltaic performance. The crystal structure is cubic or tetragonal as shown in Figure I.20A, created by a network of corner-sharing  $BX_6$  octahedra surrounding a large A-site cation.

OIHPs can be successfully employed in PV devices resulting from their (i) High absorption coefficient; (ii) Long diffusion length; (iii) Tunable and direct bandgap (1.1-1.8 eV); (iv) Facile low-temperature solution process. The crystallographic stability and probable structure can be deduced from the Goldschmidt tolerance factor  $t$ .<sup>14</sup> Its formula is given by:

$$t = \frac{r_A + r_X}{\sqrt{2}(r_B + r_X)} \quad (I.1)$$

$r_A$ ,  $r_B$ , and  $r_X$  are the ionic radii of A, B, and X, respectively. For halide perovskites, it is generally  $0.81 < t < 1.11$ .<sup>15,16</sup> If  $t$  lies between 0.89 and 1.0, the structure in Figure I.20A should be cubic. Otherwise, the crystal structure will be less symmetric, namely tetragonal or orthorhombic as shown in Figure I.2bc.

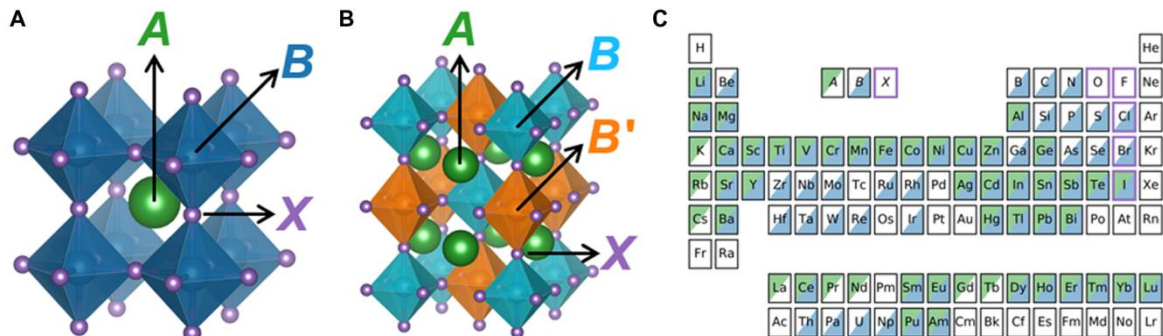


**Figure I. 20** (a)  $ABX_3$  in cubic single perovskite structure ( $Pm\bar{3}m$ ); (b)  $A_2BB'X_6$  in the rock salt double perovskite structure ( $Fm\bar{3}m$ ); (c) Map of the elements that occupy the A, B, and/or X sites.

Now, PSCs with high efficiency are generally based on the Pb and I system ( $B = Pb$  and  $X = I$ ,  $APbI_3$ ). The relationship between the tolerance factor  $t$  and the ionic radii of A-site cations is given in Figure I.21.<sup>17-19</sup> Methylammonium (MA), formamidinium (FA) and cesium (Cs) are quite

suitable for the 3D structure. It explained why most of high-efficiency PSCs included these cations. Other cations, such as potassium (K), rubidium (Rb), IA (imidazolium), EA (ethylammonium) and GA (Guanidinium) can be added as dopants to form mix cation perovskite and to improve the photovoltaic properties.<sup>15,20–23</sup>

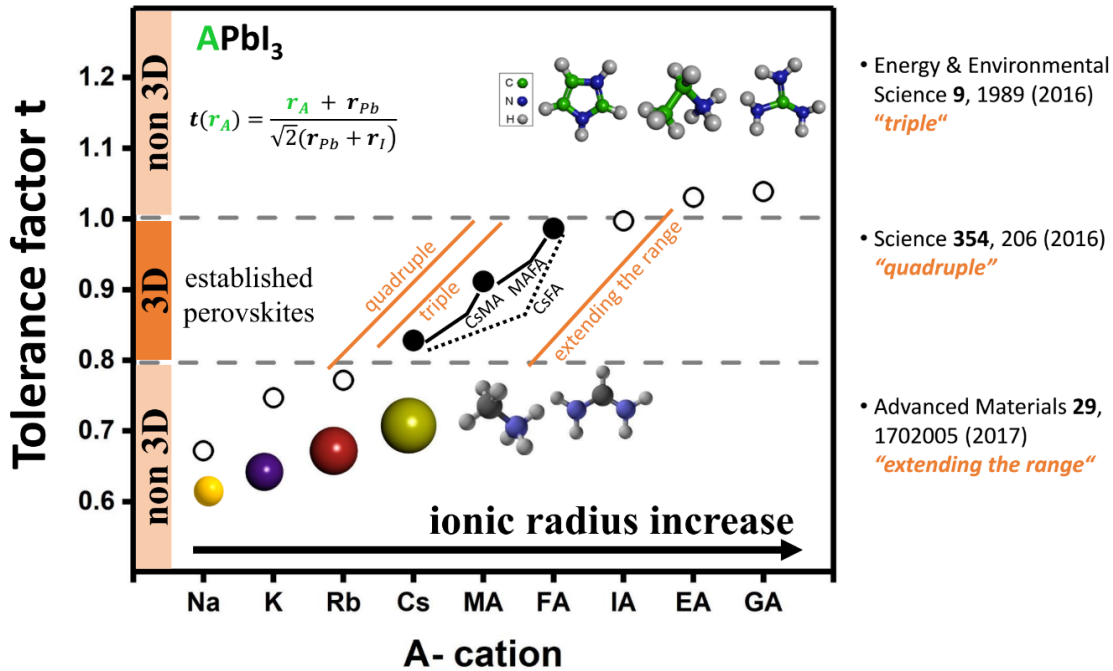


Figure I. 21 Tolerance factor  $t$  in  $\text{APbI}_3$  perovskites. [Prof. Saliba's presentation in Limoges]

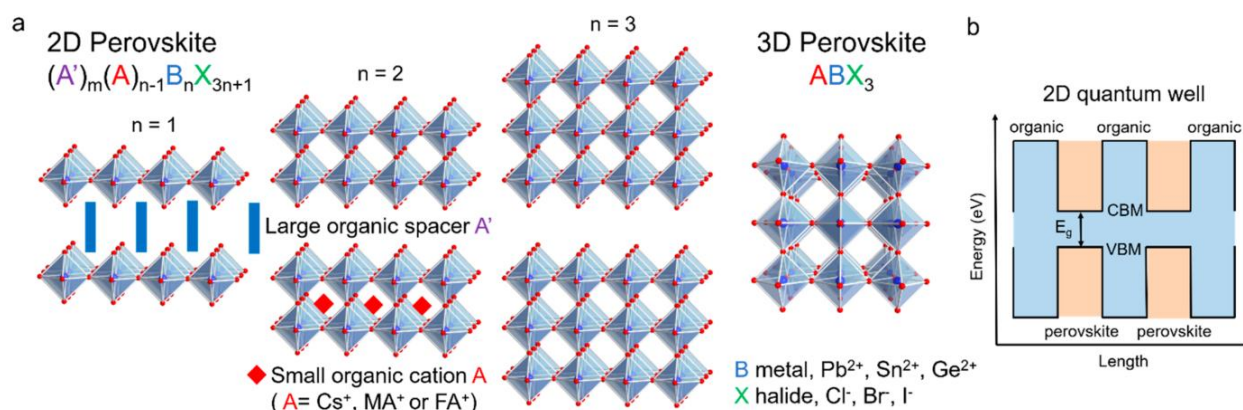
The formula (I.1) is only suitable for  $\text{ABX}_3$  chemical formula. B-sites can be occupied by two different cations, respectively, resulting in a double perovskite structure with a formula of  $\text{A}_2\text{BB}'\text{X}_6$  (Figure I.20B). Single and double perovskite materials have exceptional properties, which render them highly attractive for applications in various areas such as photovoltaics<sup>24</sup>, LED, scintillation, photodetectors<sup>25</sup>, electrocatalysis<sup>26</sup>, ferroelectrics<sup>27</sup>, and so on. Due to a large number of exception of formulae (I.1), a new tolerance factor  $\tau$  has been proposed recently by Christopher J. Bartel et al.<sup>14</sup>:

$$\tau = \frac{r_X}{r_B} - n_A \frac{r_A/r_B}{\ln(r_A/r_B)} \quad (2)$$

where  $n_A$  is the oxidation state of A,  $r_A$  and  $r_B$  are the ionic radii of A and B, defining  $r_A > r_B$ , and  $\tau < 4.18$  indicates perovskite structure. The new tolerance factor  $\tau$  requires only the chemical

composition to distinguish the many structures that are considered as perovskite and high overall accuracy of > 90% was provided. Moreover,  $\tau$  also indicates a monotonic estimate of the possibility for a material to be stable in the perovskite structure<sup>14</sup>.

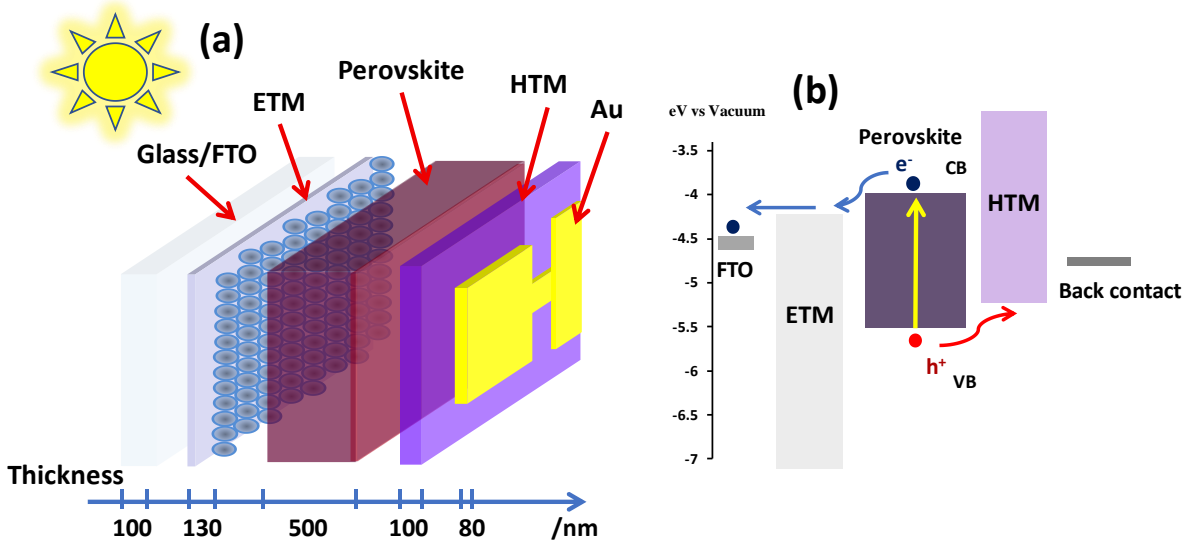
3D perovskites have great photovoltaic properties, but they lack good stability against moisture. This is the primary obstacle for a widespread diffusion of this technology. 2D materials such as phenethylammonium (PEA), butylamine (BA), have good hydrophobic properties and can replace A-site cations in the perovskite structure. An important relief from the narrow compositional diversity was found in the form of two-dimensional (2D) halide perovskites. The molecular formula can be written as  $(A')_m(A)_{n-1}B_nX_{3n+1}$  and their structures are described in Figure I.22a. A regular organic layer could be formed to present a 2D/3D staggered structure. The value of  $n$  reflects the number of inorganic structural layers between the adjacent 2D organic molecular layers. The bigger is the  $n$  values, the closer the structure is to 3D. The value of  $m$  reflects one or two 2D molecules occupied in the A-site, which depends on monovalent ( $m = 2$ ) or divalent ( $m = 1$ ) cations intercalated in the structure. The corresponding structures are named Ruddlesden-Popper (RP) and Dion-Jacobson (DJ), respectively, which have attracted great attention.<sup>28–30</sup> The alternating 2D/3D structure generates a crystallographically ordered 2D multiple-quantum-well (MQW) electronic structure that forms naturally in a bottom-up fashion through self-assembly (Figure I.22b).<sup>31,32</sup> Figure I.22b also shows the quite larger bandgap of 2D layers compared to 3D perovskite layers, which causes less absorption of near-infrared light.



**Figure I. 22** (a) Structure of 2D perovskite; (b) 2D quantum well.<sup>30</sup>

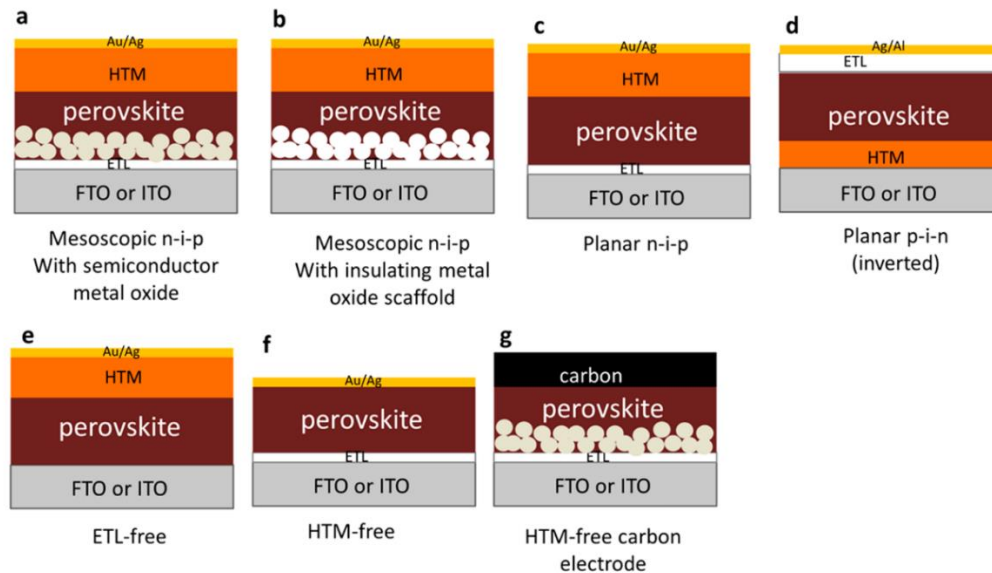
### I.3.2 The working principle of perovskite solar cells

Figure I.23a displays a typical PSCs structure of FTO/ETM/Perovskite/HTM/Au and Figure I.23b presents the corresponding energy level alignment (with FTO: F-doped tin dioxide; ETM: electron transporting materials; HTM: hole transporting materials). The most of light goes through the wide bandgap FTO and ETM layers and then is absorbed by the perovskite layer, which has a narrow bandgap and high absorption coefficient. The photogenerated electron-hole pairs are then separated in the perovskite layer and move to the ETM and the HTM, respectively. The driving forces that permit the separation of electron-hole pairs are not clear, but the traditional structure of pn junction is not necessary for good solar cells. The energy level alignments, the selective contacts, the long lifetime ( $1\mu\text{s}$ ) and the long diffusion length ( $1\mu\text{m}$ ) of the charges in perovskite materials are key properties.<sup>32,33</sup>



**Figure I. 23** (a) Structure of a perovskite solar cell; (b) Energy band diagram and working principle.

With the development of PSCs, a large variety of device architectures has been invented and they are summarized in Figure I.24.<sup>34</sup> In short, they can be sorted as mesoscopic n-i-p, planar n-i-p, planar p-i-n (inverted), ETL-free, and HTM-free perovskite solar cells. Every architecture plays an important role in further commercialization.



**Figure I. 24** Various device architectures of perovskite solar cells.<sup>34</sup>

### I.3.3 Short overview of perovskite solar cells evolution

In 1839, the German scientist Gustav Rose first discovered a natural mineral with a perovskite structure ( $\text{CaTiO}_3$ ) in the Ural mountain, Russia. For commemorating famous Russian mineralogist Lev Alexeïevich Perovskiy, he named the new mineral perovskite. In 1892, halogen-based perovskite ( $\text{CsPbX}_3$ ) materials were first synthesized by H. L. Wells.<sup>13</sup> However, until 2009, the perovskite solar cell was first reported by Prof. Miyasaka et al. with an efficiency of 3.8%. In this work, the organolead perovskite was employed as a dye adsorbed on  $\text{TiO}_2$  and a liquid electrolyte with a redox couple was still used as HTM, like that in DSSCs (Figure I.19a). The devices have a poor stability (lifetime of several minutes).<sup>35</sup> Now, we knew that the liquid electrolyte damaged the device stability, because the hybrid perovskites were sensitive to water. In 2012, Prof. N.-G. Park and Prof. M. Grätzel et al. reported an all-solid-state perovskite solar cell with efficiency exceeding 9%.<sup>36</sup> A new research field about all-solid-state PSCs was created. The aspect and schematic of the completed device are provided in Figure I.25a and b. The cell cross-section image with structure of Au/Spiro-OMeTAD/MAPbI<sub>3</sub>/TiO<sub>2</sub>/FTO glass is given in Figure I.25c. The *J-V* curve of the champion cell under light AM 1.5G is presented in Figure I.25d. Almost at the same time, Dr. Snaith and Prof. Miyasaka et al. reported efficient perovskite solar cells based on a mesoporous superstructure layer with an efficiency of 10.9% and improved stability (Figure I.26b).<sup>37</sup> The use of an  $\text{Al}_2\text{O}_3$  mesoporous layer largely enlarged the  $V_{\text{OC}}$ . It was

explained by the fact that the insulating  $\text{Al}_2\text{O}_3$  layer blocks the electrons transfer to  $\text{Al}_2\text{O}_3$  itself and the delayed electrons remained in the perovskite phase until they were collected by the compact- $\text{TiO}_2/\text{FTO}$  electrode.<sup>37</sup> In short, the interface of mesoporous  $\text{Al}_2\text{O}_3/\text{perovskite}$  has less recombination, compared to the mesoporous  $\text{TiO}_2/\text{perovskite}$  interface. In the above two papers, the thickness of the mesoporous scaffold layer was much larger than that of perovskite because perovskite still acted as a dye. In 2013, Prof. Snaith et al. reported a diffusion length of 100 nm and 1000 nm for  $\text{MAPbI}_3$  and  $\text{MAPbI}_{3-x}\text{Cl}_x$ , respectively, which are an order of magnitude greater than their absorption depth. Long diffusion length indicates that nano- or meso-structures are not necessary for highly efficient charge generation and collection. Their results hence paved the way for further advances in planar or quasi-planar (thin scaffold layer) heterojunction PSCs.<sup>38</sup>

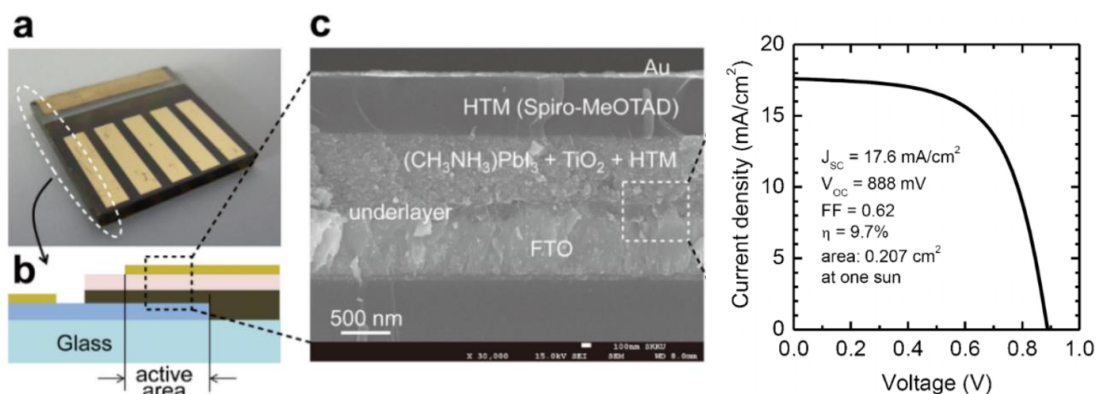


**Figure I. 25** (a) Image and (b) design diagram of solid perovskite solar cell; (c) Cross section of PSCs characterized by SEM; (d)  $J-V$  curve under AM 1.5G.<sup>36</sup>

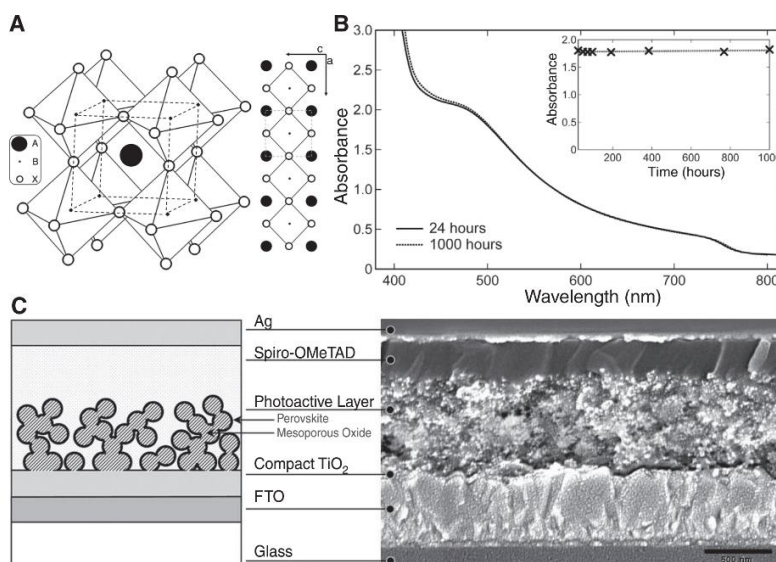


**Figure I. 26** (a) Crystal structure of OIHP; (b) Absorbance spectra and variation of the absorbance of perovskite film with time; (c) Schematic and cross-sectional SEM view of the PSCs.<sup>37</sup>

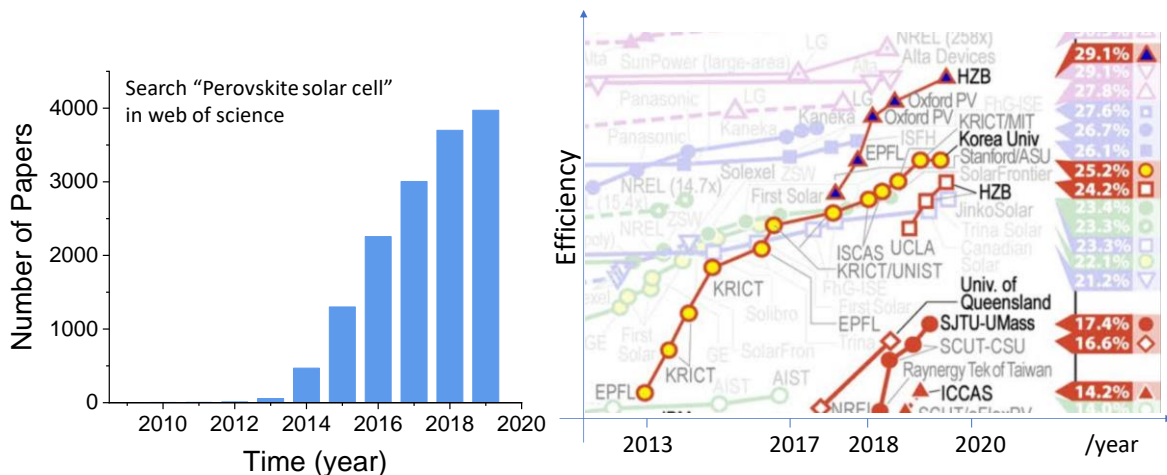


**Figure I. 27** (a) Number of papers about PSCs published each year (source: web of science); (b) The chart of certified record efficiencies by NREL.

Due to the distinguished photovoltaic properties of organic-inorganic hybrid perovskite (OIHP), many researchers have been studying PSCs since 2013. Numerous papers have been published and the record PCE values have risen continuously at an unprecedented rate (Figure I.27a). With the deeper understanding and the further process optimization of PSCs, the PCE reached 19.3% in 2014.<sup>39</sup> In 2015, Prof. Seok et al. reported an approach for depositing high-quality FAPbI<sub>3</sub> films, involving FAPbI<sub>3</sub> crystallization by the direct intramolecular exchange of dimethylsulfoxide (DMSO) molecules intercalated in PbI<sub>2</sub> with formamidinium iodide (FAI). The champion device had an efficiency higher than 20%.<sup>40</sup> This paper boosted great attention on FAPbI<sub>3</sub> perovskite, which has a rather low bandgap (1.48 eV), better thermal stability and the potential to produce highly efficient solar cells. In 2017, Prof. Seok group further improved the efficiency to 22.1% by introducing additional iodide ions into the precursor solution, which reduced the deep-level defects.<sup>41</sup> As we know, pure-FAPbI<sub>3</sub> has a serious problem of phase instability because the black perovskite  $\alpha$ -phase will spontaneously transformed in the yellow photoinactive  $\delta$ -phase at room temperature, even upon storage in vacuum or inert gas.<sup>42</sup> To resolve this problem, inorganic cation Cs<sup>+</sup> was preliminarily used for enhancing the thermal and humidity stability of FAPbI<sub>3</sub> layer by Prof. N.G. Park group and Prof. M. Grätzel group.<sup>43,44</sup> In 2016, Dr. M. Saliba et al. reported Cs-containing triple-cations (Cs/FA/MA) perovskite solar cells with highly enhanced stability and efficiency (21.17%), as shown in Figure I.28.<sup>17</sup> In 2018, the certified record efficiency has reached 23.7%.<sup>[44a]</sup> There are at least two published papers, which exhibited an efficiency of PSCs higher than 23% in 2018-2019.<sup>45,46</sup> In 2019, Prof. Jangwon Seo group synthesized a fluorene-terminated

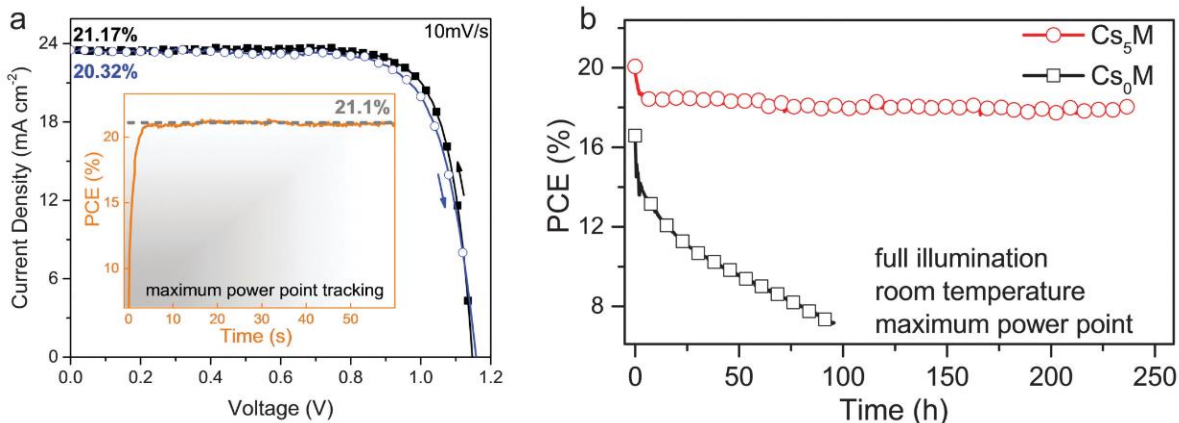


**Figure I. 28** (a)  $J$ - $V$  curves of CsFAMA PSCs and (inset) maximum power point tracking (MPP) curve; (b) Aging for 250h of high performance Cs<sub>5</sub>M and Cs<sub>0</sub>M devices in nitrogen atmosphere held at room temperature under constant illumination and maximum power point tracking (MPP).<sup>17</sup>

hole-transporting material with a fine-tuned energy level and a high glass transition temperature to ensure highly efficient (23.2%) and thermally stable PSCs.<sup>45</sup> Prof. You reported the use of an organic halide salt phenethylammonium iodide (PEAI) on perovskite films for surface defect passivation. The PEAi itself could form a layer on the perovskite surface and it resulted in highly efficient PSCs (23.32%) by passivating the defects and suppressing non-radiative recombination. Whereas, the in-situ formed 2D PEA<sub>2</sub>PbI<sub>4</sub> perovskite after annealing did not show an apparent improvement.<sup>46</sup> At the beginning of 2019, the certified record efficiency raised to 24.2% and next up to 25.2% at the end of this year (Figure I.27b). Up to now (June 2020), at least seven papers reported PSCs with an efficiency higher than 23%.<sup>45-50</sup> In these works, we have noted three interesting points which help for getting highly efficient devices: a) a high ratio of formamidinium for lowering the bandgap; b) the use of high concentration precursor solutions so that a rather thick layer is produced to absorb a maximum of solar light; c) methylammonium chloride has been employed in several works for stabilizing the intermediate  $\alpha$ -FAPbI<sub>3</sub> phase. Recently, Kim and co-workers reported a systematical study of MAcl additive in FAPbI<sub>3</sub> based perovskite films.<sup>49</sup> They presented that MAcl successfully induced an intermediate phase to the pure FAPbI<sub>3</sub> phase without annealing and that MA<sup>+</sup> can effectively stabilize the final FA<sub>1-x</sub>MA<sub>x</sub>PbI<sub>3</sub> perovskite structure through cationic substitution as shown in Figure I.29. The efficiency of the champion device reached a value as high as 24.02%. An review paper have made a summary about MAcl used as a key additive for highly efficient solar cells.<sup>51</sup>

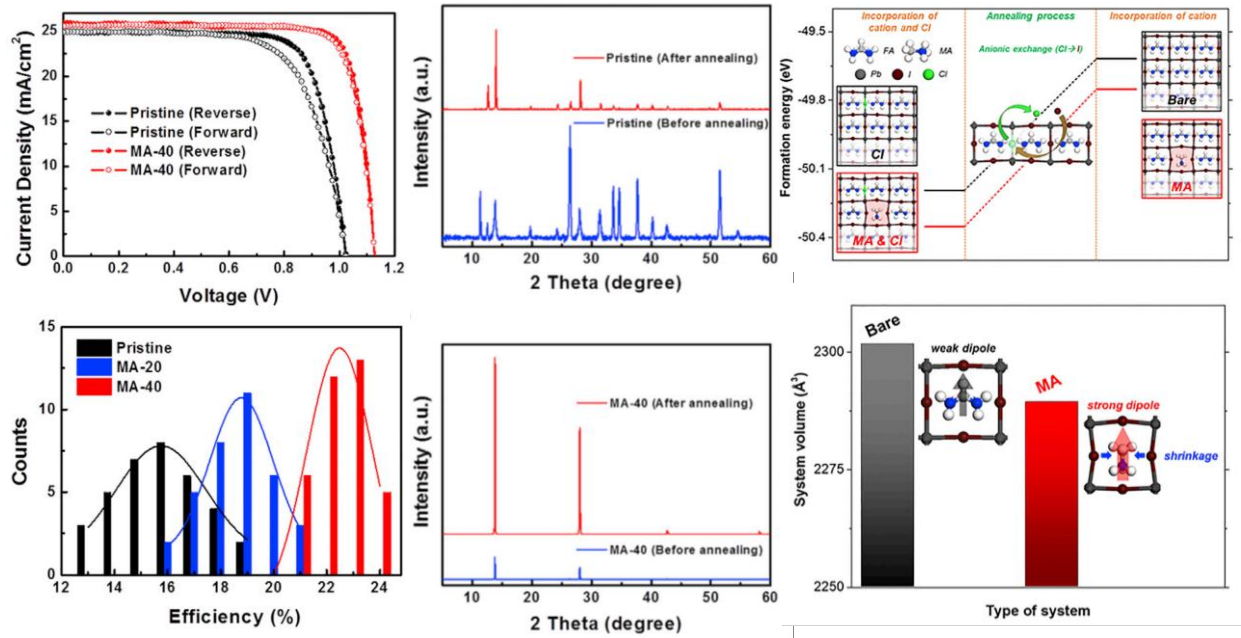


**Figure I. 29** (a)  $J$ - $V$  curves of reversed and forward scans for 40 mol% MA-Cl and pristine FAPbI<sub>3</sub> devices; (b) Comparison of efficiency distribution for pristine, 20 mol% and 40 mol% MA-Cl devices; (c) XRD patterns of pristine perovskite and (d) perovskite with 40 mol% MA-Cl additives, before and after annealing at 150°C; (e) Calculations of the bare  $\alpha$ -FAPbI<sub>3</sub> perovskite structure prepared with and without MA-Cl; (f) Strong dipole moment causing lattice shrinkage.<sup>49</sup>

#### I.4 UV-Photodetectors

In the 21<sup>st</sup> century, the rapid development of artificial intelligence (AI) accelerates the development of various detectors. Photodetectors (PDs) are devices that sense light or electromagnetic energy and convert it into a response, usually an electrical one.<sup>52</sup> As a part of the photonics system, photodetectors are developing very fast with relevant applications, such as telecommunications, photosensors, metrology, medicine, information processing, military technology, agriculture, robotics, laser material processing, biophotonics. The categories of PDs includes optical and chemical detectors, photoresistors, photodiodes, thermocouples, phototubes, solar cells, and so on. The selection of a PD depends on the requirements of a specific application, such as the wavelength of light, the speed of response and the sensitivity. Ultra-violet (UV) Photodetectors are sensitive to the light irradiation in the 400-10 nm wavelength region. This wavelength region is commonly further divided into the following subdivisions: 1. Vacuum ultraviolet (VUV), 200-10 nm; 2. Deep ultraviolet (DUV), 350-190 nm; 4. Ultraviolet-B (UV-B) 320-280 nm; 4. Ultraviolet-A (UV-A), 400-320 nm, which will be discussed in this thesis.

### I.4.1 Classification of the UV photodetectors

UV photodetectors are traditionally divided into two distinct categories, photographic and photoelectric as depicted in Figure I.30. The major advantage of photographic emulsions is their ability to store images and thus to record large amounts of data in a single exposure. However, photographic emulsions have some limitations. For instance, their sensitivity is much lower than photoelectric detectors. Photoelectric detectors have a greater sensitivity, greater stability of response, and better linear characteristics so that they have drawn various applications. According to the different applications, they can be further divided into photoconductive, photovoltaic, and photoemissive as shown in Figure I.30. The photovoltaic-type UV photodetectors are developed in Chapter II of this thesis.

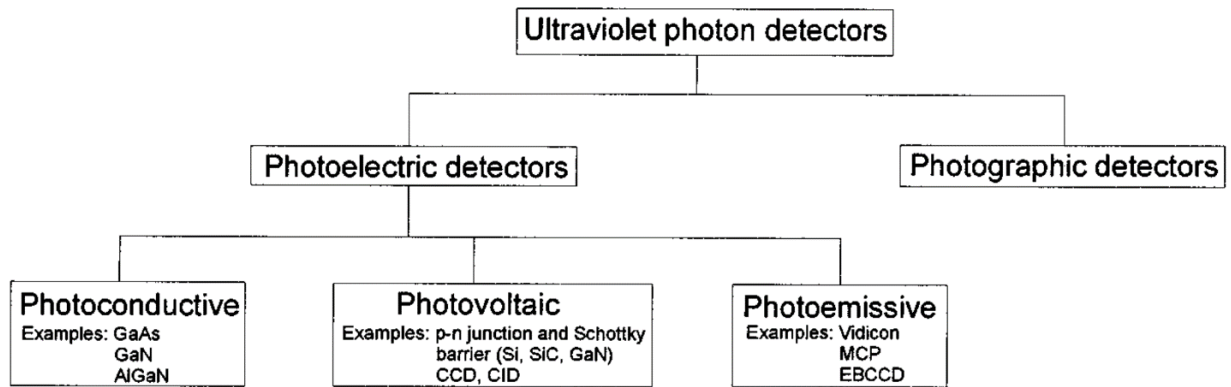


Figure I. 30 Classifications of UV-photodetectors.<sup>52</sup>

### I.4.2 Working principle of photovoltaic-type UV photodetectors

The fundamental working principle of UV PDs is the same as that of a solar cell while the focus points to evaluate the performances of UV PDs are quantum efficiency, responsivity, detectivity, and response time. P-N junction type and Schottky type are the commonly studied photovoltaic-type UV photodetectors.

#### I.4.2.1 p-n junction type UV PDs

The p-n junction type UV PDs are often referred to as simply a photodiode. The operation of a p-n junction photodiode is presented in Figure I.31. Photons with energy higher than the bandgap, captured by the semiconductors, create electron-hole pairs. Under the force of the built-in potential, the electron-hole pairs are separated and move to the opposite directions, thus generating an output photocurrent.

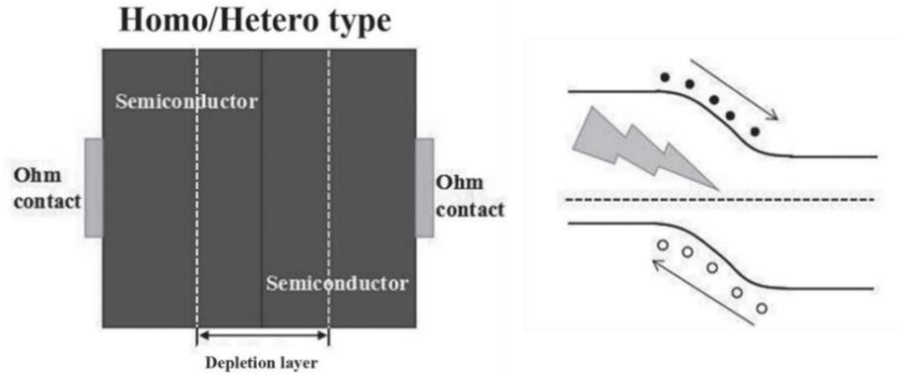


**Figure I. 31** Working principle of p-n junction type UV photodetectors.<sup>53</sup>

#### *1.4.2.2 Schottky junction type UV PDs*

Schottky junctions have been extensively studied and have also found applications in UV PDs. The typical structure of a Schottky junction is shown in Figure I.32. It mainly consists of a semiconductor and a metal contact. In general, the built-in potential, which separates the electron-hole pairs, is determined by the work function difference between the metal contact and the semiconductor. However, the practical built-in potential is seriously affected by the surface state of the semiconductor, the gap states, and/or chemical reactions at the interface. Compared to p-n junctions, Schottky junctions present some advantages: low-cost fabrication, super-fast response, and absence of high-temperature processes.<sup>53</sup>

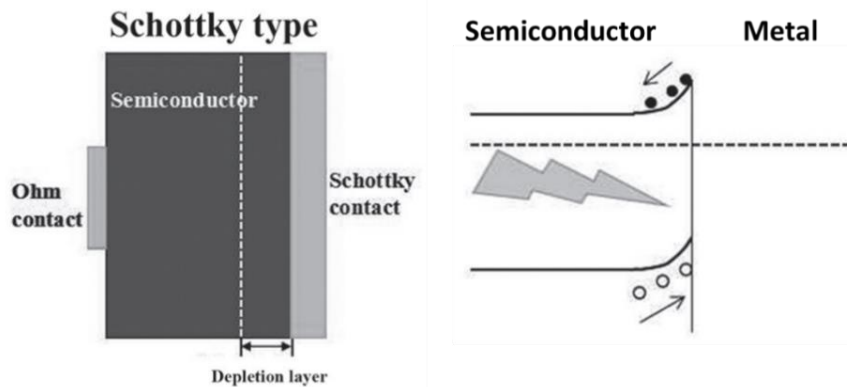


**Figure I. 32** Working principle of a Schottky type UV photodetector.<sup>53</sup>

### **1.4.3 UV photodetector parameters**

The main parameters used to evaluate the performance of UV photodetectors are summarized in Table I.1. The responsivity  $R$  represents the photoelectric conversion ability of a UV photodetector.

It is proportional to the quantum efficiency  $\eta$  and gain  $g$ , which is the number of carriers detected per photogenerated electron-hole pairs. The formula is written as  $R = \frac{\lambda\eta}{hc} qg$ . Where  $\lambda$  is the wavelength,  $h$  is Plank constant,  $c$  is light speed, and  $q$  is the elemental charge. Except in the case of avalanche,  $\eta$  cannot be higher than 100% and the gain  $g$  is equal to one. The response time indicates the signals tracking ability of a UV photodetector. The dark current, which is determined by diffusion current, recombination current, tunneling current, and ohmic leakage, reflects the quality of the junctions. In this thesis, most of the parameters in Table I.1 are characterized, except noise current and noise-equivalent power.

**Table I. 1** UV photodetector parameters. (Parameters in gray shallow are NOT characterized in this thesis)<sup>53</sup>

Responsivity	$R$	$A \cdot W^{-1}$	Photocurrent flowing in the detector divided by incident optical power.
Response time	$t_r, t_d$	s	Rise time ( $t_r$ ) and decay time ( $t_d$ ) are defined as the time in which photocurrent increase from 10% to 90% and drop from 90% to 10% of its maximum value.
Dark current	$I_d$	A	Current flowing in the absence of illumination. Under zero bias, this value is equal to zero at steady state.
Quantum efficiency	$\eta$	%	The ratio of photocurrent to photon fluence incident on the device.
Noise current	$I_{noise}$	$A \cdot Hz^{-1/2}$	The random root mean square fluctuation in current as the bandwidth is limited to 1 Hz.
Noise-equivalent power	NEP	$W \cdot Hz^{-1/2}$	The optical signal in watts at which the electrical signal-to-noise ratio in the detector is unity (0 dB), and the bandwidth is limited to 1 Hz. This value determines the minimum detectable power.
Normalized detectivity	$D^*$	$cm \cdot Hz^{-1/2} \cdot W^{-1}$ (Jones)	A measure of detector sensitivity that enables comparison even when bandwidth $B$ and detector area $A$ are different. $D^* = (A \cdot B)^{-1/2} / NEP$ .

## I.5 Conclusions

In summary, optoelectronic devices are based on semiconductor materials and keep drawing great development. Basic knowledge and various applications of inorganic, organic, and inorganic/organic hybrid semiconductors in optoelectronic devices were introduced. Two types of current carriers, electron and hole, can be created through the breakage of chemical bonds after absorbing light energy, thermal energy or other energies. Another efficient way to create carriers is doping by elements, which have extra-electron(s) or a deficiency of electron(s) in their outermost orbital. For organic semiconductors, doping by protons can largely improve their conductivity. In optoelectronic devices, the energy band model was introduced to understand and illustrate the process of charge generation, transfer and recombination. The absorbed light wavelength range is determined by their bandgaps.

The exhaustion of fossil energy and excessive emission of CO<sub>2</sub> is accelerating the deterioration of our environment. Enlarging the utilization of renewable energies is an important issue.

Photovoltaic technologies are developing at a high speed, in terms of performances and production volume, while their fabrication cost decreases continuously. A brief introduction to various PV devices has been presented. Perovskite solar cells first appeared in 2009 and this technology has experienced an unprecedented rise in PCE, from 3.8% up to 25.5%. It is considered as the next generation photovoltaic technology and promising to share the burden of the energy requirement.

A short introduction to UV-photodetectors has been provided in the end of this Chapter I. UV-photodetectors are sensitive to the light with wavelengths ranging between 400 and 10 nm. They are further classified as photoconductive, photovoltaic, photoemissive, and photographic detectors according to their different working principles. In photovoltaic-type UV PDs, the structures of p-n junction and Schottky junction were introduced. The key characteristics of UV PDs are gathered in Table I.1. They allow us to assess the performance of a UV photodetector.

In the next chapter, self-powered visible-blind UV PDs are fabricated and characterized. The response to UV-A is enhanced by the nanostructured heterointerface engineering.

## References

1. Seeger, K. *Semiconductor physics*. (Springer Science & Business Media, 2013).
2. Dimitrijević, S. *Principles of semiconductor devices*. (Oxford university press New York, 2012).
3. Kaltenbrunner, M. *et al.* Flexible high power-per-weight perovskite solar cells with chromium oxide–metal contacts for improved stability in air. *Nat. Mater.* **14**, 1032–1039 (2015).
4. Li, L. *et al.* Integrated flexible chalcogenide glass photonic devices. *Nat. Photonics* **8**, 643–649 (2014).
5. Thomson, S. Observing Phase Transitions in a Halide Perovskite Using Temperature Dependent Photoluminescence Spectroscopy. **4** (2018). (Edinburgh Instruments Ltd)
6. Anna Köhler and Heinz Bässler *Electronic Processes in Organic Semiconductors: An Introduction*. (Publisher John Wiley & Sons, 2015, ISBN3527685146, 9783527685141, Length 424 pages.)
7. Ulfa, M. Development of new selective contacts for efficient hybrid perovskite solar cells. (Dissertation, PSL University, 2019).
8. Ohl RS. Light sensitive electric device. US Patent 240252, filed 27 March 1941. Light-sensitive electric device including silicon. US Patent 2443542, filed 27 May 1941.
9. McEvoy, A., Castaner, L., & Markvart, T. *Solar cells: materials, manufacture and operation*. Academic Press (2012).

10. Lin, X. *et al.* Dipole-field-assisted charge extraction in metal-perovskite-metal back-contact solar cells. *Nat. Commun.* **8**, 613 (2017).
11. O'Regan, B. & Gratzel, M. A low-cost, high-efficiency solar cell based on dye-sensitized colloidal TiO<sub>2</sub> films. **353**, 4 (1991).
12. Wöhrle, D. & Meissner, D. Organic Solar Cells. *Adv. Mater.* **3**, 129–138 (1991).
13. Wells, H. L. Über die Cäsium- und Kalium-Bleihalogenide. *Z. Für Anorg. Chem.* **3**, 195–210 (1893).
14. Bartel, C. J. *et al.* New tolerance factor to predict the stability of perovskite oxides and halides. *Sci. Adv.* **5**, eaav0693 (2019).
15. Green, M. A., Ho-Baillie, A. & Snaith, H. J. The emergence of perovskite solar cells. *Nat. Photonics* **8**, 506–514 (2014).
16. Li, C. *et al.* Formability of ABX<sub>3</sub> (X = F, Cl, Br, I) halide perovskites. *Acta Crystallogr. B* **64**, 702–707 (2008).
17. Saliba, M. *et al.* Cesium-containing triple cation perovskite solar cells: improved stability, reproducibility and high efficiency. *Energy Environ. Sci.* **9**, 1989–1997 (2016).
18. Saliba, M. *et al.* Incorporation of rubidium cations into perovskite solar cells improves photovoltaic performance. *Science* **354**, 206–209 (2016).
19. Gholipour, S. *et al.* Globularity-Selected Large Molecules for a New Generation of Multication Perovskites. *Adv. Mater.* **29**, 1702005 (2017).
20. Abdi-Jalebi, M. *et al.* Maximizing and stabilizing luminescence from halide perovskites with potassium passivation. *Nature* **555**, 497–501 (2018).
21. Turren-Cruz, S.-H., Hagfeldt, A. & Saliba, M. Methylammonium-free, high-performance, and stable perovskite solar cells on a planar architecture. *Science* **362**, 449–453 (2018).
22. Wang, Q. *et al.* Enhancing efficiency of perovskite solar cells by reducing defects through imidazolium cation incorporation. *Mater. Today Energy* **7**, 161–168 (2018).
23. Jodlowski, A. D. *et al.* Large guanidinium cation mixed with methylammonium in lead iodide perovskites for 19% efficient solar cells. *Nat. Energy* **2**, 972–979 (2017).
24. Correa-Baena, J.-P. *et al.* Promises and challenges of perovskite solar cells. *Science* **358**, 739–744 (2017).
25. Kovalenko, M. V., Protesescu, L. & Bodnarchuk, M. I. Properties and potential optoelectronic applications of lead halide perovskite nanocrystals. *Science* **358**, 745–750 (2017).
26. Hwang, J. *et al.* Perovskites in catalysis and electrocatalysis. *Science* **358**, 751–756 (2017).
27. Cohen, R. E. Origin of ferroelectricity in perovskite oxides. *Nature* **358**, 136–138 (1992).
28. Stoumpos, C. C. *et al.* Ruddlesden–Popper hybrid lead iodide perovskite 2D homologous semiconductors. *Chem. Mater.* **28**, 2852–2867 (2016).
29. Stoumpos, C. C. *et al.* High members of the 2D Ruddlesden–Popper halide perovskites: synthesis, optical properties, and solar cells of (CH<sub>3</sub>(CH<sub>2</sub>)<sub>3</sub>NH<sub>3</sub>)<sub>2</sub>(CH<sub>3</sub>NH<sub>3</sub>)<sub>4</sub>Pb<sub>5</sub>I<sub>16</sub>. *Chem* **2**, 427–440 (2017).
30. Mao, L. *et al.* Hybrid Dion–Jacobson 2D lead iodide perovskites. *J. Am. Chem. Soc.* **140**, 3775–3783 (2018).
31. Mao, L., Stoumpos, C. C. & Kanatzidis, M. G. Two-dimensional hybrid halide perovskites: principles and promises. *J. Am. Chem. Soc.* **141**, 1171–1190 (2018).

32. Luo, T. *et al.* Compositional Control in 2D Perovskites with Alternating Cations in the Interlayer Space for Photovoltaics with Efficiency over 18%. *Adv. Mater.* **31**, 1903848 (2019).
33. Jung, H. S. & Park, N.-G. Perovskite solar cells: from materials to devices. *Small* **11**, 10–25 (2015).
34. Jena, A. K., Kulkarni, A. & Miyasaka, T. Halide perovskite photovoltaics: background, status, and future prospects. *Chem. Rev.* **119**, 3036–3103 (2019).
35. Kojima, A., Teshima, K., Shirai, Y. & Miyasaka, T. Organometal halide perovskites as visible-light sensitizers for photovoltaic cells. *J. Am. Chem. Soc.* **131**, 6050–6051 (2009).
36. Kim, H.-S. *et al.* Lead iodide perovskite sensitized all-solid-state submicron thin film mesoscopic solar cell with efficiency exceeding 9%. *Sci. Rep.* **2**, 1–7 (2012).
37. Lee, M. M., Teuscher, J., Miyasaka, T., Murakami, T. N. & Snaith, H. J. Efficient hybrid solar cells based on meso-superstructured organometal halide perovskites. *Science* **338**, 643–647 (2012).
38. Stranks, S. D. *et al.* Electron-hole diffusion lengths exceeding 1 micrometer in an organometal trihalide perovskite absorber. *Science* **342**, 341–344 (2013).
39. Zhou, H. *et al.* Interface engineering of highly efficient perovskite solar cells. *Science* **345**, 542–546 (2014).
40. Yang, W. S. *et al.* High-performance photovoltaic perovskite layers fabricated through intramolecular exchange. *Science* **348**, 1234–1237 (2015).
41. Yang, W. S. *et al.* Iodide management in formamidinium-lead-halide-based perovskite layers for efficient solar cells. *Science* **356**, 1376–1379 (2017).
42. Han, Q. *et al.* Single crystal formamidinium lead iodide (FAPbI<sub>3</sub>): insight into the structural, optical, and electrical properties. *Adv. Mater.* **28**, 2253–2258 (2016).
43. Lee, J.-W. *et al.* Formamidinium and cesium hybridization for photo- and moisture-stable perovskite solar cell. *Adv. Energy Mater.* **5**, 1501310 (2015).
44. Yi, C. *et al.* Entropic stabilization of mixed A-cation ABX<sub>3</sub> metal halide perovskites for high performance perovskite solar cells. *Energy Environ. Sci.* **9**, 656–662 (2016).
- 44a. NREL chart (2020) <https://www.nrel.gov/pv/cell-efficiency.html>
45. Jeon, N. J. *et al.* A fluorene-terminated hole-transporting material for highly efficient and stable perovskite solar cells. *Nat. Energy* **3**, 682–689 (2018).
46. Jiang, Q. *et al.* Surface passivation of perovskite film for efficient solar cells. *Nat. Photonics* **13**, 460–466 (2019).
47. Jung, E. H. *et al.* Efficient, stable and scalable perovskite solar cells using poly(3-hexylthiophene). *Nature* **567**, 511–515 (2019).
48. Yoo, J. J. *et al.* An interface stabilized perovskite solar cell with high stabilized efficiency and low voltage loss. *Energy Environ. Sci.* **12**, 2192–2199 (2019).
49. Kim, M. *et al.* Methylammonium chloride induces intermediate phase stabilization for efficient perovskite solar cells. *Joule* **3**, 2179–2192 (2019).
50. Zhu, H. *et al.* Tailored amphiphilic molecular mitigators for stable perovskite solar cells with 23.5% efficiency. *Adv. Mater.* **32**, 1907757 (2020).
51. Odysseas Kosmatos, K. *et al.* Methylammonium chloride: a key additive for highly efficient, stable, and up-scalable perovskite solar cells. *Energy Environ. Mater.* **2**, 79–92 (2019).
52. Gateva, S. *Photodetectors*. (IntechOpen, 2012).

53. Su, L., Yang, W., Cai, J., Chen, H. & Fang, X. self-powered ultraviolet photodetectors driven by built-in electric field. *Small* **13**, 1701687 (2017).

## Chapter II. Response Enhancement of Self-Powered Visible-Blind UV Photodetectors by Nanostructured Heterointerface Engineering

Development of efficient photodetectors (PDs) for ultra-violet (UV) light is of great importance for many applications. In this chapter, a novel approach is proposed for boosting the performances of self-powered PDs. Visible-blind UV-A PDs are built by combining a mesoporous TiO<sub>2</sub> layer with a Spiro-OMeTAD layer. The nanostructured heterointerface is engineered by inserting a self-assembled monolayer of organic modifiers. 4-nitrobenzoic acid (NBA), 4-chlorobenzoic acid (CBA), 4-methoxy benzoic acid (MBA), 4-nitro benzoic acid and  $\beta$ -alanine ( $\beta$ -ALA) surface modifier are studied by a combined experimental and theoretical approach. The performances of UV-A PDs are systemically characterized, which is highly related to the surface work functions.

### II.1 Introduction

The efficient photodetection of ultra-violet (UV) light has drawn considerable attention owing to its great importance in various and often strategic fields.<sup>1-12</sup> Systems have been designed for applications in environmental and biological analysis or monitoring, flame detection, military applications, geology detection, space communication, chemical and pharmaceutical analyses and industrial quality control.<sup>2-4</sup> Si-based technologies are well-established for these applications. However, due to the narrow (1.12 eV) and indirect bandgap of crystallized Si semiconductor (SC), the UV-enhanced Si technology requires the use of costly high-pass filters and phosphors to stop low energy photons. The use of thin films is preferable to save material. Moreover, wide-bandgap SCs allow direct UV detection and visible wavelength irradiation rejection without any additional device components. Among the potential candidates, oxides such as ZnO or TiO<sub>2</sub> are of utmost interest due to their high stability and their possible preparation as thin or nanostructured films from solutions. They have the advantage to be insensitive to the visible light and, therefore, they allow a visible-blind detection without any additional filters or phosphors.<sup>8,9</sup> Oxide active two-dimensional (2D) layers have been studied in UV-photodetectors (PDs) to a large extent.<sup>13</sup> Oxide one-dimensional (1D) structures, especially nanowire (NW) arrays, also present an interesting sensitivity to light for the application.<sup>10-12</sup> Furthermore, oxide NWs have allowed the miniaturization of the PD systems with the successful fabrication, in recent years, of single-

nanowire PDs, an approach which is also interesting to realize flexible self-powered PDs.<sup>4,6</sup>

Conventional UV-Photodetectors need to be driven by an external power source, such as a battery, to present suitable responsivities. It generates undesirable extra-cost, requires maintenance and generates environmental concerns. Alternatively, self-powered systems, which harvest their energy from the environment, are sustainable, maintenance-free, and self-contained. In most cases, they are driven by a built-in electric field.<sup>4</sup> There are three main strategies described in the literature to achieve self-powering: (i) p-n homojunction PDs, (ii) p-n heterojunction PDs and (iii) Schottky-junction based PDs. The preparation of high quality fully inorganic p-n heterojunction requires high temperature and/or vacuum and is costly.<sup>14,15</sup> On the other hand, oxide wide bandgap semiconductor layers and nanostructured films can be prepared easily from solutions and at low cost for n-type doping.<sup>4,11,16</sup> However, the synthesis of the p-type counterparts remains difficult and getting highly transparent p-type oxide is still challenging. Therefore, alternative solutions, easy to implement, must be proposed. Moreover, technological solutions to boost their detection properties are desirable.

Many organic compounds can be used for hole transport and which are p-doped.<sup>17,18</sup> Organic p-type SCs can be essentially divided into two subclasses: molecular and polymeric compounds.<sup>19,20</sup> The former is advantageous in terms of processability, thermomechanical stability, and higher intrinsic hole mobility. The latter is beneficial in terms of synthetic reproducibility, well-defined molecular weight and structure. Combining an inorganic n-type oxide with an organic p-type material in hybrid heterostructures in type II heterojunctions is a promising approach for the UV-A (320 nm to 400 nm) detection. In the first attempts, polymers were combined with oxides. Li *et al.* proposed a nanostructured near-UV photodetector based on ZnO nanorod/polyfluorene hybrid devices, which demonstrated a high responsivity of 0.18 A/W at 300 nm at -2 V.<sup>21</sup> Also p-type polyaniline (PANI) layers have been combined with various oxide n-type SC for the fabrication of UV-PDs such as p-polyaniline *p*-PANI/*n*-TiO<sub>2</sub>,<sup>22</sup> *p*-PANI/*n*-MgZnO,<sup>[23]</sup> *n*-ZnO/*p*-PANI/*n*-ZnO.<sup>24</sup> However, the reported responsivities were poor with a best value at 3.6 mA/W at 320 nm.<sup>4,22</sup> The use of molecular p-type SC has been poorly explored. While polymers with a conjugated chain present a rather good intrinsic conductivity, the molecular p-type SCs exhibit a low conductivity and require additives to be implemented in optoelectronic devices.<sup>19,20</sup> Some authors have investigated 2,2',7,7'-tetrakis(N,N-di-*p*-meth-methoxyphenylamine)-9,9'-spirobifluorene (Spiro-

MeOTAD) for the p-type layer in UV-PDs. This compound has a rather high  $T_g$  (above 125 °C) which is promising to achieve high device thermal stability.<sup>25-27</sup> It has been combined with various nanostructured wide bandgap oxide layers. Xie et al.<sup>28</sup> prepared UV-PDs based on Spiro-OMeTAD and TiO<sub>2</sub> nanorod arrays while Game et al.<sup>29</sup> investigated the combination of this molecular compound with ZnO NRs. Bai et al.<sup>27</sup> used a mesoporous TiO<sub>2</sub> layer as the n-type nanostructure. Molecular p-type SCs, especially Spiro-OMeTAD, allow a high pore filling of mesoporous nanostructured films. However, the maximum device responsivities were reported at 17 mA/W,<sup>28</sup> 10 mA/W,<sup>29</sup> and 18 mA/W.<sup>27</sup>

The literature survey shows the need of boosting the responsivity of self-powered hybrid UV-PDs. In this chapter, we propose a novel approach for this purpose. UV-A PDs have been built by combining a dense and mesoporous TiO<sub>2</sub> bilayer with a Spiro-OMeTAD layer. These devices are visible-blind. The interface between the two layers has been engineered by inserting a self-assembled layer of organic modifiers. In the fabrication process, the use of additives in the Spiro-OMeTAD has been avoided to prevent any interfacial change by these compounds and to improve the device stability. These interfacial modifiers presented a carboxylic acid group for their anchoring onto the oxide surface and a second para-functional group. It has resulted in a dipole moment which introduces a step of the vacuum level energy. Depending on the orientation of this dipole moment, an electric field is generated which assists or prevents the charge transfer at the heterojunction. By accurately choosing the modifier (*ad-hoc* functional group), we have been able to increase by 70% the responsivity of the hybrid UV-A PDs. The adsorption of the modifiers on the TiO<sub>2</sub> surface has been modeled by periodic Density Functional Theory (DFT) calculations. The normal component of the dipole moments to the exposed TiO<sub>2</sub> surface has been calculated and the trends obtained have been found in agreement with work function measurements. These combined studies have allowed confirming the dramatic effect of the interfacial energetics on the charge separation and device performances. Moreover, we have shown that these devices present an excellent reproducibility, excellent spectral selectivity, and a fast-dynamic response. Section II.2 is dedicated to the preparation of the TiO<sub>2</sub> layers, to their functionalizing by self-assembled monolayers (SAMs) of acid molecules and to the investigation of their fundamental properties. Section II.3 presents a DFT modeling of these systems. Section II.4 describes the preparation of the devices and the investigation of their photodetection characteristics.

## II.2 TiO<sub>2</sub> Layers Preparation and Functionalization by SAMs

### II.2.1 Experimental

#### II.2.1.1 Preparation of the TiO<sub>2</sub> layer

Fluorine-doped SnO<sub>2</sub> (FTO) substrates (TEC 7 from Pilkington) were etched by zinc powder and 10 % HCl solution and then cleaned with soap and water. The substrates were then immersed in a concentrated 2.2 M NaOH ethanol/water (10:1 v/v %) for 20 min and then cleaned with deionized water under ultrasonics for 15 min. The substrates were subsequently heated at 500 °C for 15 min. The TiO<sub>2</sub> blocking compact layer (noted *c*-TiO<sub>2</sub>) was prepared by an aerosol spray pyrolysis technique as described in the previous work of the group.<sup>30</sup> The obtained TiO<sub>2</sub> layer was dense, pinhole-free and 30-35 nm thick (Figure II.1).<sup>30</sup> The TiO<sub>2</sub> paste for the preparation of the mesoporous layer (noted *mp*-TiO<sub>2</sub>) was prepared in advance and stirred for at least 12 h. The TiO<sub>2</sub> NR30-D paste (from Greatcell) was diluted in ethanol with a 1:7 w/w ratio.<sup>46</sup> The mesoporous layer was spin coated by dropping 45 μL of the prepared TiO<sub>2</sub> paste on the compact TiO<sub>2</sub> layer and then quickly transferred to a hotplate at 70 °C and dried for 5-10 min. Finally, the *mp*-TiO<sub>2</sub> was heated at 500 °C under an air flux for 30 min, cooled down to 200 °C, and removed from the hotplate. The *mp*-TiO<sub>2</sub> layer morphology and cross-section view are displayed in Figure II.1. The thickness values are about 20 nm and 120-150 nm for compact and mesoporous TiO<sub>2</sub>, respectively.

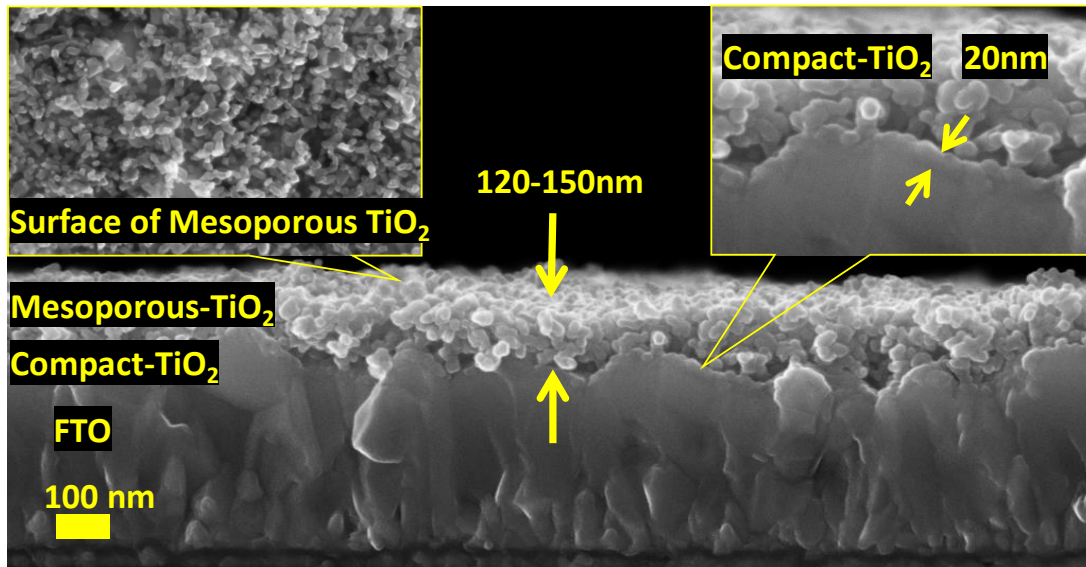


**Figure II. 1** SEM cross-section and top view of the *c*-TiO<sub>2</sub> compact layer and the *mp*-TiO<sub>2</sub> mesoporous layer.

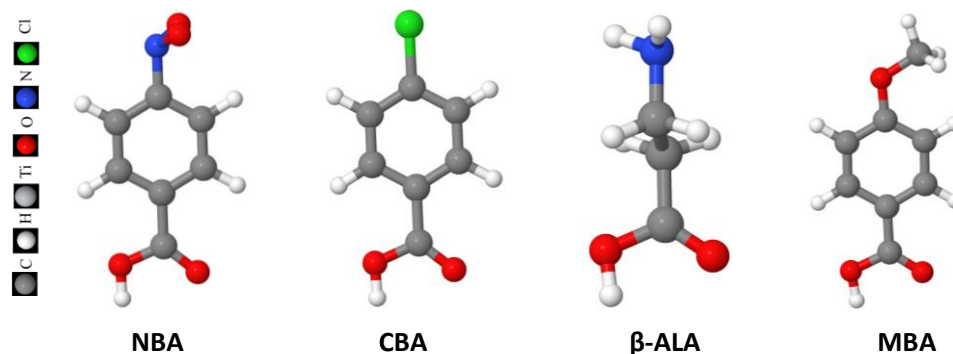


**Figure II. 2** The 3D structures of the molecules.

### *II.2.1.2 TiO<sub>2</sub> surface functionalizing*

The as-prepared mesoporous layers were transferred into a dry glovebox. The SAMs were deposited onto the *c*-TiO<sub>2</sub>/*mp*-TiO<sub>2</sub> bilayer by spin-coating. Four different acids were investigated for the mesoporous layer surface modification: 4-chlorobenzoic acid (CBA), 4-methoxy benzoic acid (MBA), 4-nitro benzoic acid (NBA) and β-alanine (β-ALA). Their molecular structures are displayed in Figure II.2. 1 mg of these molecules was dissolved in 1 mL methanol. 65 μL of the acid solutions were dropped onto the mesoporous layer, reacted 30 s before starting the spin-coater at a speed of 3000 rpm for 10 s. The samples were subsequently placed on a hotplate at 100 °C for 10 min. The same procedure was used again with pure methanol (washing with pure methanol and then annealing at 100 °C for 10 min) for removing the reactant excess.

### *II.2.1.3 Characterization methods*

**Kelvin probe:** The work function of the bare *mp*-TiO<sub>2</sub> and acid-modified *mp*-TiO<sub>2</sub> layers was investigated at the Laboratoire de Génie Électrique et Électronique de Paris (GeePs), UMR 8507 CNRS, Gif-sur-Yvette, France, using a Kelvin probe system from KP Technology (ASKP200250) equipped with a 2 mm diameter steel probe. The stability of the probe work function was evaluated on a gold reference sample provided by KP which work function was taken at 4.8 eV vs vacuum.

**UPS and IPES:** The electronic structure, work function and surface composition of the samples were investigated by photoelectron spectroscopies by Dr. S. Olthof, Department of Chemistry, Cologne University, Cologne, Germany. The samples were probed in a customized ultra-high vacuum system. UV-photoelectron spectroscopy (UPS) measurements were done using a monochromatic helium UV source (VUV5K, VG Scienta) at a photon energy of  $h\nu = 21.22$  eV. For X-ray photoelectron spectroscopy a non-monochromatic Mg K $\alpha$  source was used producing

photons at  $h\nu = 1252.6$  eV. In both cases, the photoelectrons were detected using a hemispherical analyzer (Phoibos 100, Specs). The unoccupied states were probed by inverse photoelectron spectroscopy (IPES) in an isochromat measurement mode. The low energy electrons were produced by an electron gun (ELG-2, Kimball) and the resulting photons were measured by a band-pass photon detector (IPES2000, Omnicvac).

**SEM:** The sample morphologies were examined with a high resolution Ultra 55 Zeiss FEG field-emission scanning electron microscope (FE-SEM) in the in-lens mode. The EDX spectra were measured with a Quantax system from Bruker operated at 15 kV.

**ATR-IR:** The adsorption of the acid molecules was investigated by an attenuated total reflection Fourier Transform infrared (ATR-IR) technique inspired from a previous study by my group on dye-sensitized solar cells.<sup>[47]</sup> The infrared spectra of molecules isolated and bound to TiO<sub>2</sub> nanoparticles were measured in a dry air-purged compartment of a ThermoScientific Nicolet 6700 spectrometer equipped with a mercury cadmium telluride (MCT) detector. A 1 mg/mL TiO<sub>2</sub> nanoparticle aqueous solution was prepared. A droplet of this solution was deposited on the system diamond crystal and dried under argon blowing. This process was repeated twice. The crystal was capped with a flow cell. First a reference spectrum consisting of TiO<sub>2</sub> in contact with ethanol was recorded. Afterward, starting the circulation system, the 10<sup>-3</sup> M solution of acid flowed past on the TiO<sub>2</sub> covered diamond crystal and the spectrum was recorded until no evolution of the signal was observed and then until the equilibrium state was reached (after 20-30 min). The baseline of these spectra was the ethanol/TiO<sub>2</sub> spectrum. The spectra of the isolated acids were recorded by depositing directly a concentrated solution (10<sup>-1</sup> M) of benzoic acid derivatives on the naked diamond crystal. A lower concentration, corresponding to its solubility limit, <10<sup>-2</sup> M, was employed in the case of  $\beta$ -ALA. We have checked that the results with ethanol solvent were the same as those with methanol, the solvent used for surface modification. The concentrations of the solutions employed in this experiment are gathered in Table II.1.

**Table II.1.** Solution concentration used for the FTIR study of free acids and acids adsorbed onto TiO<sub>2</sub> nanoparticles.

Volume	TiO <sub>2</sub>	CBA	MBA	NBA	$\beta$ -Alanine	solvent
10mL		10 <sup>-1</sup> M	10 <sup>-1</sup> M	10 <sup>-1</sup> M	<10 <sup>-2</sup> M	ethanol
50mL		10 <sup>-3</sup> M	10 <sup>-3</sup> M	10 <sup>-3</sup> M	10 <sup>-3</sup> M	
5mL	1 mg/mL	10 <sup>-1</sup> M				methanol

## II.2.2 Characterizations of the modified TiO<sub>2</sub> surfaces

### II.2.2.1 SEM

The top view SEM images of the *mp*-TiO<sub>2</sub> mesoporous layer with and without NBA treatment are shown in Figure II.3. No differences of the morphology are observed between the two surfaces, which means these self-assemble monolayers did not form clusters nor the aggregate of molecules onto the *mp*-TiO<sub>2</sub>.

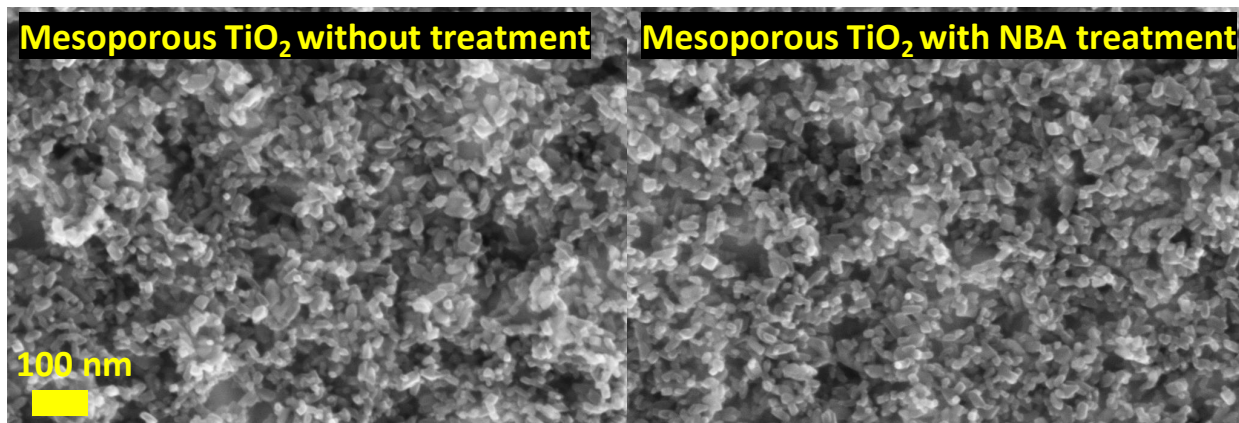


**Figure II. 3** Top views SEM images at the same magnification of the *mp*-TiO<sub>2</sub> mesoporous layer without and with NBA treatment.

### II.2.2.2 ATR-IR

The adsorption of the acids was further studied by FT-IR spectroscopy using an attenuated total reflection technique (ATR). Figure II.4 compares the ATR-IR absorbance spectra of the four acids dissolved in an organic solvent (black curves) and adsorbed onto TiO<sub>2</sub> particles (red curves). An experimental procedure was specifically designed to get reliable spectra in the latter case which is detailed in section II.2.1.2. For the benzoic acid derivatives, we observed a band at 1680-1723 cm<sup>-1</sup> (twinned in the case of NBA and CBA) which are assigned to a C=O stretching vibration.<sup>34-39</sup> This mode was shifted in the case of  $\beta$ -ALA and found at 1633 cm<sup>-1</sup>. These bands disappeared in all cases after the attachment onto the TiO<sub>2</sub> surface. The bands observed at 1533 cm<sup>-1</sup> (NBA), 1595 cm<sup>-1</sup> (CBA) and 1604/1595/1515 cm<sup>-1</sup> (MBA) remained after the binding of the benzoic acid derivatives and are assigned to C=C stretching modes. For  $\beta$ -ALA, bands were observed at 1572 cm<sup>-1</sup> and 1502 cm<sup>-1</sup> which correspond to antisymmetric and symmetric bending modes, respectively.<sup>40,41</sup> For all the isolated acids, a band was found at 1261-1265 cm<sup>-1</sup> which is assigned to the COO symmetric stretching mode ( $\nu_s$ ), while the bands at 1347 cm<sup>-1</sup> (NBA)/1401 cm<sup>-1</sup>

(CBA)/ 1428  $\text{cm}^{-1}$  (MBA)/ 1399  $\text{cm}^{-1}$  ( $\beta$ -ALA) are assigned to the antisymmetric stretching mode ( $\nu_{\text{as}}$ ) of  $-\text{COO}$ . The assignment has been confirmed by DFT calculations (refer to Table 3 in Section II.3). After adsorption, these modes were significantly shifted at higher wavenumbers (frequency) and found at 1415  $\text{cm}^{-1}$  (NBA)/ 1413  $\text{cm}^{-1}$  (CBA)/ 1410  $\text{cm}^{-1}$  (MBA)/ 1409  $\text{cm}^{-1}$  ( $\beta$ -ALA) for  $\nu_{\text{s}}$  and 1566  $\text{cm}^{-1}$  (NBA)/ 1593  $\text{cm}^{-1}$  (CBA)/ 1591  $\text{cm}^{-1}$  (MBA)/ 1580  $\text{cm}^{-1}$  ( $\beta$ -ALA) for  $\nu_{\text{as}}$ . These results indicate that there is a monolayer formed on the  $\text{TiO}_2$  particles.

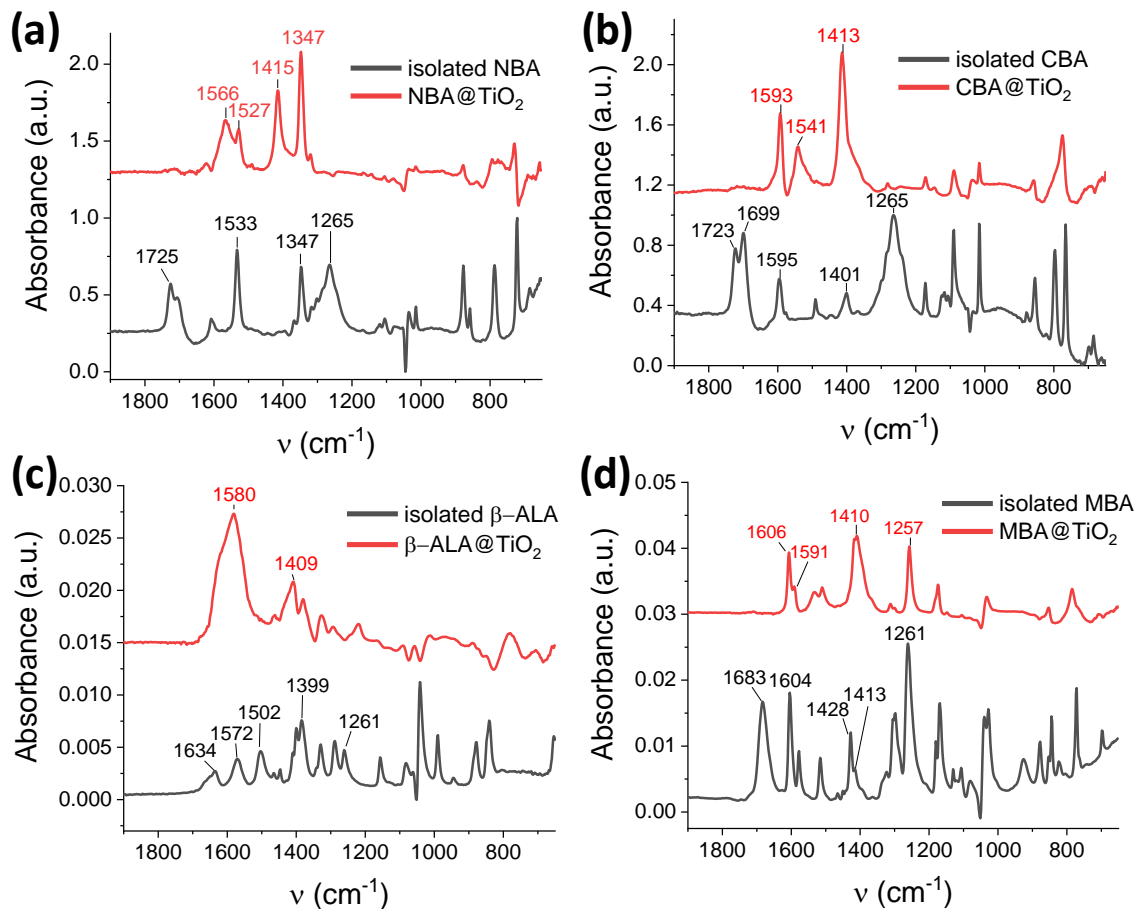


**Figure II. 4** FT-IR of the modifiers dissolved in ethanol (black) and adsorbed onto  $\text{TiO}_2$  nanoparticles (red): (a) NBA; (b) CBA; (c)  $\beta$ -ALA; (d) MBA.

### II.2.2.3 Measurements of work functions

Due to the polarization of the acid molecules, their adsorption induces the presence of a dipole moment at the  $\text{TiO}_2$  surface.<sup>45</sup> The dipole component normal to the surface ( $\mu_{\perp}$ ) introduces a step in the local vacuum level due to the electric field across this layer. The work function and the band edge of the  $\text{TiO}_2$  surface are changed by  $q\Delta V$  where  $q$  is the elemental charge.  $\Delta V$  is expressed by

the Poisson's equation:

$$\Delta V = \frac{N_s \mu \cos \theta_a}{\epsilon_r \epsilon_0} \quad \text{II.1}$$

with  $N_s$  the surface dipole density,  $\mu$  the dipole moment,  $\theta_a$  the tilt angle of the dipole versus the surface normal,  $\epsilon_r$  the dielectric constant and  $\epsilon_0$  the permittivity of free space.

The changes in the local vacuum level have been quantified by Kelvin probe measurements of the work functions of the bare and the modified TiO<sub>2</sub> layers. Work function versus the calculated normal dipole moment ( $\mu_{\perp} = \mu \cos \theta_a$ ) of the molecules adsorbed onto TiO<sub>2</sub> are shown in Figure II.5. The values of  $\mu_{\perp}$  for the adsorbed SAMs are given in Table II.2. They were obtained by DFT calculations (see Section II.3). For the blank and the benzoic acids, a linear relationship was found which was in agreement with Equation (1). A special behavior was found for  $\beta$ -ALA, which the point being outside the straight line. The work function measurements by Kelvin probe suggest that the dipole moment for adsorbed  $\beta$ -ALA should be negative.

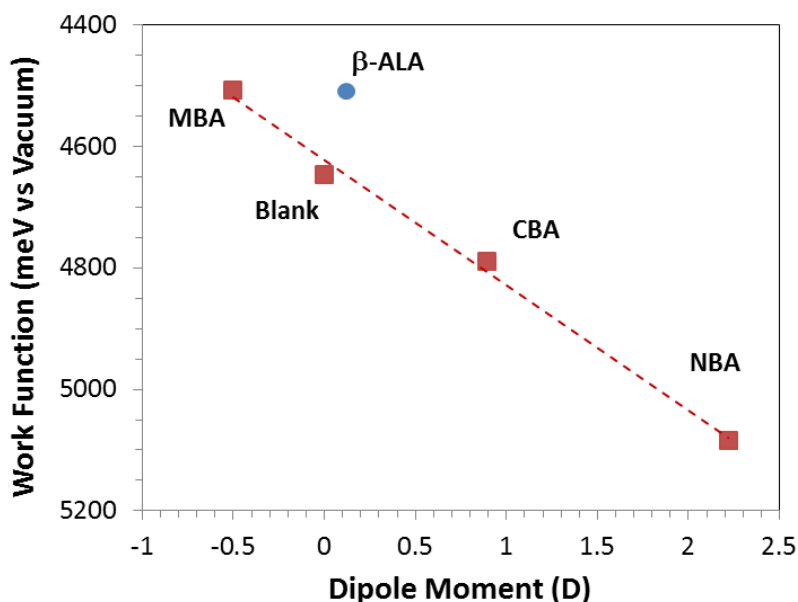


**Figure II. 5** Work function (Kelvin probe) versus the calculated dipole moment ( $\mu_{\perp}$ ) of the molecules adsorbed onto TiO<sub>2</sub>.

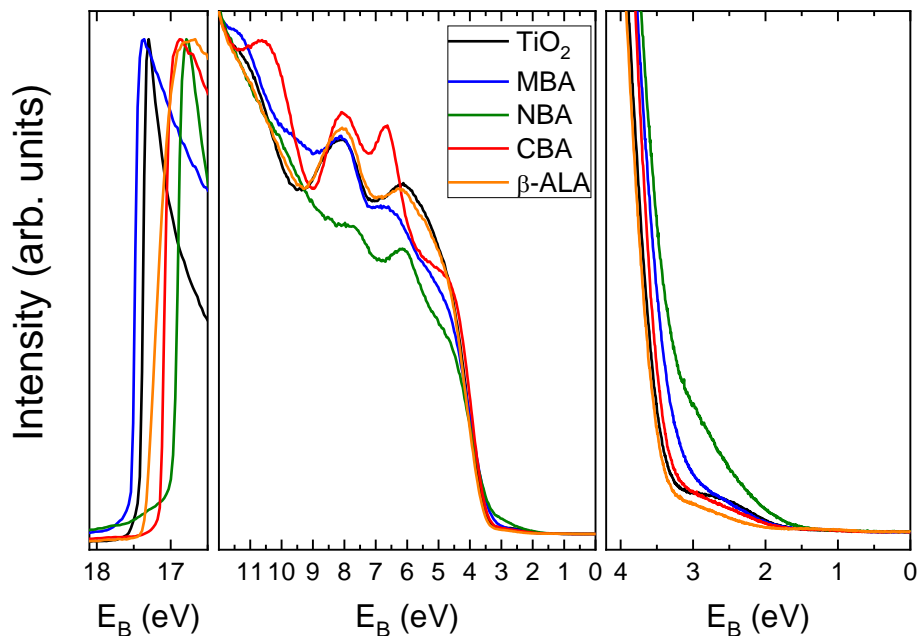


**Figure II. 6** UPS of SAMs modified TiO<sub>2</sub> layer (Drawn by Dr. Selina Olthof). The dial on the right is a zoom view of the spectra cut-off region.

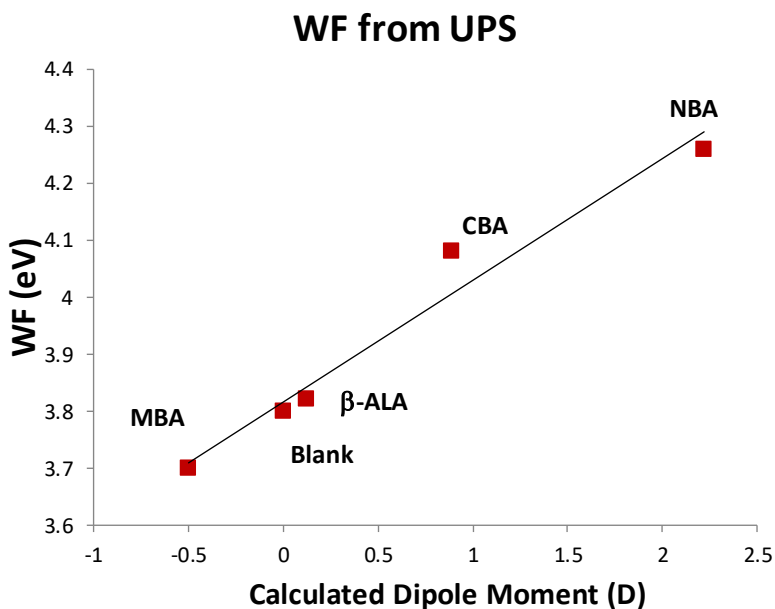


**Figure II. 7** Work function (UPS) versus the calculated dipole moment ( $\mu_{\perp}$ ) of the molecules adsorbed onto TiO<sub>2</sub>.

The UPS curves for SAMs modified *c*-TiO<sub>2</sub> and *mp*-TiO<sub>2</sub> bilayers are shown in Figure II.6. From the left part of the curves, the cut-off signal comes from the topmost layer, which is composed of the SAMs. The work functions of SAMs modified TiO<sub>2</sub> can be obtained from the intercept of the

x-axis by extending the cut-off part curves. The obtained values are gathered in Table II.2. The plot of the WFs from UPS measurements versus  $\mu_{\perp}$  is shown in Figure II.7. The result is in agreement with Kelvin probe measurements, except for  $\beta$ -ALA which falls now in the linear trend.

**Table II.2** Values of dipole moment, Cut-off and WF.

	$\mu_{\perp}$ (D)	Cut-off <sup>1</sup> (eV)	WF (eV)	WF <sup>a</sup> (eV)	Cut-off <sup>2</sup> (eV)	IE (eV)
TiO <sub>2</sub>	0	17.42	3.8	4.65	3.57	7.37
MBA	-0.5	17.52	3.7	4.50	3.44	7.13
$\beta$ -ALA	0.12	17.4	3.82	4.51	3.94	7.82
CBA	0.89	17.14	4.08	4.80	3	7.08
NBA	2.22	16.96	4.26	5.08	2.37	6.64

<sup>a</sup>: Work function by Kelvin probe; <sup>1</sup> WF, <sup>2</sup> HOMO onset

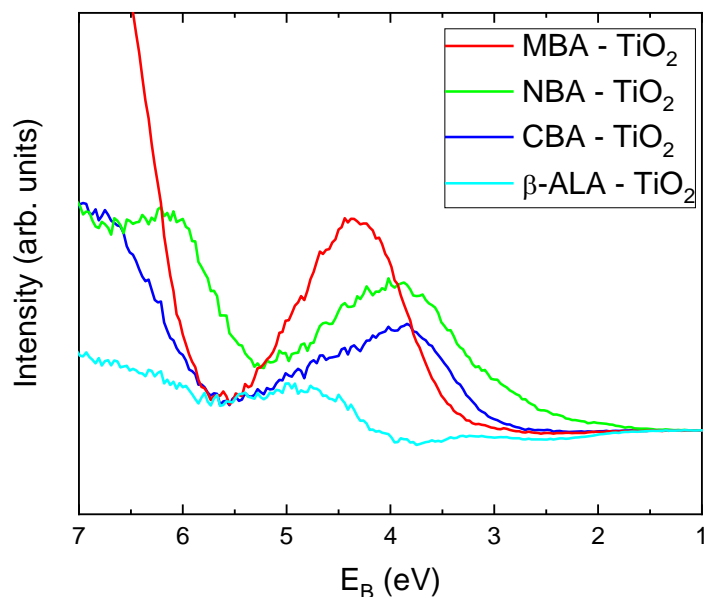


**Figure II. 8** HOMO onsets of SAMs. (Drawn by Dr. Selina Olthof).

The UPS measurement can also provide the ionic energy (IE) of the SAMs. To figure out what is the additional DOS of the SAMs, Dr. Selina Olthof subtracted the TiO<sub>2</sub> spectrum from the SAMs measurements. The results are shown in Figure II.8 and the values of HOMO onsets and IE are given in Table II.2. But this subtraction is only a very rough method that produces errors. Because the suppression of DOS features from TiO<sub>2</sub> will depend on energy and because we also know from XPS that in some cases TiO<sub>2</sub> features shift slightly in energy upon SAM coverage.

There is a way of determining what happens to the Ti states at the interface, even if in UPS the signal gets covered up in some way by the SAMs. The method consists of using XPS to see the changes in the core level of TiO<sub>2</sub>. The result is shown in Figure II.9. If there is a shift in the VB states of TiO<sub>2</sub>, then the core levels will do the same. Knowing that the pure TiO<sub>2</sub> has a valence band energy of 3.57 eV and a WF of 3.8 eV, the IE of TiO<sub>2</sub> is calculated by 3.57 eV + 3.8 eV = 7.37 eV. Next, we can use changes in XPS core level peaks to figure out how the VB of Ti must change due to interaction with the SAM. Using the changes in peak position in the Figure II.9 on the left, we obtained the new VB onsets: 3.57 - (459.09 - 459.07) = 3.55 eV for MBA modified TiO<sub>2</sub>, and in a similar way 3.37 eV was obtained for NBA-modified TiO<sub>2</sub>, 3.57 eV for CBA-modified TiO<sub>2</sub> and 3.61 eV for β-ALA-modified TiO<sub>2</sub>.

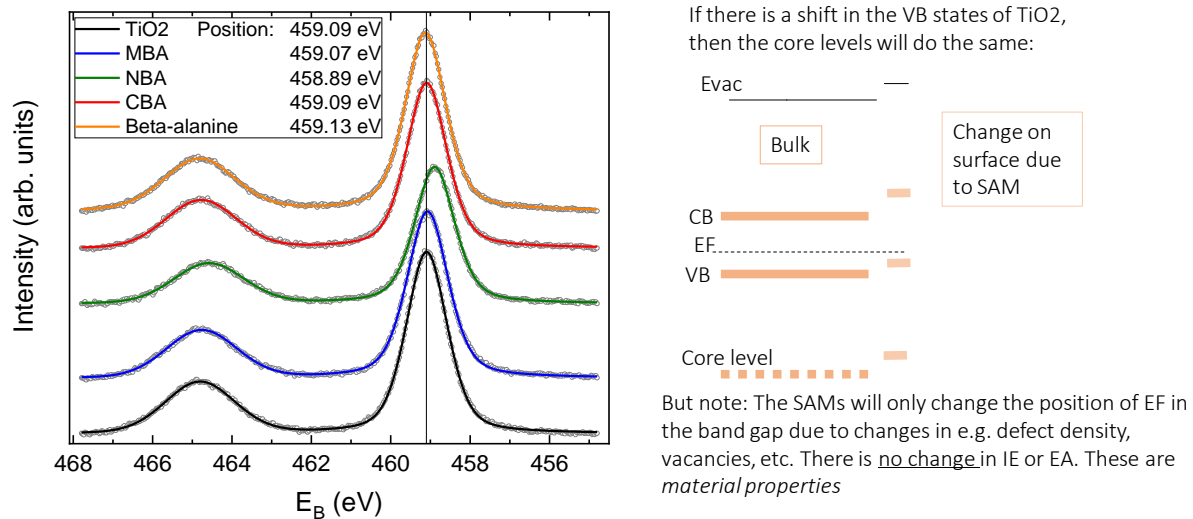


**Figure II. 9** XPS core level measurements. (Drawn by Dr. Selina Olthof).

Considering all the measurements and corrections, the energy band levels for all the SAMs modified TiO<sub>2</sub> layers are given in Figure II.10. In short, SAMs of NBA, CBA and β-ALA increases the work function of TiO<sub>2</sub> due to their positive dipole moments while MBA decreases the work function due to its negative dipole moment. The surface valence band of TiO<sub>2</sub> is affected by the SAMs, which causes the surface Fermi level shift. NBA and MBA make the Fermi level shifting down, meaning that the work function of the surface TiO<sub>2</sub> increased. β-ALA decreases this work function and CBA keeps it the same. This diagram will be important to analyze the charge movement in further devices.

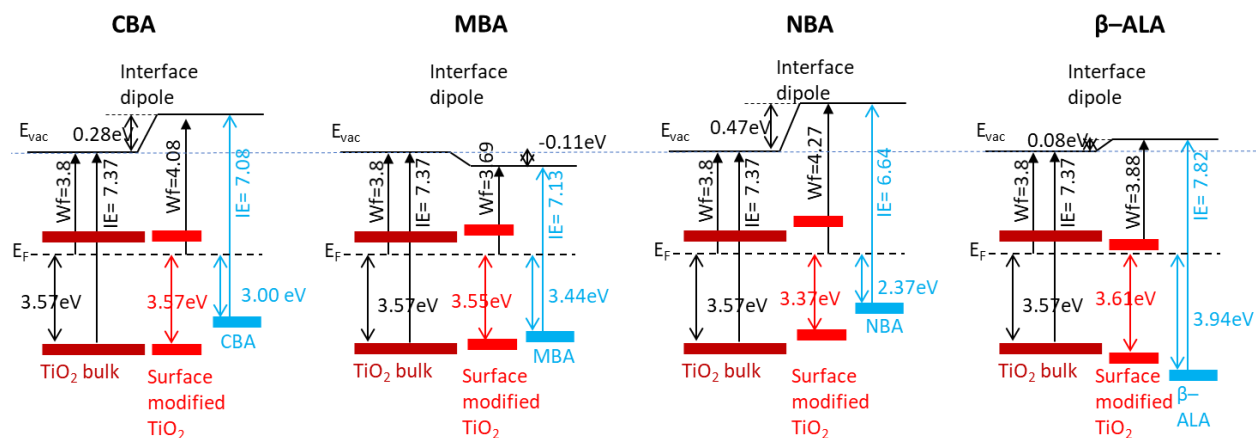


**Figure II. 10** Energy level diagram for SAMs modified TiO<sub>2</sub>.

### II.3 Modelling by Density Functional Theory

To gain a deeper insight into the effect of the modifiers on the interface energetic, electronic and vibrational properties, the adsorption of the various acids on the (101) anatase TiO<sub>2</sub> surface (the most stable one<sup>42</sup>) was modeled by DFT. This work has done by Mr. Ju Su, Dr. Frédéric Labat and Prof. Ilaria, Ciofini (Institute of Chemistry for Life and Health Sciences (i-CLeHS), Chimie-Paristech, Paris, France) with my collaboration. The computational details are provided in the Annex-II. We detail the modeling results important to fully understand the investigated modified oxide surfaces.

#### II.3.1 Modelling of the acid adsorption onto TiO<sub>2</sub>

Our first objectives were to determine the binding mode, the adsorption energy and the structural features of the four different molecules adsorbed onto the surface. The most favorable adsorption mode is the bridging bidentate one. Computed adsorption energies are gathered in Table II.3. Data in the literature support a dissociative adsorption mechanism<sup>27</sup> and a bidentate adsorption mode for carboxylic acids bind on anatase surface which is consistent with the acidity of this group.<sup>43,44</sup> The dissociative process is written:



The O-H bond is broken and the H<sup>+</sup> atom is connected to an O atom onto the anatase surface as shown in Figure II.11. In the bidentate bridging mode, each oxygen atom in the -COO functional

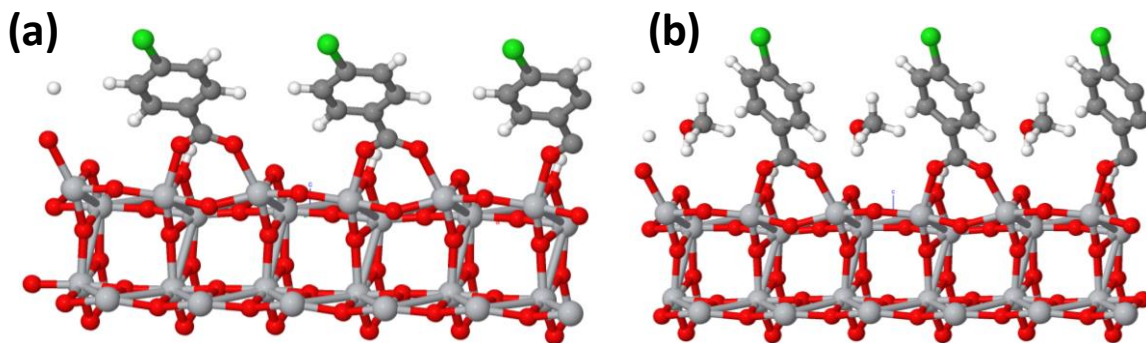


**Figure II. 11** Optimized structure of CBA molecules adsorbed on anatase  $\text{TiO}_2$  (101) surface without (a) and with (b) methanol solvent. The carbon, titanium, oxygen, chloride, and nitrogen atoms are represented by grey, silver, white, red, green, and blue balls, respectively.

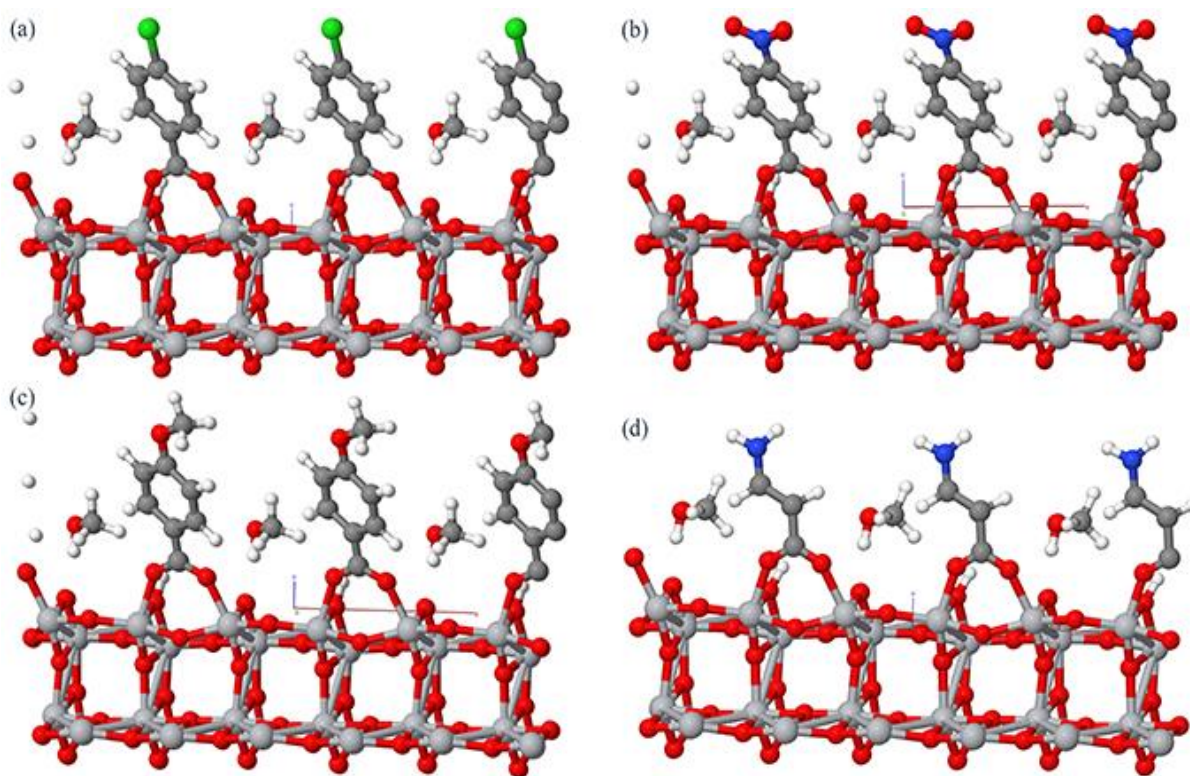


**Figure II. 12** Optimized structure of the 4 acids adsorbed onto the anatase (101) surface. The carbon, titanium, oxygen, chloride and nitrogen atoms are represented by grey, silver, white, red, green and blue balls, respectively. (a) CBA, (b) NBA, (c) MBA and (d)  $\beta$ -ALA.

group is bound to a different Ti atom of the surface, with very similar O-Ti distances. Figure II.11 presents the optimized DFT structure of CBA adsorbed on  $\text{TiO}_2$  both (a) without and (b) with an explicit methanol solvent molecule. A large tilting of the benzene ring compared to the vertical

position is observed. This tilting is found for all the benzoic acid derivatives and  $\beta$ -ALA (Figure II.12). The tilt angle versus the surface normal ( $\theta_a$ ) is reduced and the molecules are straightened when an explicit solvent molecule (here methanol which is the solvent used experimentally for the acid treatment of the surface) is considered. For instance, the angle changed from  $42^\circ$  to  $30^\circ$  in the case of CBA (Figure II.11).  $\theta_a$  for the various acids are gathered in Table II.3. The tilting is more relevant for the benzoic acids compared to  $\beta$ -ALA due to the  $\pi$ -interaction between  $H^+$  atom on the surface and the ring. The detailed geometrical parameters (distance and angles) for the isolated acids and adsorbed acids@TiO<sub>2</sub> are gathered in Table A.II.1 in Annex-II.

**Table II.3** Calculated structural tilt angle ( $\theta_a$ ), adsorption energy and normal component of the dipole moment with respect to the TiO<sub>2</sub> surface of the acids adsorbed on TiO<sub>2</sub> ( $\mu_\perp$ ). Corresponding calculated values for the isolated molecules are reported in brackets.

	NBA	CBA	$\beta$ -ALA	MBA
$\theta_a$ ( $^\circ$ )	31.6	30.3	13.4	30.6
Adsorption Energy (kcal/mol)	-11.3	-20.7	-20.2	-30.6
$\mu_\perp$ (D)	2.22 (3.72)	0.89 (1.55)	0.12 (2.79)	-0.5 (-2.57)

### II.3.2 FT-IR by theoretical calculations

Then, the harmonic vibrational frequencies were computed and compared to our FT-IR spectra measurements (Figure II.13). The calculated -COO  $\nu_{as}$  and  $\nu_s$  wavenumbers are given in Table II.4.  $\Delta_1$  is the wavenumber difference between the theoretical calculations and the experimental results. A general good agreement is obtained between the computed and the experimental data. In particular, in most cases,  $\Delta_1$  is lower than  $50\text{ cm}^{-1}$ , and a shift at higher wavenumbers is obtained after the molecule binding to the TiO<sub>2</sub> surface. The computed wavenumber difference between the antisymmetric and the symmetric stretching modes ( $\Delta_2$ ) is, as expected, the same for all the isolated benzoic acid derivatives ( $180\text{ cm}^{-1}$ ) and slightly lower in the case of isolated  $\beta$ -ALA. On the other hand, for the adsorbed compounds  $\Delta_2$  varies as a function of the acid considered. When adsorption occurs, the environment for COO- bond changes, its symmetric and antisymmetric stretchings are affected and  $\Delta_2$  value decreases. This change may also indicate the dissociation process of carboxylic acid. Furthermore, the experimental and the computed values are close as reported in Table II.4, thus validating the model developed. In particular, this confirms that a bridging bidentate binding mode is obtained for all ligands adsorbed on TiO<sub>2</sub>.

**Table II.4** Selected computed and experimental IR wavenumbers of isolated acids and acids on the anatase surface.  $\Delta_1$  is the difference between the experimental and calculated data, and  $\Delta_2$  is the difference between the wavenumber of symmetric ( $\nu_s$ ) and antisymmetric ( $\nu_{as}$ ) stretching of -COO bonds. All data in  $\text{cm}^{-1}$ .

		Isolated			Adsorbed@TiO <sub>2</sub>		
		Calc.	Exp.	$\Delta_1$	Calc.	Exp.	$\Delta_1$
CBA	$\nu_s$	1215	1265	50	1472	1413	-59
	$\nu_{as}$	1395	1401	6	1590	1593	3
	$\Delta_2$	180	136		118	180	
NBA	$\nu_s$	1215	1265	50	1473	1415	-58
	$\nu_{as}$	1395	1347	-48	1598	1566	-32
	$\Delta_2$	180	82		125	151	
MBA	$\nu_s$	1219	1261	42	1467	1410	-57
	$\nu_{as}$	1399	1428	29	1585	1591	6
	$\Delta_2$	180	167		118	181	
$\beta$ -ALA	$\nu_s$	1218	1261	43	1497	1409	-88
	$\nu_{as}$	1392	1399	7	1585	1580	-5
	$\Delta_2$	174	138		88	171	

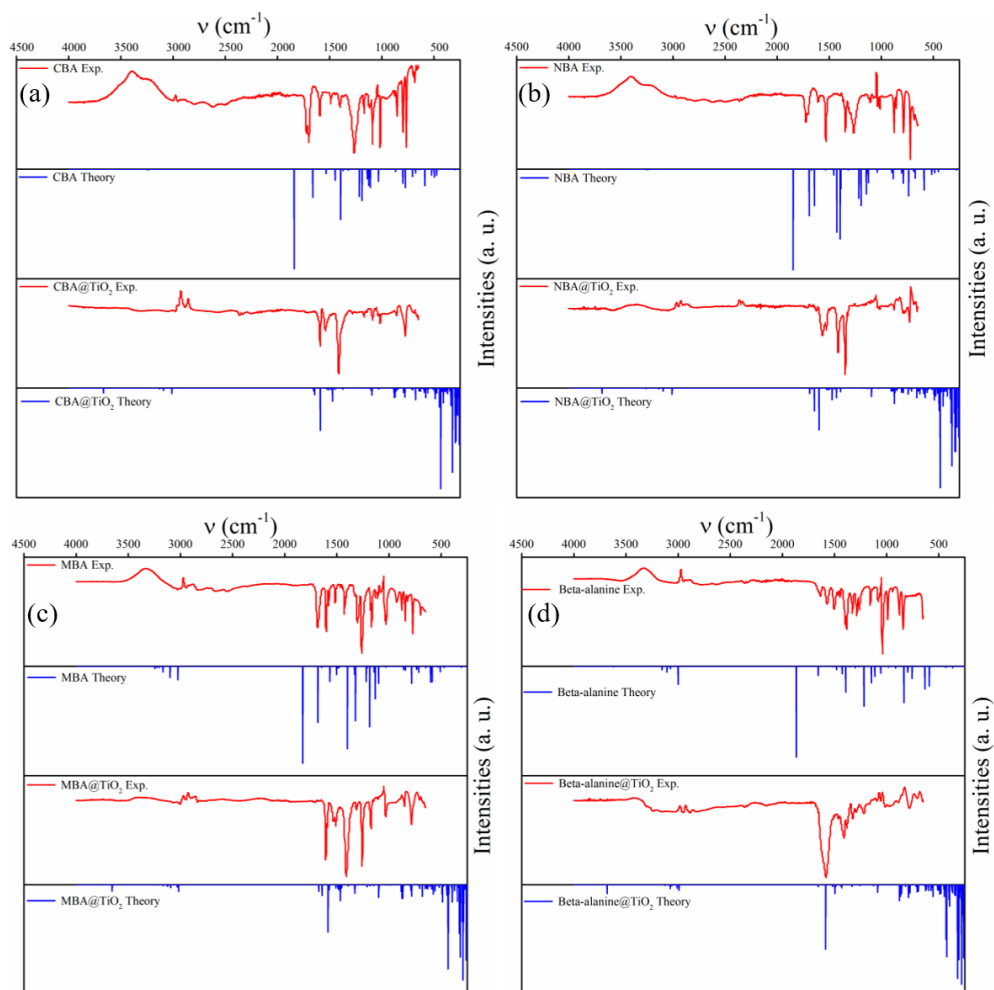


**Figure II. 13** Comparison of infrared spectra between isolated acids and adsorption cases. The red continuous line is the experimental data; the blue discrete peaks correspond to data derived from theoretical calculations.

### II.3.3 Dipole moment

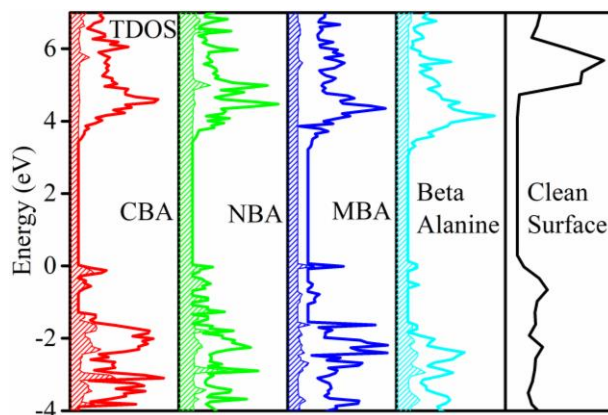
$\mu_{\perp}$  values, calculated by DFT for the various acids, are gathered in Table II.3. The order is NBA > CBA >  $\beta$ -ALA > MBA. We note that  $\mu_{\perp}$  of MBA is negative (dipole moment pointing toward TiO<sub>2</sub> in the chemistry notation). In the same table, we also report the values calculated for the free molecules. After adsorption, the magnitude of all the dipole moments decreased due to two phenomena: a charge transfer to the TiO<sub>2</sub> surface combined to the tilting of the molecules on the surface. More precisely, while a charge transfer to the TiO<sub>2</sub> surface of about 0.26 |e<sup>-</sup>| is computed for CBA, NBA and MBA,  $\beta$ -ALA shows a lower charge transfer of about 0.21 |e<sup>-</sup>|, suggesting a lower generated photocurrent in the PDs (see section II.4).

The present results show that the strong influence of adsorption on the  $\mu_{\perp}$  value and that the modeling of the adsorption of the molecules on the TiO<sub>2</sub> surface is required to properly discuss dipole moment effects.

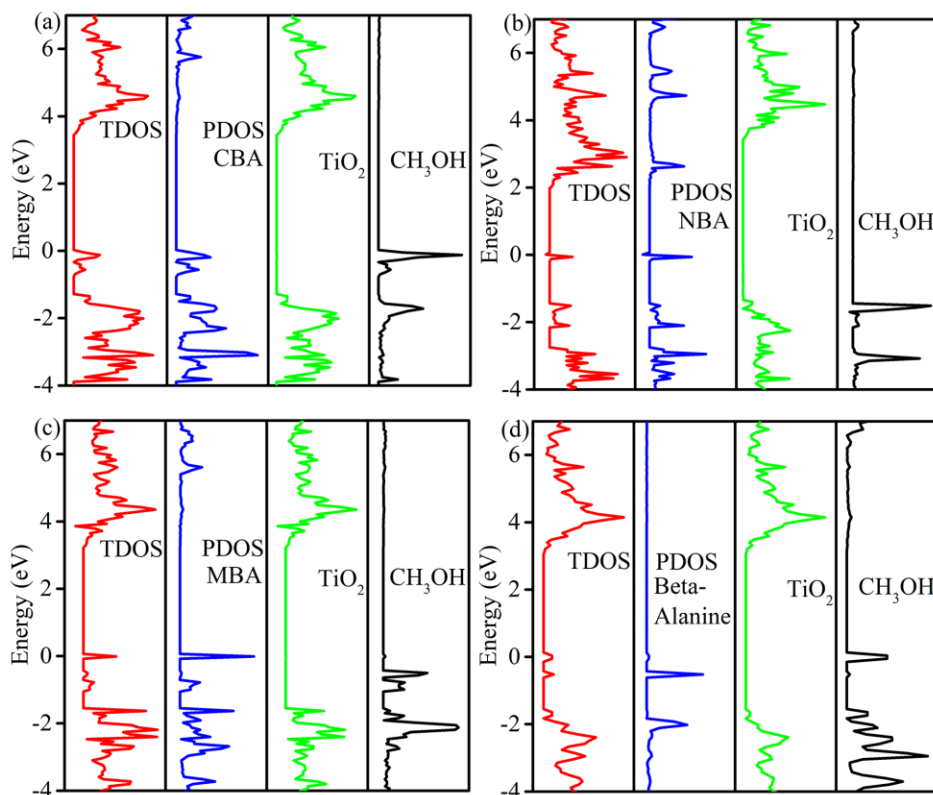
### II.3.4 Energy band level

Figure II.14 shows the total density of states (TDOS) for the four acids adsorbed on anatase (101) surface. The result for a clean surface is also provided for comparison. The shadow is the corresponding ligand project density of states (PDOS). Compared with the clean surface, bottoms of conduction band decrease a lot. This is in agreement with the dipole effects we talked about above. The PDOS shows that the adsorbed molecules contribute a lot to the valence band. Methanol here does not introduce new states in the band, which means that the chosen solvent is suitable (Figure II.15). TiO<sub>2</sub> contributes to the conduction band while ligands contribute to the valence band. The cases for CBA, NBA, MBA, and  $\beta$ -ALA are the same, which further suggests that the ligand's molecular orbitals form electronic states. The bandgaps of isolated acids and bare-TiO<sub>2</sub> film can be obtained from absorbance spectra as shown in Figure II.16. We can get electron affinity (EA) by ionic energy (IE) plus the bandgap. The comparison between experimental and calculated energy band positions are gathered in Table II.5a and b. (described by Dr. Jun Su)

It is worth to note that the valence band of NBA modified TiO<sub>2</sub> improved a lot compared to bare-TiO<sub>2</sub> in the energy band model, which is perfectly in agreement with the result from XPS core level measurement (Figure II.2.10).



**Figure II. 14** Comparison of TDOS and PDOS for ligand,  $\text{TiO}_2$  and  $\text{CH}_3\text{OH}$  for (a) CBA, (b) NBA, (c) MBA and (d)  $\beta$ -Alanine on anatase (101) surface.



**Figure II. 15** Comparison of TDOS and PDOS for ligand,  $\text{TiO}_2$  and  $\text{CH}_3\text{OH}$  for (a) CBA, (b) NBA, (c) MBA and (d)  $\beta$ -Alanine on anatase (101) surface. (basing the system of SAMs@one-layer  $\text{TiO}_2$ )

**Table II.5a.** Energy positions for isolated molecules.

SAMs@TiO <sub>2</sub>	Experiment (eV)			Calculation (in vacuum, eV)		
	IE <sup>a</sup>	EA	Bandgap <sup>b</sup>	HOMO	LUMO	Bandgap
CBA	-7.08	-1.86	5.22	-7.47	-1.49	5.98
MBA	-7.13	-2.24	4.89	-6.62	-0.90	5.72
NBA	-6.64	-1.89	4.75	-8.22	-2.90	5.31
β-ALA	-7.82	-1.62	? (6.2)	-7.15	0.24	7.39
Bare-TiO <sub>2</sub>	-7.37	-4.02	3.35 <sup>c</sup>	-8.56	-3.52	5.03

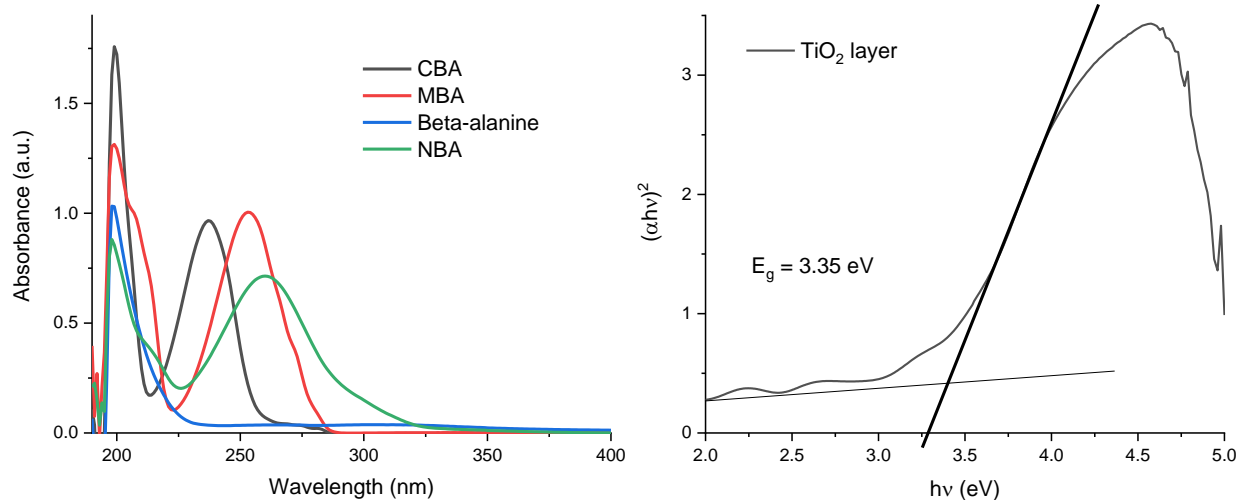
a: The values are from UPS measurement.

b: The values are from UV-vis absorbance spectrum and the molecules dissolved in methanol.

c: The value is from UV-vis absorbance spectrum and the sample is mp-TiO<sub>2</sub> film.

**Table II.5b** Energy band for SAMs@TiO<sub>2</sub> system (calculation values)

SAMs@TiO <sub>2</sub> system	Calculation		
	VB (eV)	CB (eV)	Bandgap (eV)
CBA@TiO <sub>2</sub>	-7.45	-3.96	3.49
MBA@TiO <sub>2</sub>	-6.57	-3.29	3.28
NBA@TiO <sub>2</sub>	-8.03	-4.60	3.43
β-ALA@TiO <sub>2</sub>	-6.65	-3.58	3.07
Bare-TiO <sub>2</sub> (H <sup>+</sup> )	-0.23	-4.52	4.75

**Figure II. 16** (a) absorbance of these 4 acids dissolved in methanol, (b) bandgap of TiO<sub>2</sub>.

## II.4 UV Photodetector Devices

Self-powered visible blind UV photodetectors were fabricated based on the above SAMs covered TiO<sub>2</sub>. Spiro-OMeTAD was selected as light absorber due to its suitable bandgap, good stability and easily deposition by spin-coating to form a compact film.

### II.4.1 Experimental

#### II.4.1.1 Device preparation

A fresh solution was prepared by dissolving 78 mg of Spiro-OMeTAD (Borun New Material Technology) in 1 mL of chlorobenzene. The Cobalt (Co) doped spiro-OMeTAD layer was prepared by doping 18  $\mu$ L tris(2-(1H-pyrazol-1-yl)-4-tert-butylpyridine)-cobalt(III) tris(bis(trifluoromethylsulfonyl)imide) (Dyesol, FK209) (376 mg in 1 mL acetonitrile) in the spiro-OMeTAD precursor solution. The Lithium (Li) and Co doped spiro-OMeTAD layer was prepared by doping 18  $\mu$ L Co-salt solution, 23  $\mu$ L bis(trifluoromethylsulfonyl)imide lithium salt solution (Li-TFSI) (Sigma Aldrich) (517 mg in 1 mL ACN) and 39  $\mu$ L TBP (tert-butylpyridine) in the spiro-OMeTAD precursor solution. 40  $\mu$ L of this solution was spin-coated on the bare and SAMs modified TiO<sub>2</sub> layers at 4000 rpm for 20 s. If not specified, the layer was not doped with oxidizing agents because these additives can be detrimental for the stability of the device and can modify the interface. The samples with spiro-OMeTAD layer were transferred into a nitrogen filled glovebox for one night. The devices were completed by evaporating an 80 nm thick gold contact in a vacuum chamber.

#### II.4.1.2 Characterization methods

The UV-Vis absorbance spectra were measured with a Cary 5000 UV-Vis-NIR spectrophotometer. The *J-V* curves were recorded by a Keithley 2410 digital source meter at a 50 mV/s scan rate. The p-n junctions were measured in the dark and under illumination with a 365 nm UV LED lamp at controlled irradiance (between 0.55 mW/cm<sup>2</sup> and 200 mW/cm<sup>2</sup>). The irradiance was calibrated using a coherent fieldmaxII power meter. The active surface area was about 0.26 cm<sup>2</sup>. No mask was used, and the devices were illuminated through the glass substrate. The external quantum efficiency (EQE) spectra were measured using an Oriel QUANTX-300 system. The light beam was chopped at 77 Hz. The monochromatic illumination was calibrated by a NIST-calibrated Si photodiode. The presented results are from devices that were stored for more than one month under ambient conditions.

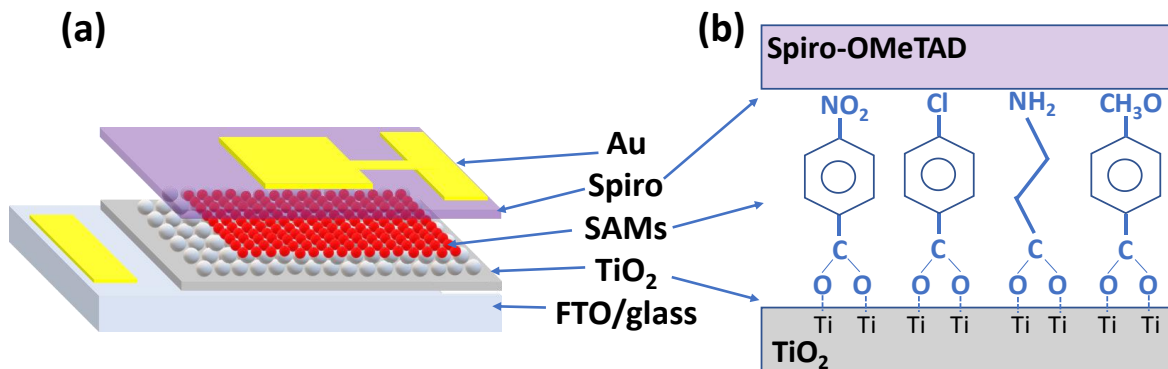


**Figure II. 17** (a) Photodetector exploded schematic view. (b) Schematic of the acids self-assembled interlayer between  $\text{TiO}_2$  and Spiro-OMeTAD. From left to right: 4-nitrobenzoate (NBA); 4-chlorobenzoate (CBA); beta-alanine ( $\beta$ -ALA) and 4-methoxybenzoate (MBA).

## II.4.2 Characterizations of the UV PDs

### II.4.2.1 J-V curves

The device structure is presented in Figure II.17a and the interfacial layer formed with the four acids between  $\text{TiO}_2$  and the Spiro-OMeTAD layer is presented in Figure II.17b. The devices were initially characterized by measuring their  $J$ - $V$  curves under 365 nm UV-light. The initial curves are shown in Figure II.18a and the detailed photovoltaic parameters were gathered in Table A.II.2a). A photovoltaic effect was found but the recorded curves were S-shaped, whether the interface was acid-modified or not. The devices did not work correctly due to undoped Spiro-OMeTAD layer has a low conductivity (estimated at  $3 \cdot 10^{-7} \text{ S} \cdot \text{cm}^{-1}$  in our previous work<sup>20</sup>). Charge extraction is then difficult, and we suggest that charge accumulation occurs at the interface that plays on the recombination process.<sup>31</sup>

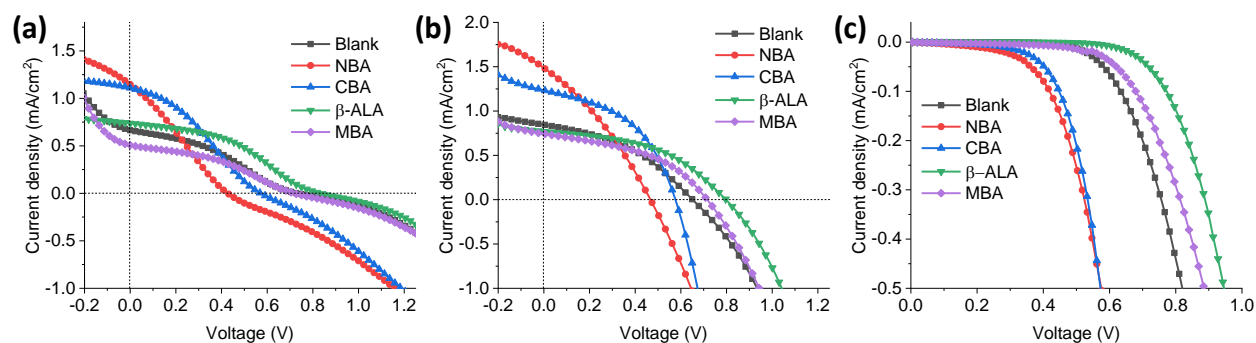


**Figure II. 18** Current Density-Voltage curves under UV light ( $\lambda = 365 \text{ nm}$ ,  $40 \text{ mW} \cdot \text{cm}^{-2}$ ). (a) Initial and (b) after one month of storage under ambient. (c) Dark current after one month of storage.

After one-month-long storage of the devices in air, a dramatic change in the  $J$ - $V$  response was found. The S-shape disappeared, the  $J_{SC}$  increased while the  $V_{OC}$  was unchanged (Figure II.18b and Table A.II.2b). The unencapsulated devices were then highly stable and showed no electrical characteristics change within several months of storage under ambient conditions. The maturation is explained by the oxidation of the Spiro-OMeTAD layer. Oxidation by  $O_2$  in the air occurred, produced the p-type doping of the molecular semiconductor and then its dramatic increase in conductivity. According to the literature,<sup>20</sup> the oxidation reaction can be written:



Figure II.19a shows that the current density at 0 V bias varies to a large extent with the modifier. The order is  $NBA > CBA > \text{Blank} > \beta\text{-ALA} > MBA$ . Interestingly, the photocurrent was increased by 70% with the NBA treatment compared to the blank and it was 10% increased by the CBA treatment. On the other hand, this parameter was reduced for the other acids, especially with MBA.

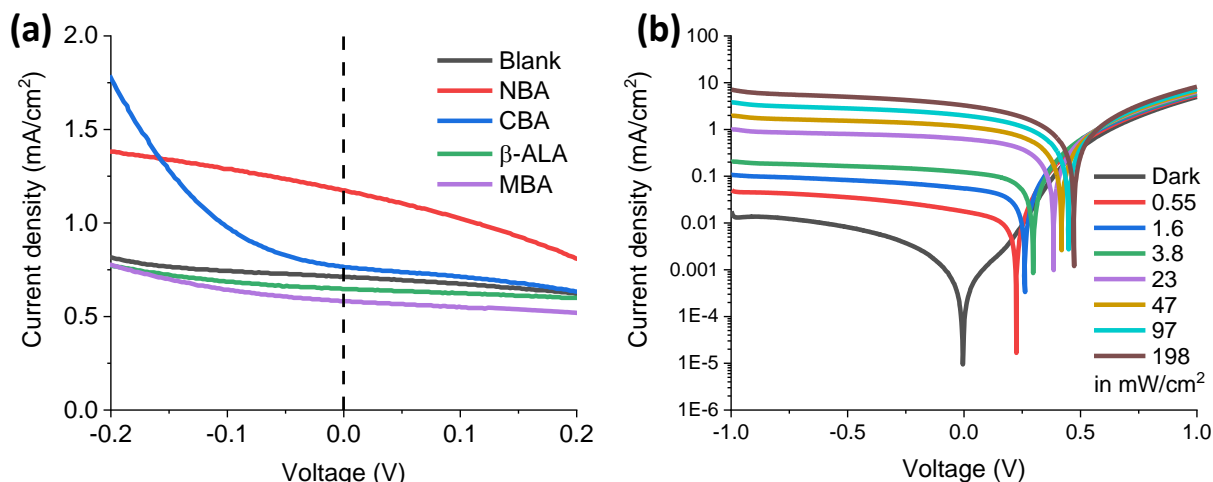


**Figure II. 19** (a) Effect of the molecular modifier on the current recorded under an irradiance of 47 mW/cm<sup>2</sup> ( $\lambda = 365$  nm); (b) Current density-voltage ( $J$ - $V$ ) curves in the dark and for increasing light irradiance of the matured NBA-modified PD ( $\lambda = 365$  nm).

**Table II.6** Effect of acid treatment on the open-circuit voltage and rejection ratio of the matured PDs ( $\lambda = 365$  nm, 40 mW.cm<sup>-2</sup>)

	Blank	NBA	CBA	MBA	$\beta$ -ALA
$V_{OC}$ (V)	0.651	0.466	0.575	0.714	0.796
Rejection Ratio <sup>a</sup>	113	159	865	3000	1600

<sup>a</sup>Ratio between the responsivity at 380 nm and at 520 nm.

In Figure II.18a and b, interesting information is that the open circuit potential varied in the opposite of  $J_{SC}$  for the blank and para-substituted benzoic acid modifiers. The order is  $\beta$ -ALA > MBA > Blank > CBA > NBA for the matured PDs (Table II.6). This series follows the order of the dark current (Figure II.18c): the lower the dark current, the higher the  $V_{OC}$ . For the benzoic acid derivatives, the dark  $J$ - $V$  curves reported in the present work are in good agreement with Ref. [32].

Figure II.19b and Figure II.20a detail the response of the PD to UV-light for the NBA-modified and blank devices, respectively. The dark current curve is typical of a p-n junction diode behavior with a clear rectifying  $J$ - $V$  characteristic. The rectification ratio (RR), measured between -1 V and +1 V, is high at about 900 for the blank and 400 for the NBA-PD. Under UV-Light, the current density continuously increased with the light irradiance. One of the advantages of operating the PD at 0 V bias or at low bias is the very high dynamic range. The sensitivities ( $J_{light}/J_{dark}$ ) at 0 V for the various devices are gathered in Table II.7. Very high and remarkable values are found, above  $10^4$  for all the PDs, except the MBA-modified PD which exhibits slightly lower values.

**Table II.7.** Sensitivity ( $J_{light}/J_{dark}$ ) of the PDs at 0V bias.

	23 mW/cm <sup>2</sup>	47 mW/cm <sup>2</sup>
NBA	$1.2 \cdot 10^4$	$2.3 \cdot 10^4$
CBA	$8.9 \cdot 10^3$	$1.5 \cdot 10^4$
Blank	$9.2 \cdot 10^3$	$2.0 \cdot 10^4$
$\beta$ -ALA	$1.6 \cdot 10^4$	$2.4 \cdot 10^4$
MBA	$5.1 \cdot 10^3$	$7.9 \cdot 10^3$

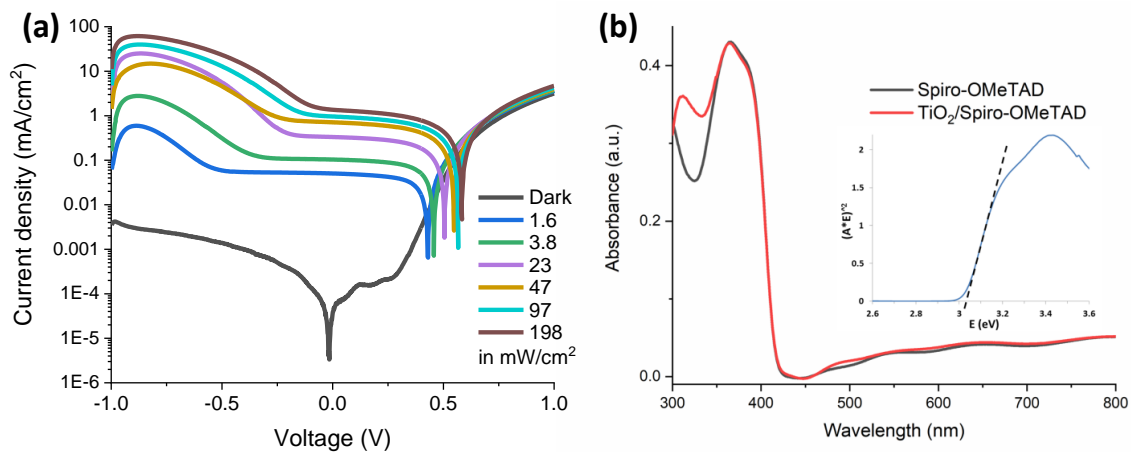


**Figure II. 20** (a)  $J$ - $V$  curves of the Blank (unmodified) PD in the dark and under various irradiances. (b) Absorbance curves of the Spiro-OMeTAD and TiO<sub>2</sub>/Spiro-OMeTAD layers.

The absorbance spectrum of the prepared devices (without the Au back contact) is shown in Figure II.21a as a dash line. The absorbance is rather flat and very low over most of the visible/NIR wavelength region. An absorption edge appears below 410 nm. It is due to light absorption in the Spiro-OMeTAD which bandgap, at about 3.0 eV (inset of Figure II.20b), is slightly lower than the anatase TiO<sub>2</sub> one.<sup>33</sup> In the same figure, the quantum efficiency (EQE) curves for the various PDs are also plotted. The EQE spectra follow the absorbance spectrum. They present a maximum at about 380 nm. Figure 3b shows the responsivity spectra of the various PDs. The maximum of the responsivity is achieved with the NBA device at 65 mA/W. It is much higher than the values reported in the literature for the hybrid organic/inorganic UV-PDs.<sup>22-24, 27-29</sup> The hybrid devices exhibit more than a two-orders of magnitude difference while illuminated in the UV and the visible light range. The rejection ratios are gathered in Table II.6 for the various devices.

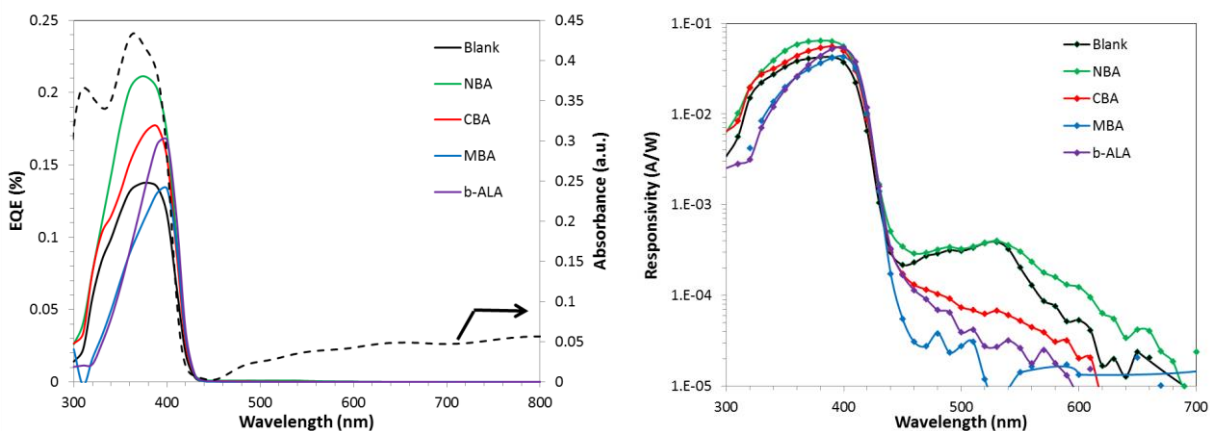


**Figure II. 21** (a) Device absorbance spectrum and EQE curves of the various PDs. (b) Responsivity spectra of the various PDs.

#### II.4.2.2 Response to UV light

Three other parameters of great importance for any PDs are the response time, the repeatability, and the stability as they often determine the suitability of a device for a specific application. The photocurrent time response was measured at 0 V bias under 365 nm light source on/off sudden switching irradiation. Figure II.22a shows that the photo response of the NBA-modified device under repeated on/off cycles is highly repeatable and stable. Similar behavior is found with the other devices in Figure II.22b. Figure II.22a and 22b display abrupt rises and decays in the photocurrent response. We have calculated the rise and decay times for the various PDs. The former is defined by the time in which the photocurrent rises from 10% to 90% of its maximum value. The

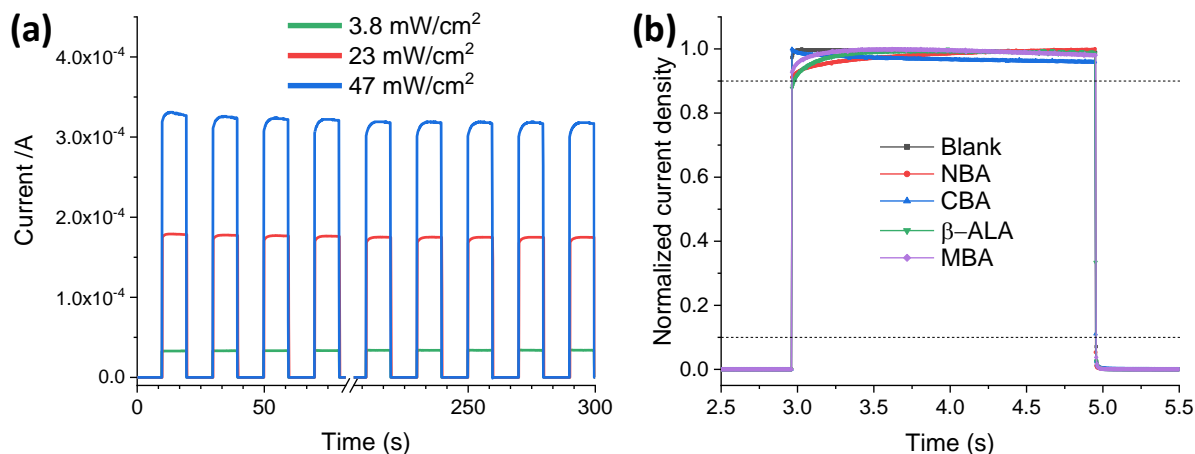


**Figure II. 22** (a) Time-response of the NBA-PD under alternate switch on/ switch off UV-Light at various irradiances. (b) Effect of surface modifier on the time response of the PDs. ( $\lambda =365$  nm)

latter is the time to drop from 90% to 10% of the photocurrent maximum value. The devices had remarkable fast response times, measured at less than 3 ms (the measurement step of the current recording system) for the rise time. The decay time was measured at 3 ms or less for all the PDs except for the  $\beta$ -ALA one which was measured at 6.5 ms.

The long-term stability of the devices is also an important parameter for the practical application. Figure II.23 shows a degradation of the performances of the unencapsulated blank device stored under ambient conditions for several months. On the other hand, the NBA PD exhibits remarkable stability. The  $J_{SC}$  is almost unchanged after 156 days of storage and the SAM plays a key role in the stabilization.

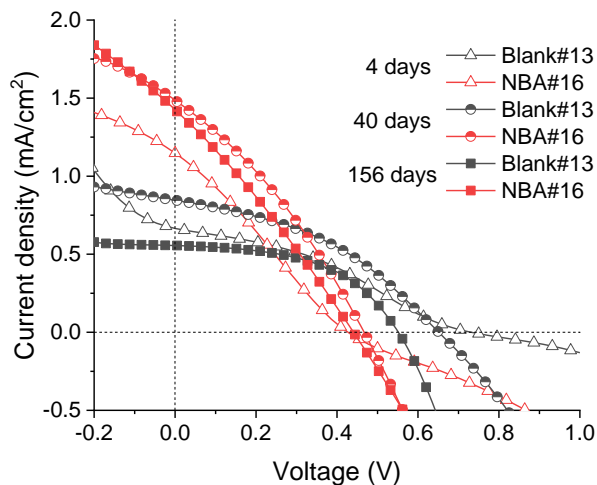


**Figure II. 23** (a)  $J$ - $V$  curves of unencapsulated blank (black traces) and NBA (red traces) PDs after 4, 40, and 156 days of storage under ambient conditions.

### II.4.2.3 Energy band alignment

The photoresponse enhancement by the interfacial modification in the UV PDs can be explained in terms of the energy band alignment. The presence of the dipoles at the interface introduces an additional electric field. When the dipole field is pointing outward titania (chemistry notation: from negative to positive), the vacuum level is shifted upwards and the work function is increased. When electron-hole pairs are photogenerated in the Spiro-OMeTAD layer, the electrons are drifted toward the TiO<sub>2</sub> layer, the charge separation and transfer are facilitated, and the measured photocurrent is enhanced. On the contrary, for the adsorbed molecules with a dipole moment pointing toward the oxide, the vacuum energy level is shifted downward, the work function is reduced. An interfacial electric field is present that reduces the electron charge transfer toward TiO<sub>2</sub> and then, the generated photocurrent in the PD.

These phenomena are schematically presented in Figure II.24. Figure II.24 also shows the effect of the modifier on the  $V_{OC}$ . The  $V_{OC}$  is limited by the  $E_C(\text{TiO}_2)-E_{HOMO}(\text{Spiro-OMeTAD})$  gap. The presence of a dipole layer changes this gap: it is reduced for a dipole with a positive  $\mu_{\perp}$  (Figure II.24a) and increased for a dipole with a negative  $\mu_{\perp}$  (Figure II.24c). Therefore, in the former case, the  $V_{OC}$  will be reduced while this parameter will be increased in the latter case. This phenomenon is clearly observed for the benzoic acid derivatives series (see Figure II.4.2).

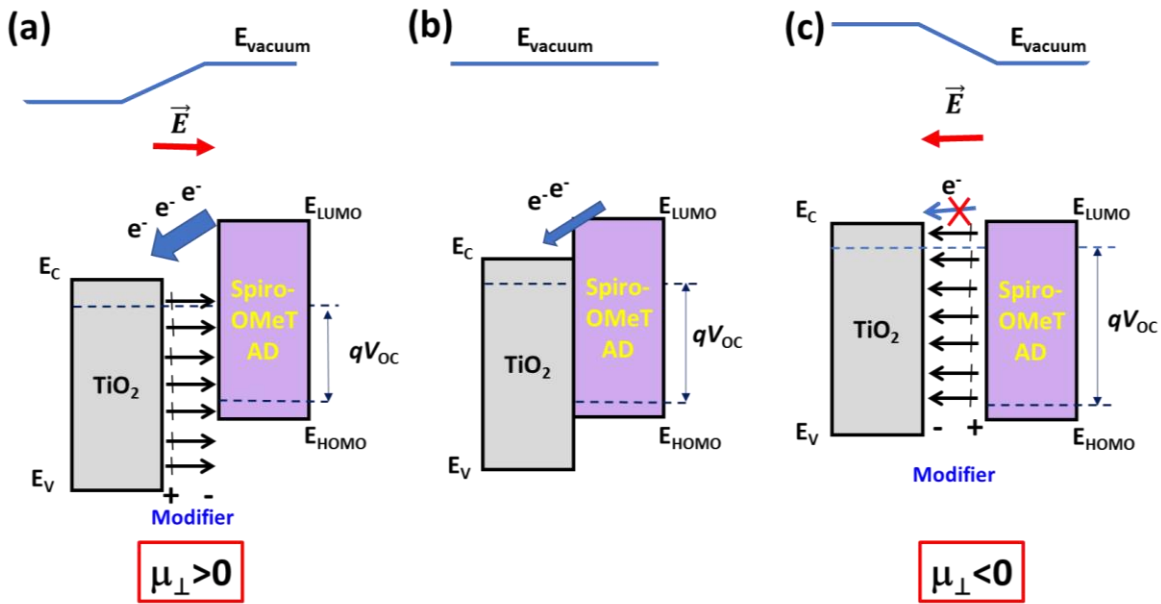


**Figure II. 24** Effect of the interfacial dipole modifiers on the energetics of the TiO<sub>2</sub>/Spiro-OMeTAD p-n heterojunction. (a) Dipole inducing a  $\mu_{\perp} > 0$  at the interface; (b) pristine interface and (c) dipole inducing a  $\mu_{\perp} < 0$  at the interface.

#### II.4.2.4 PD devices based on cobalt and/or lithium doped Spiro-OMeTAD layer

Doping is an efficient way to improve the conductivity of spiro-OMeTAD. In order to further improve the property of the photodetectors, Cobalt and/or Lithium doped spiro-OMeTAD layers were applied as the UV light absorber in this experiment, respectively.

#### PD devices based on Cobalt doped spiro-OMeTAD layer

The UV light absorbance of the PDs was not affected by doping Co-salt in spiro-OMeTAD layer as shown in Annex-II, Figure A.II.1. The onset of the absorbance curve is still at 410 nm. The dark current was recorded before and after UV light shining as shown in Figure II.25. Interestingly, the order of the curves onsets was ambiguous before UV light shining, however, this order of  $\beta$ -ALA > MBA > Blank > CBA > NBA became much clearer, with left shift of 100-200mV after UV light shining. This phenomenon is possibly associated with light soaking. We further studied this phenomenon in pure and Li&Co doped spiro-OMeTAD (hole transfer layer in perovskite solar cells) based PDs, respectively. As shown in Figure II.26, the onset voltages decreased 70 mV, 190 mV and 80 mV for pure spiro, Co-doped spiro and Li&Co-doped spiro based PDs, respectively. Co-salt seems to play an important role in the light soaking.

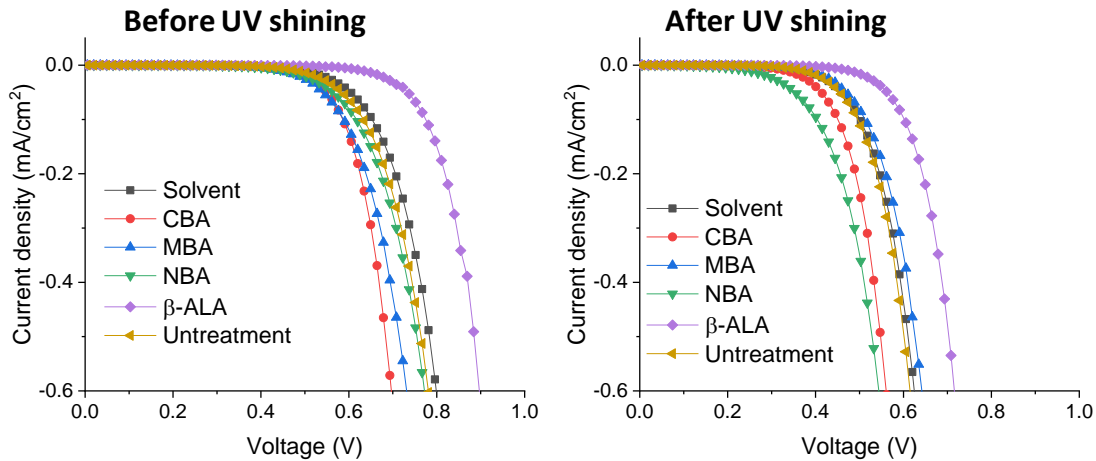
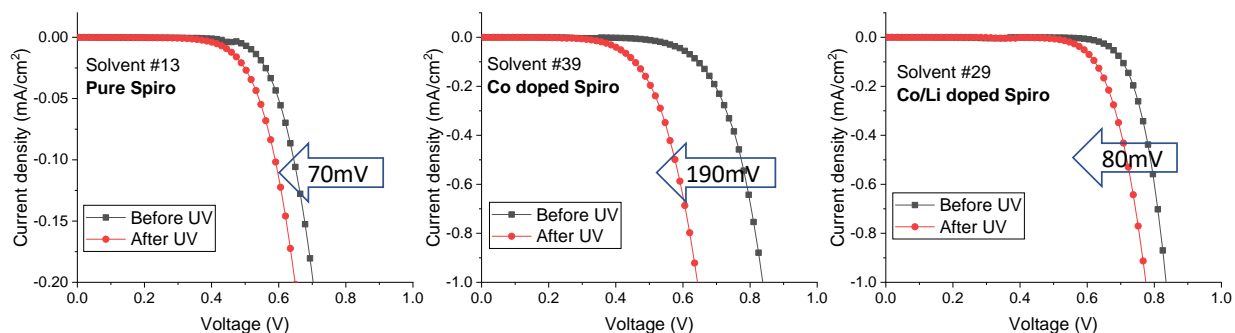
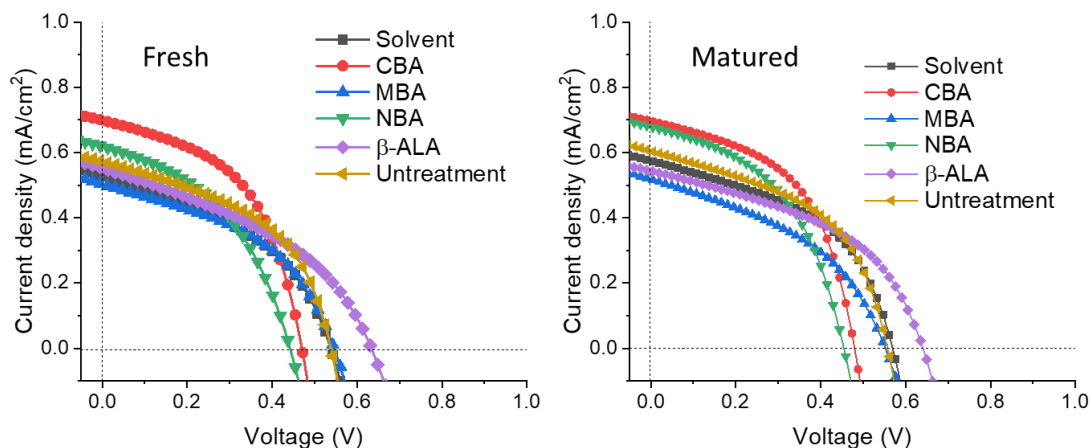


Figure II. 25 UV-vis absorbance of the heterojunction based Co doped spiro-OMeTAD.



**Figure II. 26** The dark current shifts of (a) **pure** spiro-OMeTAD, (b) **Co-doped** spiro-OMeTAD and (c) **Co&Li doped** spiro-OMeTAD.

The  $J$ - $V$  curves under UV light were characterized as before and shown in Figure II.27 and the relevant photovoltaic parameters were gathered in Table A.II.3, Annex-II. The order of current density was the same as that in pure spiro based PDs, however, the total photocurrents were not improved by doping Co in spiro-OMeTAD. Fresh samples and matured samples (aging 2 weeks in air) presented similar photocurrents. But, no S-shape curves were observed in fresh samples, which can be ascribed to the increased conductivity by doping Co.



**Figure II. 27**  $J$ - $V$  curves of (a) fresh and (b) matured (aging 2 weeks in air) Co-spiro-OMeTAD based PDs under UV light.

### PD devices based on Li&Co doped Spiro-OMeTAD layer

Li and Co doped spiro-OMeTAD layer is often used as a hole transporting material in perovskite solar cells. How does it work in SAMs modified PD devices? In this part, Li&Co-doped spiro-OMeTAD layer has been applied in UV PDs. The dark  $J$ - $V$  curves are shown in Figure II.28a. The

effect of SAMs on the onsets disappeared, which means the effect of SAMs on the work functions in the interface was destroyed. NBA modified PD devices still presented the highest photocurrent in the  $J$ - $V$  curves while a big hysteresis was observed either (Figure II.28b and Table A.II.4a in Annex). However, the total photocurrents (0.15-0.32 mA/cm<sup>2</sup>) based on Li&Co doped spiro were much lower than those based on pure spiro-OMeTAD (0.75-1.5 mA/cm<sup>2</sup>) and only Co-doped spiro (0.5-0.7 mA/cm<sup>2</sup>).

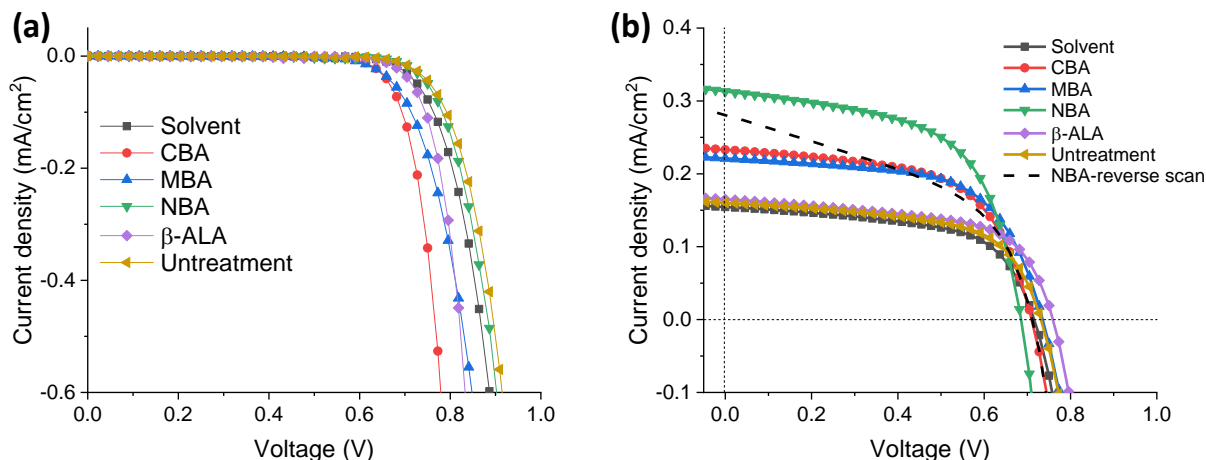


**Figure II. 28** Li-salt and Co-salt doped spiro-OMeTAD based PDs: (a) dark current and (b)  $J$ - $V$  curves under UV light.

## II.5 Conclusions

In conclusion, we have first studied the effect of modifying TiO<sub>2</sub> layers by various organic acid molecules with a dipole moment varying in a large range. The acid modifiers adsorption has been then thoroughly investigated by a combined experimental and theoretical approach. They are adsorbed at the TiO<sub>2</sub> surface by their carboxylate group in a bridging bidentate mode. The theoretical FTIR spectra have been found in good agreement with the experimental ones and clearly show the binding of the molecular dipole onto the oxide surface. The surface work functions (WFs) of these samples are characterized by Kelvin probe and UPS. A linear relationship between the WF values and the dipole moments of the adsorbed modifiers has been determined. Moreover, the energy level diagrams from the bulk TiO<sub>2</sub>, to surface TiO<sub>2</sub>, and to the SAMs have been depicted according to the obtained energy band level values.

We have then designed and fabricated solid-state nanostructured UV-A photodetectors based on

the TiO<sub>2</sub>/Spiro-OMeTAD p-n heterojunction. At the beginning, no additive was used in the Spiro-OMeTAD layer. The doping was achieved by the oxidation of the layer in air. This approach has permitted the reliable study of the effect of interfacial acid modifiers on the PD response. The prepared diode had a rectifying ratio of 900. We have shown that the UV-PD could be used in a self-powered mode. We have carefully investigated the effect of interfacial modifiers on the PD functioning and performances and we have concluded in their strong effect. The NBA modifier has permitted to boost the responsivity of the device by 70% compared to the pristine p-n junction. The responsivity was measured at 69 mA/W at 0 V. The PDs were visible-blind due to the large bandgap (3 eV) of the Spiro-OMeTAD and the rejection ratio between the UV-A and the visible light was measured higher than two orders of magnitude. The device sensitivity ( $J_{\text{light}}/J_{\text{dark}}$ ) at 0 V was remarkably high, above 10<sup>4</sup>. Moreover, we have found that their UV-light switching on/off was highly repeatable and that their photoresponse was stable. The response time was measured very fast, below 3ms.

By the interfacial engineering, a dipole moment has been introduced in which surface normal components have been calculated for the various organic acids. We have shown that their presence induces a step in the vacuum energy and that the formed dipole field dramatically affects the charge transfer and the photocurrent of the device. The higher responsivity of the NBA-modified PD has been then explained by the better and faster electron charge transfer towards the electrical contact on TiO<sub>2</sub>.

We will next investigate in Chapter III, the effect of these four organic acid modifiers on the performances of perovskite solar cells.

## References

1. M. Razeghi, A. Rogalski, *J. Appl. Phys.* **1996**, 79, 7433.
2. L. Sang, M. Liao, M. Sumiya, *Sensors* **2013**, 13, 10482.
3. Z. Alaie, S. Mohamad Nejad, M. H. Yousefi, *Sci. Semiconductor Processing* **2015**, 29, 16.
4. L. Su, W. Yang, J. Cai, H. Chen, X. Fang, *Small* **2017**, 13, 1701687.
5. V. Postica, M. Hoppe, J. Gröttrup, P. Hayes, V. Röbisch, D. Smazna, R. Adelung, B. Viana, P. Aschehoug, T. Pauporté, O. Lupan, *Solid State Sci.* **2017**, 71, 75.

6. O. Lupan, V. Postica, R. Adelung, N. Ababii, L. Chow, B. Viana, T. Pauporté, *Proc. SPIE*, **2017**, 101051Y. doi:10.1117/12.2249841.
7. K. Liu, M. Sakurai, M. Aono, *Sensors* **2010**, 10, 8604.
8. H. Kind, H. Yan, B. Messer, M. Law, P. Yang, *Adv. Mater.* **2002**, 14, 158.
9. Y. Zou, Y. Zhang, Y. Hu, H. Gu, *Sensors* **2018**, 18, 2072.
10. H. Zhang, A. V. Babichev, G. Jacopin, P. Lavenus, F. H. Julien, A. Yu. Egorov, Th. Pauporté, M. Tchernycheva, *J. Appl. Phys.* **2013**, 114, 234505.
11. O. Lupan, S. Koussi-Daoud, B. Viana, T. Pauporté, *RSC Advances* **2016**, 6, 68254.
12. T. Pauporté, O. Lupan, V. Postica, M. Hoppe, L. Chow, R. Adelung, *Physica Status Solidi (a)* **2018**, 215, 1700824. DOI: 10.1002/pssa.201700824.
13. H. Shen, C. Shan, B. Li, B. Xuan, D. Shen, *Appl. Phys. Lett.* **2013**, 103, 232112.
14. C. -L. Hsu, Y. -D. Gao, Y. -S Chen, T. -J. Hsueh, *ACS Appl. Mater. Interfaces* **2014**, 6, 4277.
15. B. Zhao, F. Wang, H. Chen, L. Zheng, L. Su, D. Zhao, X. Fang, *Adv. Funct. Mater.* **2017**, 27, 1700264.
16. O. Game, U. Singh, T. Kumari, A. Banpurkarc, S. Ogale, *Nanoscale* **2014**, 6, 503.
17. I. E. Jacobs, A. J. Moulé, *Adv. Mater.* **2017**, 29, 1703063.
18. J. Burschka, A. Dualeh, F. Kessler, E. Baranoff, N.-L. Cevey-Ha, C. Yi, M. K. Nazeeruddin, M. Grätzel, *J. Am. Chem. Soc.* **2011**, 133, 18042.
19. M. Ulfa, T. Zhu, F. Goubard, T. Pauporté, *J. Mater. Chem. A* **2018**, 6, 13350.
20. M. Ulfa, T. Pauporté, T. T. Bui, F. Goubard, *J. Phys. Chem. C* **2018**, 122, 11651.
21. Y. Li, C. Chen, W. Yen, W. Su, C. Ku, J. Wu, *Appl. Phys. Lett.* **2008**, 92, 233301.
22. L. Zheng, P. Yu, K. Hu, F. Teng, H. Chen, X. S. Fang, *ACS Appl. Mater. Interfaces* **2016**, 8, 33924.
23. H. Chen, P. Yu, Z. Zhang, F. Teng, L. Zheng, K. Hu, X. S. Fang, *Small* **2016**, 12, 5809.
24. S. Yang, J. Gong, Y. Deng, *J. Mater. Chem.* **2012**, 22, 13899.
25. T. Leijtens, I-K. Ding, T. Giovenzana, J. T. Bloking, M. D. McGehee, A. Sellinger, *ACS Nano* **2012**, 6, 1455.
26. T. -T. Bui, M. Ulfa, F. Maschietto, A. Ottochian, M. -P. Nghiem, I. Ciofini, F. Goubard, T. Pauporté, *Org. Electron.* **2018**, 60, 22.
27. H. Bai, T. Shen, J. Tian, *J. Mater. Chem. C* **2017**, 5, 10543.
28. Y. Xie, L. Wei, Q. Li, G. Wei, D. Wang, Y. Chen, J. Jiao, S. Yan, G. Liu, L. Mei, *Appl. Phys. Lett.* **2013**, 103, 261109.
29. O. Game, U. Singh, T. Kumari, A. Banpurkarc, S. Ogale, *Nanoscale*, **2014**, 6, 503.
30. P. Wang, Z. Shao, M. Ulfa, T. Pauporté, *J. Phys. Chem. C* **2017**, 121, 9131.
31. A. Sundqvist, O. J. Sandberg, M. Nyman, J. H. Smatt, R. Osterbacka, *Adv. Energy. Mater.* **2016**, 6, 1502265.
32. J. Kruger, U. Bach, M. Gratzel, *Adv. Mater.* **1999**, 12, 447.

33. C. Magne, F. Dufour, F. Labat, G. Lancel, O. Durupthy, S. Cassaignon, T. Pauporté, *J. Photochem. Photobiol. A* **2012**, 232, 22.
34. N. Sundaraganesan, B. Anand, C. Meganathan, B. Joshua, *Spectrochimica Acta Part A: Molecular and Biomolecular Spectroscopy* **2008**, 69, 871.
35. X. Luo, J. Shen, X. Zhao, Z. Wang, B. Wu, L. Li, X. Zhou, *Inorganica Chimica Acta* **2016**, 446, 169.
36. S. Badilescu, P. Ashrit, V. Truong, *Appl. Phys. Lett.* **1988**, 52, 1551.
37. S. Hyouk, H. Chang, H. Kim, K. Kim, *Appl. Spectrosc.* **1998**, 52, 1047.
38. S. Shao, F. Liu, G. Fang, B. Zhang, Z. Xie, L. Wang, *Org. Electron.* **2011**, 12, 641.
39. M. A. Palafox, M. Gil, J. Nunez, *Appl. Spectrosc.* **1994**, 48.1, 27.
40. M. Mohamed Ali Jinnah, M. Umadevi, V. Ramakrishnan, *J. Raman Spectrosc.* **2004**, 35.11, 956.
41. M. T. S. Rosado, M. L. R.S. Duarte, R. Fausto, *J. Mol. Struct.* **1997**, 410, 343.
42. F. Labat, P. Baranek, C. Adamo, *J. Chem. Theory Comput.* **2008**, 4, 341.
43. A. G. Thomas, J. J. Mark, W. Michael, R. Hanna, S. Karen, A. Johan, L. Anna, M. Natalia, *Langmuir* **2014**, 30, 12306.
44. F. Labat, C. Adamo, *J. Phys. Chem. C* **2007**, 111, 15034.
45. C. Goh, S. R. Scully, M. D. McGehee, *J. Appl. Phys.* **2007**, 101, 114503.
46. M. Ulfa, P. Wang, Z. Shao, B. Viana, T. Pauporté, *Proc. SPIE* **2018**, 105332R. doi: 10.1117/12.2294941.
47. T. Le Bahers, T. Pauporté, F. Labat, G. Lefèvre, I. Ciofini, *Langmuir* **2011**, 27, 3442.
48. R. Dovesi, V. Saunders, C. Roetti, R. Orlando, C. Zicovich-Wilson, F. Pascale, B. Civalleri, K. Doll, N. Harrison, I. Bush, *Crystal* **2006**, 06.
49. A. Barnard, P. Zapol, *Phys. Rev. B* **2004**, 70, 235403.
50. A. Barnard, P. Zapol, L. Curtiss, *Surf. Sci.* **2005**, 582, 173.
51. C. Arrouvel, M. Digne, M. Breysse, H. Toulhoat, P. Raybaud, *J. Catal.* **2004**, 222, 152.
52. J. Berthelat, P. Durand, *Gazzetta Chimica Italiana* **1978**, 108, 225.
53. J. Barthelat, P. Durand, A. Serafini, *Molecular Physics* **1977**, 33, 159.
54. C. Adamo, V. Barone, *J. Chem. Phys.* **1999**, 110, 6158.
55. S. Grimme, G. Semiempirical, *J. Comput. Chem.* **2006**, 27, 1787.

## Chapter III. Interfacial Engineering through Chloride-Functionalized Self-Assembled Monolayers for High-Performance Perovskite Solar Cells

In the last chapter, we demonstrated a response enhancement in PD devices through SAMs modifying *mp*-TiO<sub>2</sub>. It was assigned to SAMs increased the surface work function of TiO<sub>2</sub> and an electric field induced by their dipole moment facilitating the charge injection. The principle may also be applied to solar cells. Recently, Organic-inorganic hybrid perovskites (OIHPs) have emerged as the most promising family of materials for an application in photovoltaic devices with very high efficiency. In this chapter, the effect of a series of self-assembled monolayers placed at the TiO<sub>2</sub>-perovskite interface, on the functioning of triple cation perovskite solar cells has been investigated. We show that employing 4-chlorobenzoic acid leads to the marked boosting of the solar cell performances. The starting pristine cell had a 20.3% power conversion efficiency (PCE) and the chemical engineering permitted to reach a PCE up to 21.35%. Our experimental study completed by density functional theory (DFT) calculations and modeling shows that this improvement is due to the reduction of interfacial states, to the improvement of the quality of the OIHP material and the structural continuity between TiO<sub>2</sub> and the OIHP. Especially, we demonstrate that the interfacial chemical interactions are important to consider in the design of highly efficient devices.

### III.1 Introduction

Over the last few years, organic-inorganic hybrid perovskites (OIHPs) have emerged as one of the most promising family of materials for applications in various fields such as lasers, LED, photodetectors, scintillation and photovoltaic solar cells.<sup>1-14</sup> This material family exhibits excellent optoelectronic properties, tunable bandgap, long charge carrier lifetime, low cost and low-temperature solution processability. OIHPs thin films can be printed on flexible substrates for lightweight devices. The record efficiency for solar irradiation power conversion of perovskite solar cells (PSCs) raised rapidly and continuously during the last decade and reaches a current certified world record of 25.5%.<sup>15</sup> PSCs are presently the most performant thin film solar cell technology and they are close to the efficiency of the best silicon technology.

In the most popular architecture delivering high efficiency and stable power output, a TiO<sub>2</sub>

mesoporous structure, deposited on top of a TiO<sub>2</sub> hole blocking layer is employed.<sup>16</sup> The OIHP absorber film is grown on top of this layer and is covered by a p-type molecular semiconductor, typically Spiro-OMeTAD. In the inverted cell structure, the OIHP layer is deposited on top of the p-type selective contact. The oxide n-type semiconductor layer blocks the hole transfer and ensures the electron transport.<sup>16</sup> The injection of the photogenerated electrons is a key step in the photovoltage and photocurrent generation. High efficiency requires a high quality of the interfaces and correct energy band matchings between the various layers. Engineering the interfaces with facile solution-based processes is an attractive means to boost the PSC functioning and performances. Self-assembled monolayers (SAMs) are very interesting for this purpose. SAMs of organic compounds have been implemented in PSC interfaces and they can potentially induce various positive effects:

- (i) They can influence the morphology of the perovskite layer, favor the crystallinity, the grain size and the absence of pinholes in the absorber material.
- (ii) Organized and aligned SAMs of polar molecules produce a permanent molecular dipole moment normal to the surface. This polar layer changes the work function and generates an electric field that can favor the extraction of the photogenerated charges from the perovskite layer.
- (iii) SAMs can passivate the trap states on the oxide selective contact.
- (iv) they can also passivate trap states in the perovskite layer.
- (v) They can delay the charge recombination and act as an insulating layer.<sup>17</sup>
- (vi) SAMs can also act as the barrier between perovskite and the underlayer and avoid them to react to each other.<sup>18,19</sup>

Recent results illustrate the interest of applying SAMs to PSCs.<sup>20-22</sup> For instance, Li et al.<sup>23</sup> introduced the 4-aminobenzoic acid at the interface between TiO<sub>2</sub> and CH<sub>3</sub>NH<sub>3</sub>PbI<sub>3</sub> (MAPI). Their PSCs had a poor efficiency, but the treatment was beneficial to the performances. Zuo et al.<sup>24</sup> applied C3-SAMs to planar solar cells based on ZnO electron transporting layer (ETL). The interfacial engineering improved the MAPI layer morphology and passivated the trap states. Moreover, the authors claimed a better energy level alignment due to the reduction of the work function of the ZnO ETL (dipole moment of the C3 molecule). More recently, ZnO was engineered by a dual-functional SAM.<sup>25</sup> The treated cells achieved an 18.8% PCE. Wang et al.<sup>26</sup> explored the effect SAMs on NiO-based inverted structure PSCs. They found that 4-bromobenzoic acid could

effectively play the role of the surface passivation. It reduced the trap-assisted recombination, improved the surface wettability and minimized the energy offset between NiO and MAPI perovskite.  $\beta$ -alanine was also employed in inverted structures. The amino group was attached to PEDOT-PSS while carbonyl terminal group interacted with MAPI. The dipole moment of the molecular interface modifier favored the charge extraction.<sup>27</sup> Palomares et al. directly used SAMs to replace the commonly used PEDOT:PSS contact layer and reached an efficiency of 17.3% in inverted structure MAPI PSCs.<sup>28</sup> In the present literature on PSC, most SAMs employed feature C60, amine, or ammonium groups.<sup>19</sup> Will et al. reported that the interfacial chemical composition can be controlled from Pb-poor to Pb-rich by the SAMs.<sup>27</sup> Also, SAMs have been investigated on the top of the perovskite layer.<sup>29</sup> It has been shown that thiol group forms firm coordination with the perovskite.<sup>30,31</sup> Hydrophobic molecular SAMs have been used notably to protect OIHP from moisture and increase the device durability.<sup>30-33</sup>

In Chapter III, the effect of SAM interfaces on the functioning of triple cation perovskite solar cells has been investigated. The same series of acids with a benzene spacer and various functional (terminal) groups employed in Chapter II has been tested. By varying the functional group, the strength and sign of their molecular dipole moment have been monitored over a wide range. Moreover, the data have been completed by the study of  $\beta$ -alanine ( $\beta$ -ALA). In these molecules, –COO was the anchoring group, permitting the SAMs formation and attachment onto TiO<sub>2</sub> in a bridging bidentate mode. We show that employing SAMs with a chloride functional group leads to the marked boosting of the triple cation perovskite solar cell performances. The starting pristine cells had high performances (PCE up to 20.3%) but the interfacial engineering permitted to reach a PCE up to 21.35% (stabilized at 20.9%). Our experimental and theoretical study shows that this improvement is due to the reduction of interfacial states, to the improvement of the quality of the OIHP material and to the structural continuity between TiO<sub>2</sub> and the OIHP. To our knowledge, it is the first time that chloride terminated SAMs are shown to boost the efficiency of PSCs and that acid-modified interface PSCs achieve an efficiency higher than 21%. The next main text of this Chapter is organized into 3 parts. Section III.2 is dedicated to the preparation of PSCs, especially, the preparation of perovskite layers. The procedure of SAMs modified *mp*-TiO<sub>2</sub> is the same as that described in Chapter II.2. Section III.3 presents the characterization of the perovskite film on SAMs@TiO<sub>2</sub>. Section III.4 describes the characterization of PSC devices and the discussion about the effect of SAMs on PSCs performances.

## III.2 Experimental

The preparation of substrate, compact TiO<sub>2</sub> layer, mesoporous TiO<sub>2</sub> layer and the adsorption of SAMs were conducted as described in Chapter II, Section II.2.1. All the characterizations of the SAMs@TiO<sub>2</sub> were also included in Chapter II, Section II.2.2.<sup>33a</sup>

### III.2.1 Preparation of the MAPbI<sub>3</sub> and Cs<sub>8</sub>FAMA Films

The MAPI precursor solution had a 1.45M concentration. 668.5 mg PbI<sub>2</sub> and 230.5 mg MAI were mixed in 1ml dimethyl sulfoxide (DMSO). The solution was stirred and kept warm at 100°C for 2h before use. The spin-coating program was 1000 rpm for 10s and 4000 rpm for 30 s. 100 μL of chlorobenzene was dripped 30s after the starting of the spinning routine. The layers were finally annealed on a hotplate at 105 °C for 60 min. The best performances were achieved after the device preparation. These layers are hereafter denoted MAPI.

A precursor solution corresponding to a Cs<sub>0.08</sub>FA<sub>0.80</sub>MA<sub>0.12</sub>Pb(I<sub>0.88</sub>Br<sub>0.12</sub>)<sub>3</sub> perovskite layer composition was prepared by mixing 179 mg of formamidinium iodide (FAI), 17.4 mg of methylammonium bromide (MABr), 27.0 mg of CsI, 548 mg of PbI<sub>2</sub> and 57.1 mg of PbBr<sub>2</sub> in 220 μL DMSO and 780 μL dimethylformamide (DMF). The solution was stirred for a minimum of 3-4 h at room temperature in a N<sub>2</sub> filled glovebox before use.<sup>34,35</sup> 45 μL of this solution was placed on top of the substrates. A two-step spin-coating program was employed: first spinning at 1000 rpm for 10 s and then at 6000 rpm for 30 s. 100 μL of chlorobenzene was dripped 20 s after the starting of the spinning routine. The films were then annealed at 105 °C for 1 h in a dry atmosphere. The best performances and lower hysteresis index (HI) were achieved after 7-8 days of storage in the N<sub>2</sub> filled glovebox. These layers are hereafter denoted Cs<sub>8</sub>FAMA.

The hole transporting material (HTM) solution was prepared by dissolving 78 mg of Spiro-OMeTAD (Borun New Material Technology) in 1 mL of chlorobenzene. Then, 17.9 μL of bis(trifluoromethylsulfonyl)imide lithium salt solution (Li-TFSI) (Sigma Aldrich) solution (517 mg in 1 mL ACN), 30.4 μL of TBP (tert-butylpyridine) (Sigma Aldrich) and 14 μL of tris(2-(1H-pyrazol-1-yl)-4-tert-butylpyridine)-cobalt(III) tris (bis(trifluoromethylsulfonyl)imide) (Dyesol, FK209) (376 mg in 1 mL acetonitrile) were added to this solution. 40 μL of the HTM solution was spin-coated at 4000 rpm for 30 s. Perovskite and HTM layers were fabricated in a dry air glovebox with RH < 10%. Finally, the device was completed by thermally evaporating a 70-80 nm thick gold back contact on the Spiro-OMeTAD layer.

### III.2.2 Characterization methods

The structure of the organolead perovskite film was characterized by a PANalytical X-Pert high-resolution X-ray diffractometer (XRD) operated at 40 kV and 45 mA and using the  $\text{CuK}\alpha$  radiation with  $\lambda = 1.5406 \text{ \AA}$ . The film specular absorbance was measured by a Cary 5000 UV-Vis-NIR spectrophotometer. A glass/FTO/ $\text{TiO}_2$ /*mp*- $\text{TiO}_2$  sample was used as the baseline. The photoluminescence spectra were measured by a Cary Eclipse fluorescence spectrophotometer. The sample morphologies were examined with a high resolution Ultra 55 Zeiss FEG field-emission scanning electron microscope (FE-SEM) in the in-lens mode. The time-resolved photoluminescence (TRPL) measurements were performed under microscope observation (numerical aperture 0.7). The perovskite layers were spin-coated onto a glass/FTO/*c*- $\text{TiO}_2$ /*mp*- $\text{TiO}_2$  substrate. The top of the OIHP layers was excited by a 470 nm diode laser (Picoquant) and the emission was filtered by a 488-nm longpass filter. It was analyzed for time-resolved photoluminescence decay, by a PerkinElmer SPCM avalanche photodiode combined with a PicoHarp acquisition card (500 ps characteristic time of the total system response function) used with the laser in a pulsed mode at a 10 nW excitation power (pulse duration 70 ps).

The *J-V* curves were recorded at room temperature by a Keithley 2410 digital sourcemeter, using a  $0.1 \text{ V}\cdot\text{s}^{-1}$  voltage scan rate. The solar cells, under ambient atmosphere, were illuminated with a solar simulator (Abet Technology Sun 2000) filtered to mimic AM 1.5G conditions.<sup>36</sup> The illuminated surface was delimited by a black mask with an aperture diameter of 3 mm. The power density was calibrated at  $100 \text{ mW}\cdot\text{cm}^{-2}$  by the use of a reference silicon solar cell.<sup>37</sup> The tracking experiments were performed under ambient conditions. The current was followed at the voltage of the maximum power. For the stability tests, the cells were stored in a  $\text{N}_2$  filled glovebox under ambient lighting between the PV measurements.

The external quantum efficiency (EQE) spectra were measured using an Oriel QUANTX-300 system. The light beam was chopped at 77 Hz. The monochromatic illumination was calibrated by a NIST-calibrated Si photodiode.

### III.3 Characterizations of Perovskite Films

#### III.3.1 XRD

The crystallinity of the Cs8FAMA films prepared on pristine TiO<sub>2</sub> and the acid-modified TiO<sub>2</sub> underlayers was investigated by X-ray diffraction (XRD). In Figure III.1, the characteristic peaks at 14.1°, 20.0°, 24.3°, 28.4° and 31.8° are indexed to the (100), (110), (111), (200) and (210) crystal planes, respectively.<sup>38</sup> The peaks present the same intensity and position for the various samples. They are also characterized by similar FWHMs. The FWHM of the (100), (110) and (200) peaks were measured at about 0.11°, 0.09° and 0.12°, respectively. From these similarities, we conclude that the SAMs presence and the chemical nature of the interfacial modifiers do not significantly influence the perovskite layer crystallinity. The broaden peak at 12.7° shows the presence of PbI<sub>2</sub> impurity. It is noteworthy that more PbI<sub>2</sub> is found in the MBA sample.

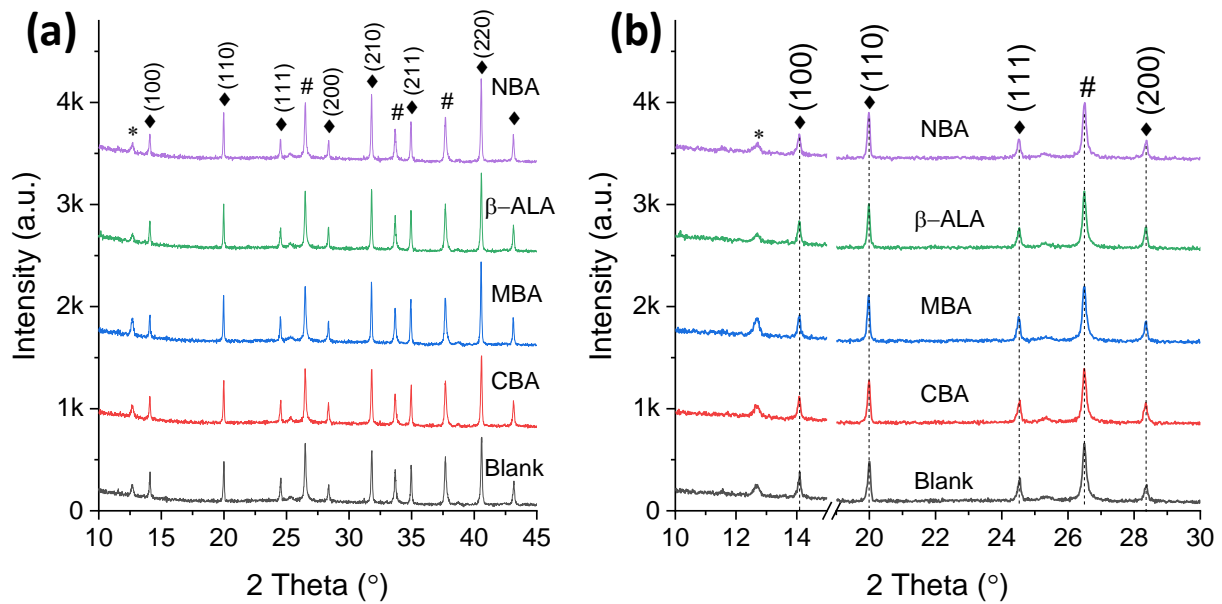


**Figure III. 1** (a) XRD patterns of Cs8FAMA layers deposited on pristine and SAMs modified TiO<sub>2</sub> substrate; (b) is a zoom of (a).

#### III.3.2 SEM

The morphology of Cs8FAMA deposited on the various underlayers is compared in Figure III.2. The layers are perfectly covering and pinhole-free. They are made of well-crystallized grains with a size in the 210-280 nm range. No significant change in the grain shape, size, and size dispersion could be observed on these views. Therefore, on the contrary to what was found for instance in the

case of  $\text{MAPbI}_3$  on a  $\text{NiO}$  underlayer,<sup>16</sup> surface modifiers have no significant effect on the growth and crystallinity of the perovskite. The EDX measurement was used to investigate composition of the obtained  $\text{Cs}_8\text{FAMA}$  perovskite film. The composition table is attached in Annex-III and the result is basically in agreement with the composition in the precursor solution.

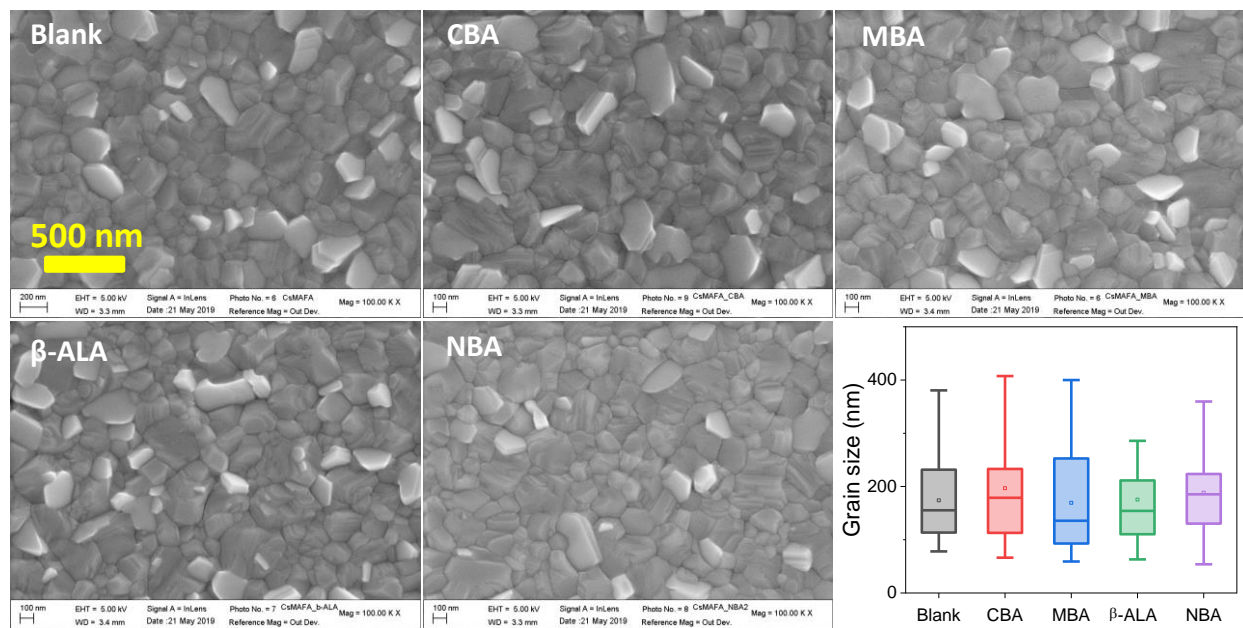


**Figure III. 2** Top view SEM of pristine and acid-treated  $\text{Cs}_8\text{FAMA}$  layers and the statistics of grains sizes.

### III.3.3 UV-Vis absorbance and steady-state PL spectroscopies

The absorbance spectra of the various perovskite samples are presented in Figure III.3a. they are characterized by an absorption edge at 750-780 nm. The curves for  $\text{Cs}_8\text{FAMA}$  on the pristine  $\text{TiO}_2$  and the acid-treated  $\text{TiO}_2$  overlap. It shows that the perovskite layer thickness is unchanged after the treatment with the various acids and that all the samples have the same perovskite thickness. The direct bandgap of  $\text{Cs}_8\text{FAMA}$  is determined at 1.60 eV and is independent of the interlayer chemical nature (Figure III.3b). The normalized photoluminescence spectra are presented in Figure III.3a. The spectra overlap and are centered at 770 nm.

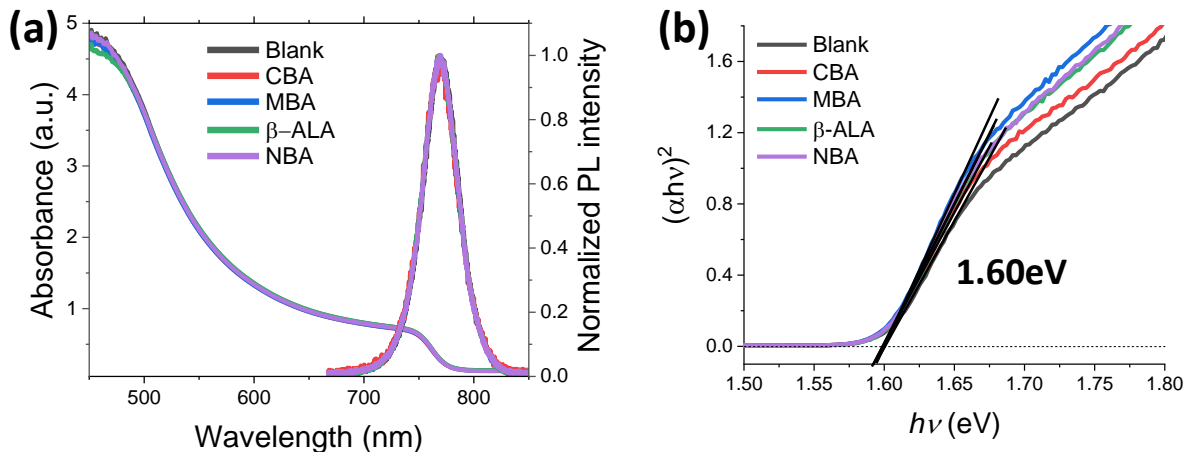


**Figure III. 3** (a) UV-Vis absorbance and normalized photoluminescence of Cs8FAMA perovskite layers. (b) Bandgaps of Cs8FAMA on pristine *mp*-TiO<sub>2</sub> and SAMs@TiO<sub>2</sub>.

### III.3.4 Time-resolved and steady-state PL spectroscopies

The quality of the formed Cs8FAMA layer for various acid-treated TiO<sub>2</sub> underlayers was probed by measuring the slow photoluminescence decay of the perovskite which is assigned to the bimolecular recombination.<sup>39</sup> The absorber was excited at 470 nm with a diode laser. The curves in Figure III.4a provide the following decay lifetimes in the slow region: 183 ns, 117 ns, 79 ns, 64 ns, and 18 ns, for CBA, MBA, blank, β-ALA and NBA cells, respectively. The more detailed fitting parameters are gathered in Table III.1. The irregular steady-state PL curves are presented in Figure III.4b. The PL intensity of perovskites on *mp*-TiO<sub>2</sub> cannot reflect the quality of the devices because this intensity are dependent on the perovskite quality and charge transfer.

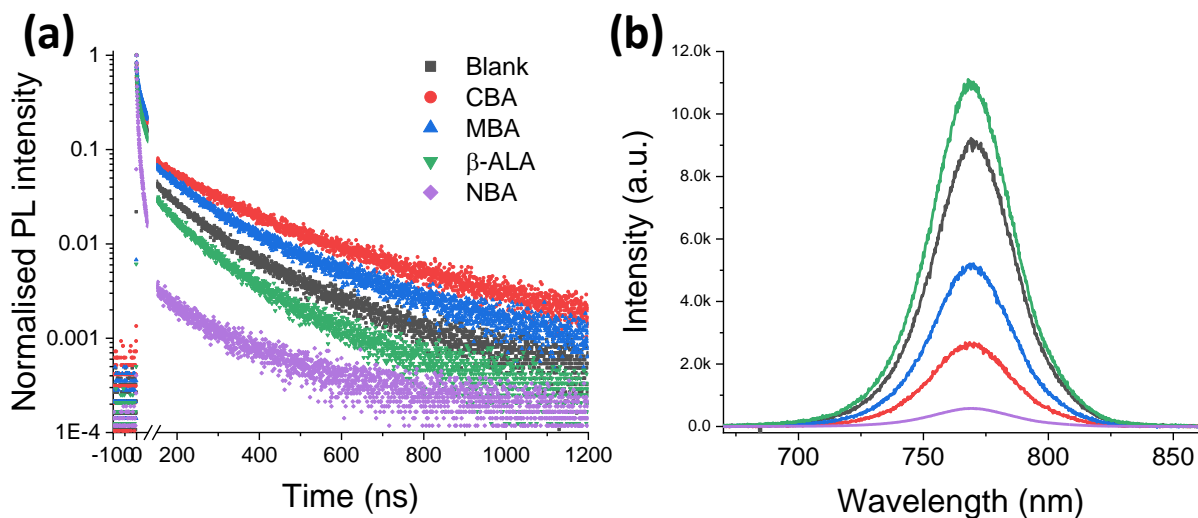


**Figure III. 4** (a) Time-resolved photoluminescence (TRPL) curves. (b) Steady-state PL curves.

**Table III.1** The obtained parameters by fitting the TRPL curves.

Model	ExpDec3				
Equation	$y = A1*\exp(-x/t1) + A2*\exp(-x/t2) + A3*\exp(-x/t3) + y0$				
Plot	Blank	CBA	MBA	$\beta$ -ALA	NBA
A1	0.50	0.49	0.39	0.56	0.33
t1/ns	1.62	<b>1.47</b>	1.57	1.47	8.99
A2	0.30	0.31	0.39	0.28	0.64
t2/ns	28.2	32.4	29.7	25.6	1.64
A3	0.15	0.16	0.19	0.14	0.03
<b>t3/ns</b>	<b>117.0</b>	<b>182.6</b>	<b>135.8</b>	<b>97.5</b>	<b>58.2</b>

We found a good correlation between the slow decay time ( $\tau_{sl}$ ) and the cells  $J_{SC}$ : the higher  $\tau_{sl}$ , the higher  $J_{SC}$  (see Section 4). This parameter reflects the quality of the OIHP material and high values reflect low quenching phenomena in the bulk. Our data shows that Cs8FAMA formed on the CBA, and to a less extent, on the MBA has better structural quality than the pristine material. Figure III.4b shows the corresponding steady-state photoluminescence (PL). We should note that the charge transfer in the interface and charge recombination in the bulk perovskite synergistically affected the steady-state PL intensity.

We further compared the steady-state PL intensity emitted by shining the layers from their front and back sides (Figure III.5). The intensity measured from the front side was 10 times higher than that measured from the backside for fresh Cs8FAMA layers on CBA and MBA modified *mp*-TiO<sub>2</sub>. This shows a better charge transfer at the interface compared to the blank sample.  $\beta$ -ALA sample also shows lower PL intensities by measuring from the back. NBA sample shows the lower PL intensity for both sides among all the investigated samples. However, we got different results (Figure A.III.1 in Annex-III) for CBA, MBA, and  $\beta$ -ALA samples when these samples were measured again after 4 days, which might be influenced by the mature process of the perovskite Cs8FAMA (Section III.4.2). This mature process might change the interface of perovskite/SAMs/TiO<sub>2</sub>.

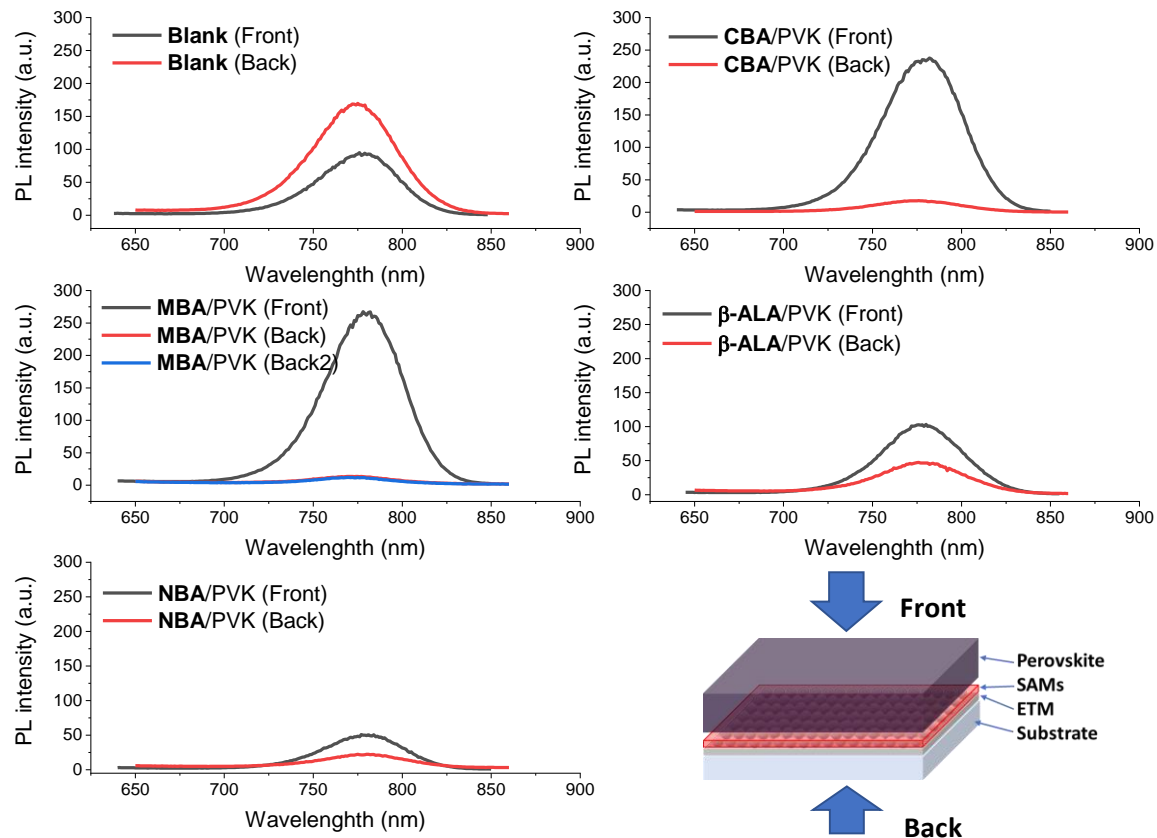


**Figure III. 5** Steady-state PL spectra of Cs8FAMA layer on SAMs measured from the front and the backside of the layers.

### III.3.5 UPS and IPES

The perovskite layer was also investigated using photoelectron spectroscopy techniques (UPS and IPES). Figure III.6 shows the high binding energy cutoff as well as the valence and conduction band regions of a matured (storing 3 days in N<sub>2</sub> glovebox) and aged (storing 10 days in N<sub>2</sub> glovebox) Cs8FAMA sample. Notably, the cutoff energy shifts, corresponding to a decrease in work function as given in the right table. Furthermore, a difference in the shape of the VB is notable, which probably comes from surface contamination, which will suppress states close to the Fermi level. Using linear slopes to the onset DOS, we find in both cases a valence band onset of 1.25 eV and a conduction band onset of 0.5 eV; the measured electronic bandgap, therefore, does not change. It should be noted that as usual for this linear readout, the gap is somewhat overestimated<sup>40,41</sup>, in this case by about 150 meV. The extracted values for the ionization energy (IE) and electron affinity (EA) are also listed in the right table. Whether the found changes in these values upon aging is due to a change in the perovskite material itself, or they are a result of some surface contamination is

however not discernable. Therefore, the values extracted for the matured sample should be viewed with precaution. (done by Dr. Selina Olthof)

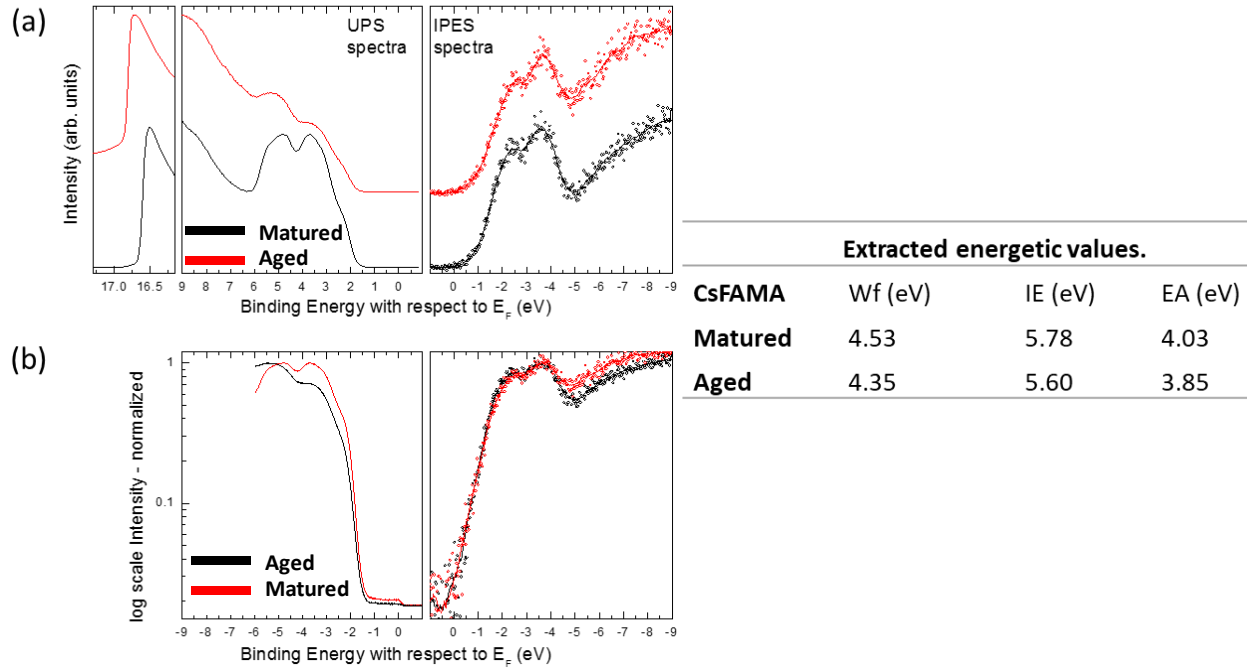


**Figure III. 6** (a) UPS and IPES spectra for the matured (3 days in  $N_2$ ) and aged (10 days in  $N_2$ ) Cs8FAMA layers. (b) normalized curves of (a). (Drawn by Dr. Selina Olthof)

### III.4 Characterizations of PSCs

#### III.4.1 $J-V$ curves and IPCE

We have fabricated solar cells based on the device structure depicted in Figure III.7a to investigate the effect of the  $TiO_2$ /perovskite interface engineering on the cell functioning and performances.<sup>14</sup> The SEM view of the PSC cross-section is presented in Figure III.7b and the thickness of perovskite layer is about 600 nm. The current-voltage ( $J-V$ ) curves of the best cells are presented in Figure III.8 and the data for the reverse and forward scans are gathered in Table III.2. The performances varied significantly with the SAMs treatment. The blank cell achieved an efficiency of 20.3% ( $V_{OC} = 1.11$  V,  $J_{SC} = 23.3$  mA.cm<sup>-2</sup>, FF= 78.5). Compared to the untreated cells, the CBA-Cs8FAMA devices presented much better performance. The highest efficiency was up to 21.35% ( $V_{OC} = 1.10$  V,  $J_{SC} = 24.25$  mA.cm<sup>-2</sup>, FF = 79.8). The performance of the MBA cell was close to the blank one.  $\beta$ -ALA cells were less efficient than the blank cell while this compound has been

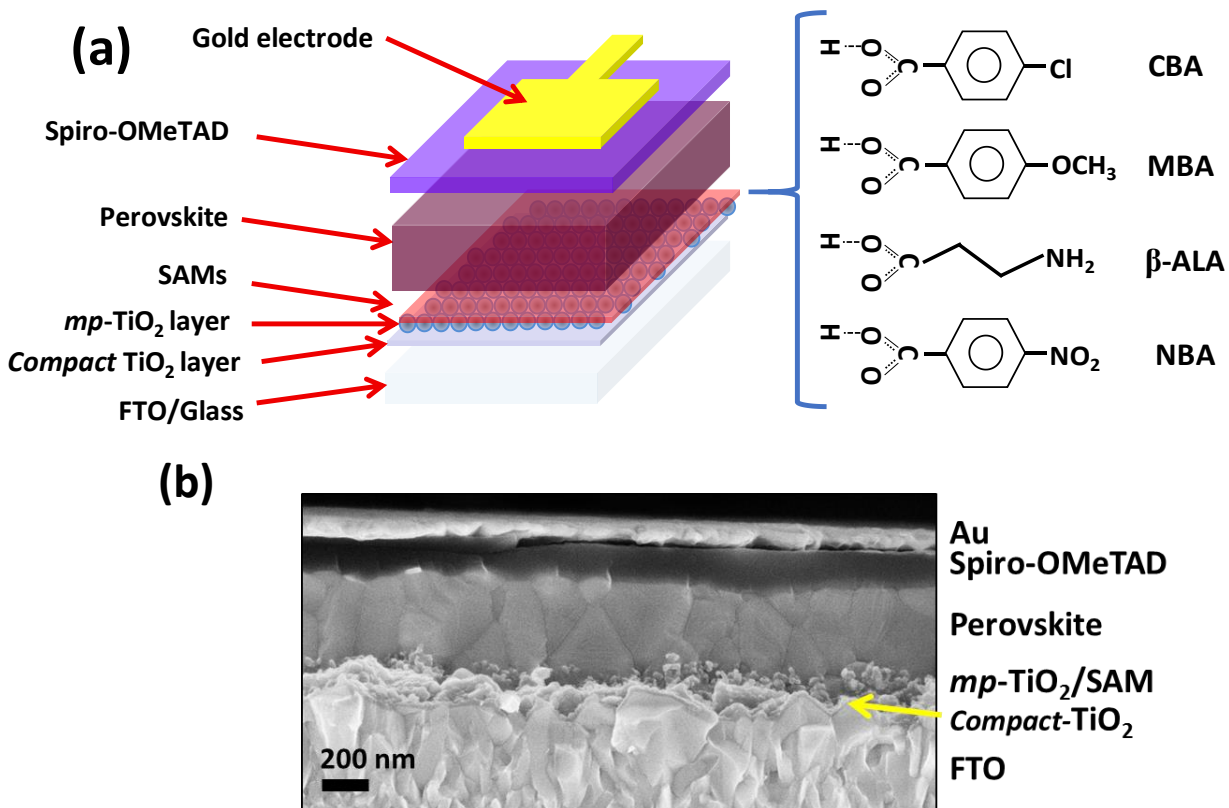


**Figure III. 7** (a) Schematic presentation of the investigated mesoscopic perovskite solar cells. The mesoporous *mp*-TiO<sub>2</sub> layer was covered by SAMs (in red) of various para-substituted benzoic acids and  $\beta$ -alanine before to be covered by the Cs8FAMA perovskite layer. (b) SEM view of the PSC cross-section.

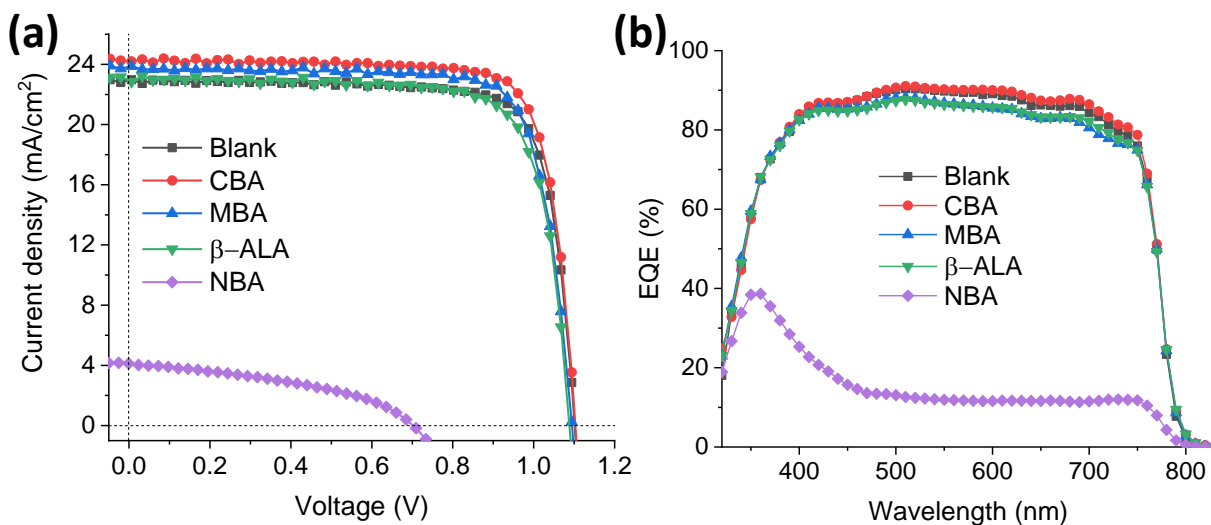


**Figure III. 8** (a) Reverse scan  $J$ - $V$  curves and (b) EQE of PSCs engineered by various acids.

**Table III.2** Photovoltaic  $J$ - $V$  parameters of best Cs8FAMA cells.

Cell	Scan direction	$V_{oc}$ /V	$J_{sc}$ /mA/cm <sup>2</sup>	$FF$ /%	$PCE$ /%	$HI$ /%
<b>Blank</b>	Reverse	1.110	23.29	78.53	20.30	6.6
	Forward	1.105	23.27	73.81	18.97	
<b>CBA</b>	Reverse	1.101	24.25	79.81	21.35	12.9
	Forward	1.086	24.26	70.59	18.60	
<b>MBA</b>	Reverse	1.094	23.87	79.29	20.73	19.3
	Forward	1.068	23.85	65.70	16.73	
<b><math>\beta</math>-ALA</b>	Reverse	1.096	23.10	76.69	19.43	12.6
	Forward	1.075	23.10	68.42	16.99	
<b>NBA</b>	Reverse	0.696	4.19	37.86	1.11	9.0
	Forward	0.702	3.49	41.28	1.01	

described in the literature to boost the PCE of various MAPI solar cells.<sup>24,29,39</sup> NBA cells exhibited a very low efficiency. The presence of NBA SAM deteriorated all the  $J$ - $V$  parameters, and the efficiency was very low. It is probable that this additive introduces trap states and defects at the interface which are at the origin of large parasitic charge recombination reaction. The EQE spectra are reported in Figure III.8b. Excluding NBA, the EQE values were very high with the highest quantum efficiencies for the CBA cells, in good agreement with the superior  $J_{SC}$  for this device.

The statistical analysis in Figure III.9 and the averaged values in Table III.3a confirm the consistency of the performance trend. The PCE of the CBA cells is markedly superior to the blank due to higher  $V_{OC}$  and  $J_{SC}$  parameters. On the other hand, NBA is detrimental to the device functioning. The  $J_{SC}$  is very low with an average value of about 3 mA.cm<sup>-2</sup>. Combined with the low  $V_{OC}$  and low  $FF$ , it generates a PCE of only 1%.

We also applied the SAMs in MAPI cells and a similar result was gathered in Table III.3b, except that the performances of the MBA cells were inferior to the blank one. We preliminary tested two other benzoic acid derivatives for SAMs, namely 4-aminobenzoic acid (ABA) and 4-bromobenzoic acid (BrBA) in PSCs. The solar cells performances are summarized in Table III.3c. BrBA is beneficial for the performances of PSCs while ABA-modified cells are less efficient than the blank ones. Finally, CBA was the best modifier and these two additional acids were not further investigated.

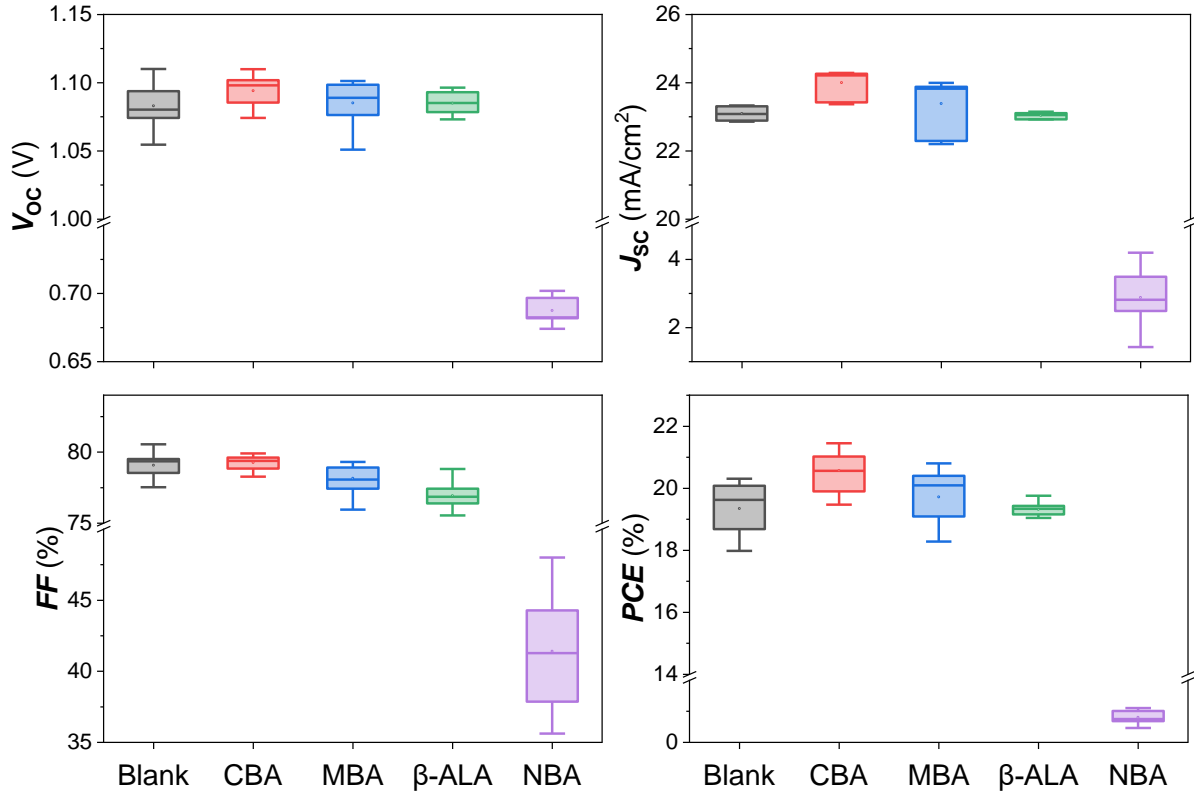


**Figure III. 9** Statistical analysis of the  $J-V$  curve parameters of 20 cells from the same batch.

**Table III.3a** Averaged photovoltaic reverse scan  $J-V$  parameters with standard deviation of CsFAMA PSCs.

Average data	$V_{oc}$ /V	$J_{sc}$ /mA.cm <sup>-2</sup>	$FF$ /%	$PCE$ /%
<b>Blank</b>	1.083±0.027	23.09±0.24	79.07±1.47	19.34±0.96
<b>CBA</b>	1.094±0.016	24.00±0.29	79.26±0.65	20.57±0.88
<b>MBA</b>	1.085±0.016	23.38±0.61	78.14±1.15	19.72±1.08
<b>β-ALA</b>	1.085±0.011	23.04±0.11	76.92±1.89	19.32±0.44
<b>NBA</b>	0.687±0.015	2.88±1.31	41.41±6.60	0.802±0.30

**Table III.3b** Averaged photovoltaic reverse scan  $J-V$  parameters with standard deviation of MAPI PSCs.

	$V_{oc}$ /V	$J_{sc}$ /mA.cm <sup>-2</sup>	$FF$ /%	$PCE$ /%
<b>Blank</b>	1.029±0.023	21.98±1.08	71.29±7.01	16.69±0.74
<b>CBA</b>	1.023±0.029	22.55±1.48	73.27±4.19	17.28±1.09
<b>MBA</b>	0.934±0.082	21.04±0.84	62.56±10.56	12.29±2.87
<b>β-ALA</b>	1.016±0.017	22.10±1.02	71.53±6.80	16.82±0.64
<b>NBA</b>	0.700±0.030	2.19±0.65	36.45±3.63	0.56±0.20

**Table III.3c** Evaluation of the effect of additional benzoic acid derivative SAMs on Cs8FAMA PSCs performances.  $J$ - $V$  curve parameter and PCE(%) averaged for several cells. ABA: 4-aminobenzoic acid; BrBA: 4-bromobenzoic acid.

Average	Direction	$V_{oc}/V$	$J_{sc}/mA.cm^{-2}$	FF/ %	PCE/ %	HI/ %
<b>Blank</b>	Reverse	0.972	20.13	76.44	14.96	0.167
	Forward	0.950	20.15	65.03	12.45	
<b>CBA</b>	Reverse	0.958	22.16	75.99	16.13	0.231
	Forward	0.916	22.13	60.94	12.36	
<b>BrBA</b>	Reverse	0.948	22.19	75.27	15.84	0.229
	Forward	0.904	22.19	60.83	12.21	
<b>ABA</b>	Reverse	0.905	21.00	66.91	12.72	0.351
	Forward	0.822	20.93	48.32	8.31	

In Table III.2, the hysteresis index (HI) is also reported. This index is larger for the acid treated samples compared to the blank cell (HI = 6.6%). The highest HI is found for the MBA PSC with HI = 19.3%. The stabilized efficiency was determined by tracking experiments. The results are gathered in Figure III.10a and Figure III.11. We note that the superior performance of the CBA cells is confirmed with a stabilized PCE of 20.9% reached after 2 min while the blank cell achieved only a 20.0% stabilized PCE. We also notice that the systems have a slower response time in the case of the acid-modified cells. For instance, the steady-state maximum power was reached after 80 s for the CBA PSC while it was found after only 20 s in the case of blank one. More generally, the SAMs modified devices always exhibit a slower rise than the blank pristine one (Figure III.11). The rise can be attributed to the re-organization of the interface upon polarization. This re-organization is linked with the mobility of ions in the Cs8FAMA perovskite and to the ionic redistribution. Interesting information is that the different time scale in the tracking curves is related to the hysteresis. The longer is the time to reach the steady state, the higher is the hysteresis in the  $J$ - $V$  curve. Also, we have shown elsewhere that the slow electrical phenomena are also related to the low-frequency capacitance measured on PSCs.<sup>16,42</sup>

An important question is whether the hysteresis is detrimental to the high steady-state efficiency of our PSCs. In Figure III.10b, we have plotted the maximum steady-state power point (MPP) of the CBA cell. This parameter is close to the reverse scan  $J$ - $V$  curve. It does not look influenced by the hysteresis. Similarly, for the blank cell and the  $\beta$ -ALA cell, the MPP is close to the reverse scan  $J$ - $V$  curve (Figure III.11). Our data show that in the high-efficiency triple cation solar cells, the hysteresis is not a problem for the steady-state efficiency of the device. It corresponds to ionic

reorganizations and a larger hysteresis only means that achieving the steady-state current will take a longer time.

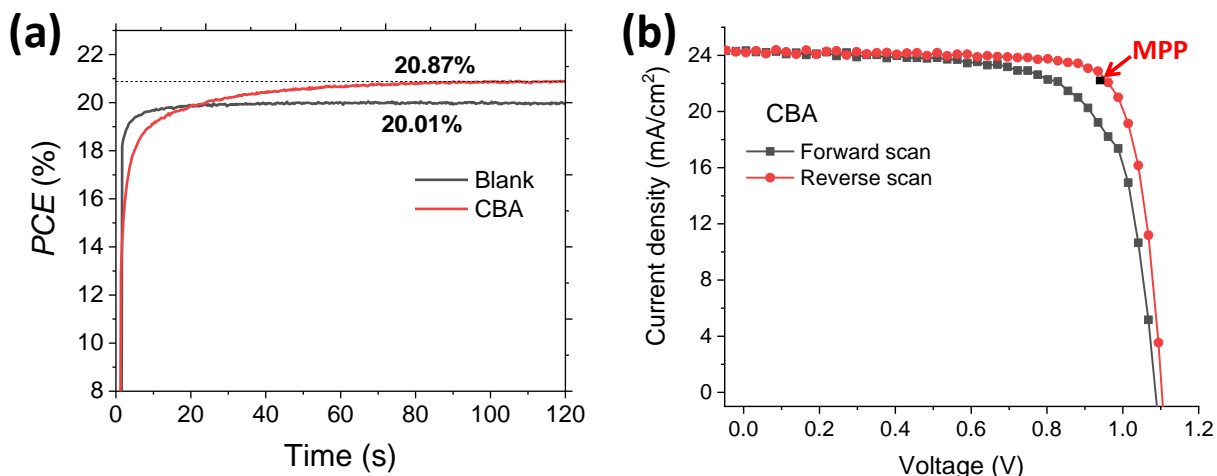


**Figure III. 10** (a) Tracking of the maximum overall power conversion efficiency of the CBA and blank cells. (b) Forward and reverse  $J-V$  curves of a CBA cell with the stabilized maximum power point (MPP).

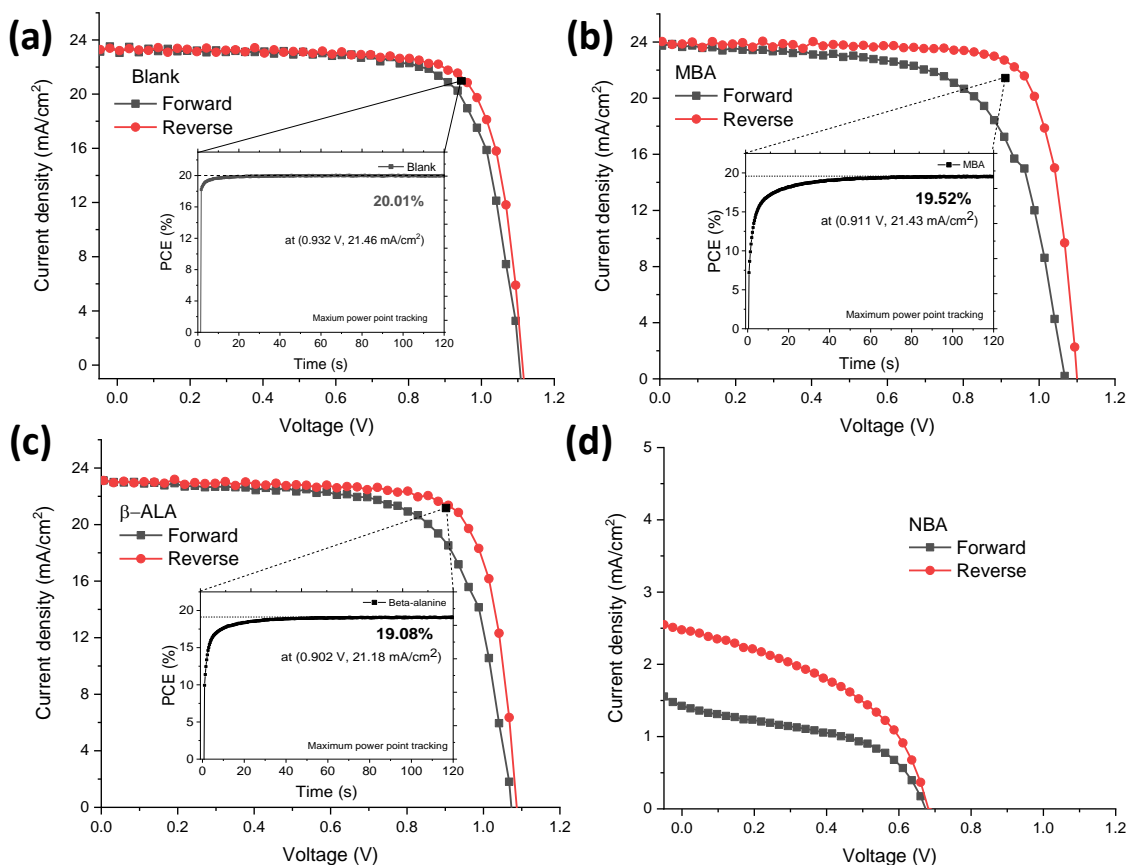


**Figure III. 11** Forward and reverse  $J-V$  curve scans, efficiency tracking at the maximum power efficiency (Inset) and maximum working power point of (a) Blank, (b) MBA, (c)  $\beta$ -ALA and (d) NBA. The black square is the maximum power point.

### III.4.2 Stability

#### III.4.2.1 Cs8FAMA perovskite solar cells

The stability of unencapsulated cells has been followed for two months as shown in Figure III.12a. In this measurement, the cells were stored in a N<sub>2</sub>-filled glovebox. All the PSCs exhibited good stability and had a similar evolution. It is concluded that the interface modification is not detrimental for stability. Because the SAMs are placed under the OIHP layer and that no significant increase in perovskite grain size was induced by the presence of SAMs, no improvement in stability was found. We can note that some groups have successfully implemented the strategy of placing SAMs with hydrophobic properties on top of the OIHP layer to enhance the device stability.<sup>30,33</sup> Therefore engineering the interfaces of the perovskite on both sides could be a successful strategy to get highly efficient and stable PSCs. In Figure III.12a, we can see that the MBA cells were less stable. It can be linked to the larger amount of PbI<sub>2</sub> present in the OIHP of these cells as shown by the XRD patterns in Figure III.1.<sup>43</sup>

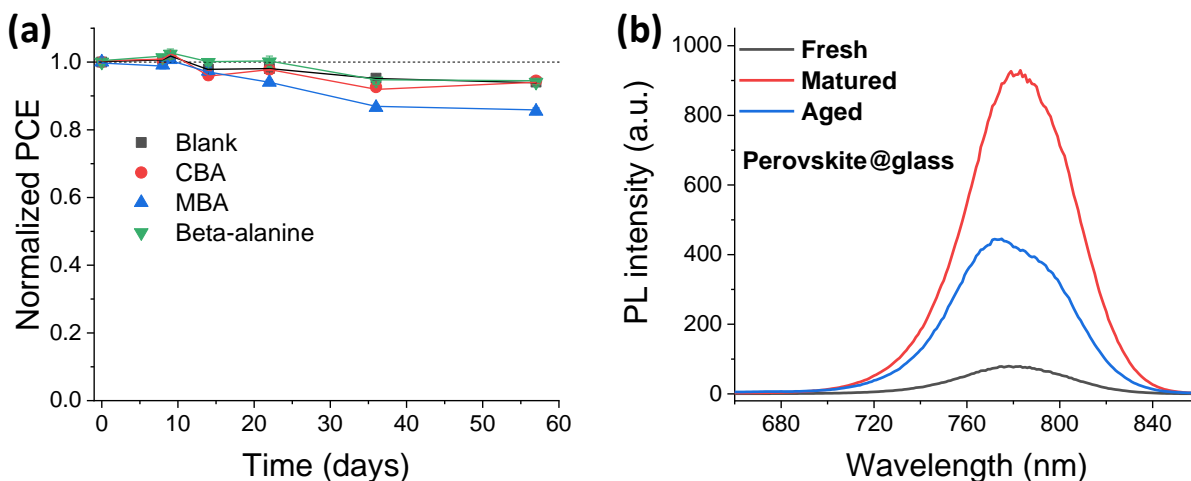


**Figure III. 12** (a) Stability test of unencapsulated cells treated with various acids. (b) PL emission spectra of fresh, three days matured and 12 days aged Cs8FAMA layer deposited on glass.

A more attentive scrutinizing of the evolution curves (Figure III.12a) shows that the efficiency of all the devices increased during the first few days. A surprising maturation period is found at the beginning. To elucidate this performance improvement phenomenon, photoluminescence measurements were conducted. Figure III.12b shows the spectra of a fresh layer and a three-days old layer. The PL intensity is about ten times higher after the few days of storage. Therefore, during this maturation step, the structural quality of the HP is improved, defects are annealed/passivated

and the radiative recombination increases. Then, when the layer is further aged, the PL intensity decreases due to the perovskite degradation (Figure III.12b).

### III.4.2.1 MAPbI<sub>3</sub> perovskite solar cells

The SAMs were also applied in MAPbI<sub>3</sub> based PSCs. And the effect of SAMs on PSCs performance was nearly the same, except the rather low performances of MBA cells and the total efficiencies lower than those of Cs8FAMA solar cells. The photovoltaic parameters for all the investigated MAPbI<sub>3</sub> devices are recorded in the Annex III. Table III.4 shows a rather low decrease of the PCEs from reverse scans after 150 days of storage in an N<sub>2</sub>-filled glovebox. However, the PCEs from forward scans were dramatically reduced. It resulted in a huge hysteresis for the aged devices. Stability tests of MAPI films on SAMs modified TiO<sub>2</sub> in an ambient environment were also conducted. As shown in Figure III.13, these SAMs did not improve the stability apparently, except the NBA sample while the efficiencies of NBA cells were too poor.

**Table III.4** Photovoltaic data in MAPI system. 27-09-2018 to 28-02-2019 (150 days in N<sub>2</sub>.)

MAPbI <sub>3</sub>	Scan direction	Fresh PCE /%	Aged PCE /%	Decreased ratio	Average
Blank	Reverse	13.35	12.27	8%	28%
	Forward	9.41	4.91	47%	
CBA	Reverse	18.37	17.51	4.7%	23%
	Forward	13.02	7.99	38%	
MBA	Reverse	13.74	12.73	7.3%	38%
	Forward	10.38	3.48	66.5%	
β-ALA	Reverse	16.44	15.49	5.8%	31%
	Forward	12.11	5.47	54.8%	
NBA	Reverse	0.75	0.82	-9.3%	-35%
	Forward	0.58	0.93	-60.3%	

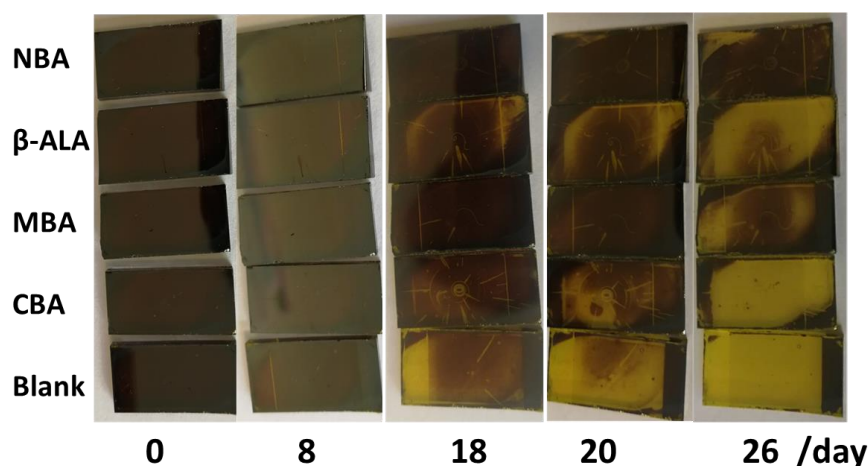


**Figure III. 13** Stability test of MAPI layer on SAMs, at 25°C 40-60% of relative humidity.

### III.4.3 Discussion about the effect of SAMs on the PSCs performances

The effect of SAMs on MAPI cells is nearly the same as that on Cs8FAMA cells, whatever XRD, SEM, UV, steady-state PL (see Figure A.III.2-6 in Annex III), and even TRPL. The TRPL curves are presented in Figure III.14. The order of the curves was magically the same, which means the same interfaces of SAMs/MAPI and SAMs/Cs8FAMA in terms of charge injection and recombination. In addition, the bandgaps of MAPbI<sub>3</sub> (1.598 eV) and Cs8FAMA (1.60 eV) are basically the same but Cs8FAMA device has apparently larger  $J_{SC}$ . It is explained through the fact that Cs8FAMA has better charge injection efficiency, which is deduced from the fast decay at the beginning of the TRPL figure. The possible charge behaviors in the interface are depicted in Figure III.15. The excited electrons can come back to the ground state by fluorescence process ①, or quenching on trap states ② and ④, charge transferring to electrode ③, power generation ⑤.<sup>39</sup>

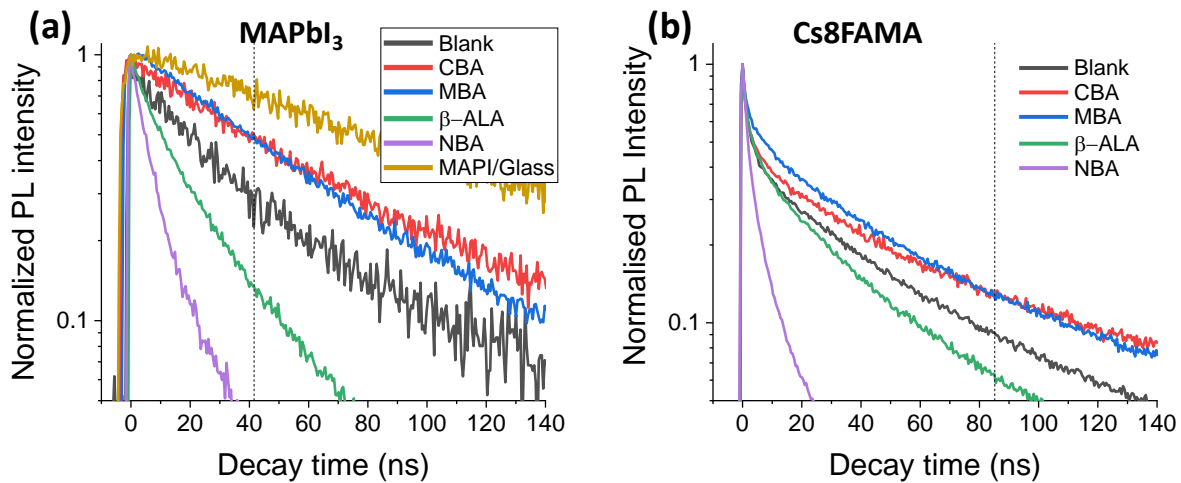


Figure III. 14 TRPL for (a) MAPI and (b) Cs8FAMA on SAMs@TiO<sub>2</sub>.

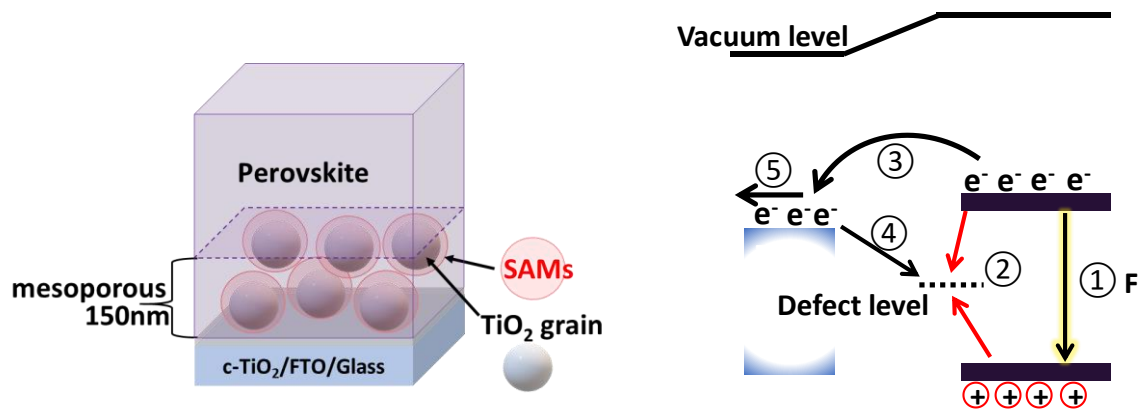
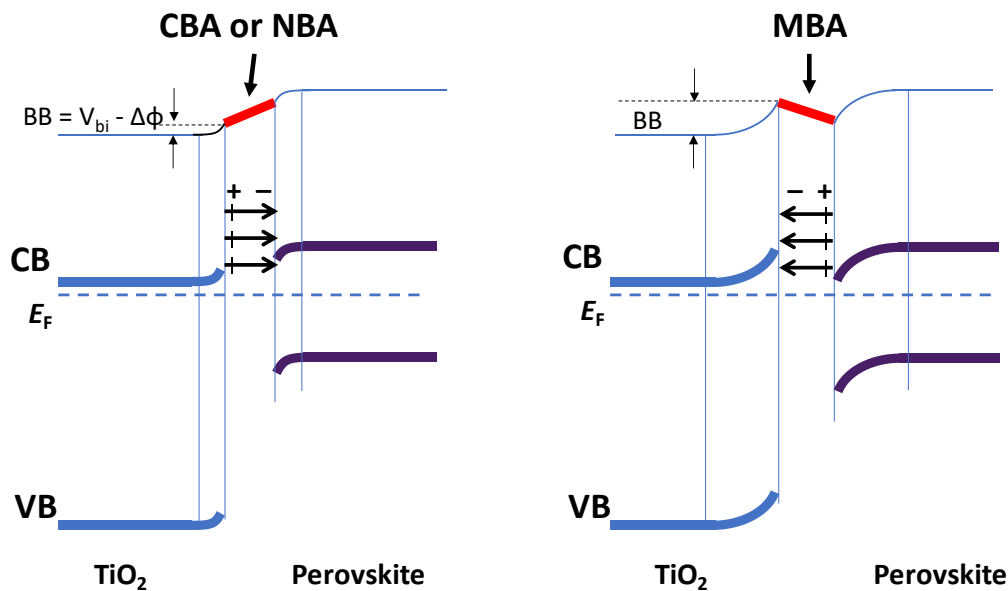


Figure III. 15 (a) Model of the interface perovskite/SAMs/*mp*-TiO<sub>2</sub>. (b) Schematic diagram for the charge dynamics at PVK/TiO<sub>2</sub> interface: 1. Photoluminescence process; 2 and 4. PL quenching via trap states; 3. Charge transfer process; 5. Power generation.

### III.4.3.1 Dipole moment and electric field

We have detailed, in Chapter II.3, the normal dipole moments and the surface work functions of the various SAMs@TiO<sub>2</sub> surface. We can draw energy band levels as shown in Figure III.16 (if the perovskite layer were thick enough). CBA and NBA reduce the band bending and the induced electric fields favor electrons transfer. Considering that CBA is bound to perovskite, its dipole moment decreases further (see Section III.4.3.3) and the details are given in Table III.5. On the other hand, MBA increases the band bending and the induced electric field blocks the electron transfer. The adsorbed  $\beta$ -ALA has a very small normal dipole moment (0.12 D), which changes little the surface WF (3.82 eV vs. 3.8 eV). So, this case is not further discussed. In terms of the energy band bending, CBA and NBA should both produce good cells. There are two questions unsolved: 1. NBA cells are very bad; 2. Perovskite/CBA/TiO<sub>2</sub> samples did not present fast decay in TRPL curve, so it is real that the CBA improved the charge injection?



**Figure III. 16** Effect of the adsorbed molecules dipole moment direction on the interface energy level diagram.

**Table III.5** Dipole moment component normal to the surface of CBA calculated at various interfaces. The perovskite (PVK) employed for the calculations is CH<sub>3</sub>NH<sub>3</sub>PbI<sub>3</sub>.

	Isolated	TiO <sub>2</sub> -CBA	CBA-PVK	TiO <sub>2</sub> -CBA-PVK
$\mu_{\perp}$ (D)	1.55	0.89	0.88	0.61

### III.4.3.2 Chemical interaction and the trap states

Chemical interactions are very important in the interface.<sup>39</sup> The SAMs might reduce or increase the surface defects too. Especially in such a mesoporous structure, SAMs have more chances to contact the perovskite to increase the chemical interactions.

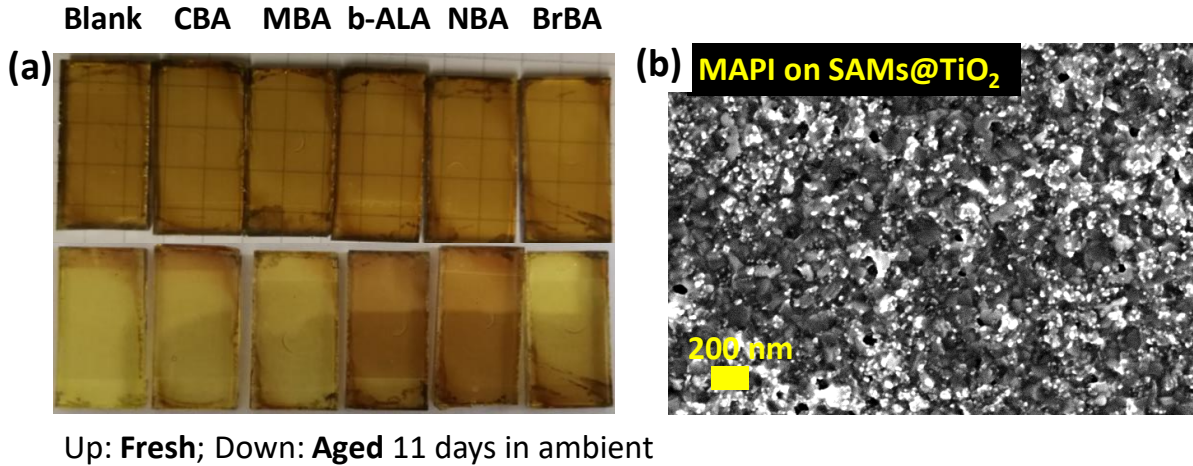


**Figure III. 17** (a) Low concentration (0.35M) MAPI on SAMs@TiO<sub>2</sub>. (b) SEM of low concentration of MAPI on SAMs@TiO<sub>2</sub>.

To study the chemical interactions between SAMs and perovskites, we fabricated very thin MAPI perovskite films on SAMs@TiO<sub>2</sub> by decreasing the concentration of the precursor solution at 0.35 M (Figure III.17). Perovskite crystals embedded in mesoporous structure as shown in Figure III.17b. The aging test further confirmed a better stability for the NBA and  $\beta$ -ALA samples. By carefully checking the back-side PL data (Figure III.18), NBA and  $\beta$ -ALA curves exhibits a slight shift to left, which possibly indicates that 2D-like perovskites were formed.

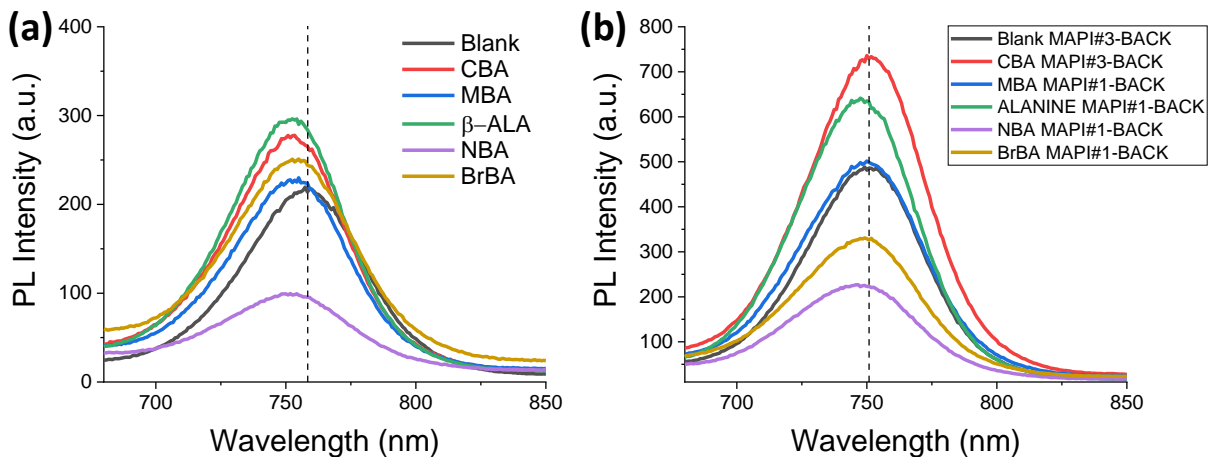


**Figure III. 18** PL spectra of low concentration MAPI on SAMs@TiO<sub>2</sub> from front (a) and back sides (b).

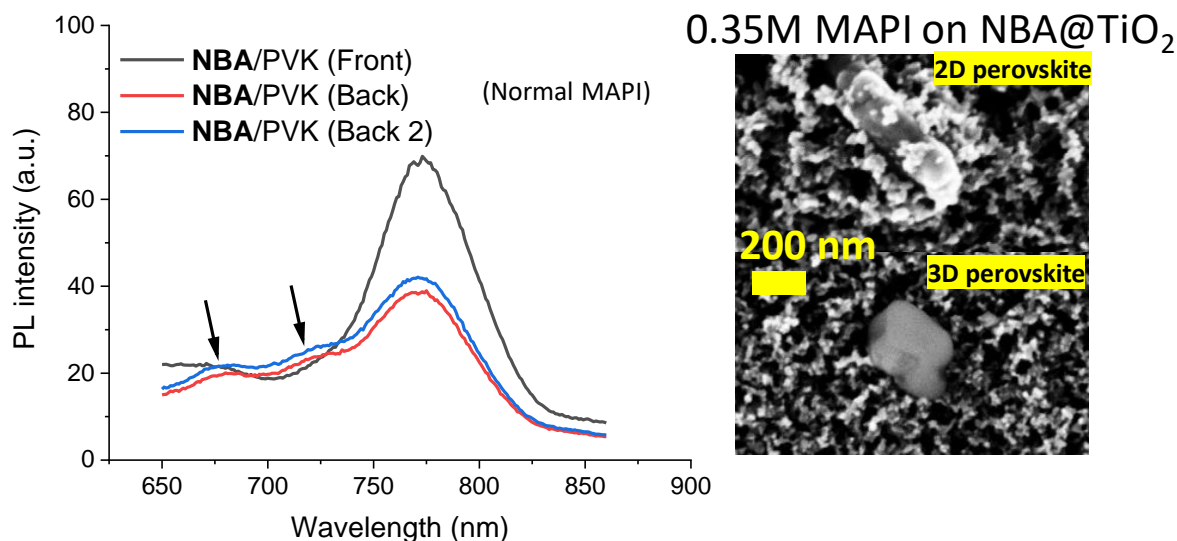


**Figure III. 19** Steady-state PL spectra of normal 1.45M MAPI on NBA@TiO<sub>2</sub> and SEM for 0.35M MAPI on NBA@TiO<sub>2</sub>.

As shown in the energy band diagrams in Figure II.2.10, the IE values of TiO<sub>2</sub>, CBA, MBA, NBA and  $\beta$ -ALA are 7.37 eV, 7.08 eV, 7.13 eV, 6.64 eV and 7.82 eV, respectively. The shallow VB of NBA can be a recombination center, which can cause serious PL quenching in solar cells. Figure III.19 shows two slight PL peaks at 675 nm and 725 nm, which can be ascribed to the trap states or 2D/3D perovskites formed in the interface. A special crystal with an aspect quite different than 3D perovskite crystal was observed under SEM characterization as shown in Figure III.19.

#### III.4.3.3 Modeling of perovskite/CBA/TiO<sub>2</sub> interface

To further explain the remarkable enhancement of the cell performance with CBA SAM, we collaborated with the "Modeling of Complex Systems" group of the laboratory with the aim to get a model of the heterostructure by periodic hybrid DFT calculations. Since band alignment between the perovskite and the oxide is a key point for efficient electron injection in the cell, all calculations were performed at the computationally demanding hybrid DFT level. Chloride was supposed to strongly interact with the inorganic framework of the perovskite, creating a structural continuity between TiO<sub>2</sub> and the perovskite. To validate this hypothesis, an interface model was built. MAPI was chosen as the perovskite instead of Cs8FAMA since: (i) the former is structurally simpler than the latter, with the different moieties playing the same role in both systems, (ii) the efficiency enhancement has also been proven with CBA in MAPI cells (see Table III.3.b). From a structural

viewpoint, conclusions obtained for the MAPI-based model should, therefore, be qualitatively similar to those obtained with a Cs8FAMA-based model. The modeling procedure is detailed in the Annex-III.

Figure III.20a and 20b show the interface structure after geometry optimization. The left Figure III.20a is the whole interface model and the right one focuses on the interfacial region. The optimized a and b cell parameters for the obtained structure are 14.821 Å and 11.003 Å, respectively, and the  $\gamma$  angle is 108.0°. These values are close to those of the TiO<sub>2</sub> supercell considered to build the model, with only a small shrinking after relaxation. Based on the data reported in Figure III.20b, we can conclude that the interface obtained between MAPI, CBA and TiO<sub>2</sub> is mainly ensured by both Ti-O and Pb-Cl bonds. Indeed, a bridging bidentate mode is involved between the carboxylate group of CBA and TiO<sub>2</sub>, while strongly distorted PbI<sub>5</sub>Cl octahedra can be evidenced between MAPI and CBA. It should however be noted that the Cl atoms and deprotonated CH<sub>3</sub>NH<sub>3</sub><sup>+</sup> groups are competitively binding to the Pb atoms. For instance, Pb atoms 2 and 4 bind to neighboring Cl atoms with distances close to 3.5 Å. On the other hand, Pb atoms 1 and 3 present larger distances with Cl (around 4.6 Å) than with the NH<sub>2</sub> groups of the deprotonated CH<sub>3</sub>NH<sub>3</sub><sup>+</sup> moieties (around 2.5 Å). It should also be noted that the four CBA ligands

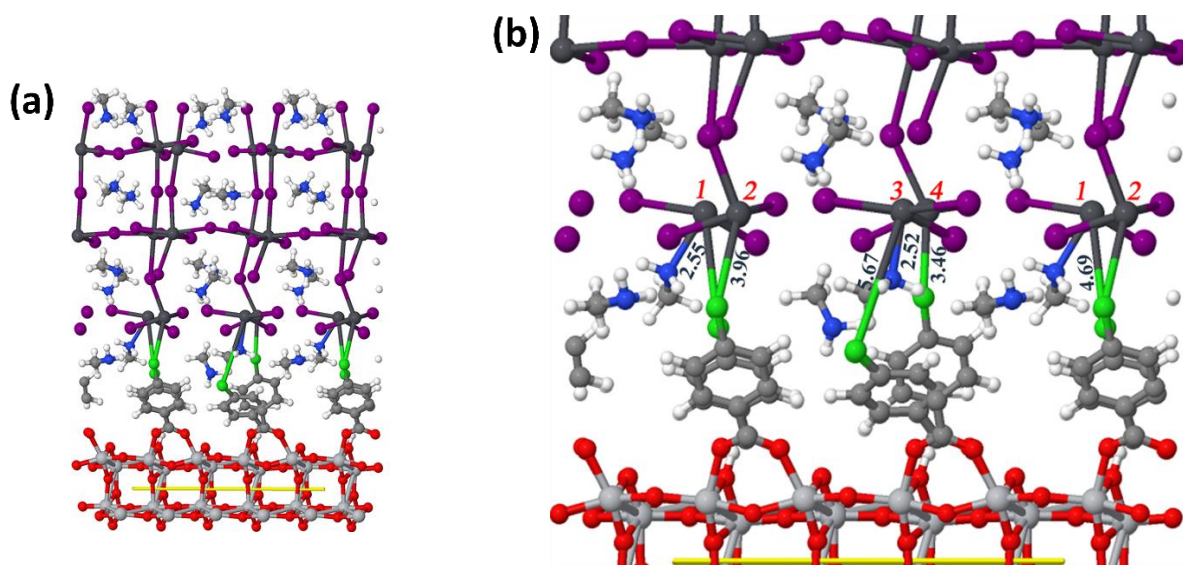


**Figure III. 20** Schematic drawing of the MAPI/CBA/TiO<sub>2</sub> interface unit cell. (a) Whole system; (b) zoomed portion of the MAPI/CBA/TiO<sub>2</sub> binding. Data in black correspond to distances (in Å), while the red ones correspond to atom numbers mentioned in the text. The solid yellow line represents the unit cell. Red, light grey, white, green, purple, dark grey, blue and grey spheres correspond to O, Ti, H, Cl, I, Pb, N and C atoms, respectively.

in the interface unit cell have tilting angles with respect to the  $c$  axis of  $30.0^\circ$ ,  $38.6^\circ$ ,  $38.6^\circ$  and  $46.9^\circ$ . These values are generally larger than the  $30.3^\circ$  value obtained for the adsorption of CBA on  $\text{TiO}_2$  anatase (101) (See Chapter II, Section II.3.1), indicating that the CBA ligands can lay on the  $\text{TiO}_2$  surface with favorable  $\text{H}^+/\pi$  interactions in order to act as efficient linkers for the interface formation. Moreover, benzene ring possibly plays an important role in reducing the defects of perovskite according to Ref.<sup>44</sup>.

From the computed data, the presence of a halogen substituent on the ligand (Cl in the case of CBA) seems an important requirement for a stable bonding with the perovskite. On the other hand, the relatively fixed conformation of the CBA ligand imposed by its binding to the  $\text{TiO}_2$  surface built a favorably organized CBA- $\text{TiO}_2$  interface for the binding of perovskite. This is probably not the case when more flexible ligands are chosen (such as the NBA interfacial modifier).

To better clarify the effect of the structural continuity between MAPI and  $\text{TiO}_2$  by the CBA SAM bridge, electron injection from MAPI to  $\text{TiO}_2$  was analyzed using an approach that has been developed notably for dye-sensitized solar cells<sup>45,46</sup> and quantum-dot sensitized solar cells<sup>47</sup>. More precisely, the spin density of the reduced MAPI/CBA/ $\text{TiO}_2$  system has been computed and the corresponding isodensity plot is shown in Figure II.21. It is clear that the computed spin density is mainly delocalized over the  $\text{TiO}_2$  part, with a 99.94% contribution of the added electron on the  $\text{TiO}_2$  substrate. This value is a quantification of the injection efficiency of the photogenerated electrons and indicates an almost quantitative electron transfer from MAPI to  $\text{TiO}_2$  through the

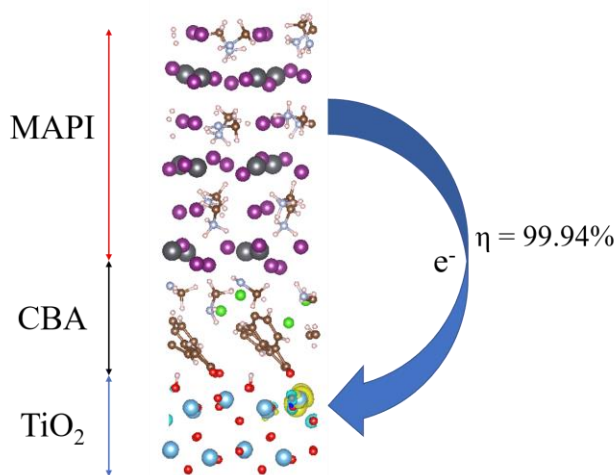


**Figure III. 21** Spin density of the reduced MAPI-CBA- $\text{TiO}_2$  interface system (excess of  $\alpha$ -electron is indicated in yellow), isosurface contour value:  $|0.00271|$  a.u.  $\eta$  is the calculated electronic charge injection efficiency.<sup>48</sup>

CBA ligand. From the fast and efficient electronic charge transfer, it results that charge recombinations are suppressed and that a high  $J_{SC}$  is generated. Using a Newns-Anderson model and the computed electronic structure of the MAPI/CBA/TiO<sub>2</sub> system, the electron injection time is estimated to be 24 fs, indicating an ultrafast electron injection.

### III.5 Conclusions

In summary, we have demonstrated that the engineering of the interface between perovskite and titania is important to get highly efficient perovskite solar cells. By using this strategy, we have been able to prepare PSCs reaching a PCE of 21.3% (stabilized at 20.9%). We have shown that in high-efficiency triple cation PSCs, the chloride-functionalized benzoic acid molecule provides a significant beneficial effect. CBA forms a SAM at the TiO<sub>2</sub> surface and is attached in a bridging bidentate mode. This interlayer did not change the perovskite film morphology and crystallinity. We have also shown that its effect cannot be due to the band energy level management by its molecular dipole moment, which is reduced to a large extent while sandwiched between TiO<sub>2</sub> and the perovskite. Our experimental and theoretical investigations emphasize that CBA SAMs at the oxide/perovskite interface is beneficial for the structural continuity, the trap state reduction and for the global quality of the perovskite. We show that the presence of a halogen substituent on the ligand (Cl in the case of CBA) is a significant requirement to establish a stable bonding with the perovskite. We have pointed out that the interfacial chemical interactions are important to consider for the design of highly efficient interfaces and that the relatively fixed conformation of the CBA ligand, imposed by its binding to the TiO<sub>2</sub> surface, built a favorably organized CBA-TiO<sub>2</sub> interface for the binding of the perovskite. By modeling, fast charge injection (24 fs) and efficient electronic charge transfer (99.94%) have been calculated for the TiO<sub>2</sub>/CBA/MAPI system.

Cs8FAMA and MAPbI<sub>3</sub> have a bandgap of 1.6 eV, which limits the photocurrent not more than 25 mA/cm<sup>2</sup>, regardless of SAMs we used. The most suitable bandgap for single junction solar cells should be close 1.3 eV.<sup>49</sup> In the next chapter, we will focus on the development of lower bandgap (1.48 eV) perovskite-FAPbI<sub>3</sub> based PSCs.

## References

1. Veldhuis, S. A.; Boix, P. P.; Yantara, N.; Li, M.; Sum, T. C.; Mathews, N.; Mhaisalkar, S. G. Perovskite Materials for Light-Emitting Diodes and Lasers. *Adv. Mater.* **2016**, *28*, 6804–6834.
2. Kim, H. S.; Lee, C. R.; Im, J. H.; Lee, K. B.; Moehl, T.; Marchioro, A.; Moon, S. J.; Humphry-Baker, R.; Yum, J. H.; Moser, J. E.; Grätzel, M. Lead Iodide Perovskite Sensitized All-Solid-State Submicron Thin Film Mesoscopic Solar Cell with Efficiency Exceeding 9%. *Sci. Rep.* **2012**, *2*, 591.
3. Lee, M. M.; Teuscher, J.; Miyasaka, T.; Murakami, T. N.; Snaith, H. J. Efficient Hybrid Solar Cells Based on Meso-Superstructured Organometal Halide Perovskites. *Science* **2012**, *338*, 643–647.
4. Liu, M.; Johnston, M. B.; Snaith, H. J. Efficient Planar Heterojunction Perovskite Solar Cells by Vapour Deposition. *Nature* **2013**, *501*, 395–398.
5. Burschka, J.; Pellet, N.; Moon, S. J.; Humphry-Baker, R.; Gao, P.; Nazeeruddin, M. K.; Grätzel, M. Sequential Deposition as A Route to High-Performance Perovskite-Sensitized Solar Cells. *Nature* **2013**, *499*, 316–319.
6. Zhang, J.; Barboux, P.; Pauporté, T. Electrochemical Design of Nanostructured ZnO Charge Carrier Layers for Efficient Solid-State Perovskite-Sensitized Solar Cells. *Adv. Energy Mater.* **2014**, *4*, 1400932.
7. Nie, W.; Tsai, H.; Asadpour, R.; Blancon, J. C.; Neukirch, A. J.; Gupta, G.; Crochet, J. J.; Chhowalla, M.; Tretiak, S.; Alam, M. A.; Wang, H. L. High-Efficiency Solution-Processed Perovskite Solar Cells with Millimeter-Scale Grains. *Science* **2015**, *347*, 522–525.
8. Zhang, J.; Juárez-Pérez, E. J.; Mora-Seró, I.; Viana, B.; Pauporté, T. Fast and Low Temperature Growth of Electron Transport Layers for Efficient Perovskite Solar Cells. *J. Mater. Chem. A* **2015**, *3*, 4909.
9. Zhang, J.; Pauporté, T. Effects of Oxide Contact Layer on the Preparation and Properties of  $\text{CH}_3\text{NH}_3\text{PbI}_3$  for Perovskite Solar Cell Application. *J. Phys. Chem. C* **2015**, *119*, 14919–14928.
10. Zhang, J.; Pauporté, T. One-Dimensional Self-Standing  $\text{TiO}_2$  Nanotube Array Layers Designed for Perovskite Solar Cell Applications. *ChemPhysChem* **2015**, *16*, 2836–2841.
11. Tu, Y. G.; Xu, G. N.; Yang, X. Y.; Zhang Y. F.; Li, Z. J.; Su R.; Luo D. Y.; Yang, W. Q.; Miao, Y.; Cai R.; Jiang L. H.; Du, X. W.; Yang, Y. C.; Liu, Q. S.; Gao, Y.; Zhao, S.; Huang, W.; Gong, Q. H.; Zhu, R. Mixed-Cation Perovskite Solar Cells in Space. *Sci. China-Phys. Mech. Astron.* **2019**, *62*, 974221-1–974221-4.
12. Yang, W. S.; Park, B. W.; Jung, E. H.; Jeon, N. J.; Kim, Y. C.; Lee, D. U.; Shin, S. S.; Seo, J.; Kim, E. K.; Noh, J. H.; Seok, S. I. Iodide Management in Formamidinium-Lead-Halide-Based Perovskite Layers for Efficient Solar Cells. *Science* **2017**, *356*, 1376–1379.
13. Leblanc, A.; Mercier, N.; Allain, M.; Dittmer, J.; Fernandez, V.; Pauporté, T. Lead-and Iodide-Deficient  $(\text{CH}_3\text{NH}_3)\text{PbI}_3$  (d-MAPI): The Bridge between 2D and 3D Hybrid Perovskites. *Angew. Chem., Int. Ed.* **2017**, *56*, 16067–16072.
14. Wang, P.; Ulfa, M.; Pauporté, T. Effects of Perovskite Monovalent Cation Composition on the High and Low Frequency Impedance Response of Efficient Solar Cells. *J. Phys. Chem. C* **2018**, *122*, 1973.
15. NREL chart (2019) <https://www.nrel.gov/pv/cell-efficiency.html>
16. Wang, P.; Shao, Z.; Ulfa, M.; Pauporté, T. Insights into the Hole Blocking Layer Effect on the Perovskite Solar Cell Performance and Impedance Response. *J. Phys. Chem. C* **2017**, *121*, 9131–9141.
17. Qiao, R.; Zuo, L. Self-Assembly Monolayers Boosting Organic–Inorganic Halide Perovskite Solar Cell Performance. *J. Mater. Res.* **2018**, *33*, 387–400.

18. Hu, T.; Becker, T.; Pourdavoud, N.; Zhao, J.; Brinkmann, K. O.; Heiderhoff, R.; Gahlmann, T.; Huang, Z.; Olthof, S.; Meerholz, K.; Többers, D. Indium-Free Perovskite Solar Cells Enabled by Impermeable Tin-Oxide Electron Extraction Layers. *Adv. Mater.* **2017**, *29*, 1606656.
19. Olthof, S.; Meerholz, K. Substrate-Dependent Electronic Structure and Film Formation of MAPbI<sub>3</sub> Perovskites. *Sci. Rep.* **2017**, *7*, 40267.
20. Yang, Z.; Dou, J. J.; Wang, M. Q. Interface Engineering in n-i-p Metal Halide Perovskite Solar Cells. *Sol. RRL* **2018**, *2*, 1800177.
21. Lim, K. G.; Ahn, S.; Lee, T. W. Energy Level Alignment of Dipolar Interface Layer in Organic and Hybrid Perovskite Solar Cells. *J. Mater. Chem. C* **2018**, *6*, 2915–2924.
22. Choi, K.; Choi, H.; Min, J.; Kim, T.; Kim, D.; Son, S. Y.; Kim, G. W.; Choi, J.; Park, T. A Short Review on Interface Engineering of Perovskite Solar Cells: A Self-Assembled Monolayer and Its Roles. *Sol. RRL* **2019**, 1900251.
23. Li, B.; Chen, Y.; Liang, Z.; Gao, D.; Huang, W. Interfacial Engineering by Using Self-Assembled Monolayer in Mesoporous Perovskite Solar Cell. *RSC Adv.* **2015**, *5*, 94290.
24. Zuo, L.; Gu, Z.; Ye, T.; Fu, W.; Wu, G.; Li, H.; Chen, H. Enhanced Photovoltaic Performance of CH<sub>3</sub>NH<sub>3</sub>PbI<sub>3</sub> Perovskite Solar Cells Through Interfacial Engineering Using Self-Assembling Monolayer. *J. Am. Chem. Soc.* **2015**, *137*, 2674–2679.
25. Azmi, R.; Hadmojo, W. T.; Sinaga, S.; Lee, C. L.; Yoon, S. C.; Jung, I. H. Jang, S. Y. High-Efficiency Low-Temperature ZnO Based Perovskite Solar Cells Based on Highly Polar, Nonwetting Self-Assembled Molecular Layers. *Adv. Energy Mater.* **2017**, *7*, 1701683.
26. Wang, Q.; Chueh, C. C.; Zhao, T.; Cheng, J.; Eslamian, M.; Choy, W. C.; Jen, A. K. Y. Effects of Self-Assembled Monolayer Modification of Nickel Oxide Nanoparticles Layer on the Performance and Application of Inverted Perovskite Solar Cells. *ChemSusChem* **2017**, *10*, 3794–3803.
27. Will, J.; Hou, Y.; Scheiner, S.; Pinkert, U.; Hermes, I. M.; Weber, S. A.; Hirsch, A.; Halik, M.; Brabec, C.; Unruh, T. Evidence of Tailoring the Interfacial Chemical Composition in Normal Structure Hybrid Organohalide Perovskites by A Self-Assembled Monolayer. *ACS Appl. Mater. Interfaces* **2018**, *10*, 5511–5518.
28. Yalcin, E.; Can, M.; Rodriguez-Seco, C.; Aktas, E.; Pudi, R.; Cambarau, W.; Demic, S.; Palomares, E. Semiconductor Self-Assembled Monolayers as Selective Contacts for Efficient PiN Perovskite Solar Cells. *Energy Environ. Sci.* **2019**, *12*, 230–237.
29. Gu, Z.; Zuo, L.; Larsen-Olsen, T. T.; Ye, T.; Wu, G.; Krebs, F. C.; Chen, H. Interfacial Engineering of Self-Assembled Monolayer Modified Semi-Roll-to-Roll Planar Heterojunction Perovskite Solar Cells on Flexible Substrates. *J. Mater. Chem. A* **2015**, *3*, 24254–24260.
30. Cao, J.; Yin, J.; Yuan, S.; Zhao, Y.; Li, J.; Zheng, N. Thiols as Interfacial Modifiers to Enhance the Performance and Stability of Perovskite Solar Cells. *Nanoscale* **2015**, *7*, 9443.
31. Lu, J.; Lin, X.; Jiao, X.; Gengenbach, T.; Scully, A. D.; Jiang, L.; Tan, B.; Sun, J.; Li, B.; Pai, N.; Bach, U. Interfacial Benzenethiol Modification Facilitates Charge Transfer and Improves Stability of cm-Sized Metal Halide Perovskite Solar Cells with up to 20% Efficiency. *Energy Environ. Sci.* **2018**, *11*, 1880–1889.
32. Wang, Q.; Dong, Q.; Li, T.; Gruverman, A.; Huang, J. Thin Insulating Tunneling Contacts for Efficient and Water-Resistant Perovskite Solar Cells. *Adv. Mater.* **2016**, *28*, 6734.
33. Zhang, J.; Hu, Z.; Huang, L.; Yue, G.; Liu, J.; Lu, X.; Hu, Z.; Shang, M.; Han, L.; Zhu, Y. Bifunctional Alkyl Chain Barriers for Efficient Perovskite Solar Cells. *Chem. Commun.* **2015**, *51*, 7047.

- 33.a Zhu, T.; Su, J.; Alvarez, J.; Lefèvre, G.; Labat, F.; Ciofini, I.; Pauporté, T. Response Enhancement of Self-Powered Visible-Blind UV Photodetectors by Nanostructured Heterointerface Engineering. *Adv. Funct. Mater.* **2019**, *29*, 1903981.
34. Nazeeruddin, M. K.; Braukyla, T.; Xia, R.; Daskeviciene, M.; Malinauskas, T.; Gruodis, A.; Jankauskas, V.; Roldán-Carmona, C.; Mombiona, C.; Getautis, V.; Fei, Z. Inexpensive Hole Transporting Materials Derived from Tröger's Base Afford Efficient and Stable Perovskite Solar Cells. *Angew. Chem. Int. Ed.* **2019**, *58*, 11266–11272.
35. Xia, R.; Fei, Z.; Drigo, N.; Bobbink, F. D.; Huang, Z.; Jasiūnas, R.; Franckevičius, M.; Gulbinas, V.; Mensi, M.; Fang, X.; Roldán-Carmona, C. Retarding Thermal Degradation in Hybrid Perovskites by Ionic Liquid Additives. *Adv. Funct. Mater.* **2019**, *29*, 1902021.
36. Guérin, V. M.; Elias, J.; Nguyen, T. T.; Philippe, L.; Pauporté, T. Ordered Networks of ZnO-Nanowire Hierarchical Urchin-Like Structures for Improved Dye-Sensitized Solar Cells. *Phys. Chem. Chem. Phys.* **2012**, *14*, 12948–12955.
37. Magne, C.; Dufour, F.; Labat, F.; Lancel, G.; Durupthy, O.; Cassaignon, S.; Pauporté, T. Effects of TiO<sub>2</sub> Nanoparticle Polymorphism on Dye-Sensitized Solar Cell Photovoltaic Properties. *J. Photochem. Photobiol. A* **2012**, *232*, 22–31.
38. Huang, Y.; Li, L.; Liu, Z.; Jiao, H.; He, Y.; Wang, X.; Zhu, R.; Wang, D.; Sun, J.; Chen, Q.; Zhou, H. the Intrinsic Properties of FA<sub>(1-x)</sub>MA<sub>x</sub>PbI<sub>3</sub> Perovskite Single Crystals. *J. Mater. Chem. A* **2017**, *5*, 8537.
39. Zuo, L.; Chen, Q.; De Marco, N.; Hsieh, Y. T.; Chen, H.; Sun, P.; Chang, S. Y.; Zhao, H.; Dong, S.; Yang, Y. Tailoring the Interfacial Chemical Interaction for High-Efficiency Perovskite Solar Cells. *NanoLett.* **2017**, *17*, 269–275.
40. Olthof, S. Research Update: The electronic structure of hybrid perovskite layers and their energetic alignment in devices. *APL Mater.* *4*, 091502 (2016).
41. Endres, J. et al. Valence and conduction band densities of states of metal halide perovskites: a combined experimental–theoretical study. *J. Phys. Chem. Lett.* *7*, 2722–2729 (2016).
42. Ulfa, M.; Wang, P.; Zhang, J.; Liu, J.; de Marcillac, W. D.; Coolen, L.; Peralta, S.; Pauporté, T. Charge Injection and Electrical Response in Low-Temperature SnO<sub>2</sub>-Based Efficient Perovskite Solar Cells. *ACS Appl. Mater. Interfaces* **2018**, *10*, 35118–35128.
43. Tumen-Ulzii, G. et al. Detrimental Effect of Unreacted PbI<sub>2</sub> on the Long-Term Stability of Perovskite Solar Cells. *Adv. Mater.* *32*, 1905035 (2020).
44. Zhuang, J. et al. Interfacial Passivation for Perovskite Solar Cells: The Effects of the Functional Group in Phenethylammonium Iodide. *ACS Energy Lett.* **4**, 2913–2921 (2019).
45. Bahers, T. Le; Pauporté, T.; Lainé, P.P.; Labat, F.; Adamo, C.; Ciofini, I.; *J. Phys. Chem. Lett.* **2013**, *4*, 1044.
46. Bahers, T. Le; Labat, F.; Pauporté, T.; Lainé, P.P.; Ciofini, I.; *J. Am. Chem. Soc.* **2011**, *133*, 8005.
47. Szemjonov, A.; Pauporté, T.; Ithurria, S.; Pedetti, S.; Lequeux, N.; Dubertret, B.; Ciofini, I.; Labat, F.; *J. Mater. Chem. A* **2016**, *4*, 13081.
48. Su, J.; Zhu, T.; Pauporté, T.; Ciofini, I.; Labat, F. Improving the heterointerface in hybrid organic–inorganic perovskite solar cells by surface engineering: Insights from periodic hybrid density functional theory calculations. *J. Comput. Chem.* **2020**, doi:10.1002/jcc.26215.
49. Turren-Cruz, S.-H.; Hagfeldt, A.; Saliba, M. Methylammonium-free, high-performance, and stable perovskite solar cells on a planar architecture. *Science* **2018**, *362*, 449–453.

## Chapter IV. High Efficiency and Stable Solar Cells Based on MACl Mediated Grown $\text{FA}_{0.94}\text{MA}_{0.06}\text{PbI}_3$ Perovskite and 2D Materials Post-Treatment

The record efficiency of PSCs increased continuously from 23.7% to 25.5% during the past 2 years. The fast development towards higher efficiency is unprecedented. Nowadays, complex chemistry and precursor solution compositions are developed to stabilize hybrid perovskite films and boost the efficiency of PSCs. The obtained perovskite layers have various compositions, which caused distinguished photovoltaic properties. The perovskites with wider bandgaps can theoretically produce devices with higher photovoltages while their photocurrents inevitably reach a bottleneck. For instance, Cs8FAMA and MAPI in the last chapter can reach a photovoltage of 1.1 eV but their photocurrents will be hardly more than 25 mA/cm<sup>2</sup>. Alpha-phase  $\text{FAPbI}_3$  ( $\alpha\text{-FAPbI}_3$ ) has a theoretical bandgap of 1.48 eV, which is quite suitable for single junction solar cells. However, pure  $\alpha\text{-FAPbI}_3$  is very easy to transform to yellow delta-phase  $\text{FAPbI}_3$  ( $\delta\text{-FAPbI}_3$ ), which has a yellow aspect and poor photovoltaic properties. In this chapter, perovskite  $\text{FAPbI}_3$  is developed through adding methylammonium chloride (MACl) in the precursor solution. A post-treatment to perovskite layer is conducted for the further improvement of the photovoltaic properties.

### IV.1 Introduction

Formamidinium lead tri-iodide ( $\text{FAPbI}_3$ ) perovskite is one of the best suited OIHP materials for PSC from the point of view of the bandgap for light harvesting of irradiation wavelengths ranging from the near-IR to the near-UV. This compound also allows the generation of a rather large photovoltage output.<sup>17,18</sup> However, due to the large size of the FA cation,  $\text{FAPbI}_3$  is stable at room temperature in its non-perovskite yellow  $\delta$ -phase which is poorly active in solar cells.<sup>20</sup> The stabilization of the photo-active black 3D perovskite  $\alpha$ -phase needs the incorporation of an extra monovalent cation such as cesium ( $\text{Cs}^+$ ), rubidium ( $\text{Rb}^+$ ), methylammonium ( $\text{MA}^+$ ).... or of their mixture. Another important observation is that the most efficient OIHPs contain methylammonium ( $\text{MA}^+$ ) as extra organic cation.<sup>21-26</sup> High efficiency and high stability require dense, well-covering, uniform, pin-hole free perovskite layers as well as high phase purity.  $\text{PbI}_2$  must be absent and the OIHP layer must be made of large crystal grains which go through the entire perovskite thin film.<sup>26a,26b</sup>

To increase the performances of PSCs, one must both optimize the OIHP layer and the interfaces with the selective contact layers.<sup>27</sup> Complex recipes have been developed for the preparation of high structural quality OIHP layers. Chloride anion additive is known, for a long time, to be beneficial to the formation of large crystal grains and has been used to a large extent in MAPbI<sub>3</sub> perovskite layer synthesis.<sup>28,29</sup> Only a few numbers of papers have employed chloride additives for the growth of mixed cation perovskite based on formamidinium and methylammonium.<sup>22,26,29-31</sup> MACl was used in several works in sequential processes upon the perovskite spin-coating.<sup>33-35</sup> It has been shown recently that MACl additive increases the solubility of GeI<sub>2</sub> and permits the doping of the mixed cation perovskite layer with Ge.<sup>36</sup> Mu et al. used MACl combined with FAI to force the introduction of Cl in perovskite and obtained mixed anion compounds.<sup>30</sup> Kim et al. showed that MACl employed in the perovskite precursor solution successfully induces an intermediate to the pure FAPbI<sub>3</sub>  $\alpha$ -phase without annealing.<sup>26</sup> However, the methylammonium content must be minimized to reduce the hydrophilicity of the material and its destabilization by degazing/degradation (in CH<sub>3</sub>I and NH<sub>3</sub>).<sup>18</sup>

For the interfaces, the perovskite/hole transporting layer (HTL) one is of utmost importance. The intercalation of an ad-hoc buffer layer enables the fast extraction of holes and their transfer to the HTL. 2-Phenylethylammonium iodide (PEAI) focused our attention since this compound has been employed for the passivation of the OIHP grain boundaries and surfaces in several works.<sup>37</sup> You et al. found that PEAi itself can effectively passivate the perovskite defects and therefore improve the efficiency of the devices.<sup>22</sup> PEAi can also form a (PEA)<sub>2</sub>PbI<sub>4</sub> 2D-perovskite compound after reaction with I and Pb sources.<sup>38</sup>

In this Chapter, we present PSCs which achieved very high-power conversion efficiencies by the engineering of the OIHP precursor solution and interfaces. We used non-stoichiometric precursor solutions in which methylammonium chloride additive acted as a mediator to the growth of dense layers made of large crystal grains. By this technique, a small amount of MA cation was incorporated in FAPbI<sub>3</sub>, at the best for the  $\alpha$ -phase stability. One of the interests of the presented recipe is that the solution has a rather low concentration of precursor. The technique is also reliable, robust and gives high efficiency with low result dispersion for a large range of additive concentration. The MACl best molar fraction is found at 48mol.%. At lower concentrations, the OIHP grain size was smaller and more grain boundaries were present. At higher concentrations,

more charge recombinations occurred which mitigated the device  $V_{oc}$ . We also show that the PEAI treatment without thermal annealing leads notably to the spontaneous formation of  $(PEA)_2PbI_4$  perovskite at the surface. It favors a fast transfer of the holes towards the HTL. A comprehensive investigation of the systems by impedance spectroscopy shows that recombinations are markedly reduced by using this buffer layer. Overall, the prepared cells were almost hysteresis free. Their power conversion efficiency was greater than 22.1%. The power output of the produced devices was remarkably stable. These PSCs were proved resistant to electrical stresses, to light irradiation and to moisture. The next main text of this chapter is organized into 4 parts. Section IV.2 is dedicated to the preparation of FAMAPbI<sub>3</sub> film and the post-treatment methods. The other procedures are the same as those described in Chapter II.2 and Chapter III.2. Section IV.3 details the effect of the MACl concentration on the films. IV.4 presents the effect of the PEAI treatment on perovskite films and devices. Section IV.5 gives the characterizations of PSC devices.

## **IV.2 Experimental**

The preparation of substrates, compact TiO<sub>2</sub> layer and mesoporous TiO<sub>2</sub> layer are as detailed in Chapter II.2.1. The HTM and Gold contacts are prepared as described in Chapter III.2.

### **IV.2.1 Preparation of FAMAPbI<sub>3</sub> films**

A mixed cation precursor solution with a 1.2M concentration was prepared by mixing 206 mg of formamidinium iodide (FAI, greatcell), 553 mg of PbI<sub>2</sub> (TCI), and 32.4 mg, 38.9 mg and 44.6 mg (40 mol.%, 48 mol.% and 55 mol.%, respectively) of methylammonium chloride (MACl, Alfa Aesar) in 800  $\mu$ L DMF and 200  $\mu$ L DMSO. The solutions were stirred for a minimum of 2 h at room temperature in a N<sub>2</sub> glovebox. 45  $\mu$ L of this solution was placed on top of the substrates. A two-step spin-coating program was employed: first spinning at 1000 rpm for 10 s and then at 6000 rpm for 30 s. 100  $\mu$ L of chlorobenzene was dripped 20 s after the starting of the spinning routine. The films were then annealed at 153 °C for 13 min. These films and corresponding solar cells are noted MC40, MC48 and MC55.

### **IV.2.2 Post-treatment method**

The PEAI post-deposition treatment consisted of dropping 60  $\mu$ L of a 10 mM 2-Phenylethylamine Hydroiodide (PEAI) solution (2.49 mg in 1 mL of isopropanol) onto the cold perovskite film. A one-step spin-coating program was employed: 2000 rpm/s acceleration, 3000rpm for 20s.

### IV.2.3 Characterization methods

The layers characterizations by XRD, SEM, UV-vis absorbance, steady-state PL and TRPL are described in Chapter III.2. The film elemental compositions were determined from EDX spectra, measured with a Quantax system from Bruker operated at 15 kV. NMR ( $^1\text{H}$  and  $^{13}\text{C}$ ) spectra were recorded on a Bruker Avance 500 MHz Neo spectrometer. Chemical shifts are given in ppm using the residual DMSO solvent signal as the internal reference. Perovskite layers deposited on a sprayed *c*-TiO<sub>2</sub> layer were dissolved in DMSO-d<sub>6</sub> solvent (99.96 %D, H<sub>2</sub>O < 0.01%, Euriso-top) and the NMR spectra of solutions were measured.

**Methylamonium iodide:**  $^1\text{H}$  NMR (DMSO, 500 MHz):  $\delta = 2.37$  (s, CH<sub>3</sub>).  $^{13}\text{C}$  NMR (DMSO, 125 MHz):  $\delta = 24.7$ .

**Formamidinium iodide:**  $^1\text{H}$  NMR (DMSO, 500 MHz):  $\delta = 7.84$  (s, CH).  $^{13}\text{C}$  NMR (DMSO, 125 MHz):  $\delta = 157.4$ .

***N*-methyl formamidinium iodide:**  $^1\text{H}$  NMR (DMSO, 500 MHz):  $\delta = 7.94$  (s, CH), 2.81 (s, CH<sub>3</sub>).  $^{13}\text{C}$  NMR (DMSO, 125 MHz):  $\delta = 155.4$  (CH), 28.0 (CH<sub>3</sub>).

***N, N'*-dimethyl formamidinium iodide:**  $^1\text{H}$  NMR (DMSO, 500 MHz):  $\delta = 2.96$  (s, CH<sub>3</sub>NH<sub>2</sub>CH=NCH<sub>3</sub>), 2.81 (s, CH<sub>3</sub>NH<sub>2</sub>CH=NCH<sub>3</sub>).

The measurements of *J-V* curves, maximum power point tracking and EQE spectra of the devices were described in Chapter III.2. The electrical impedance spectra were measured at room temperature, between 1 MHz and 100 mHz, with a 20 mV AC signal, using a PGSTAT 12 apparatus from Autolab. All the measured cells had the same contact geometries. The impedance spectra were measured at room temperature, over a large applied voltage ( $V_{\text{appl}}$ ) range, under a  $\sim 0.9$  sun light power density supplied by a halogen Schott lamp. The cell illuminated area was delimited by a 0.16 cm<sup>2</sup> mask. The spectra were analyzed using the Z-view software from National Instrument.

### IV.2.4 Fitting of the time resolved PL curves

The decay curves were first normalized and fitted by the tri-exponential function:

$$PL(t) = y_0 + Ae^{-t/\tau_{fast}} + Be^{-t/\tau_{int}} + Ce^{-t/\tau_{slow}} \quad (\text{IV.1})$$

The relative contribution (*rc*) of each of these three terms to the static PL has been evaluated by integrating the relative exponential traces.

The integral is equal to the product of the amplitude and the decay time. Therefore, fast,

intermediate and slow component relative contributions are defined as:

$$r_{C_{fast}}(\%) = A\tau_{fast} / (A\tau_{fast} + B\tau_{int} + C\tau_{slow}) \quad (IV.1a)$$

$$r_{C_{int}}(\%) = B\tau_{int} / (A\tau_{fast} + B\tau_{int} + C\tau_{slow}) \quad (IV.1b)$$

$$r_{C_{slow}}(\%) = C\tau_{slow} / (A\tau_{fast} + B\tau_{int} + C\tau_{slow}) \quad (IV.1c)$$

#### IV.2.5 Analysis of the impedance spectra

The experimental impedance spectra have been fitted using simplified electrical equivalent circuits (EEC) derived from the following general one.

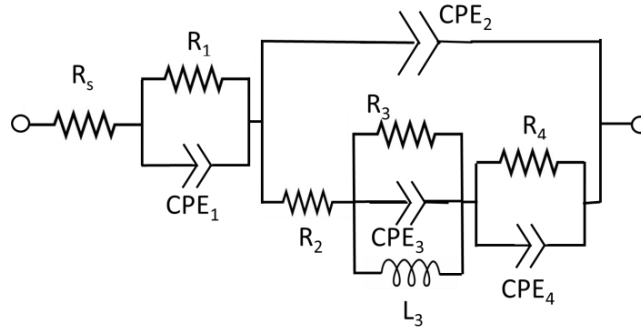


**Figure IV. 1** General equivalent electrical circuit for the analysis of PSC impedance spectra. Defined in Pauporté et al.<sup>40</sup>

where R elements are resistors,  $L_3$  is an inductor and CPE are capacitive elements called constant phase elements. In this chapter, we have used simplified EEC<sub>s</sub> deduced from the general one. For instance, the  $L_3$  element, for PSCs under light irradiation, is characteristic of an inductive loop that we have never observed in our cells and that Pauporté et al. have shown characteristic of poorly working PSCs.<sup>16</sup>  $R_1$  and  $CPE_1$  are present in the case of poorly efficient selective contacts, especially undoped HTLS.<sup>40</sup>

The various R and CPE electrical elements have been determined from the fits for each applied voltage. The resistances can also be read on the spectra from the intersection of the arc of the circle with the x-axis as shown in the Figure:

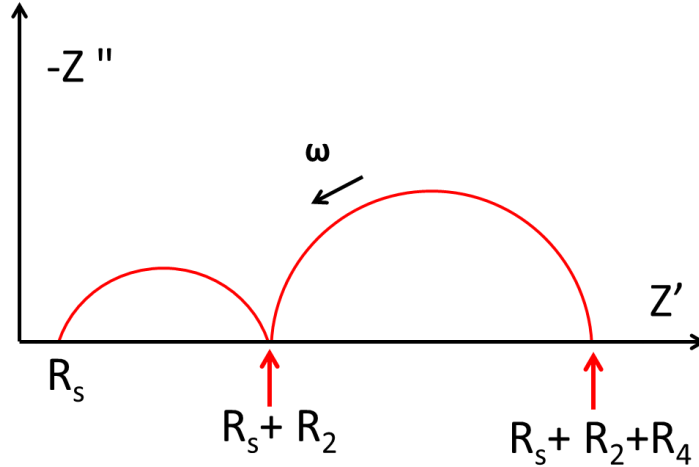


**Figure IV. 2** Resistance reading on a Nyquist plot with two relaxations.

We have used CPE elements and not capacitances for the fits because the arcs of a circle are not a semi-circle but is flattened. We have then determined the  $C_2$  and  $C_4$  capacitances from the  $CPE_2$  and  $CPE_4$  parameters. The CPE impedance is defined by  $Z_{CPE} = \frac{1}{T(i\omega)^p}$  where  $\omega$  is the angular frequency related to the frequency by  $f = \frac{\omega}{2\pi}$ ,  $i$  is the square root of  $-1$ , and  $p$  is lower than 1. The exact formulae to get  $C_2$  and  $C_4$  for one or two relaxations are:

$$C_2 = \left[ \left( \frac{1}{R_s} + \frac{1}{R_2} \right)^{p_2-1} T_2 \right]^{1/p_2}$$

$$C_4 = \left[ \left( \frac{1}{R_s + R_2} + \frac{1}{R_4} \right)^{p_4-1} T_4 \right]^{1/p_4}$$

The  $C_2$ ,  $1/C_4$ ,  $R_2$  and  $R_4$  have been then plotted for the various cells as a function of the applied voltage in Figures IV.21, 23 and 25.

### IV.3 Characterizations of Perovskite Films

#### IV.3.1 SEM

We have investigated the preparation of OIHP layers from precursor solutions containing a stoichiometric amount of FAI and  $PbI_2$  and various fractions of methylammonium chloride additive, namely 40 mol.%, 48 mol.% and 55 mol.% of MAcl. The related layers are noted MC40,

MC48 and MC55, respectively. The precursor concentration was rather low at 1.2M while a large amount of MAcl was employed. The latter was crucial to govern the growth of the perovskite layers. The morphology of perovskite films with three different MAcl additive molar fractions (40 mol%, 48 mol% and 55 mol%, the films and cells are denoted MC40, MC48 and MC55, respectively) are presented in Figure IV.3a-c. The layers were uniform, compact, contained no pinholes and were made of remarkably large size perovskite grains. The various MAcl fractions employed gave a similar morphology. The statistical analysis of the grain size, done with the Image J software, is presented in Figure IV.3d. The average values were 604 nm, 775 nm and 982 nm for MC40, MC48 and MC55 films, respectively. The grain size gradually increased with the MAcl molar fraction used. The results of our study are quite different from those reported by Kim et al.<sup>26</sup> who used much more concentrated perovskite precursor solutions and found a maximum at 40 mol% of MAcl. The cross-sectional views of the layer in the solar cells confirmed the large size of the grains (Figure IV.3e). Remarkably, they also showed monolithic large grains, which their thickness was the perovskite layer thickness. Therefore, we conclude that, in the solar cells, each crystal grain is contacted by the electron transporting layers on one side (TiO<sub>2</sub>) and by the hole transporting layer on the other side (Spiro-OMeTAD) (Figure IV.3e).

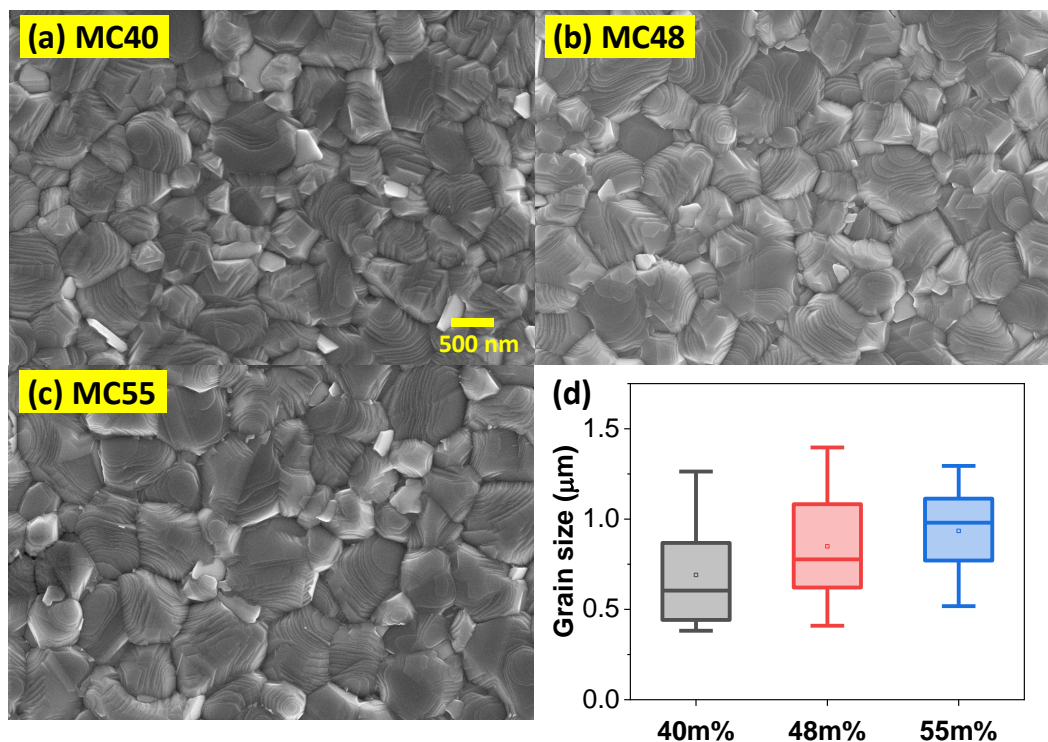


**Figure IV.3** (a-c) Typical SEM top-view images of the perovskite layers surface: (a) MC40, (b) MC48, (c) MC55, (d) Statistical analysis of the effect of MAcl additive fraction on the grain size. (continued)

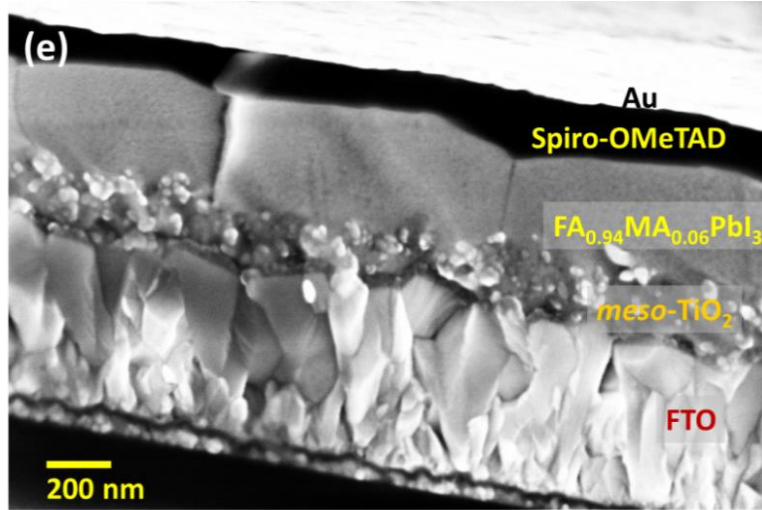


**Figure IV. 3** (e) Cross-sectional SEM view of a MC48 perovskite layer in a PSC.

### IV.3.2 XRD

X-ray diffraction (XRD) was employed to check the phase and the purity of the produced compounds. The patterns are shown in Figure IV.4a and 4b correspond to the ultra-pure cubic  $\alpha$ -phase perovskite. The reflection peaks have been indexed accordingly. The fact that the strongest diffraction peaks belong to the ( $h00$ ) family of plane shows a strong texturation of the layer with a preferential orientation along the [100] crystallographic direction. No parasitic phase due to unreacted  $\text{PbI}_2$  was found. Moreover, there was no  $\text{FAPbI}_3$  perovskite  $\delta$ -phase present. The prepared layers were of remarkable phase purity. The XRD peak intensity increased with the MA/Cl additive fraction due to the grain enlargement with increasing the chloride concentration and quite thicker layers obtained for MC55 as shown below. Another interesting information extracted from the XRD patterns is that the peak positions are almost unchanged with the fraction of MA/Cl and that these parameters are very close to those of the  $\alpha$ - $\text{FAPbI}_3$  compound (Figure IV.4c). On the other hand, the XRD peaks of the  $\text{FA}_{1-x}\text{MA}_x\text{PbI}_3$  are significantly shifted compared to the  $\text{MAPbI}_3$  compound (Figure IV.4). Replacing FA by MA is known to produce a shrinkage of the crystal lattice and a reduction of the lattice parameter.<sup>26</sup> It suggests that, in the present case,  $x$  in  $\text{FA}_{1-x}\text{MA}_x\text{PbI}_3$  does not change significantly with the initial amount of MA/Cl in the precursor solution.

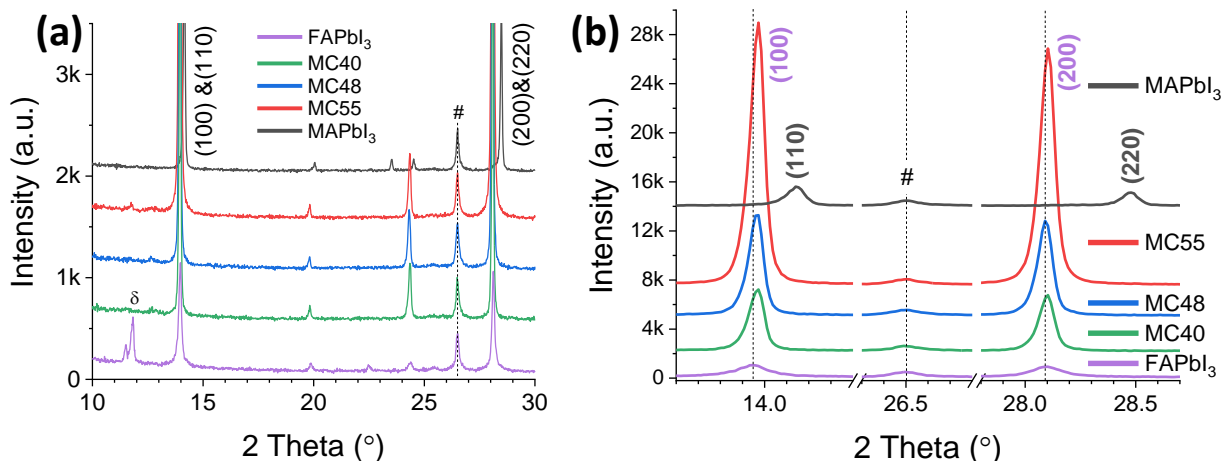


**Figure IV. 4** XRD patterns of the perovskite layers. (a) FAPbI<sub>3</sub>, MC40, MC48, MC55 and MAPbI<sub>3</sub>; (b) is a zoom view of (a). # symbol marks a FTO substrate peak;  $\delta$  is delta-phase FAPI.

### IV.3.3 Perovskite compositions

#### IV.3.3.1 EDX

Energy dispersive x-ray spectrometry (EDX) allowed us to determine the layers I/Pb atomic ratio. The main results are gathered in Table IV.1 and other details are included in Annex-IV, page 166-177. The average values were 2.96, 3.15 and 3.06 for MC40, MC48 and MC55 samples, respectively. The theoretical ratio is 3 and the presence of PbI<sub>2</sub> would reduce this parameter. Within the uncertainty of the technique, the compounds were close to the stoichiometry without a significant amount of PbI<sub>2</sub> present. Also, EDX analysis showed us that the final layers, after annealing, were almost free of chloride element, regardless of the MAI fraction in the precursor solution. In hybrid 3D perovskite, the integration of iodide is thermodynamically much more favorable than that of chloride. In the precursor solution employed, I is added in a stoichiometric ratio and no Cl need to be integrated into the structure for its stabilization.<sup>22</sup> Therefore, almost all chloride ions provided were eliminated during the annealing step at a rather high temperature (153°C). For the charge compensation, cations must be eliminated with Cl<sup>-</sup>. A small amount of MA is integrated into the structure to stabilize the black  $\alpha$ -phase of perovskite while the organic cation excess is also eliminated upon the layer annealing.

**Table IV.1** EDX measurement for perovskite layer. (Atoms ratio)

PVK	Measurement	Pb (M-series)	I (L-series)	Cl (K-series)	I/Pb at. %
MAPI	1	5.58	16.68		2.98
	2	5.14	16.53		3.21
FAMA 40%	1	10.03	30.06	0.23	3.0
	2	9.52	30.34	0.18	2.91
FAMA 55%	1	10.51	32.61	0.27	3.10
	2	10.42	31.48	0.35	3.02
FAMA 48%	1	8.92	28.12	0.04	3.15
	2	9.03	28.61	0.17	3.17
	3	9.12	28.7	0.04	3.15
FAMA 48%_ PEAI	1	8.75	26.74	0.1	3.06
	2	8.14	25.56	0.1	3.14
	3	7.98	25.81	0	3.23

#### IV.3.3.2 NMR

To accurately determine how much MA is incorporated in the films and then to answer the critical issue of the actual organic cation composition of the prepared layers, an NMR study was conducted. The organic components incorporated in the perovskite layers were identified and titrated by liquid NMR measurements. To the best of our knowledge, in the works investigating perovskite composition by NMR, the analyzed compounds are precipitated powders,<sup>15,41-43</sup> crystals,<sup>15,42,44</sup> or films produced by drop-casting<sup>41</sup> or by spin-coating combined with vacuum evaporation.<sup>45</sup> By using them, one can get a quite large amount of material that permits solid-state- and/or liquid-NMR investigations. However, the drawback of these techniques is that they deviate from the ones employed for very high-efficiency PSC fabrication. In our case, we have investigated the films actually employed in the perovskite solar cells. They have been directly dissolved in DMSO-d<sub>6</sub> solvent (see the Section IV.2.3). The liquid-state <sup>1</sup>H-NMR and <sup>13</sup>C-NMR spectra of the MC48 layer and their correlation Figure are disclosed in Annex-IV (Figure A.IV.1a-e).

In the NMR spectra, we observed more peaks than expected from our MAI and FAI reference spectra (Figure IV.5a and 5b, respectively). The <sup>1</sup>H NMR spectrum showed a singlet at  $\delta$  7.84 ppm, who was correlated with the <sup>13</sup>C NMR peak at  $\delta$  157.4 ppm, and a singlet at  $\delta$  2.37 ppm who was correlated with the <sup>13</sup>C NMR peak at  $\delta$  24.7 ppm.<sup>41</sup> Based on our reference spectra (Figure IV.5a and 5b), these peaks were attributed to the CH of the formamidinium and the CH<sub>3</sub> of methylammonium, respectively.<sup>43</sup> We also observed a small <sup>1</sup>H peak at  $\delta$  7.94 ppm, correlated with the <sup>13</sup>C peak at  $\delta$  155.4 ppm and a <sup>1</sup>H peak at  $\delta$  2.81 ppm correlated with a <sup>13</sup>C peak at 28.0

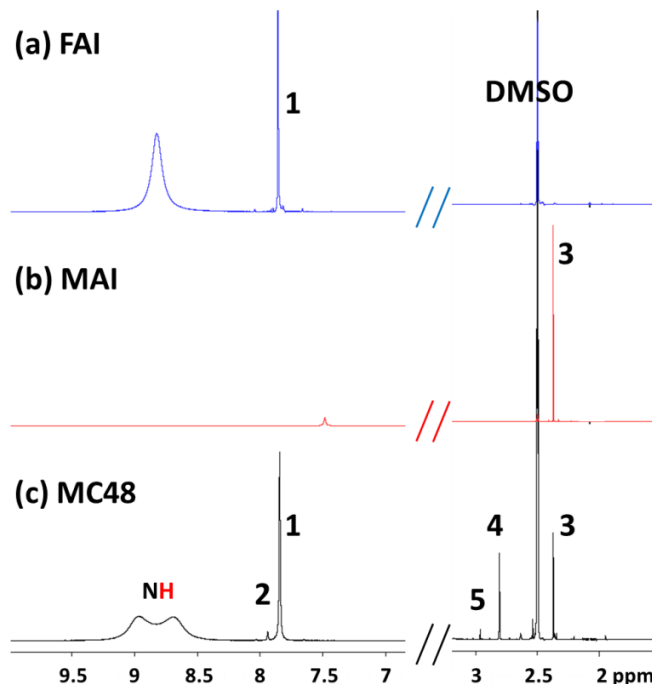
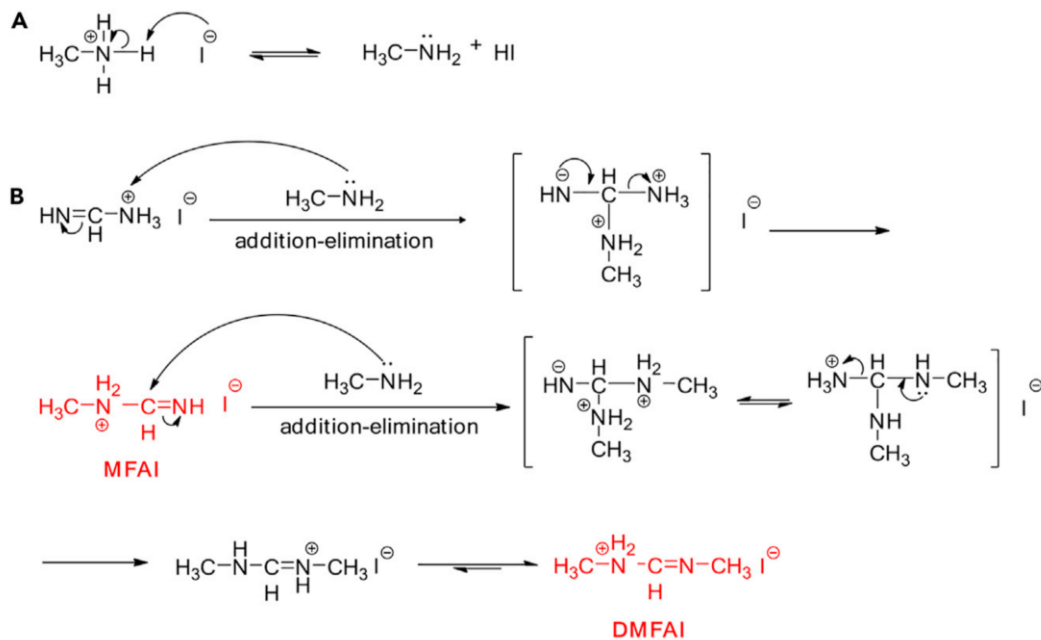


**Figure IV. 5**  $^1\text{H}$ -NMR spectra of (a) MAI, (b) FAI and (c) MC48 layer with indexation. 1.  $\text{NH}=\text{CHNH}_3\text{I}$ ; 2.  $\text{CH}_3\text{NH}_2\text{CH}=\text{NHI}$ ; 3.  $\text{CH}_3\text{NH}_3\text{I}$ ; 4.  $\text{CH}_3\text{NH}_2\text{CH}=\text{NHI} + \text{CH}_3\text{N}=\text{CHNH}_2\text{CH}_3\text{I}$ ; 5.  $\text{CH}_3\text{N}=\text{CHNH}_2\text{CH}_3\text{I}$  (*N,N'*-dimethyl FAI).

ppm. A very small  $^1\text{H}$  peak was also detected at  $\delta$  2.96 ppm. These three features are absent from the FAI and MAI NMR spectra (Figure IV.5) and it suggests that they result from reaction products between FA and MA. MAI in solution undergoes deprotonation and methylamine and HI is formed in equilibrium with MAI (Reaction A in Scheme IV.1).

Upon the writing of this chapter, an article by Wang et al.<sup>43</sup> appeared which shows that the nucleophilic N atom in MA can react with the electrophilic imine group of FAI (See Scheme 1). It results in the formation of *N*-methyl FAI ( $\text{CH}_3\text{-NH}_2\text{-CH}=\text{NH}\cdot\text{HI}$ ) by condensation. The  $^1\text{H}$ -NMR peak at  $\delta$  7.96 ppm fits with the CH in *N*-methyl FAI and that at  $\delta$  2.81 ppm with the  $\text{CH}_3$  in this compound. The very small peak at  $\delta$  2.96 ppm could be assigned to  $\text{CH}_3$  in *N,N'*-dimethyl FAI ( $\text{CH}_3\text{-NH}_2\text{-CH}=\text{N-CH}_3\cdot\text{HI}$ ) formed by a second condensation reaction. We conclude that, following the layer dissolution in DMSO solution, *N*-methyl FAI is formed by the partial reaction between FAI and MA and that this compound is detected on the NMR spectra. A small amount of *N,N'*-dimethyl FAI is also formed. The spectra were similar for the three investigated layers, MC40, MC48 and MC55 (Figure A.IV.1a-e). The  $^1\text{H}$ -NMR peaks of formamidinium, methylammonium, *N*-methyl FAI and *N,N'*-dimethyl FAI were present with about the same ratio.



**Scheme IV.1** Possible reaction mechanism in the MOC perovskite solutions.<sup>43</sup>

(A) The deprotonation of MAI

(B) The addition-elimination reactions between MA and FAI in MOC perovskite solution

The main advantage of the liquid-state  $^1\text{H-NMR}$  technique is its high sensitivity. As a consequence, by integrating the spectrum peaks, we have been able to titrate precisely the relative amount of FA and MA incorporated in the perovskite layers used in the solar cells. The DMSO peak was retained as an internal reference. The integration value of MAI peak was corrected of the  $^{13}\text{C}$  satellite of DMSO. The  $\text{CH}_3$  of *N*-methyl FAI peak was corrected of the second *N*-methyl FAI peak which appeared at the same chemical shift. We have also supposed that the two  $\text{CH}_3$  of *N,N'*-dimethyl FAI had the same integration. The results gave  $x$  values in  $\text{FA}_{1-x}\text{MA}_x\text{PbI}_3$  equal to 0.063, 0.063 and 0.060 for MC40, MC48 and MC55, respectively. The remarkable point is that this parameter is almost irrespective of the MAI mol% present in the precursor solution which was varied to a large extent. We can conclude that this value corresponds to the optimum one for which the prepared  $\alpha$ -phase perovskite is the most stable. The excess of MAI is removed upon the annealing at  $153^\circ\text{C}$  by decomposition/sublimation.<sup>18</sup> For the charge and chemistry balance, a few amounts of FA must be also eliminated likely by similar processes. The incorporation of a small amount of MA for the stabilization of FAPI is in agreement with a recent computational investigation which calculated in  $\text{FA}_{1-x}\text{MA}_x\text{PbI}_3$  a minimum of the Gibbs free energy for  $x < 0.2$ , while this parameter continuously increases at higher  $x$ .<sup>46</sup>

We conclude that the chemical composition of the prepared perovskite film is  $\text{FA}_{0.94}\text{MA}_{0.06}\text{PbI}_3$  whatever the MACl additive fraction employed.

#### IV.3.4 UV-vis absorbance

The optical properties of the layers were characterized by measuring their absorbance curves. The spectra of  $\text{FA}_{0.94}\text{MA}_{0.06}\text{PbI}_3$  layers are compared to those of  $\text{MAPbI}_3$  and  $\text{FAPbI}_3$  in Figure IV.6a. They exhibit an absorption edge at about 820 nm which is due to the direct optical transition in the metalorganic perovskite material. We observed that  $\text{FAPbI}_3$ , MC40 and MC48 layers had about the same absorbance in the 550 nm-800 nm range while the MC55 was more absorbent. It can be related to larger grains and likely to a higher thickness. The Tauc plots are presented in Figure IV.6b. From the linear fit intersection with the energy axis, an optical bandgap energy ( $E_g$ ) of 1.537 eV was found whatever the precursor solution composition. It confirms the same stoichiometry for the three perovskite layers prepared. This value was very close to the  $E_g$  value of  $\text{FAPbI}_3$ , 1.528 eV, and far apart that of  $\text{MAPbI}_3$  (1.597 eV). These results are in line with the NMR study (Section IV.3.3.2). This low  $E_g$  is a positive property for the light harvesting in the near-IR.

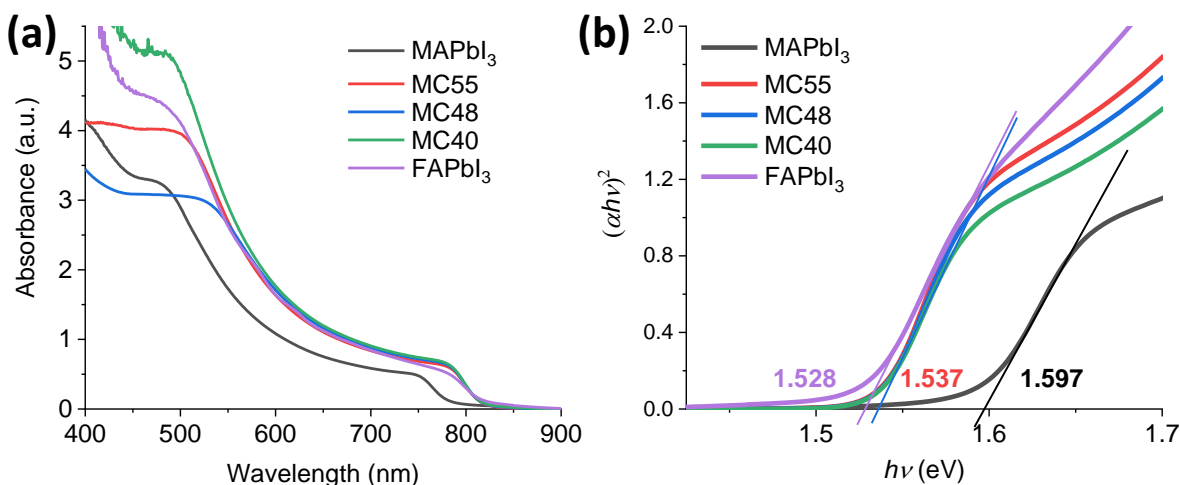


**Figure IV. 6** (a) UV-vis absorbance and (b) Absorbance Tauc plots.

#### IV.3.5 Steady-state PL and TRPL curves

We have also measured the photoluminescence (PL) spectra of the layers. The maximum emission wavelength was the same for the three prepared mixed cation perovskites and their normalized spectra overlapped (Figure IV.7a). In the same figure, we have reported the  $\text{FAPbI}_3$  and  $\text{MAPbI}_3$  spectra.  $\text{FA}_{0.94}\text{MA}_{0.06}\text{PbI}_3$  layers had a maximum emission wavelength (811 nm) very close to that

of FAPbI<sub>3</sub> (814 nm). Using the approximation of a linear variation and the emission maximum of MAPbI<sub>3</sub>, we found  $x$  at  $7.5 \pm 2.5\%$ , which is in agreement with the NMR study.

Time resolved photoluminescence (TRPL) decay curves are presented in Figure IV.7b. They were analyzed using three exponential decay components as detailed in Section IV.2.4. The fitting parameters are gathered in Table IV.2. The slower component had the best relative contribution ( $rc$ ) to PL (Table IV.2) and was assigned to the bimolecular recombination of the photogenerated charges in the bulk perovskite. The slow decay time is related to the structural quality of the perovskite layers. The longer is this parameter, the higher is the structural quality of the material. From the fits, we measured  $\tau_{\text{slow}}$  at 99 ns, 102 ns and 100 ns for MC40, MC48 and MC55 samples, respectively. The prepared materials exhibited a high emission lifetime.

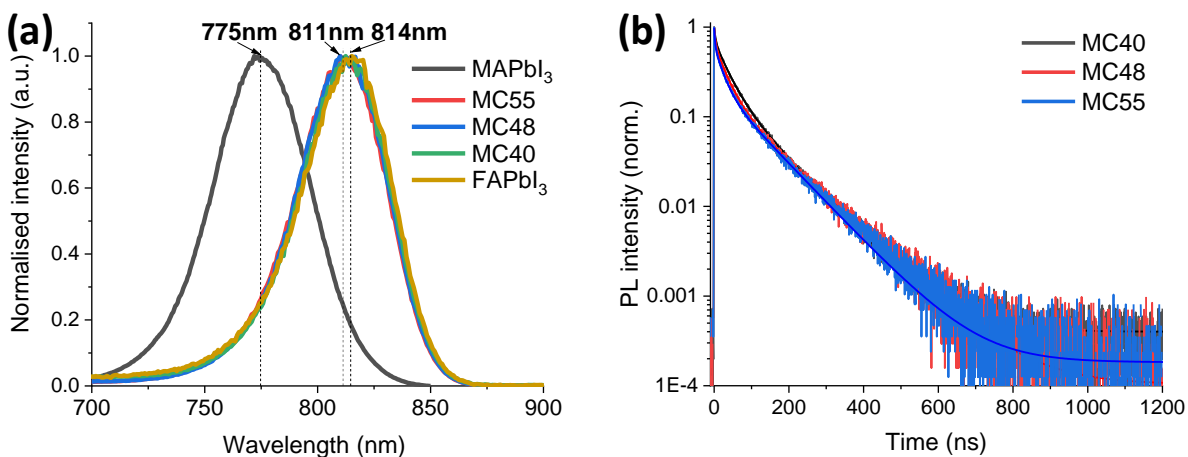


**Figure IV. 7** (a) normalized photoluminescence spectra of  $\alpha$ -FAPbI<sub>3</sub>, MAPbI<sub>3</sub>, MC40, MC48 and MC55 layers. (b) TRPL of MC40, MC48 and MC55.

**Table IV.2** TRPL curve parameters determined by a triple-exponential decay function fitting.

	$A_1$	$\tau_{\text{fast}}$	$rc_{\text{fast}}^a$	$A_2$	$\tau_{\text{int}}$	$rc_{\text{int}}^a$	$A_3$	$\tau_{\text{slow}}$	$rc_{\text{slow}}^a$
MC40	0.247	3.29	0.020	0.470	32.9	0.379	0.247	99.2	0.601
MC48	0.323	2.81	0.027	0.457	28.0	0.380	0.196	102	0.593
MC55	0.360	2.10	0.024	0.400	22.3	0.279	0.223	99.8	0.697
MC48-PEAI	0.87	0.47	0.037	0.102	24.10	0.222	0.070	117	0.740

<sup>a</sup> $rc_{xx}$ : fast, intermediate and slow relative contributions.

## IV.4 Characterizations of PEAI Treated Perovskite Film

In this section, we focus on the MC48 perovskite films which led to the best performances.

### IV.3.1 SEM

This treatment was done after the preparation of the perovskite layer and before the HTL deposition. The solution of PEAI was spin-coated on top of the perovskite surface and, importantly, no post-deposition processing was implemented (especially no thermal annealing). On SEM views (Figure IV.8), the PEAI treatment produced a change in the aspect of the perovskite grains surface, especially of the flat parts of the crystals suggesting a surface modification by a chemical reaction. We also observed the presence of an extra-phase with a haze aspect that accumulated in the deepest zones where most grain (multi-)boundaries are present.

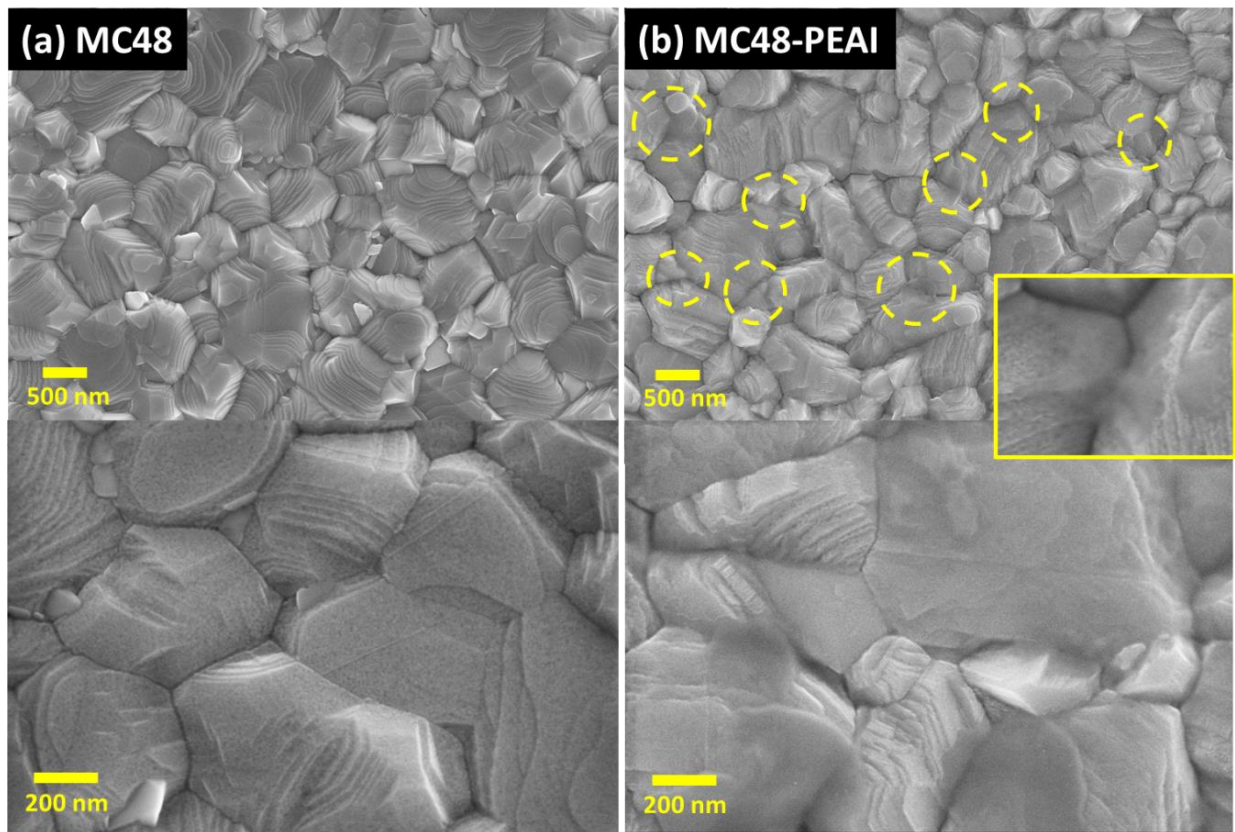


**Figure IV. 8** SEM images of the MC48 perovskite layers surface, (a) before and (b) after the PEAI deposition. Yellow circled are regions where PEAI accumulates. The inset is a zoom view.

### IV.3.2 XRD

On the layer XRD patterns (Figure IV.9a), measured immediately after the PEAI treatment, an

extra-peak appeared at an angle of  $5.35^\circ$ . It is assigned to the (001) plane of the 2D perovskite with  $(\text{PEA})_2\text{PbI}_4$  composition.<sup>22</sup> No PEAI diffraction peak at  $4.7^\circ$  was observed (Figure IV.9b) therefore no crystallized PEAI was present on the surface.<sup>22</sup> The formation of the  $(\text{PEA})_2\text{PbI}_4$  nanolayer could be favored by the fact that IPA, the solvent employed is known to dissolve MA and FA.<sup>47</sup>

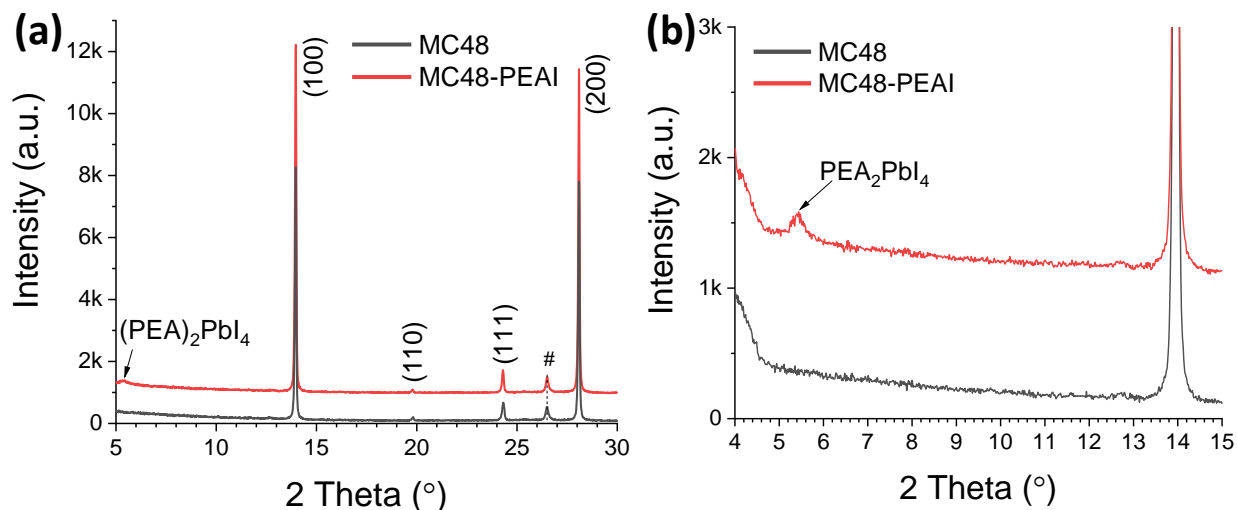


**Figure IV. 9** (a) XRD patterns of MC48 and MC48-PEAI layers.

### IV.3.3 Absorbance

The presence of 2D perovskite was further confirmed on the absorbance spectra (Figure IV.10). An absorption edge at 520 nm which corresponds to the near band edge transition in  $(\text{PEA})_2\text{PbI}_4$  is revealed in the differential curve (Figure IV.10)

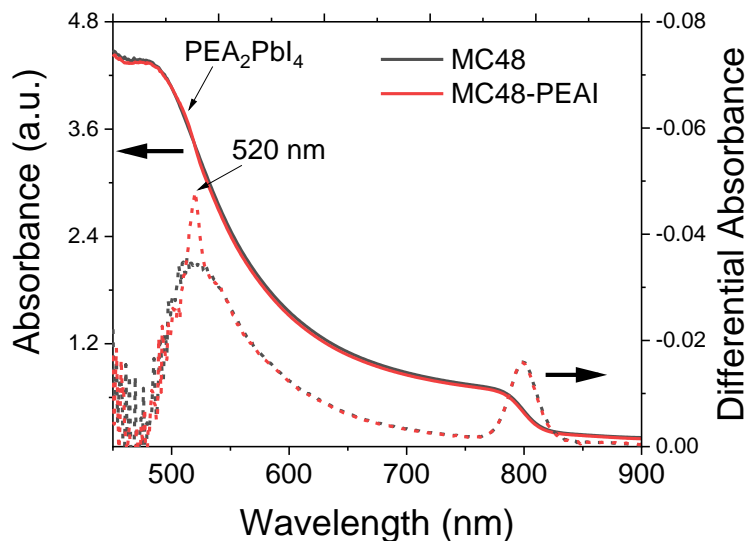


**Figure IV. 10** Absorbance (left) and differential absorbance (right) curves of MC48 and MC48-PEAI layers.

### IV.3.4 Steady-state PL and TRPL

On the TRPL curves (Figure IV.11a), we observed a more intense initial emission for the PEAI treated sample. We also observed a faster initial decay of PL for the treated sample. The latter trend was confirmed on the normalized TRPL curves shown in Figure IV.12. Table IV.2 in Section

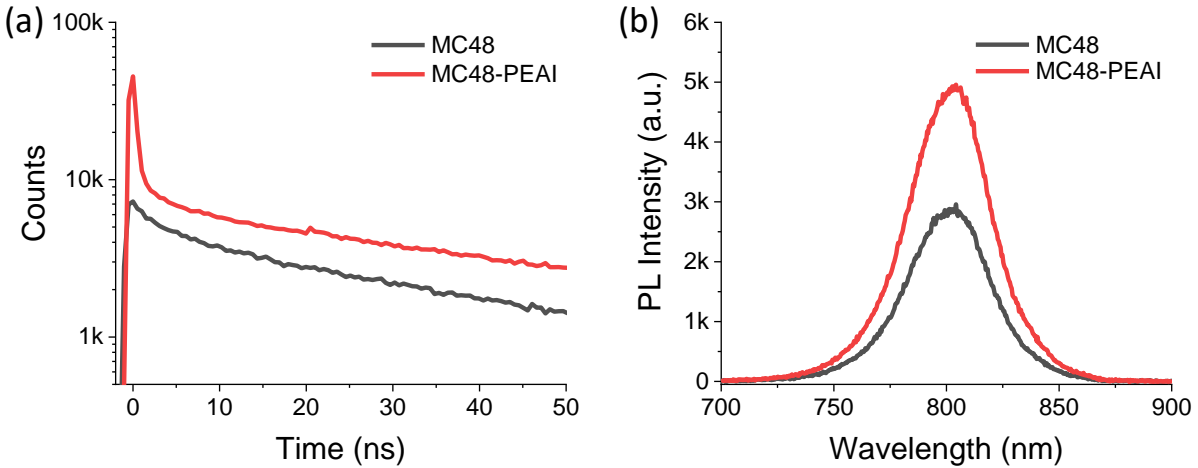


**Figure IV. 11** (a) Effect of the PEAI treatment on the TRPL at a short time and (b) on steady-state PL spectrum.

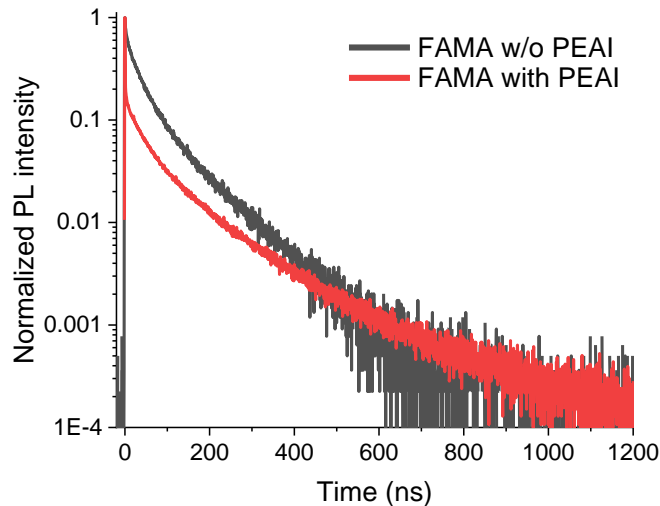


**Figure IV. 12** Effect of the PEAI treatment on the normalized TRPL spectra.

IV.3.5 reports that the fast component was much faster for MC48-PEAI (0.47 ns) compared to the untreated MC48 sample (2.8 ns). We explain the initial stronger emission by the fact that the treatment passivates defects near the layer front surface (the irradiated one) and enhance the radiative recombination. However, the faster decay is analyzed as an efficient quenching of the

radiative recombination by the fast transfer of the hole toward the PEAI-based surface layer. Table IV.2 also compares  $\tau_{\text{slow}}$  of the pristine and treated samples. We measured 100-110 ns for the former sample and about 117 ns after the surface treatment. It can be analyzed by an improvement of the crystal quality at the perovskite layer near surface and defect passivation. The effect of the treatment on the steady-state PL spectra of the layers is shown in Figure IV.11b. After the treatment, the PL intensity was stronger due to the stronger emission observed in Figure IV.11a.

In summary, a  $(\text{PEA})_2\text{PbI}_4$  nanolayer was formed spontaneously on the  $\text{FA}_{0.94}\text{MA}_{0.06}\text{PbI}_3$  film surface, without any post-PEAI-deposition thermal annealing treatment. It is assigned to the higher thermodynamic stability of the 2D compound compared to the 3D one.<sup>38</sup> PEAI could remain present in an amorphous state in the deep zones of the perovskite layer. However, this deposit looks poorly attached to the perovskite surface, which is possible to be partly removed upon the Spiro-OMeTAD deposition by spin-coating.

## IV.5 Characterizations of PSCs

### IV.5.1 *J-V* curves

The solar cell structure is presented in Figure IV.13a. The  $\text{FA}_{0.94}\text{MA}_{0.06}\text{PbI}_3$  perovskite layer was contacted by selective contacts:  $\text{TiO}_2$  on one side and a spin-coated Spiro-OMeTAD layer on the other side. A gold contact was evaporated on the back of the cell. On the SEM cross-sectional view in Figure IV.3e, the *mp*- $\text{TiO}_2$  layer thickness was measured at about 130 nm. This layer was soaked with  $\text{FA}_{0.94}\text{MA}_{0.06}\text{PbI}_3$  material. The thickness of the capping pure perovskite layer was about 390 nm. The top Spiro-OMeTAD layer was about 150 nm thick. The performances of the PSCs were evaluated by measuring their *J-V* curves under one sun AM 1.5G illumination. The curves of cells prepared with various conditions and with and without PEAI are displayed in Figure IV.13b. Table IV.3 gathers the *J-V* curve parameters of the devices. The hysteresis between the reverse and the forward scans were small due to the low defect density in the perovskite material and the large grains. We have reproducibly observed that the use of the PEAI treatment increased cell efficiency. The beneficial effect was found on both the short circuit current,  $J_{SC}$ , and on the open-circuit voltage,  $V_{OC}$ , parameters. The higher  $J_{SC}$  with the treatment agrees with the TRPL results detailed in Section IV.3.4. The PEAI-passivation surface nanolayer dramatically reduces the non-radiative recombination by passivating the perovskite surface defects. Moreover, the hole charges are

quickly separated by transfer to the nanolayer and it reduces the charge recombination in the perovskite. This fast charge transfer is beneficial for the solar cell current generation. The  $V_{OC}$  is increased significantly with the PEAI treatment due to surface defects passivation and reduction of the interfacial charge recombinations. This point will be confirmed in Section IV.5.5 by the electrical impedance spectroscopy (EIS) study. On average, the post-deposition treatment boosted the PCE by about 10%. Another beneficial effect of the treatment is the reduction of the hysteresis as shown in Table IV.3.

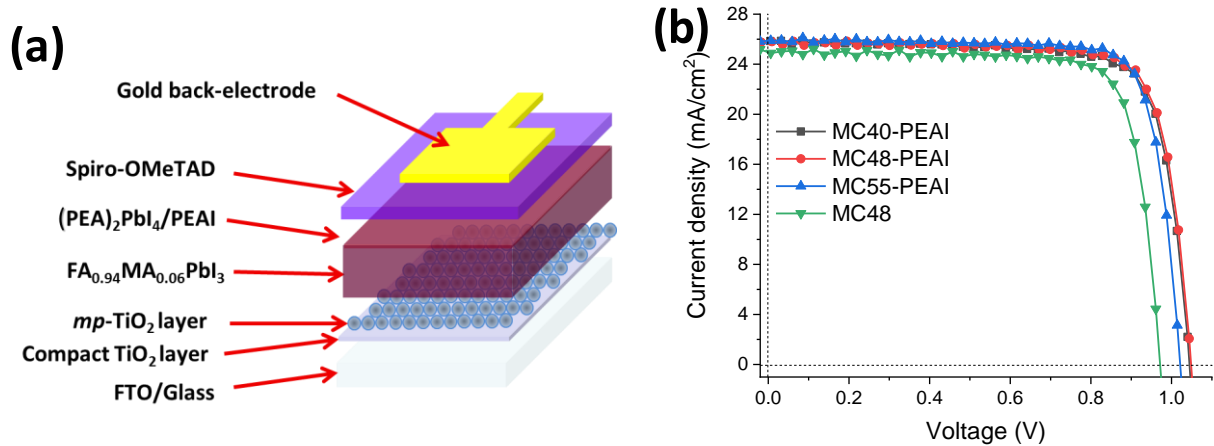


**Figure IV. 13** (a) Device structure employed in the chapter with the  $c$ -TiO<sub>2</sub>/ $mp$ -TiO<sub>2</sub> bottom contact and PEAI-based buffer layer. (b) Typical  $J$ - $V$  curves of PSCs prepared with various MACl% with and without the PEAI surface post-deposition treatment.

**Table IV.3** Photovoltaic  $J$ - $V$  parameters of best FA<sub>0.94</sub>MA<sub>0.06</sub>PbI<sub>3</sub> cells prepared with various MACl%, with and without the PEAI surface post-deposition treatment (under AM 1.5G conditions, 100 mW.cm<sup>-2</sup>).

Cell	Scan direction	$V_{oc}$ /V	$J_{sc}$ mA/cm <sup>2</sup>	$FF$ /%	$PCE$ /%	$HI^a$ /%
MC40-PEAI	Reverse	1.043	25.79	78.21	21.05	3.3
	Forward	1.035	25.82	76.11	20.34	
MC48-PEAI	Reverse	1.060	25.94	80.62	22.18	3.7
	Forward	1.052	25.93	78.26	21.35	
MC55-PEAI	Reverse	1.024	25.90	80.75	21.41	4.5
	Forward	1.014	25.93	77.77	20.44	
MC48	Reverse	1.002	24.73	82.3	20.37	4.5
	Forward	0.994	24.47	80.02	19.46	

<sup>a</sup> HI: Hysteresis index defined as  $[PCE(\%)_{rev} - PCE(\%)_{for}] / PCE(\%)_{rev}$

MACl additive molar fraction has also a significant effect on the cell electrical properties. In Table IV.3,  $J_{SC}$  is the highest for MC48-PEAI and MC55-PEAI and the best  $V_{OC}$  is achieved by MC48-

PEAI. Overall, the best power output was reached for the MC48-PEAI devices. The improvement between MC40-PEAI and MC48-PEAI cells can be explained by larger grains and higher structural quality. The  $V_{OC}$  parameter depends on the recombination rate, especially on the recombinations at and near the perovskite/selective contact interfaces. The lower efficiency of the MC55-PEAI cells compared to the MC48-PEAI ones is the effect of lower  $FF$  and  $V_{OC}$ . We will show in Section IV.5.5 that these components are related to the internal resistances of the devices which are themselves related to the charge recombinations. We can conclude that MC55-PEAI devices are not the best due to lower quality of the interfaces.

Overall, choosing MAI at 48mol.% appears as the best choice for the best performances. The observation made for the best cells was confirmed by the statistics of the  $J$ - $V$  curve parameter distribution (Figure IV.14). The large grains, high crystallinity and high absorbance over a large visible-near infrared range of the produced perovskite layers gave rise to high performances. We have also noted that the PEA treatment especially boosts the  $J_{SC}$  and the  $V_{OC}$  of the cells by improving the perovskite/HTM interface, reducing the surface defects and favoring the fast charge transfer towards the selective contact. It also reduces the PCE dispersion. Table IV.3 shows that the best PCE was measured at 22.18%. This cell had a hysteresis index of only 3.7%. Importantly, this device was tracked at its maximum power output. It reached a stabilized efficiency of 22.08% after about 80s. This value is very close to the measurement on the reverse scan (Figure IV.15a).

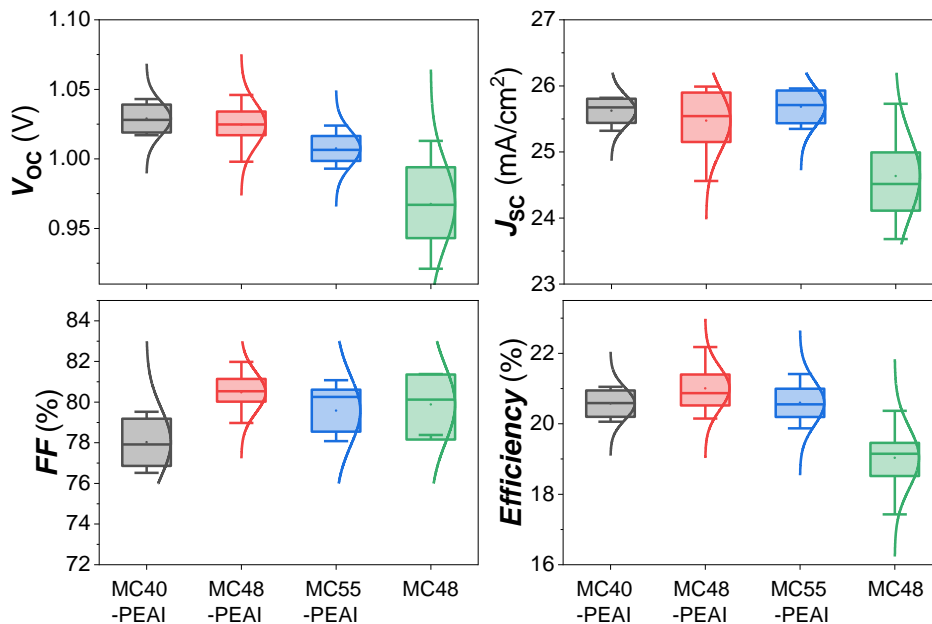


**Figure IV. 14** Statistical analysis of the PSC performances and  $J$ - $V$  curve parameters.

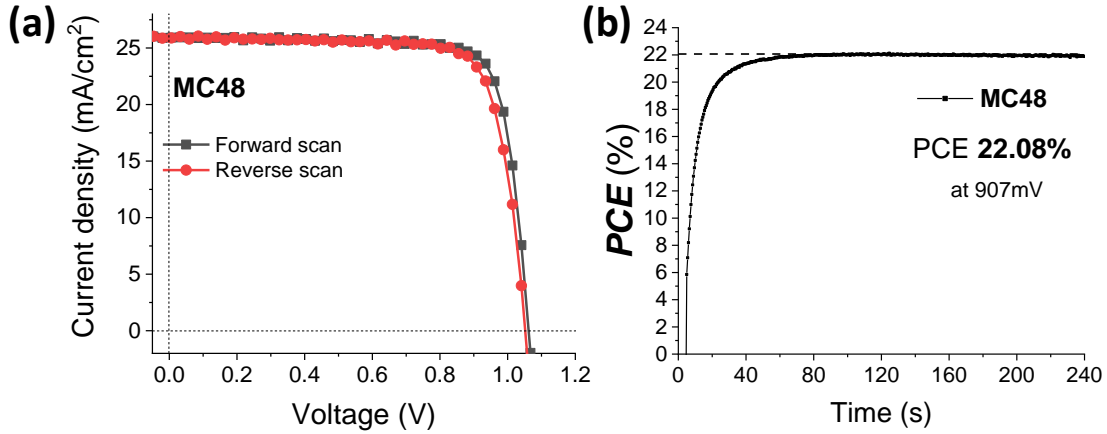


**Figure IV. 15** (a) J-V curves of forward and reverse scan the best cell. (b) Tracking curve and steady-state PCE of the best cell.

#### IV.5.2 EQE curves

The ability of the cells to collect light over a large wavelength range and to generate charge with high efficiency was confirmed by measuring their EQE spectra. The effect of PEAI on the EQE spectrum is presented in Figure IV.16a. EQE was enhanced with the treatment over the whole visible range. It confirms that the treatment favors the charge generation and charge extraction at the perovskite/HTL interface. Figure IV.16b shows the effect of the MACl molar fraction on the EQE spectra. This parameter mainly influenced the red/near-infrared part of the spectrum, so the radiations with the deeper absorption depth. Increasing MACl% favors the charge generation and extraction in this wavelength range. By integrating the curves,  $J_{SC}$  as high as  $25.4 \text{ mA}\cdot\text{cm}^{-2}$  were calculated, in good agreement with the  $J$ - $V$  curve data ( $24.9 \text{ mA}\cdot\text{cm}^{-2}$ ,  $25 \text{ mA}\cdot\text{cm}^{-2}$  and  $25.4 \text{ mA}\cdot\text{cm}^{-2}$  for MC40-PEAI, MC48-PEAI and MC55-PEAI in Figure IV.16b, respectively). And the  $J_{SC}$  values are much higher than those of MAPI and Cs8FAMA cells.

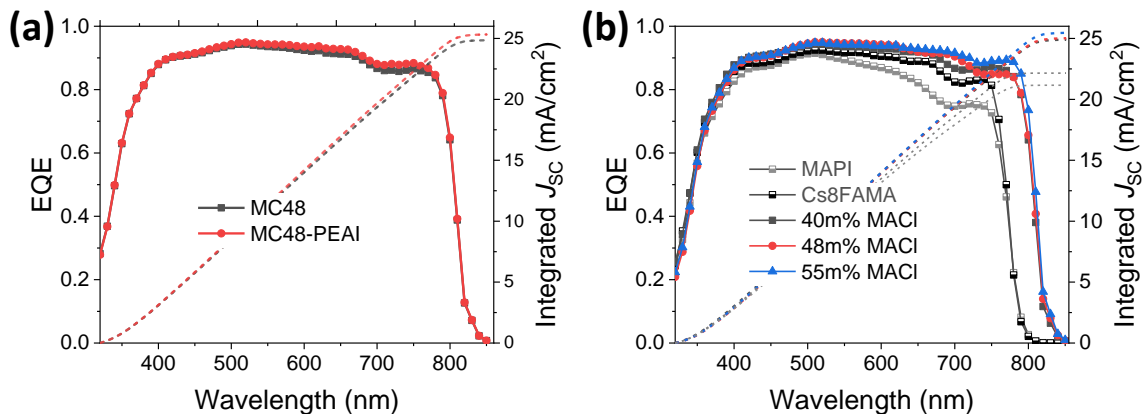


**Figure IV. 16** (a) EQE curves with and without PEAI treatment. (b) EQE curves of various perovskites.

### IV.5.3 Ideality factor

We also performed the analysis of the  $V_{OC}$  as a function of the white light illumination power density. The curves with and without PEAI treatment are presented in Figure IV.17. For the investigated cells, the  $V_{OC}$  was superior to all the light intensity range after the PEAI treatment. The  $V_{OC}$  scaled logarithmically with the light power density ( $I$ ) and followed the relationship:

$$qV_{OC} = E_g + n_{ID}kT \ln(I/I_0) \quad (1)$$

with  $q$  the elementary charge,  $k$  the Boltzmann constant,  $T$  the absolute temperature and  $n_{ID}$  the ideality factor. The latter parameter is related to the main recombination phenomena occurring at the  $V_{OC}$ .<sup>39</sup> We found  $1.40 < n_{ID} < 1.50$  for matured cells (cells stored several days in  $N_2$  atmosphere) (Figure IV.17). A smaller slope was found after the PEAI treatment (Figure IV.17a). It is known that deviation of  $n_{ID}$  from 1 reflects the occurrence of defect-assisted recombination in the PSCs.  $n_{ID}$  values suggest that, at the open circuit, a Shockley-Read-Hall (SRH) recombination mechanism through perovskite intragap defects is the dominating recombination process at the  $V_{OC}$ . We have observed that, like in the case of  $MAPbI_3$  perovskite,<sup>39</sup>  $n_{ID}$  increases with aging and SRH recombination increases with this parameter.

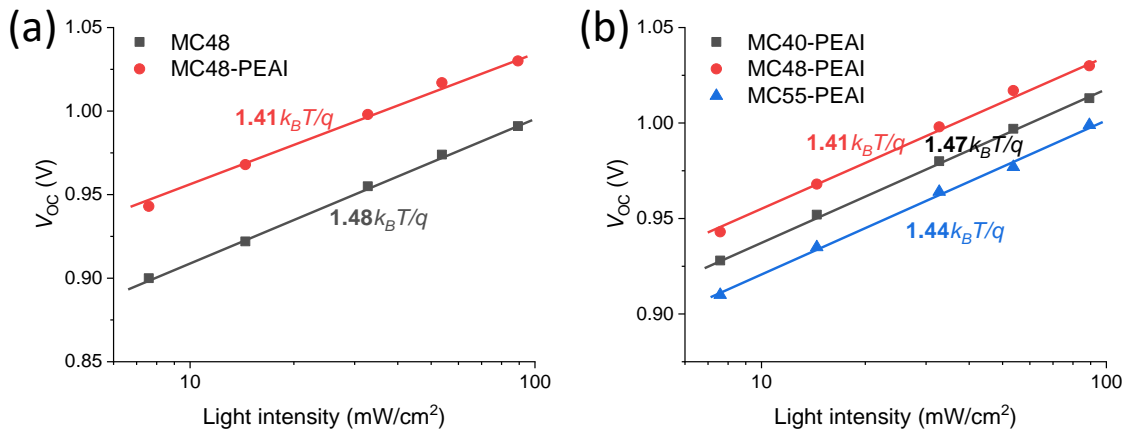


**Figure IV. 17**  $V_{OC}$  versus light intensity (power density) curves. (a) MC48 cells with and without PEAI treatment. (b) Effect of MACl%. The curve slopes provide the ideality factor,  $n_{ID}$ , values (numbers in bold).

### IV.5.4 Stability

#### IV.5.4.1 Stability under 1 sun shining

We have also noted that the prepared cells had good stability. The photostability was followed for 5 hours under a continuous one sun AM 1.5G illumination at 45% of relative humidity (RH).

Figure IV.18 compares unencapsulated MC48, MC48-PEAI, Cs8FAMA and MAPI cells. We do not compare with a FAPI cell since the FAPI cells prepared had a very low efficiency (PCE < 10%) and were not stable when stored under ambient conditions (PCE < 10%). The power output was highly stable and unchanged in the case of the FA<sub>0.94</sub>MA<sub>0.06</sub>PbI<sub>3</sub> cell of the present study. On the other hand, the MAPI and Cs8FAMA cell power output continuously decreased during the same test. After the 300 min-long tracking tests, the *J-V* curves of these cells were measured again as shown in Figure IV.19. Large hysteresis were observed for MAPI and Cs8FAMA cells, while the hysteresis remained low for the MC48 cells with and without PEA treatment.

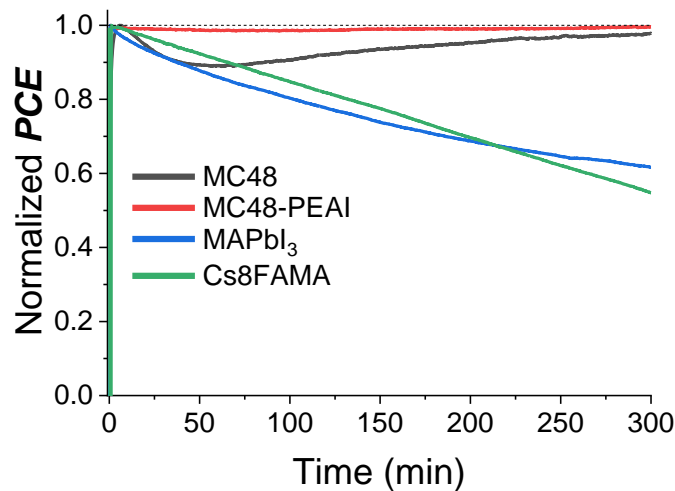


**Figure IV. 18** (a) Tracking of MAPI, Cs8FAMA, MC48 and MC48-PEAI solar cell normalized power outputs under continuous one sun AM1.5G illumination (unencapsulated devices, 45% RH).

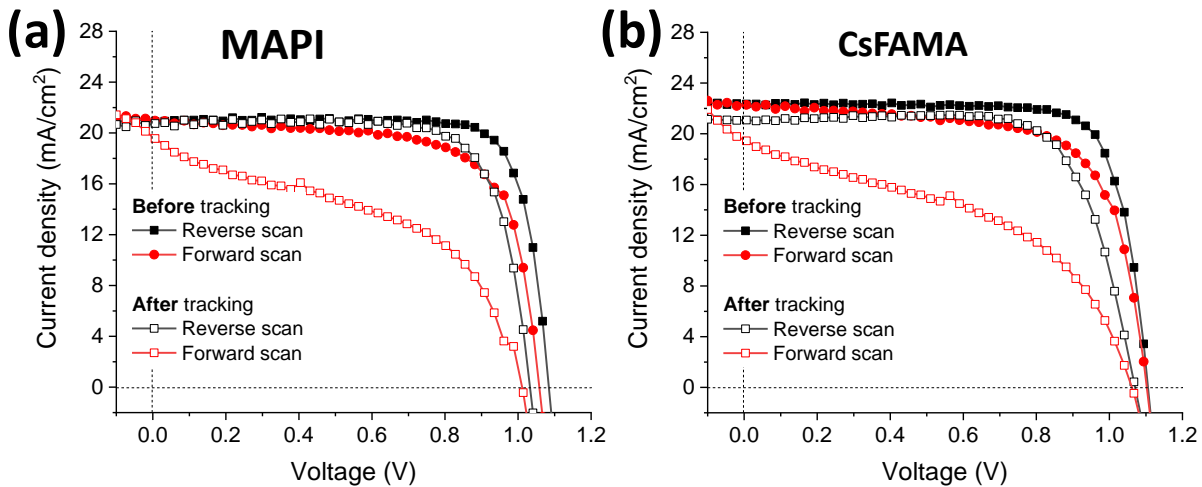


**Figure IV.19ab** *J-V* curves before and after tracking (a) MAPI, (b) Cs8FAMA. (continued)

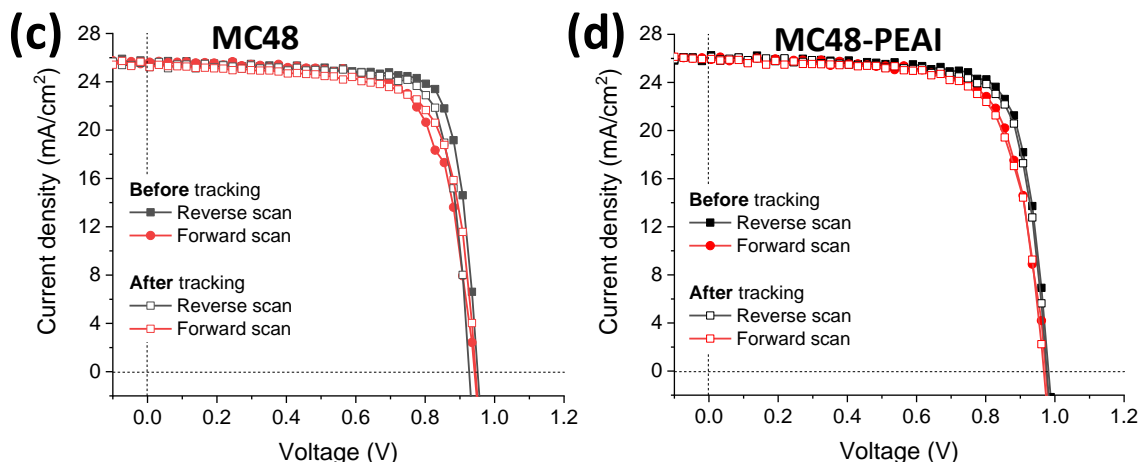


**Figure IV. 19** *J-V* curves before and after tracking: (c) MC48 and (d) MC48-PEAI (a,b,c measuring immediately after tracking; d, measuring after one night).

#### IV.5.4.2 Stability in high humidity environment

The stability against moisture was tested by storing the unencapsulated cells in a chamber with 90% RH and ambient light conditions (Figure IV.20). The MC48 power output was stable for 20h. The MAPI cell lost 60 % of its initial PCE within only 20h. The variations of the *J-V* curve parameters are shown in Figure IV.21. This high stability is explained by the optimal incorporation of a minimum of MA for the  $\alpha$ -phase stabilization and large grains. However, a sharp decrease of the efficiency was observed for MC48 sample after 24 h. We speculate that the  $\text{MA}^+$  ions were leaving the perovskite structure gradually within the 24 h. When there are few  $\text{MA}^+$  in the structure, the  $\delta$ -phase  $\text{FAPbI}_3$  will be formed very fast. (See Chapter V)

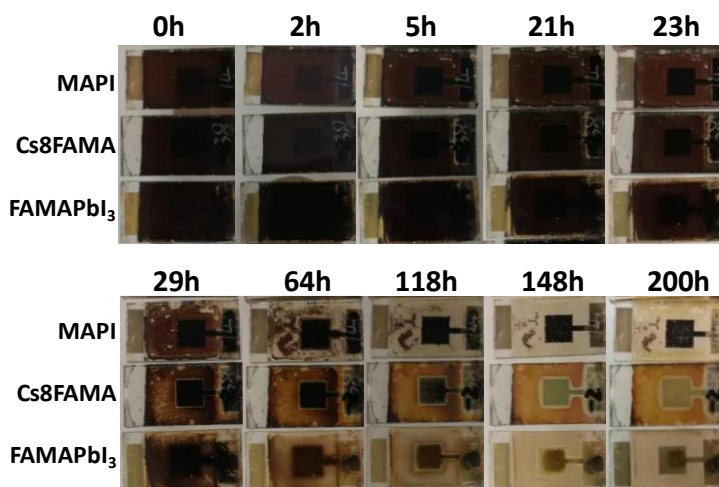


**Figure IV. 20** Images of MAPI, Cs8FAMA and FAMAPbI<sub>3</sub> (MC48) aging for 200h in a chamber with a 90% RH and ambient light condition.

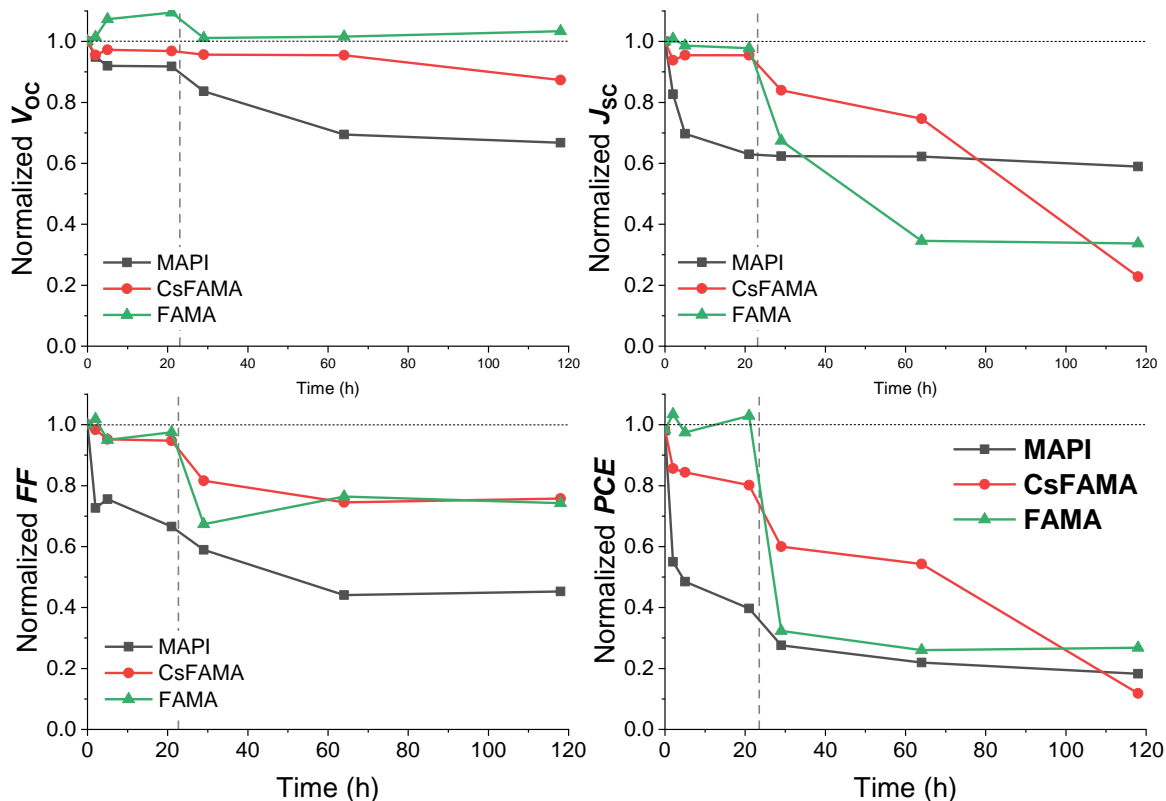


**Figure IV. 21**  $J$ - $V$  curve parameters followed upon the unencapsulated PSCs aging at 90 %RH.

#### IV.5.4.3 Evolution of ideality factors over time

The variation of ideality factors over time were measured for PSCs with and without PEAI treatment (Figure IV.22). For the samples without PEAI treatment, the ideality factors decrease with time, regardless of the devices efficiencies. However, the ideality factors increase with time for the samples with PEAI treatment, which can be ascribed to the increased charge recombination in the interface. With time goes, more and more stable 2D  $\text{PEA}_2\text{PbI}_4$  perovskite phases can be formed gradually. Small amounts of 2D  $\text{PEA}_2\text{PbI}_4$  favors the charge injection while they are not beneficial for passivating the defects in the perovskite and reducing the charge recombination.<sup>22</sup> In addition, the more 2D perovskite formed, the more 3D perovskite destroyed, under the premise we obtained a  $\text{PbI}_2$ -free perovskite. The increased ideality factors indicate the increased interfacial recombination in the PEAI-treated cells.

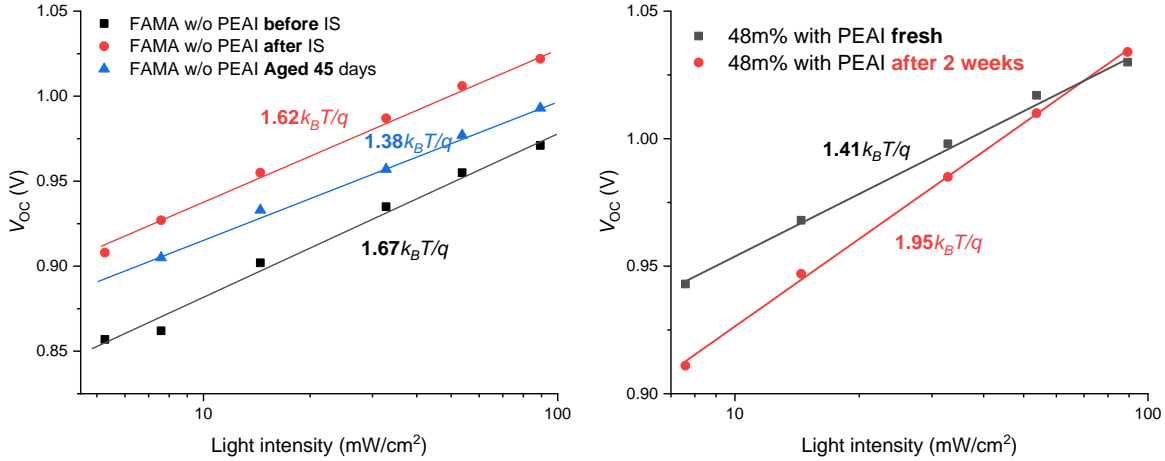


**Figure IV. 22** Ideality factor variations with time for samples with and without PEAI treatment.

#### IV.5.5 Impedance spectroscopy study of PSCs

To gain further insight into the cell functioning, the effects of the buffer layer and cell maturation, PSCs have been studied by EIS. EIS is an *in operando* characterization technique which is safe for the device and provides fruitful information on its functioning.<sup>40,48-51</sup> The PSCs have been investigated under white light irradiation with a power density of about 0.9 sun. The applied voltage ( $V_{\text{appl}}$ ) was varied between the short circuit and the open-circuit conditions.

The Nyquist plots (imaginary part versus the real part of the complex impedance) of fresh cells polarized at various applied voltages and which underwent or not the PEAI treatment are presented in Figure IV.23a. Their shape was rather unusual for solar cells under illumination.<sup>17</sup> At high frequencies ( $f > 50-150$  Hz), an arc of circle was found. After an inductive transition at an intermediate frequency, a special behavior was found that cannot be fitted with a classical electrical circuit. The imaginary part of the impedance was negative but was pinned, remaining almost constant over a large frequency range, while at the same time, the real part of the spectra decreased as the frequency decreased. We have focused our analysis on the arc-of-circle at  $f > 50-150$  Hz. It was fitted with the equivalent electrical circuit (EEC) shown in Figure IV.23b. We have employed in this Chapter the same notation as in the general EEC for the analysis of PSC impedance spectra presented in our previous work<sup>40</sup> and shown in Figure IV.1.  $R_s$  is a series resistance measured at high frequencies which is due to the contacts and wires. The flattened arc of circle was fitted by a constant phase element (CPE) in parallel with a resistance. The capacitances were extracted from the  $Z_{\text{CPE}}$  parameters using the approach described by Brug et al.<sup>16,17,40,50,51</sup> The formulae employed,

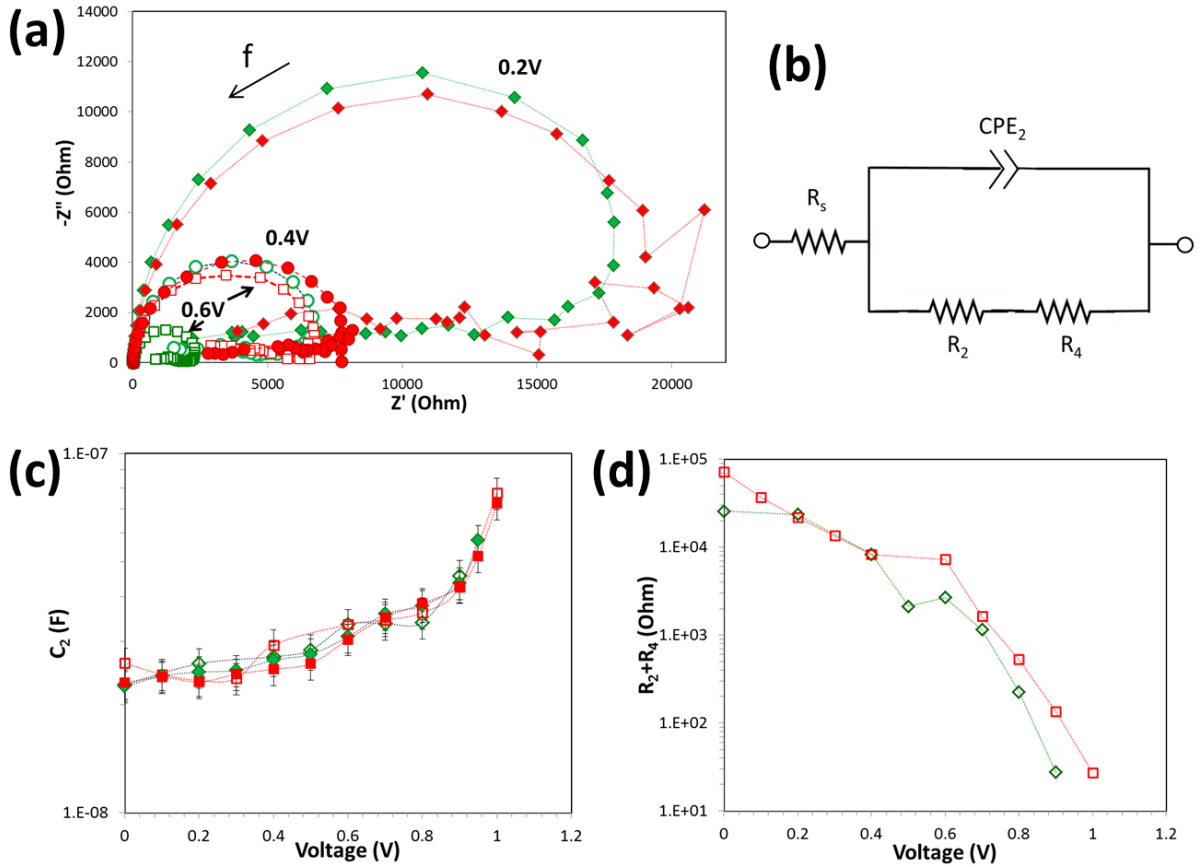


**Figure IV. 23** (a) Impedance spectra of MC48 and MC48-PEAI solar cells measured at various applied voltages. Green symbols: MC48; Red symbols: MC48-PEAI. (b) Equivalent electrical circuit used to fit the high-frequency part of the spectra. (c)  $C_2$  parameter of fresh and matured cells. (d)  $R_2+R_4$  parameter of fresh cells. Symbols: green diamonds = MC48 cell, red squares = MC48-PEAI cell; open symbols fresh cells; full symbols, matured cells (stored several days in a  $N_2$ -filled glovebox).

and the analysis protocol is given in Section IV.2.5.  $C_2$  versus  $V_{app}$  of fresh cells is displayed as open symbols in Figure IV.23c.  $C_2$  is assigned to the intrinsic dielectric relaxation capacitance of the perovskite and to a depletion capacitance above 0.7 V. We show below that its behavior is unchanged with the cell aging. Therefore, the bulk perovskite did not evolve during the first days of the PSC life. The resistance measured was quite large and, based on the general EEC,<sup>40</sup> is assigned to the sum of two recombination resistances,  $R_2$  and  $R_4$ . The large values result from the domination of the  $R_4$  parameter. The special low-frequency behavior of the cell can be assigned to the interfacial reactivity and slow processes that occur at the interfaces. Perovskite/selective contacts interfaces in fresh cells would not be stabilized either for the pristine or PEAI-treated cells. Further characterizations of the PSCs were carried out after their aging for days in a  $N_2$  filled glove

**Table IV.5** *J-V* curve parameters of MC48-PEAI PSC in fresh and matured status (AM 1.5G conditions, 100 mW/cm<sup>2</sup>).

	<b>Voc /V</b>	<b>Jsc /mA/cm<sup>2</sup></b>	<b>FF /%</b>	<b>PCE /%</b>
<b>Fresh</b>	0.997	25.65	80.63	20.62
<b>Matured</b>	1.025	25.77	80.79	21.33

-box (typically 6-7 days). This maturation period of the solar cells results in an increase of the overall efficiency of the PSC mainly due to the increase of the  $V_{OC}$  and the  $J_{SC}$  in a less extent as shown in Table IV.5. After this period, the Nyquist plots exhibited two main relaxations as shown in Figure IV.24a-c. It suggests that during the maturation, reactions occurred that results in the stabilization of the low-frequency signal. These spectra have been fitted with the EEC presented in Figure IV.24d and also derived from the general EEC (Figure IV.1). Figure IV.24a presents the effect of applied voltage on the Nyquist impedance plot. When the voltage was increased, the two arcs of circle were reduced in size due to a reduction of both  $R_2$  and  $R_4$  resistance as schematically displayed in Figure IV.2. Figure IV.24b reports the impedance spectra of a pristine and a PEAI-treated cell. The amplitude of the circles was increased by the treatment and therefore  $R_2$  and  $R_4$  were increased. Figure IV.24c shows that the amplitude of the arcs of circle also varied with the MAI molar fraction employed to prepare  $FA_{1-x}MA_xPbI_3$ . To quantify these changes, the spectra were fitted using the simplified EEC presented in Figure IV.24d. Due to the appearance of a second arc of circle, we added a CPE capacitive element, noted  $CPE_4$ , in parallel with  $R_4$  in the EEC of Figure IV.21b.  $C_4$  capacitance values were extracted from  $CPE_4$  as detailed in Section IV.2.5. No inductive loop was found and we stopped the analysis at 0.1 Hz since at lower frequency, the signal could be rather noisy.

$C_2$  is a light insensitive element.<sup>17</sup> Figure IV.23c and Figure IV.24e show that this parameter remained the same with a battery of changed parameters: the cell age, the PEAI treatment and the MAI additive fraction in the perovskite precursor solution. The curves were similar over the whole investigated applied voltage range. Below 0.5V, this capacitance remained almost constant. It is assigned to the intrinsic dielectric relaxation of the perovskite.<sup>17,40</sup> The composition of the perovskite of the various cells is about the same, consequently, this parameter did not vary significantly in Figure IV.23c. Above 0.6 V,  $C_2$  increased due to a charge storage effect. At high  $V_{app}$ ,  $C_2$  is dominated by the capacitance due to the charge stored in a depleted region at the  $TiO_2$ /perovskite layers. In the literature, the depleted region has been described as mainly

extending either in the titania layer and/or in the doped perovskite layer.<sup>48,452,53</sup> The Mott-Schottky plot of  $C_2$  in Figure IV.25 results in a linear section. The linear fits extrapolate at the same potential for the various cells, between 1.08 V-1.12 V. It can be reasonably assigned to the built-in potential ( $V_{bi}$ ).<sup>54</sup>

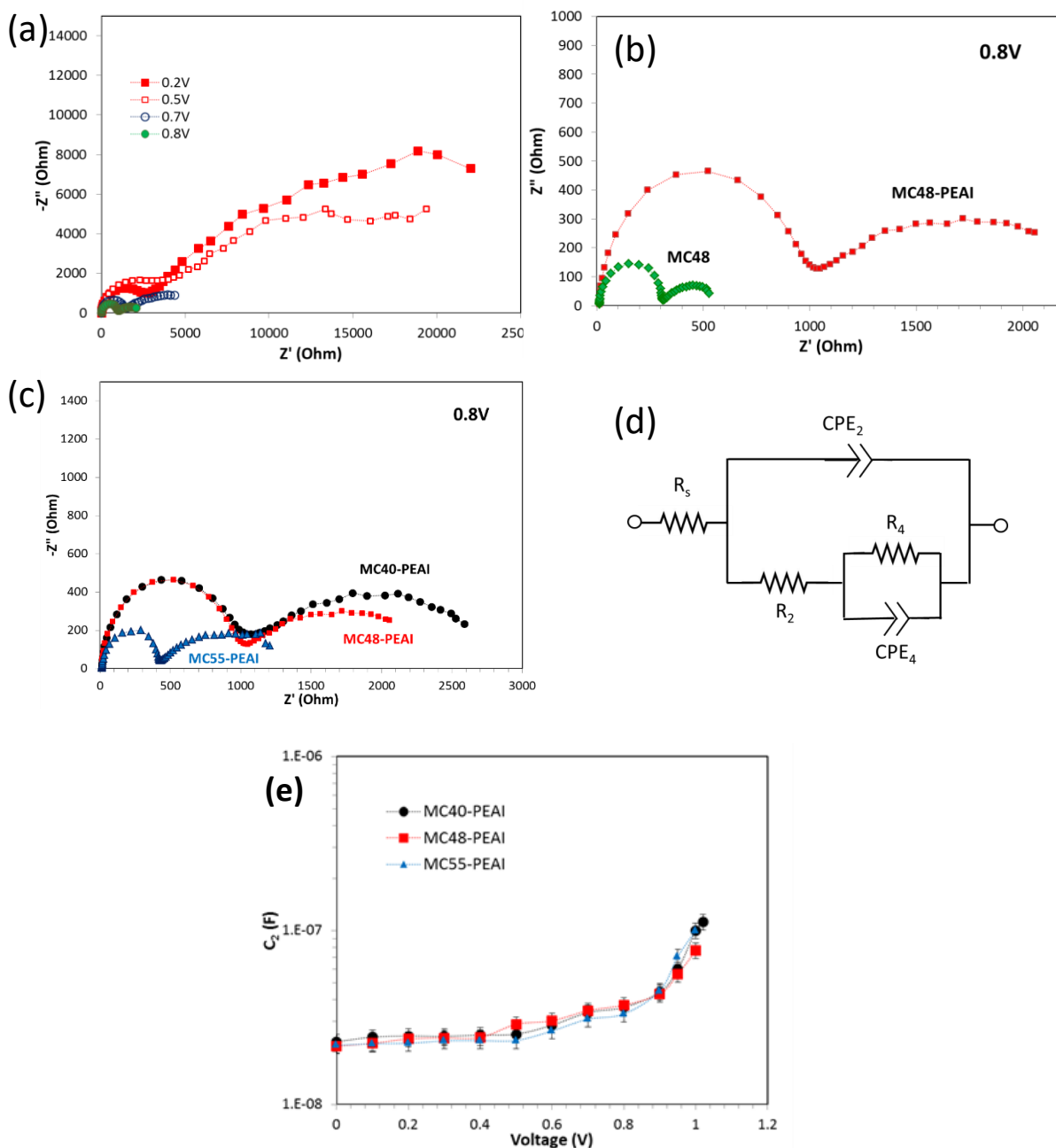


**Figure IV. 24** Nyquist plots of the EIS spectra. (a) Effect of the applied voltage on a 7 days old MC48-PEAI cell. (b) Effect of PEAI (MC48 and MC48-PEAI,  $V_{appl}=0.8V$ ); (c) Effect of MACl (PEAI-treated cells,  $V_{appl}=0.8V$ ) and (d) Electrical equivalent circuit used to analyze the data. (e) Effect of MACl molar fraction on  $C_2$  parameter versus the applied voltage.

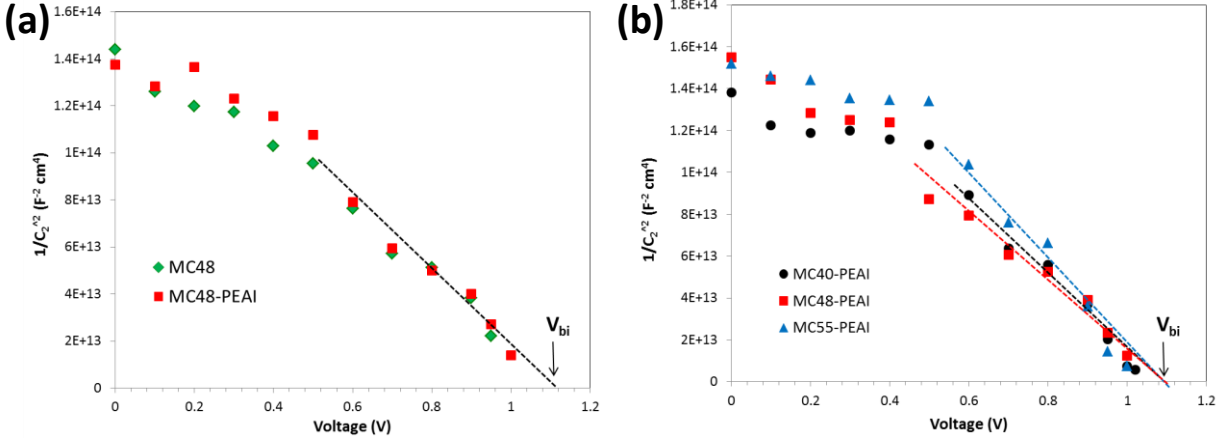


**Figure IV. 25** Mott-Schottky plots of  $C_2$  capacitance. (a) Comparison of pristine and PEAI treated solar cells. (b) Effect of MACl additive: black 40%, red 48% and blue 55%.  $V_{bi}$  is the built-in potential.

The other electrical elements,  $R_2$ ,  $R_4$  and  $C_4$  were light-sensitive and we will see that all of them are related to charge recombination phenomena. For  $R_2$ , the PEAI treatment results in a significant increase of this parameter (Figure IV.26a). A consequence is that, above 0.7 V, it shifts the resistance to a higher potential. The same behavior was found for  $R_4$  which is also a recombination resistance. Recombination resistances are inversely related to the recombination rate and they provide a direct quantitative view of the recombination processes. The higher is this resistance, the lower is the recombination rate. The fact that the PEAI nanolayer shift  $R_2$  and  $R_4$  curves toward higher voltage is favorable for the cell performances since it increases the cell  $V_{OC}$ .

$C_4$  is a light sensitive parameter which value dramatically increases with the light irradiation and can reach very high values. In our case, at high  $V_{app}$ ,  $C_4$  attained  $1.10^{-1} F.cm^{-2}$ . There is little doubt that  $C_4$  is also related to the recombination of charges. Because charge recombinations in PSC are a phase delayed phenomenon, in addition to the real component, an imaginary component is also introduced. This imaginary component is analyzed here as a capacitance in the equivalent electrical circuits used to fit our data (Figures IV.24d). It is the main contribution of  $C_4$ . This delayed recombination process is a particular behavior occurring in PSCs due to the ionic conductivity of the perovskite. The movements of ions introduce defects that act as recombination centers and affect the dynamics of the charges. In Figures IV.26a-c, the three parameters  $R_2$ ,  $R_4$  and  $1/C_4$  clearly appear as related since they exhibit a similar behavior. We can also note that their shape reproduces the  $J-V$  curve shape since the  $R_s+R_2+R_4$  sum is the total resistance of the devices at the steady state. These three parameters increased markedly with the PEAI treatment which passivates

the interfacial defects, favors the hole transfer toward the HTL and lower the recombination phenomena. Therefore, higher  $J_{SC}$  and  $V_{OC}$  are achieved when the treatment is done (Figure IV.13).

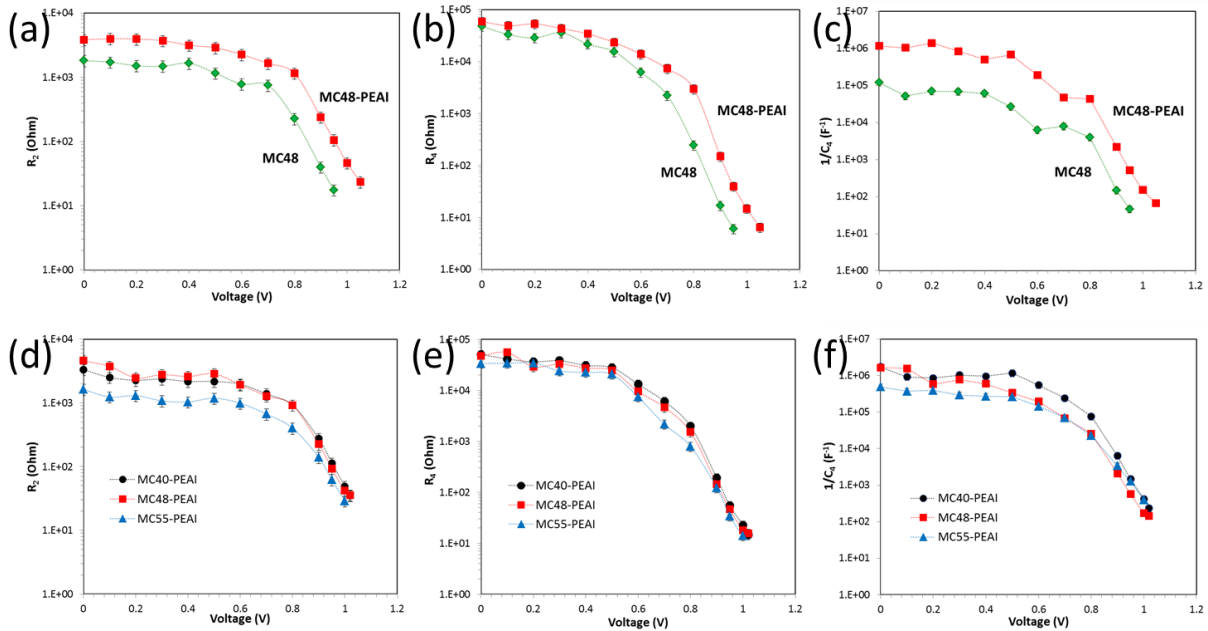


**Figure IV. 26** (a-c) Effect of PEAI treatment on the impedance spectra parameter versus  $V_{appl}$ . (a)  $R_2$ ; (b)  $R_4$  and (c)  $1/C_4$ . Effect of MAI additive molar fraction: (d)  $R_2$ ; (e)  $R_4$ ; and (f)  $1/C_4$ .

Figure IV.26d-f shows some differences in the electrical behavior of cells prepared with various MAI additive fraction contents. The main one is the marked lowering of the  $R_2$  parameter for the MC55-PEAI cells.  $R_4$  and  $1/C_4$  are also slightly lower. We can conclude that more recombinations occurred in these cells especially at high voltage. The surface of the MC55 film was more defective and the passivation was a little less effective for these cells. Consequently, the FF and  $V_{OC}$  were the most impacted parameters which were significantly reduced at the high MAI molar fraction (Figure IV.14). Because of the ion mobility in the perovskite and the dynamics of defect formation and repair described, it is rather difficult to go further in the analysis and assigned a sound origin of  $R_2$  and  $R_4$ . However, in Figure IV.26, we remark that the behavior of  $1/C_4$  is similar to that of  $R_2$  which leads us to tentatively assign the later resistance to recombination occurring in the bulk, likely near the interface because this element is sensitive to the surface treatment. On the other hand,  $R_4$  would be an interfacial recombination resistance.

Impedance spectroscopy is a stressing operating mode for the cells. The operated devices are then submitted to continuous light irradiation, to various applied voltages and to a superimposed ac

stimulus. The full characterization of a solar cell by EIS lasts more than one hour. For each cell investigated, we controlled their stability by measuring their  $J$ - $V$  curves before and after the EIS characterization. Results for some of them are gathered in Table IV.6. The performances of the pristine and of the PEAI-treated devices were slightly higher after EIS characterizations due to a better  $V_{OC}$ . The prepared devices presented a high robustness and they met the stability requirement for reliable EIS characterizations as defined by Pauporté et al. in Ref.<sup>49</sup>

**Table IV.6**  $J$ - $V$  curve parameters before and after EIS study of PSC prepared with different conditions (AM 1.5G conditions, 100 mW/cm<sup>2</sup>).

Cell	Impedance measurement	$V_{oc}$ /V	$J_{sc}$ mA/cm <sup>2</sup>	$FF$ /%	$PCE$ /%	$\square PCE$ /% <sup>a</sup>
MC40-PEAI	Before	1.028	25.82	78.21	20.76	+1.4
	After	1.043	25.79	78.20	21.05	
MC48-PEAI	Before	1.035	25.65	79.62	21.13	+0.76
	After	1.044	25.71	79.36	21.29	
MC55-PEAI	Before	0.996	25.38	78.65	19.88	+0.10
	After	1.016	25.29	77.48	19.90	
MC48 (no PEAI)	Before	0.949	24.01	81.22	18.50	+8.38
	After	1.011	24.50	80.89	20.05	

<sup>a</sup>  $PCE$ : PCE change upon EIS measurement, defined as  $[PCE(\%)_{after} - PCE(\%)_{before}] / PCE(\%)_{before}$

## IV.6 Conclusions

We have developed the use of methylammonium chloride as an additive in rather low concentration mixed organic cation precursor solutions. MA<sub>2</sub>Cl is shown to mediate the growth of the layers. The resulting films were uniform, compact, with no pinholes and made of remarkably large size perovskite crystal grains. By this technique, a small amount of MA cation was incorporated in FAPbI<sub>3</sub>, stabilizing the pure  $\alpha$ -phase with FA<sub>0.94</sub>MA<sub>0.06</sub>PbI<sub>3</sub> composition. The excess was removed by sublimation and degradation. The presented growth technique is reliable, robust and gives devices efficient over a large range of additive concentration. The best MA<sub>2</sub>Cl molar fraction is found at 48mol.%. To further increase the PCE of the solar cells, a treatment with PEAI solution has been implemented. This treatment, without any thermal annealing step, leads to the spontaneous formation of (PEA)<sub>2</sub>PbI<sub>4</sub> perovskite at the surface. This buffer layer has been shown to favor a fast transfer of the holes towards the HTL and to reduce the recombinations at the perovskite/HTL interface. Overall, the optimized devices had a PCE higher than 22.1%. A

comprehensive investigation of the systems by impedance spectroscopy has been carried out. The change in the impedance spectra within the first days of the device storage corresponds to a maturation step which involves reactions at the interface(s). The high frequency capacitance was irrespective of the PSC age and treatment was assigned at low  $V_{\text{appl}}$  to the intrinsic dielectric relaxation of the perovskite. The high frequency resistance  $R_2$  and  $R_4$  were analyzed as recombination resistances and  $C_4$  as a recombination capacitance. Furthermore, our results indicate that  $R_2$  and  $C_4$  are likely related to recombination centers localized near the interface whereas  $R_4$  would correspond to an interfacial recombination resistance. Overall, the variations of  $R_2$ ,  $R_4$  and  $1/C_4$  explain the variations in  $FF$  and  $V_{\text{OC}}$  of the PSCs with the MAI mol.% and the PEAI treatment. The power output of the produced devices was remarkably stable. These PSCs were proved resistant to electrical stresses, to light irradiation and to moisture.

However, the expected stability in a high humidity environment was not observed in these FAMAPbI<sub>3</sub> cells, according to Figure IV.20 and 21. It can be ascribed to the unstable MA<sup>+</sup> ions that are easily released from the structure. To realize the long-time stability against moisture, we have developed in Chapter V hydrophobic 2D materials introduced into 3D perovskite structure.

## References

1. B. Saparov and D. B. Mitzi, *Chem. Rev.* 116 (2016) 4558–4596.
2. Leblanc, N. Mercier, M. Allain, J. Dittmer, T. Pauporté, V. Fernandez, F. Boucher, M. Kepenekian and C. Katan, *ACS Appl. Mater. Interfaces* 11 (2019) 20743–20751.
3. S. A. Veldhuis, P. P. Boix, N. Yantara, M. Li, T. C. Sum, N. Mathews and S. G. Mhaisalkar, *Adv. Mater.* 28 (2016) 6804–6834.
4. H. S. Kim, C. R. Lee, J. H. Im, K. B. Lee, T. Moehl, A. Marchioro, S. J. Moon, R. Humphry-Baker, J. H. Yum, J. E. Moser and M. Grätzel, *Sci. Rep.* 2 (2012) 591.
5. M. M. Lee, J. Teuscher, T. Miyasaka, T. N. Murakami and H. J. Snaith, *Science* 338 (2012) 643–647.
6. M. Liu, M. B. Johnston and H. J. Snaith, *Nature* 501 (2013) 395–398.
7. J. Burschka, N. Pellet, S. J. Moon, R. Humphry-Baker, P. Gao, M. K. Nazeeruddin and M. Grätzel, *Nature* 499 (2013) 316–319.
8. J. Zhang, P. Barboux and T. Pauporté, *Adv. Energy Mater.* 4 (2014) 1400932.

9. W. Nie, H. Tsai, R. Asadpour, J. C. Blancon, A. J. Neukirch, G. Gupta, J. J. Crochet, M. Chhowalla, S. Tretiak, M. A. Alam and H. L. Wang, *Science* 347 (2015) 522–525.
10. J. Zhang, E. J. Juárez-Pérez, I. Mora-Seró, B. Viana and T. Pauporté, *J. Mater. Chem. A* 3 (2015) 4909–4915.
11. J. Zhang and T. Pauporté, *J. Phys. Chem. C* 119 (2015) 14919–14928.
12. J. Zhang and T. Pauporté, *ChemPhysChem* 16 (2015) 2836–2841.
13. Y. G. Tu, G. N. Xu, X. Y. Yang, Y. F. Zhang, Z. J. Li, R. Su, D. Y. Luo, W. Q. Yang, Y. Miao, R. Cai, L. H. Jiang, X. W. Du, Y. C. Yang, Q. S. Liu, Y. Gao, S. Zhao, W. Huang, Q. H. Gong and R. Zhu, *Sci. China-Phys. Mech. Astron.* 62 (2019) 974221-1–974221-4.
14. W. S. Yang, B. W. Park, E. H. Jung, N. J. Jeon, Y. C. Kim, D. U. Lee, S. S. Shin, J. Seo, E. K. Kim, J. H. Noh and S. I. Seok, *Science* 356 (2017) 1376–1379.
15. A. Leblanc, N. Mercier, M. Allain, J. Dittmer, V. Fernandez and T. Pauporté, *Angew. Chem., Int. Ed.* 56 (2017) 16067–16072.
16. P. J. Wang, Z. Shao, M. Ulfa and T. Pauporté, *J. Phys. Chem. C* 121 (2017) 9131–9141.
17. P. Wang, M. Ulfa and T. Pauporté, *J. Phys. Chem. C* 122 (2018) 1973–1981.
18. S. -H. Turren-Cruz, A. Hagfeldt and M. Saliba, *Science* 362 (2018) 449–453.
19. NREL chart (2020) <https://www.nrel.gov/pv/cell-efficiency.html>
20. T. Leijtens, G. E. Eperon, N. K. Noel, S. N. Habisreutinger, A. Petrozza, H. J. Snaith, *Adv. Energy Mater.* 5 (2015) 1500963.
21. N. J. Jeon, H. Na, E. H. Jung, T. Y. Yang, Y. G. Lee, G. Kim, H. W. Shin, S. I. Seok, J. Lee and J. Seo, *Nature Energy* 3 (2018) 682–689.
22. Q. Jiang, Y. Zhao, X. W. Zhang, X. L. Yang, Y. Chen, Z. M. Chu, Q. F. Ye, X. X. Li, Z. G. Yin and J. B. You, *Nature Photonics* 13 (2019) 460–466.
23. E. H. Jung, N. J. Jeon, E. Y. Park, C. S. Moon, T. J. Shin, T. Y. Yang, J. H. Noh and J. Seo, *Nature* 567 (2019) 511–515.
24. J. J. Yoo, S. Wieghold, M. C. Sponseller, M. R. Chua, S. N. Bertram, N. T. P. Hartono, J. S. Tresback, E. C. Hansen, J. P. Correa-Baena, V. Bulovic, T. Buonassisi, S. S. Shin and M. G. Bawendi, *Energy Environ. Sci.* 12 (2019) 2192–2199.
25. Y. H. Liu, S. Akin, L. F. Pan, R. Uchida, N. Arora, J. V. Milic, A. Hinderhofer, F. Schreiber, A. R. Uhl, S. M. Zakeeruddin, A. Hagfeldt, M. I. Dar and M. Gratzel, *Sci. Adv.* 5 (2019) eaaw2543.
26. M. Kim, G. -H. Kim, T. K. Lee, I. W. Choi, H. W. Choi, Y. Jo, Y. J. Yoon, J. W. Kim, J. Lee, D. Huh, H. Lee, S. K. Kwak, J. Y. Kim and D. S. Kim, *Joule* 3 (2019) 1–14.
27. T. Zhu, J. Su, F. Labat, I. Ciofini, T. Pauporté, *ACS Appl. Mater. Interfaces* 12 (2020) 744–752.
28. E. Edri, S. Kirmayer, S. Mukhopadhyay, K. Gartsman, G. Hodes and D. Cahen, *Nat. Commun.* 5 (2014) 3461.
29. A. Buin, P. Pietsch, J. X. Xu, O. Voznyy, R. Comin and E. H. Sargent, *Nano Lett.* 14 (2014) 6281–6286.
30. C. Mu, J. Pan, S. Feng, Q. Li and D. Xu, *Adv. Energy Mater.* 7 (2017) 1601297.
31. N. J. Jeon, H. Na, E. H. Jung, T. -Y. Yang, Y. G. Lee, G. Kim, H. -W. Shin, S. I. Seok, J. Lee and J. Seo, *Nature Energy* 3 (2018) 682–689.

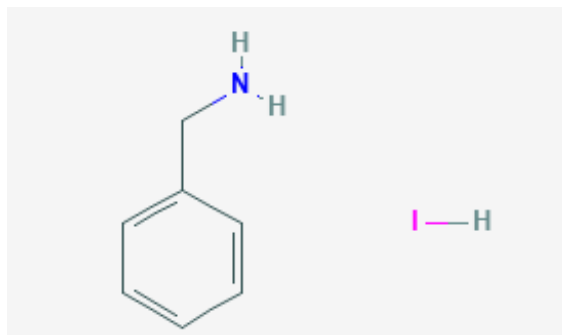
32. K. T. Cho, G. Grancini, Y. Lee, E. Oveisi, J. Ryu, O. Almora, M. Tschumi, P.A. Schouwink, G. Seo, S. Heo, J. Park, J. Jang, S. Paek, G. Garcia-Belmonte and M. K. Nazeeruddin, *Energy Environ. Sci.* 11 (2018) 952–959.
33. F. X. Xie, C. -C. Chen, Y. Wu, X. Li, M. Cai, X. Liu, X. Yang and L. Han, *Energy Environ. Sci.* 10 (2017) 1942–1949.
34. Y. -H. Wu, Y. Ding, X. -Y. Liu, X. Pan, J. -H. Wu and S. -Y. Dai, *Sol. RRL* 4 (2020) 1900183.
35. M. Mateen, Z. Arain, Y. Yang, X. Liu, S. Ma, C. Liu, Y. Ding, X. Ding, M. Cai and S. Dai, *ACS Appl. Mater. Interfaces* 12 (2020) 10535–10543.
36. G. M. Kim, A. Ishii, S. Öz and T. Miyasaka, *Adv. Energy Mater.* 10 (2020) 1903299.
37. J. -W. Lee, Z. Dai, T. -H. Han, C. Choi, S. -Y. Chang, S. -J. Lee, N. De Marco, H. Zhao, P. Sun, Y. Huang and Y. Yang, *Nat. commun.* 9 (2018) 3021.
38. L. N. Quan, M. Yuan, R. C. O. Voznyy, E. M. Beaugard, S. Hoogland, A. Buin, A. R. Kirmani, K. Zhao, A. Amassian, D. H. Kim and E. H. Sargent, *J. Am. Chem. Soc.* 138 (2016) 2649–2655.
39. W. Tress, M. Yvari, K. Domanski, P. Yadav, B. Niesen, J. P. Correa Baena, A. Hagfeldt and M. Graetzel, *Energy Environ. Sci.* 11 (2018) 151–165.
40. M. Ulfa, T. Zhu, F. Goubard and T. Pauporté, *J. Mater. Chem. A* 6 (2018) 13350–13358.
41. W. T. M. Gompel, R. Herckens, G. Reekmans, B. Ruttens, J. D’Haen, P. Adriaenssens, L. Lutsen, D. Vanderzande, *J. Phys. Chem. C* **2018**, 122, 4117–4124.
42. A. Leblanc, N. Mercier, M. Allain, J. Dittmer, T. Pauporté, V. Fernandez, F. Boucher, M. Kepenekian, C. Katan, *ACS Appl. Mater. Interfaces* **2019**, 11, 20743–20751.
43. X. Wang, Y. Fan, L. Wang, C. Chen, Z. Li, R. Liu, H. Meng, Z. Shao, X. Du, H. Zhang, G. Cui, S. Pang, *Chem* **2020**, DOI : 10.1016/j.chempr.2020.02.016.
44. W. M. Franssen, B. J. Bruijnaers, V. HL Portengen, A. P. M. Kentgens, *ChemPhysChem* **2018**, 19, 3107–3115.
45. T. Moot, A. R. Marshall, L. M. Wheeler, S. N. Habisreutinger, T. H. Schloemer, C. C. Boyd, D. R. Dikova, G. F. Pach, A. Hazarika, M. D. McGehee, H. J. Snaith, J. M. Luther, *Adv. Energy Mater.* **2020**, 1903365.
46. L. T. Schelhas, Z. Li, J. A. Christians, A. Goyal, P. Kairys, S. P. Harvey, D. H. Kim, K. H. Stone, J. M. Luther, K. Zhu, V. Stevanovic, J. J. Berry, *Energy Environ. Sci.* **2019**, 12, 1341–1348.
47. J. J. Yoo, S. Wiegold, M. C. Sponseller, M. R. Chua, S. N. Bertram, N. T. P. Hartono, J. S. Tresback, E. C. Hansen, J.-P. Correa-Baena, V. Bulović, T. Buonassisi, S. S. Shin, M. G. Bawendi, *Energy Environ. Sci.* **2019**, 12, (2019), 2192–2199.
48. D. A. Jacobs, H. Shen, F. Pfeffer, J. Peng, T. P. White, F. J. Beck and K. R. Catchpole, *J. Appl. Phys.* 124 (2018) 225702.
49. D. Pitarch-Tena, T. T. Ngo, M. Vallés-Pelarda, T. Pauporté and I. Mora-Seró, *ACS Energy Lett.* 3 (2018) 1044–1048.
50. M. Ulfa, P. Wang, J. Zhang, J. Liu, W. Daney de Marcillac, L. Coolen, S. Peralta and T. Pauporté, *ACS Appl. Mater. Interfaces* 10 (2018) 35118–35128.
51. M. Ulfa, T. Pauporté, T. T. Bui and F. Goubard, *J. Phys. Chem. C.* 122 (2018) 11651–11658.
52. A. Guerrero, E. J. Juarez-Perez, J. Bisquert, I. Mora-Sero and G. Garcia-Belmonte, *Appl. Phys. Lett.* 105 (2014) 133902.

53. C. -S. Jiang, M. Yang, Y. Zhou, B. To, S. U. Nanayakkara, J. M. Luther, W. Zhou, J. J. Berry, J. van de Lagemaat, N. P. Padture, K. Zhu and M. M. Al-Jassim, *Nat. Commun.* 6 (2015) 8397.
54. O. Almora, C. Aranda, E. Mas-Marzá and G. Garcia-Belmonte, *Appl. Phys. Lett.* 109 (2016) 173903.

## Chapter V. Stability and Efficiency of Benzylamine Hydroiodide (BEI)-Based Mixed-Dimensional Perovskite Solar Cells

Nowadays, PSCs are sufficiently efficient and low-cost devices for commercialization. However, the instability of the perovskite layer is still a tricky problem. To improve the perovskite stability, hydrophobic 2D materials could be inserted into perovskite layers to form a layer-by-layer structure, which can protect the 3D perovskite structure from humidity. On the other hand, we have shown in Chapter IV that the MA cation content must be minimized to improve the FAPbI<sub>3</sub> perovskite stability and efficiency.

This Chapter V focus on 2D/3D perovskites based on FAI and a large cation, Benzylamine Hydroiodide (also named Phenylmethylanmine Hydroiodide, or Phenylmethylanmonim Iodide) (See Schematic V.1) that we will abbreviate BEI. We have systematically studied FAI and BEI-based 2D/3D perovskites. We include characterizations of the 2D/3D perovskite films and the study the corresponding photovoltaic devices. The composition of the films has been optimized to increase their stability and their photovoltaic performances.



**Schematic V. 1** Molecular structure of Benzylamine Hydroiodide (BEI) (also named Phenylmethylanmine Hydroiodide or Phenylmethylanmonium Iodide).

### V.1 Introduction

The stability of the hybrid perovskites can be improved by introducing hydrophobic 2D materials into their structures. The organic spacer group Ruddlesden-Popper (RP) and Dion-Jacobson (DJ) layered 2D perovskites are the most reported crystal structures<sup>1,2</sup>, with molecular formula which can be written as  $A'_2A_{n-1}Pb_nI_{3n+1}$  and  $A''A_{n-1}Pb_nI_{3n+1}$ , respectively. The detailed description of

these structures is provided in Chapter I, Section I.3. RP-phase perovskites are reported to have an excellent robustness against moisture. Therefore, these structures can be employed to improve the stability. However, the bad conductivity of 2D materials and their larger bandgaps may impede their photovoltaic performances. In order to find the accurate balance between the stability and the photovoltaic performances, it is important to optimize the amount of incorporated 2D materials (n optimum in quasi-2D,  $n \leq 5$  or quasi-3D,  $n > 5$  materials). In general, when the n value decreases, the stability of the perovskite solar cells is claimed to increase but the efficiency decreases.<sup>3</sup> However, we believe that there should be a premise that the 2D/3D perovskite has a pure phase, or the mixed quasi-2D phases disperse homogeneously in the structure. As far as we know, all the reported quasi-2D or quasi-3D perovskites in solar cells are not pure phase and the distribution of quasi-2D phases is not homogeneous either.<sup>3-9</sup> Recently, Lin et al. unveiled the operation mechanism of layered perovskite films formation. On the direction perpendicular to the substrate, quasi-2D phases are preferentially formed at the layer bottom while quasi-3D phases are preferentially formed near the surface as illustrated in Figure V.1.<sup>9</sup> The 3D-like crystal tends to precipitate first during the annealing process. As more and more 3D-like crystals precipitate, the ratio of BA to MA in leftover solution gradually increases and the BA-rich solution facilitates the nucleation and growth of afterward layered perovskite.<sup>9</sup> Wu et al. proposed a nearly opposite mechanism: the 2D-like crystals tend to precipitate first. Because they observed that the calculated formation enthalpy was lowered with the lower n values (the formation enthalpy is defined as the free energy difference between the precursors and the target material).<sup>4</sup> However, 2D/3D phases distributed at the bottom of the layer cannot accurately play the role of protecting the 3D perovskite phase.

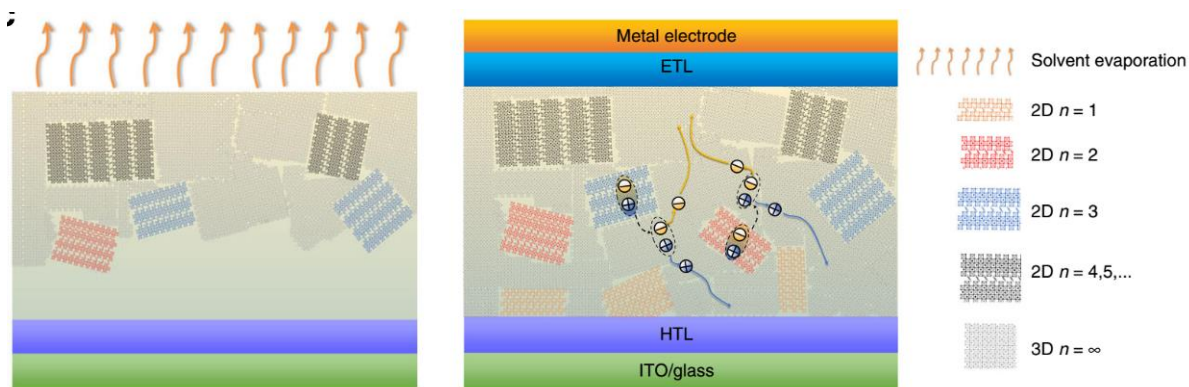


**Figure V. 1** Growth kinetics, morphology and device operation mechanism model.<sup>9</sup>

In 2018, Dr. Zheng et al.<sup>10</sup> reported that Benzylamine hydroiodide (BEI) can improve the stability of FAPbI<sub>3</sub> cells. However, they only made 2D/3D perovskite samples with  $n = 9$ , which structure was close to the 3D perovskite. The 2D phases were observed by XRD but the peak at an angle of 8.66°, indexed as the (002) plane, was ambiguous. The corresponding  $n$  value was unclear either. Their work was fragmentary and insufficient for explaining the operation of BEI in the perovskite films. On the other hand, the XRD patterns for aged samples in this paper only presented PbI<sub>2</sub> phase and no  $\delta$ -phase FAPbI<sub>3</sub>, which means the 2D materials really inhibited the  $\delta$ -phase transition of FAPbI<sub>3</sub>. This result is quite surprising since the  $\delta$ -phase FAPbI<sub>3</sub> was always the final stable phase in our experiments.

In this Chapter, BEI and FAPbI<sub>3</sub> based 2D/3D perovskite solar cells have been systematically studied. The highest efficiencies of quasi-2D ( $n = 5$ ) and quasi-3D ( $n = 9$ ) PSCs have reached 17.32% and 19.56% PCEs, respectively. We have found that  $n = 9$  is more stable than the other 2D/3D phases ( $n = 2, 3, 5$ ), due to a higher phase purity.

## V.2. Experimental

The substrate, the compact TiO<sub>2</sub> layer and mesoporous TiO<sub>2</sub> layer were prepared as already described in Chapter II.2.1. The HTM and Gold contacts were deposited as detailed in Chapter III.2. All the characterization methods have also been reported in Chapter III and IV.

### Preparation of 2D/3D perovskite films with various $n$ values

The precursor solutions were prepared by dissolving specific stoichiometric quantities of BEI (Benzylamine hydroiodide from TCI), FAI (Greatcell) and PbI<sub>2</sub> (TCI) in DMSO/DMF (volume ratio 1:4) mixed solution with a concentration of 1.2 M. 36 mol.% MAI was used as additive (which represents 36 mol.% of the precursor solution FAI content). The detailed precursor solution compositions for  $n = 1, 2, 3, 5, 9$  and  $\infty$  are gathered in Table V.1. The solutions were first stirred for a minimum of 2 h at room temperature in a N<sub>2</sub> glovebox. Other procedures for making the perovskite films were the same as those described in Section IV.2. The perovskite films used for solar cell devices were treated with a PEAI solution as detailed in Section IV.2.

**Table V. 1** Precursor mass and molar content for the preparation of 2D/3D perovskite layers.

<b>1.2M</b>	<b>BEI</b> /mg (MW 235.07g.mol <sup>-1</sup> )	<b>FAI</b> /mg (MW 171.97 g.mol <sup>-1</sup> )	<b>PbI<sub>2</sub></b> /mg (MW 461.01 g.mol <sup>-1</sup> )	<b>MACl</b> /mg (MW 67.52g.mol <sup>-1</sup> )	<b>DMF/DMSO</b>
n=1	282.1 (1.2mol)	0	276.606 (0.6mol)	0	400/100 μl
n=2	141.2 (0.6mol)	34.4 (0.3mol)	276.606 (0.6mol)	7.29 (0.108mol)	400/100 μl
n=3	94.03 (0.4mol)	68.8 (0.4mol)	276.606 (0.6mol)	9.72 (0.144mol)	400/100 μl
n=5	56.5 (0.24mol)	82.5 (0.48mol)	276.606 (0.6mol)	11.66 (0.1728mol)	400/100 μl
n=9	31.3 (0.1333mol)	91.8 (0.534mol)	276.606 (0.6mol)	12.98 (0.192mol)	400/100 μl
n=∞	0	103.18 (0.6mol)	276.606 (0.6mol)	14.6 (0.216mol)	400/100 μl

### V.3 Characterizations of the Perovskite Films

#### V.3.1 XRD

2D/3D perovskite films were prepared by a one-step spin coating method. The chemicals in the precursor solution were BEI, FAI, MACl and PbI<sub>2</sub>. Most of Cl<sup>-</sup> and MA<sup>+</sup> present initially were evaporated during the annealing process at 153°C according to our analysis in Chapter IV, Section IV.3.3. Based on Table V.1, the theoretical perovskite compounds formulas are written as (BE)<sub>2</sub>FA<sub>n-1</sub>Pb<sub>n</sub>I<sub>3n+1</sub> with n = 1, n = 2, n = 3, n = 5, n = 9, n = ∞. The perovskite films were characterized by X-ray diffraction as shown in Figure V.2. No PbI<sub>2</sub> phase was detected except for n = 2 sample. All the peaks were indexed, especially, the 2D/3D ones were distinguished according to the literature data and the regularity of their spacing.<sup>3,11</sup> Fresh 3D (n = ∞), n = 9 and n = 1 samples had a good purity because no other suspicious peaks were observed. For films with n = 2, 3, 5, mixed peaks which belong to n = 2, n = 3 and 3D phases could be distinguished. It indicates that the obtained 2D/3D perovskite films were not phase pure but composed of several phases. For instance, using a n = 3 precursor solution, we might obtain a perovskite film with equal molar n = 1 and n = 5. Only the average n value can be promised the same as that in precursor solution. Except n = 1, all the mixed dimensional (MD) perovskites contained the 3D phases. With the n values increasing, the (100) and (200) peaks shift to left (Figure V.2b), which means the lattice size of MD perovskite increased. Prof. Y. Yang group reported a similar result in PEAI doped FAPbI<sub>3</sub> films and they attributed it to compressive strain associated with the added 2D perovskite.

They speculated that the reduction in lattice parameters could be related to the enhanced phase purity of cubic  $\text{FAPbI}_3$  as it would have equivalent effects with incorporation of smaller ‘A’ site cations on the tolerance factor and thus enthalpy of formation.<sup>12</sup> We propose another possibility here that the (111) peaks of quasi-2D phases are possibly approaching to (100) and (200) 3D peaks with increasing  $n$  values. For  $n = 2$  and  $n = 3$  samples, shoulder peaks of (100) were observed, which can be indexed as (111) peak of  $n = 2$  and  $n = 3$  phases.<sup>3,7</sup> It is worth noting that (0k0) plane of  $n > 3$  phases were not observed in all the XRD patterns because they are inclined to be perpendicular to the substrate if the  $n > 3$ .<sup>7</sup> Otherwise, the crystallinity of  $n > 3$  phases are poor.  $n = 9$  sample presented only 3D peaks in the XRD pattern, which means an orientation exactly perpendicular to the substrate. This is quite different from the results reported in Ref.<sup>10</sup> for the  $\text{BE}_2\text{FA}_8\text{Pb}_9\text{I}_{28}$  perovskite film. We have repeated their experiments and the peaks of quasi-2D phases (for instance,  $n = 2$  and  $n = 3$ ) could be observed in XRD patterns and UV absorbance spectra for the samples with  $n = 9$  to 11 as shown in Annex-V (Figure A.V.6). It indicates that our  $n = 9$  samples have a much higher purity.

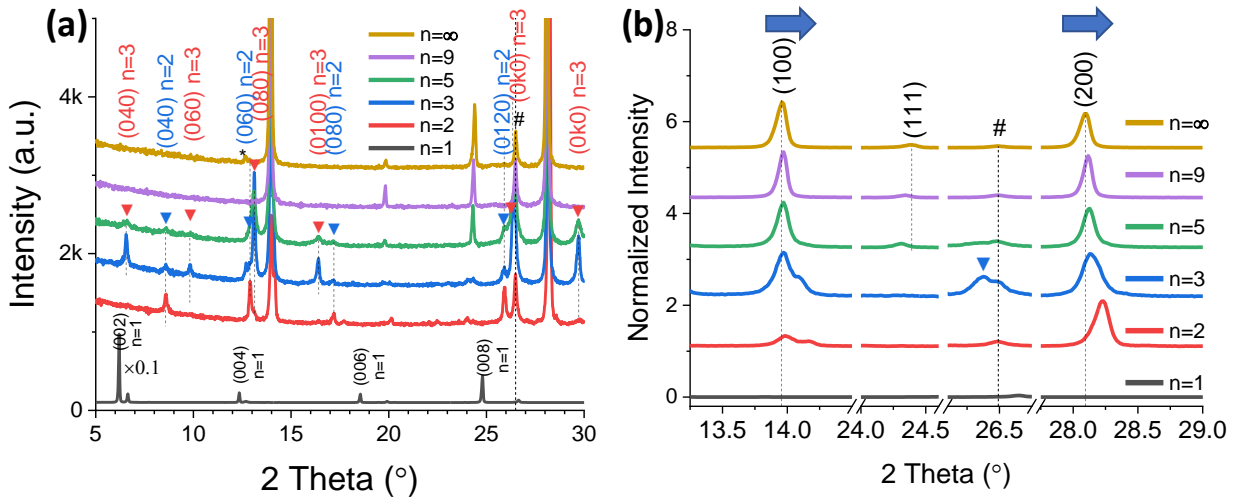


**Figure V. 2** (a) XRD patterns of 2D/3D perovskite films ( $n = 1, 2, 3, 5, 9$  and  $\infty$ ). (b) zoom of 3D peaks of these perovskite films. \* belongs to  $\text{PbI}_2$  and # belongs to FTO. The peaks indexation has been done based on Refs.<sup>3,11</sup>.

### V.3.2 UV-Vis absorbance

2D phases in the films were also investigated by UV-Vis absorbance spectroscopy. As shown in Figure V.3a, the absorption edges from left to right are 532 nm, 582 nm, 640 nm, 682 nm, 716 nm and 802 nm. They are assigned to single-phase of  $(\text{BE})_2\text{FA}_{n-1}\text{Pb}_n\text{I}_{3n+1}$ , where  $n = 1, n = 2, n = 3, n$

= 4, n = 5, n = ∞, respectively. Through differentiating the absorbance curves, the small quasi-2D peaks were revealed. The samples band gaps were measured by the Tauc plots, supposing a direct transition bandgap ( $(\alpha h\nu)^2 = A(h\nu - E_g)$ ) at 2.31 eV, 2.09 eV, 1.92 eV, 1.79 eV, 1.72 eV, 1.54 eV and 1.53 eV for n = 1, n = 2, n = 3, n = 4, n = 5, n = 9 and n = ∞, respectively. The corresponding figures were given in the Annex-V (Figure V.A.1). The intensity of the 3D peaks in this series increased with the n values. Samples of n = 1, n = 9, and n = ∞ presented single absorption peaks at about 535 nm, 805 nm and 806 nm, respectively, which means that quite pure phases were obtained. It is in agreement with the XRD patterns. On the other hand, as reported in many papers<sup>3-9</sup>, mixed quasi-2D phases were found for the 2D/3D perovskite films ( $2 \leq n \leq 5$ ). For instance, sample n = 2 also has n = 3, n = 4, and n = ∞ phases in the absorbance curves, which indicates that n = 1 phase must also exist in the films (Figure V.3b).

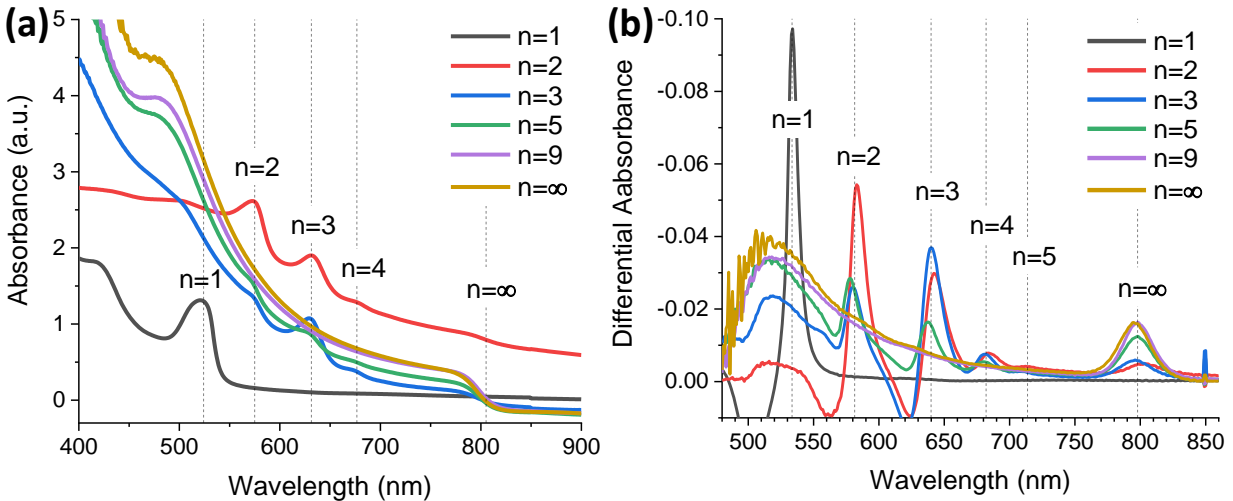


**Figure V. 3** (a) UV-Vis absorbance spectra of the 2D/3D perovskite films. (b) the differential figure of (a).

### V.3.3 Steady-state PL spectra

Steady-state PL spectra of the films are shown in Figure V.4a. Mixed 2D/3D peaks are observed for n = 2, n = 3 and n = 5 samples. It is in agreement with the results of XRD and UV-Vis measurements. Besides, the 3D peaks in PL are blue shifted from 812 nm to 797 nm with the n values decreasing. To examine if these 2D/3D phases distribute randomly, the steady-state PL spectra were collected under two different excitation configurations: from the top side (perovskite side) and the bottom side (glass side). Figure V.4b presents the result for the sample n = 5. Its 3D peaks were observed at 805 nm, irrespective of the excitation side. However, the 2D peaks were

only observed when the layers were excited from the bottom side. We have observed this phenomenon for all our quasi-2D perovskite samples ( $n = 2$ ,  $n = 3$  and  $n = 5$  samples) and it is in agreement with the literature.<sup>3-9</sup> The inhomogeneous distribution is a common phenomenon in 2D/3D perovskite films as shown in Figure V.1. The vertical distribution, starting from the transparent electrode, with wide bandgap 2D perovskites, to narrow 3D perovskites would contribute for the absorption of the photons and electron transfer.<sup>4,9,13</sup> However, the fact that hydrophobic quasi-2D perovskites are mainly distributed at the bottom of the perovskite layer restricts the expected stability improvement.

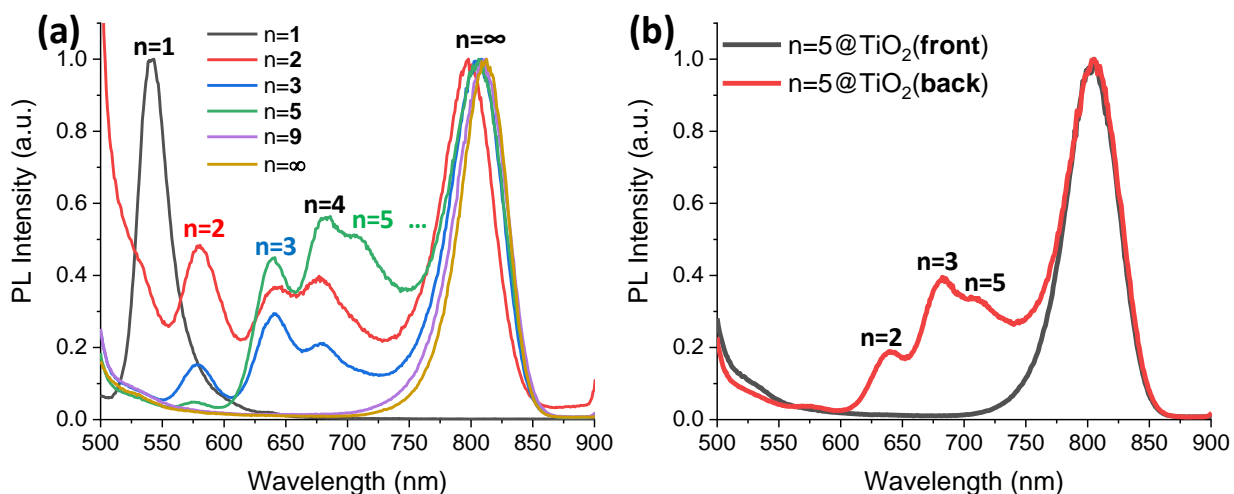


**Figure V. 4** (a) Steady-state PL spectra of 2D/3D perovskite films (measured from backside); (b) PL spectra of  $n = 5$  measured from back and front side.

### V.3.4 SEM

The morphologies of these samples were investigated by SEM as shown in Figure V.5. Other magnification images are presented in the Annex-V (Figure V.A.2). The  $n = 1$  sample presents a staggered branch-like structure. For  $n = 2$ , the branch-like structures are reduced, and some small cubic grains appeared. For  $n = 3$ , there are only small grains with 150 nm average size on the surface. For  $n = 5$ , the grains sizes get bigger (800 nm) and the surface is quite compact and smooth. For  $n = 9$  and  $n = \infty$ , the grains sizes approach to 1  $\mu\text{m}$ . No  $\text{PbI}_2$  crystals were found on the surface. The big grain size can be assigned to the use of the chloride additive (MACl). The picture of the general layer aspect shows that the color of the samples change from orange to red, then to black with the  $n$  values increasing.

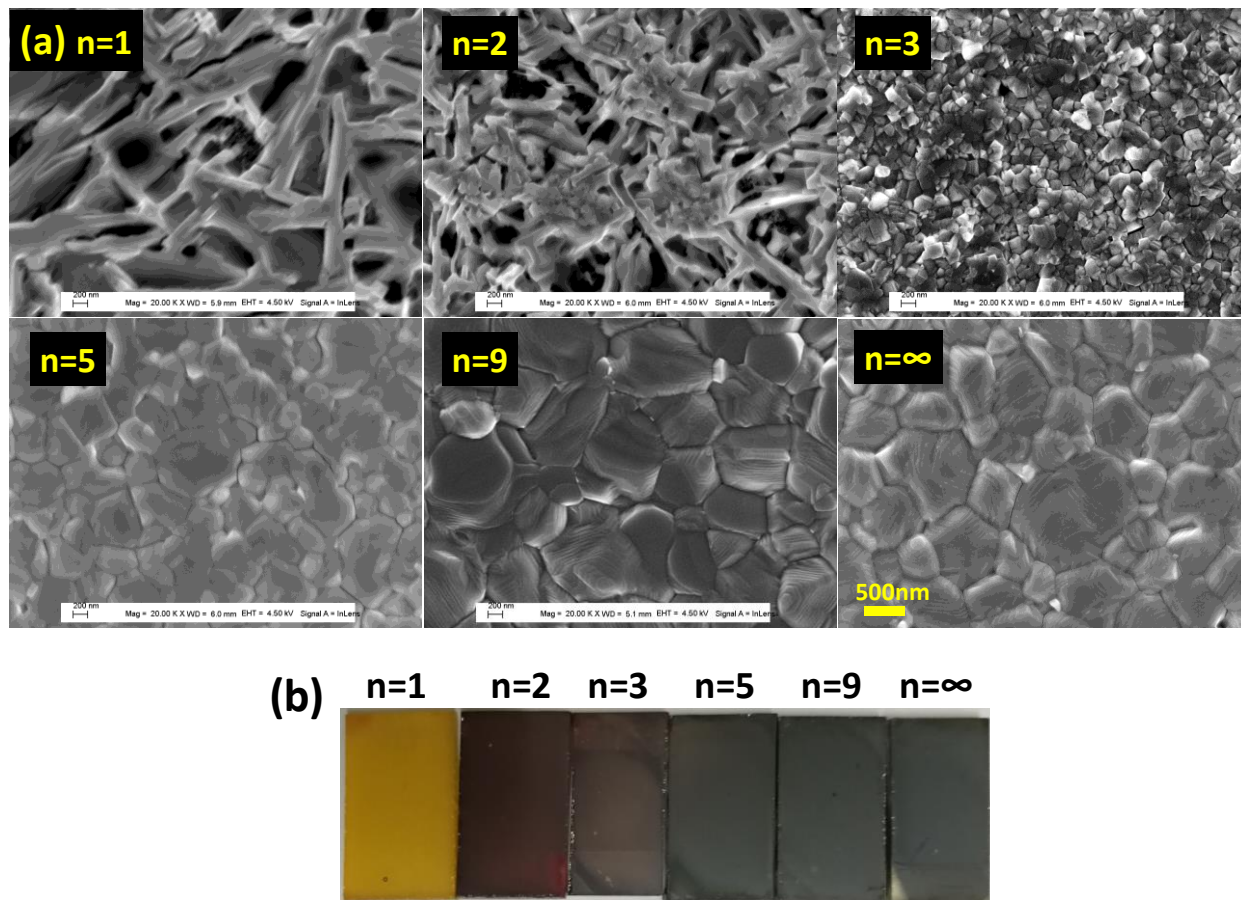


**Figure V. 5** (a) SEM top views of the perovskite films morphologies. (b) Picture of the general layers aspect and color.

## V.4 Characterizations of 2D/3D PSCs

### V.4.1 $J$ - $V$ curves and EQE

Solar cells with the Au/Spiro/MD-perovskite/ $mp$ -TiO<sub>2</sub>/ $c$ -TiO<sub>2</sub>/FTO/glass direct structure were fabricated. Their typical  $J$ - $V$  curves are shown in Figure V.6a and the corresponding photovoltaic parameters are gathered in Table V.2. The photocurrents and efficiencies increased with the  $n$  values because the 3D-phase gradually dominated in the structure. The voltages increased from  $n = 1$  to  $n = 5$ , which could be ascribed to the reduction of the interface recombination and shunting with the reduction of the branch-like structure. From  $n = 5$  to  $n = \infty$ , the voltages slightly decreased, which could be ascribed to the bandgap reduction. The best 2D/3D perovskite solar cell was  $n = 9$  devices, which presented a  $V_{OC}$  of 1.028 V,  $J_{SC}$  of 24.97 mA/cm<sup>2</sup>,  $FF$  of 76.31 and  $PCE$  of 19.6%. The corresponding  $J$ - $V$  curves are as shown in Figure 6b.

The charge generation efficiency over a large wavelength range was characterized by EQE spectra measurements (Figure V.6c). The integrated  $J_{SC}$  values are 0.2, 3.0, 2.0, 15.0, 22.7 and 24.9  $\text{mA}/\text{cm}^2$  for  $n = 1$ ,  $n = 2$ ,  $n = 3$ ,  $n = 5$ ,  $n = 9$  and  $n = \infty$ , respectively. The integrated photocurrents for 2D and quasi-2D cells are much lower than the photocurrents we obtained from solar simulator. We speculate that the deficit in  $J_{SC}$  results from the non-uniform distribution of the 2D and quasi-2D phases in the MD perovskite film. EQE peaks of  $n = 2$  and  $n = 3$  were observed in the quasi-2D cells (Figure V.6c and d). This agrees with XRD, UV, and PL results. The 3D onsets of samples  $n = 2$  and  $n = 3$  in EQE curves are very small (Figure V.6d) and the EQE of sample  $n = 5$  decreases apparently with the wavelength increasing in the visible light range. The lower integrated photocurrents might be caused by the 2D phases are preferentially formed at the bottom of the perovskite layer.

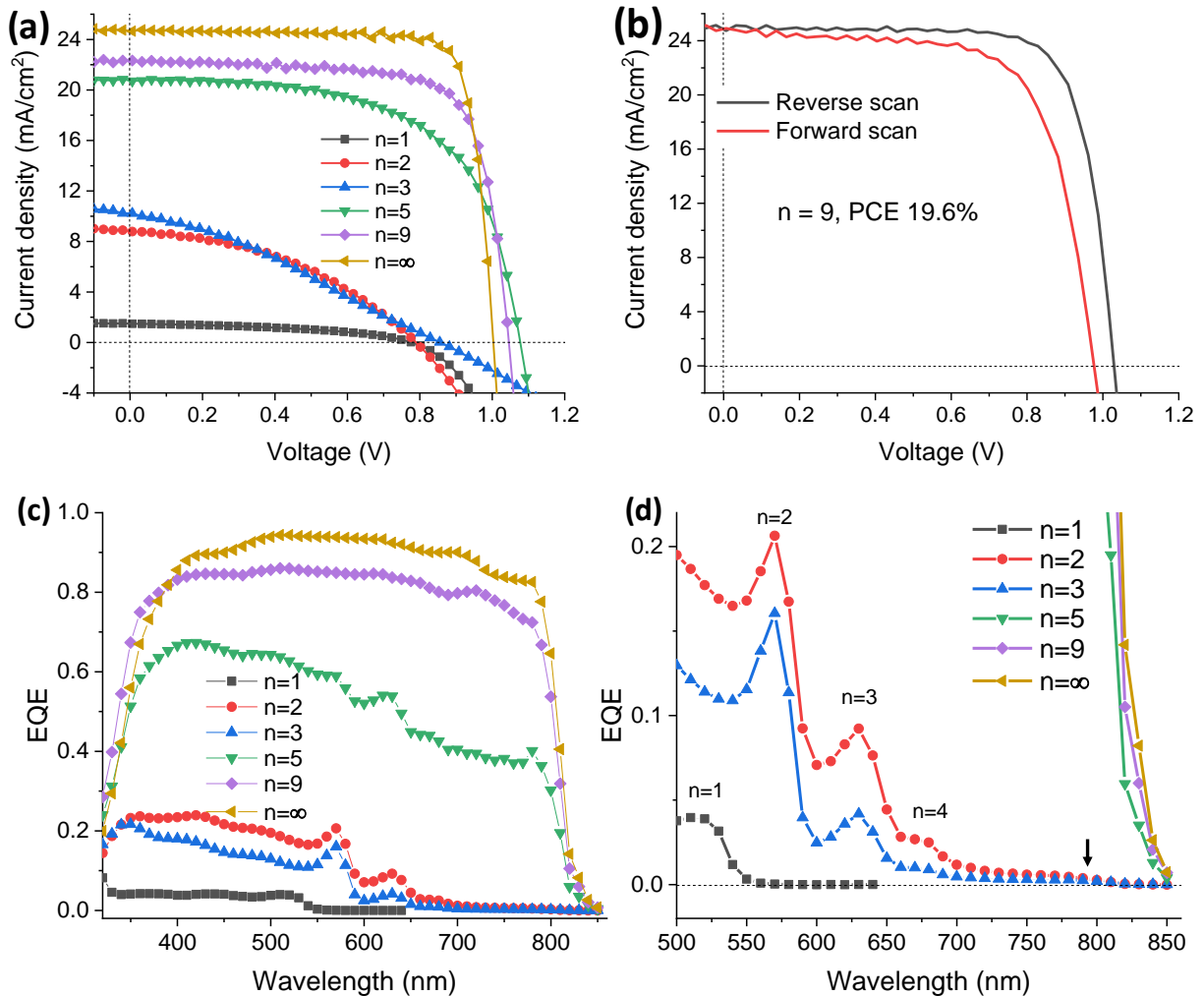


**Figure V. 6** (a)  $J$ - $V$  curves for all the 2D/3D PSCs; (b)  $J$ - $V$  curves of forward and reverse scans for the best 2D/3D cell; (c) EQE curves of 2D/3D PSCs. (d) zoom view of (c).

**Table V. 2** Typical *J-V* curve parameters of 2D/3D PSCs and the best PCE in the brackets. (The forward *J-V* curves were not measured for the low efficiency cells.)

Cell 36%MAcI	Scan direction	<i>V</i> <sub>oc</sub> /V	<i>J</i> <sub>sc</sub> mA/cm <sup>2</sup>	<i>FF</i> /%	<i>PCE</i> /%	<i>HI</i> /%
<b>n=1</b>	Reverse	0.776	1.49	44.80	0.52 (0.52)	
	Forward	/	/	/	/	
<b>n=2</b>	Reverse	0.788	8.80	41.21	2.86 (3.6)	
	Forward	/	/	/	/	
<b>n=3</b>	Reverse	0.856	10.18	30.86	2.69 (2.8)	
	Forward	/	/	/	/	
<b>n=5</b>	Reverse	1.076	20.78	61.30	13.71 (15.3)	14.5
	Forward	1.075	20.97	52.01	11.72	
<b>n=9</b>	Reverse	1.026	23.78	72.43	17.68 (19.6)	10.7
	Forward	1.000	23.65	66.68	15.78	
<b>n=∞</b>	Reverse	1.017	25.56	80.15	20.84 (22.1)	4.4
	Forward	0.999	25.57	77.94	19.92	

## V.4.2 Aging Test

### V.4.2.1 XRD and UV-Vis absorbance

The main purpose of introducing 2D materials into perovskite structure is to improve their stability against moisture. All the 2D/3D samples were tested under ambient environment (Temperature: 15-28°C, relative humidity (RH) 35-70%, day and night). Through comparing the intensities of the feature peaks (00k) in XRD patterns, *n* = 5 and *n* = 9 were found to be the most stable samples (Figure V.7). The zoom view for the peaks in Figure V.7d, e, and f are gathered in Annex-V (Figure A.V.4). After 76 days in the RH 60% laboratory environment, *n* = 9 sample first presented  $\delta$ -phase FAPbI<sub>3</sub> in the XRD pattern. (Note: sample *n* = ∞ is a supplementary data. The environment humidity was lower than before due to the season went into end of autumn and the opening of the heaters in the school. This means the real stability of sample *n* = ∞ should be worse than presented Figure V.7f.) A group of new peaks marked with ♣ quickly appeared for all the aged 2D or quasi-2D perovskite films, which mean this phase was unrelated to FA<sup>+</sup> or MA<sup>+</sup> ions.

The better stability of samples *n* = 5 and *n* = 9 were confirmed by the corresponding UV absorbance spectra in Figure V.8. For sample *n* = 5, the absorbance curves (Figure V.8d) can be divided at 700 nm. The absorbance decreased obviously with the aging time when the wavelength was lower than 700 nm while it kept constant when the wavelength was higher than 700 nm. It is ascribed to the unstable *n* = 2, *n* = 3 and *n* = 4 phases, in which the absorbance edges are located at 582 nm,

640 nm, 682 nm, respectively. It is worth noting that 3D absorbance edges in  $n = 2$  and  $n = 3$  samples disappeared fast while the 2D onsets still existed. This further proves that serious phase separation cannot protect the 3D perovskite phase.

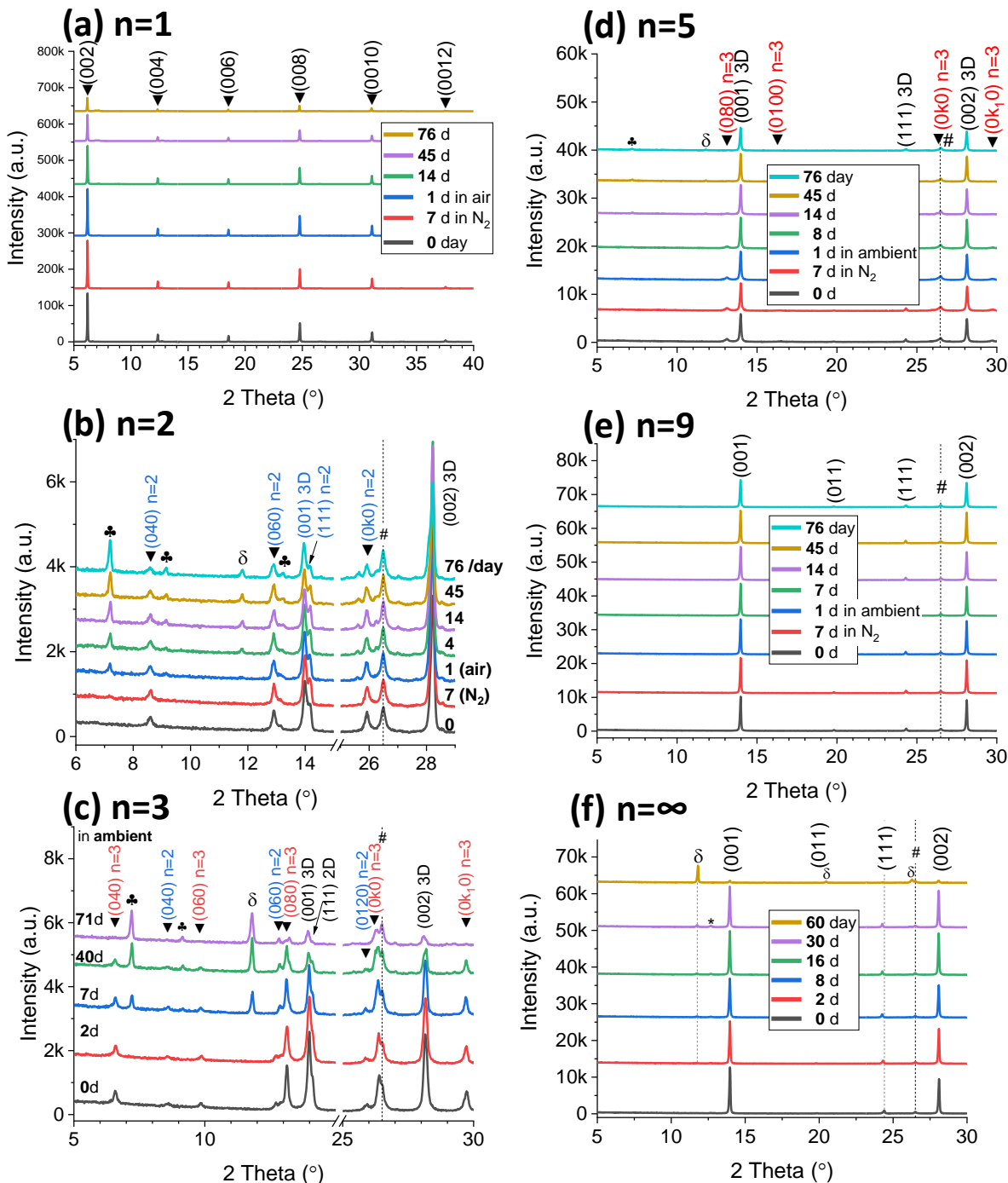


**Figure V. 7** Variations of XRD patterns upon aging time under ambient laboratory conditions for  $n = 1$  to  $n = \infty$  layers. Note: sample  $n = \infty$  is a supplementary data. The environment humidity was lower than before due to the season went into end of autumn and the opening of the heaters in the school. This means the real stability of sample  $n = \infty$  should be worse than we presented Figure V.7f. (RH60 vs. RH35)

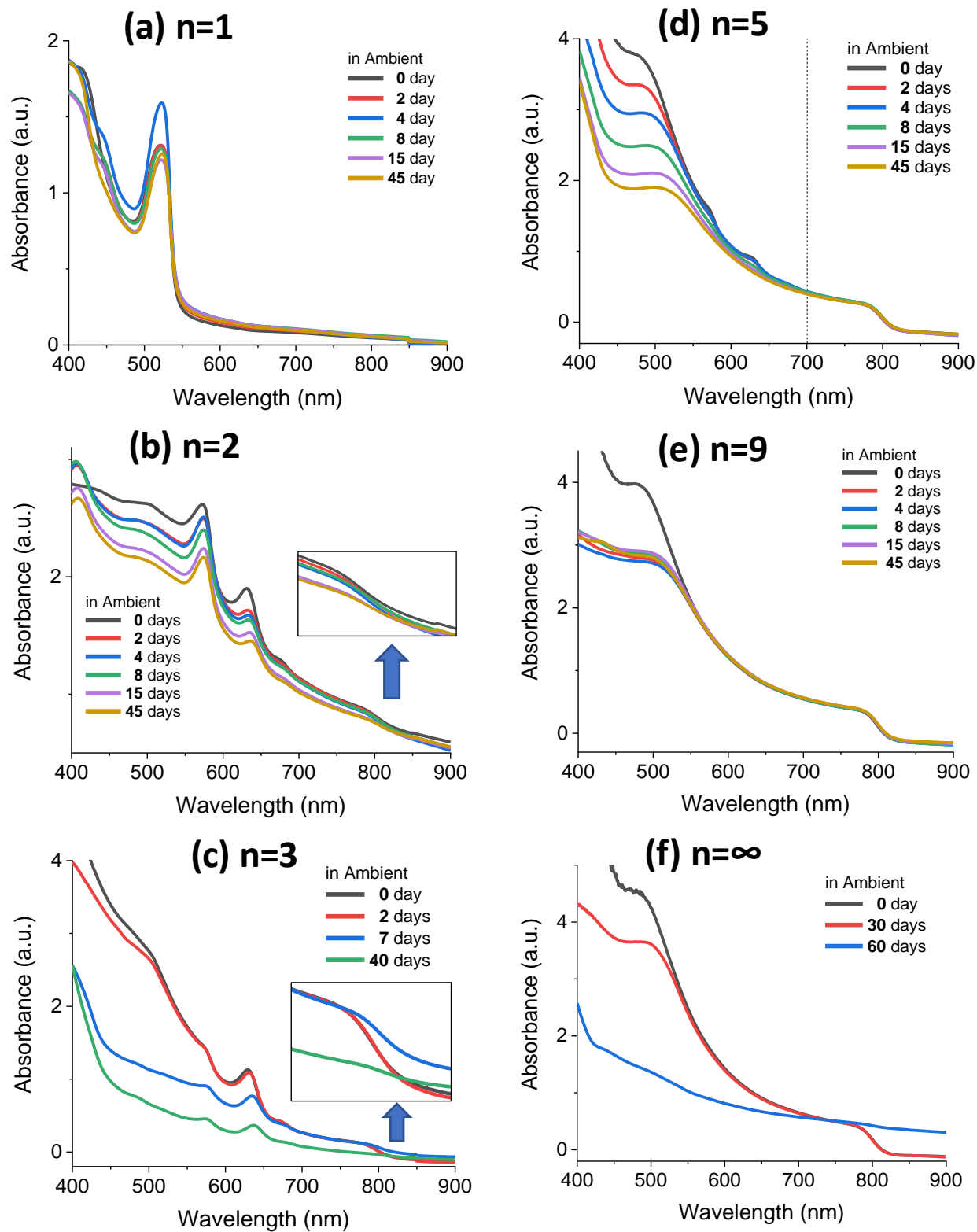


**Figure V. 8** Variations of UV-Vis absorbance curves upon aging time under ambient laboratory condition for  $n = 1$  to  $n = \infty$  layers. Note: the same as caption of Figure V.7.

### V.4.2.2 Stability of the solar cells

#### Against moisture

According to the above results,  $n = 5$  and  $n = 9$  were considered as the most stable samples. The stability against moisture was preliminarily tested by storing the unencapsulated cells in a chamber with a 75-90% RH and ambient light condition. The variations of the  $J$ - $V$  curve parameters with aging time are shown in Figure V.9. The  $n = 9$  cell was slightly more stable than the  $n = 5$  cell, and both are more stable than  $n = \infty$  cell.

The images of the solar cells degradation are disclosed in Figure V.10. The  $n = 5$  and  $n = 9$  cells preserved the black phase more than 200 hours while the  $n = \infty$  cell degraded seriously after 29 hours. We compared the back images of  $n = 5$  and  $n = 9$  cells as shown in Figure V.10b. It is obvious that  $n = 5$  cell was more seriously damaged while their front-side images showed a similar degradation (Figure V.10a). This indicates that there is a more unstable 3D structure  $\text{FAPbI}_3$  in the upper part of the  $n = 5$  layer while the  $n = 9$  film is more homogeneous.

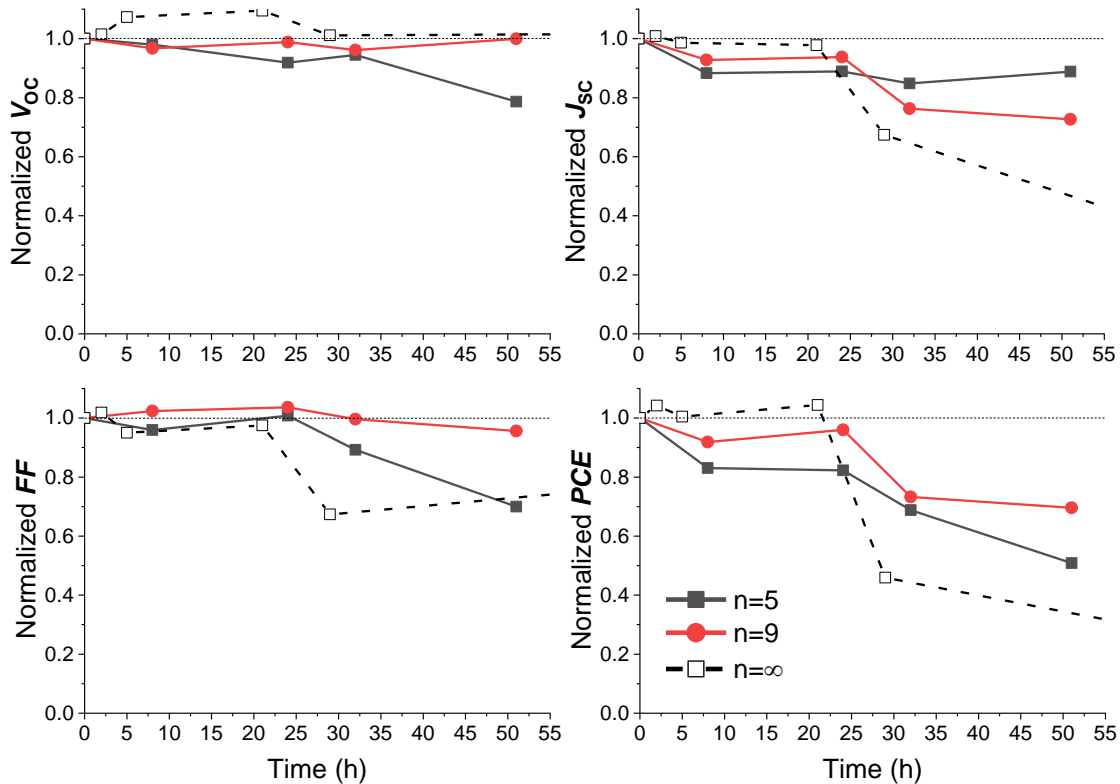


**Figure V. 9** Variations of the  $J$ - $V$  curve parameters with aging time. Note: the cell of  $n = \infty$  originates from another batch in the same condition.

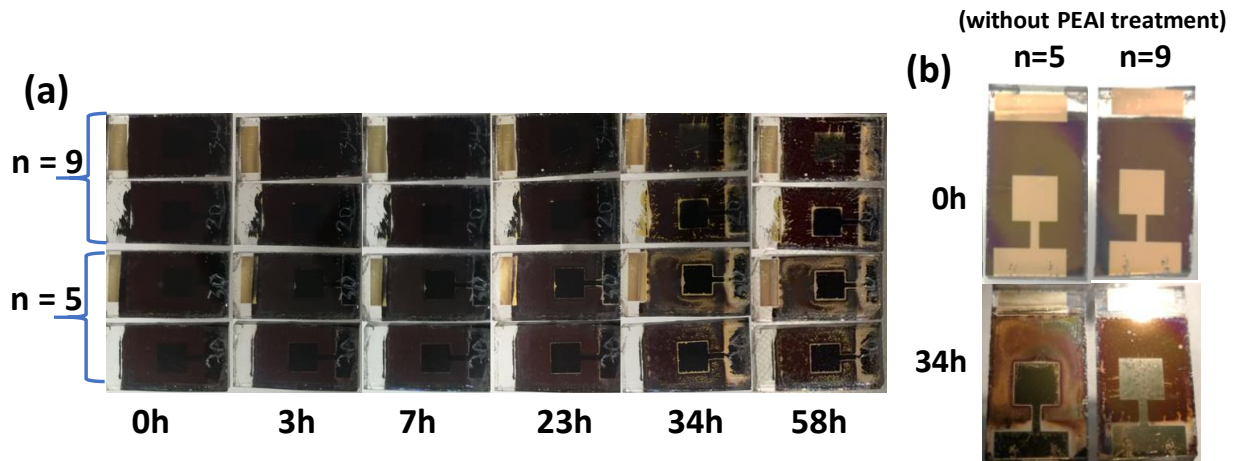


**Figure V. 10** (a) Front-side and (b) back-side images of the solar cells degradation in a high humidity environment of 75-90%RH at 20°C and under ambient light.

### Light stability

The up to 5-hours MPP tracking measurements under continuous 1 sun shining in ambient conditions were conducted on unencapsulated  $n = 9$  samples. Unfortunately, their light stability was not satisfying since the efficiencies decreased continuously (Figure V.11a). Comparing the  $J$ - $V$  curves before and after the tracking, a large reduction of the photocurrents is found in Figure V.11b. On the other hand, the big hysteresis often appeared for fresh sample  $n = 9$  and  $n = 20$  (see Table A.V.1 in Annex-V).

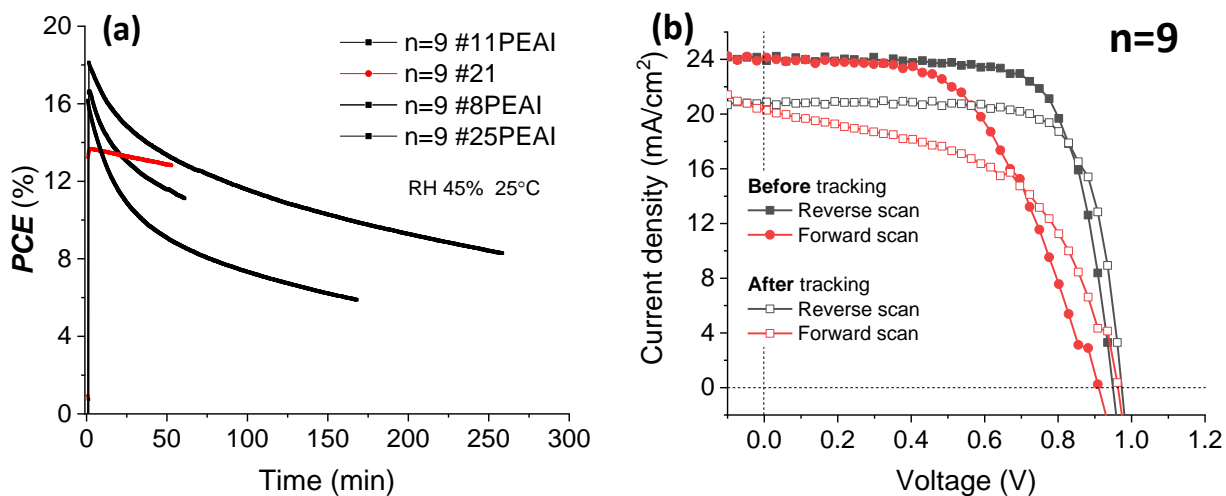


**Figure V. 11** (a) MPP tracking curves of unencapsulated  $n = 9$  samples under 1 sun and in ambient. (b)  $J$ - $V$  curves before and after 5-hours tracking.

## Stability under ambient conditions

The stability of the unencapsulated cells was also tested under ambient conditions. According to the evolution of cell aspects,  $n = 9$  and  $n = 20$  samples have kept dark color for 33 days while sample  $n = \infty$  started to decompose from the 10<sup>th</sup> day as shown in Figure V.12a. The quasi-3D solar cells are much stable than the 3D one if just judging from the aspects of the cells. However, all of them presented a big efficiency reduction as depicted in Figure V.12b ( $n = 20$  cell is a supplementary experiment, the J-V curve parameters are gathered in Table A.V.1, Annex-V). We speculate that the unstable properties under light for quasi-3D PSCs ( $n = 9$  and  $n = 20$ ) are related to the poor interfaces and the formation of new phase ♣.

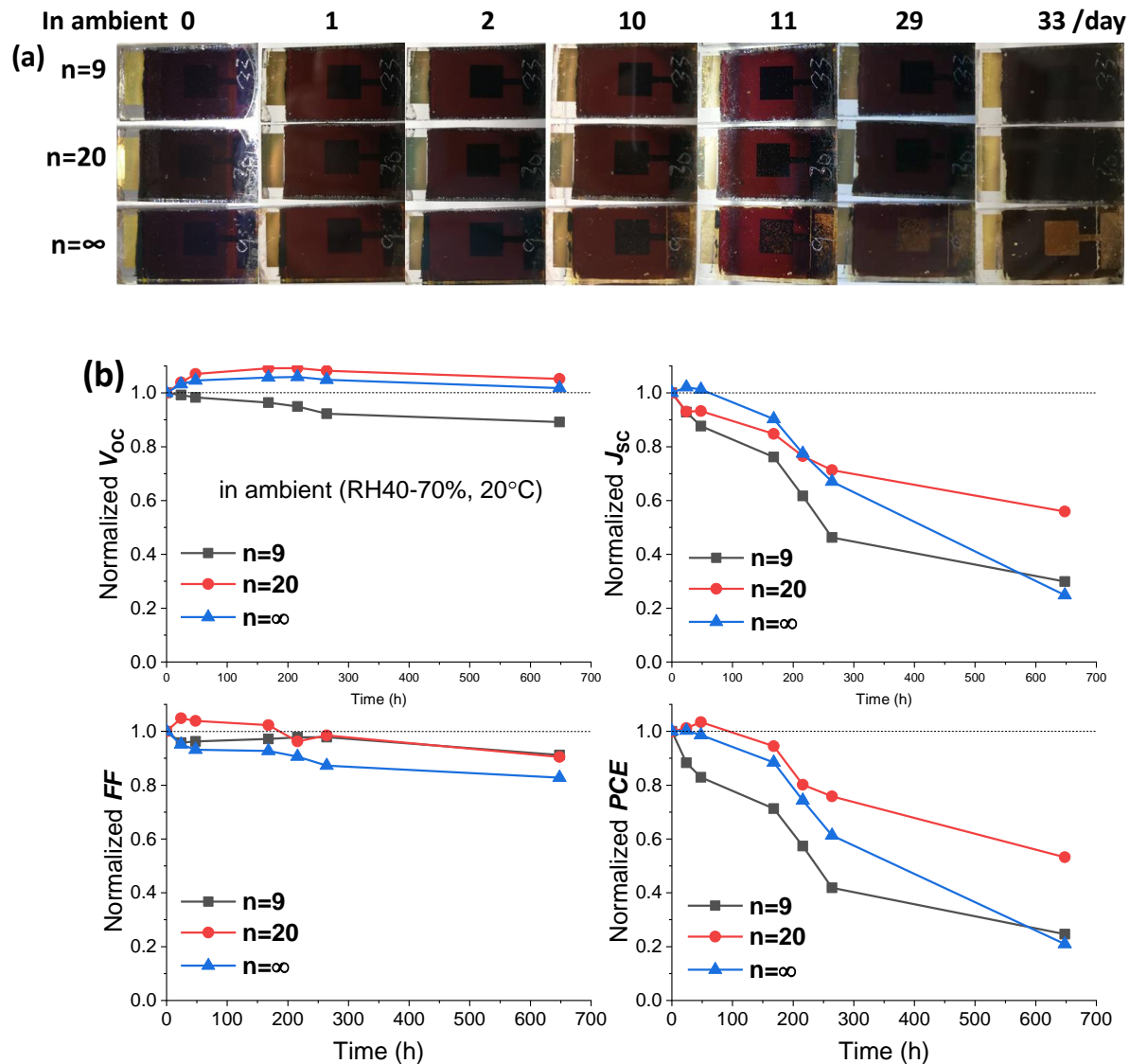


**Figure V. 12** Stability of the  $n = 9$ ,  $n = 20$  and  $n = \infty$  unencapsulated cells in ambient: (a) Images of the evolution of the cell aspects. (b) The evolution of the cell J-V curves parameters.

During the thesis, I have implemented further work on the precursor solution chemistry which has allowed me to find conditions for the stabilization of the 2D/3D perovskite layer while better PCEs were obtained. However, this work is under patenting and is not shown in this dissertation.

#### V.4.2.3 Discussion about the Stability of $(BE)_2PbI_4$ ( $n = 1$ )

##### XRD patterns

The 2D perovskite layers deserved special attention regarding their aging behavior. The aging process of  $(BE)_2PbI_4$  sample was followed by XRD measurements (Figure V.13). The intensity of [00k] direction gradually decreased with aging time. For fresh  $n = 1$  sample, a small  $PbI_2$  peak noted as \* was observed. However, the  $PbI_2$  peak disappeared after 6 days of aging and even did not reappear after 50 days of aging. This indicates that the initially unreacted  $PbI_2$  reacted during the aging time. Meanwhile, two new group peaks ♣ and ♥ were rising with aging time, which possibly means other non-perovskite phases.

We have tried to use a 1: 1 molar ratio of BEI and  $PbI_2$  to make films (noted 1\*) (excess  $PbI_2$  compared to the 2D compound). The XRD patterns are given in Figure V.14 (black one). A strong new phase ♥ was observed and no normal 2D  $(BE)_2PbI_4$  ▼ phase existed. The new phase ♥ was

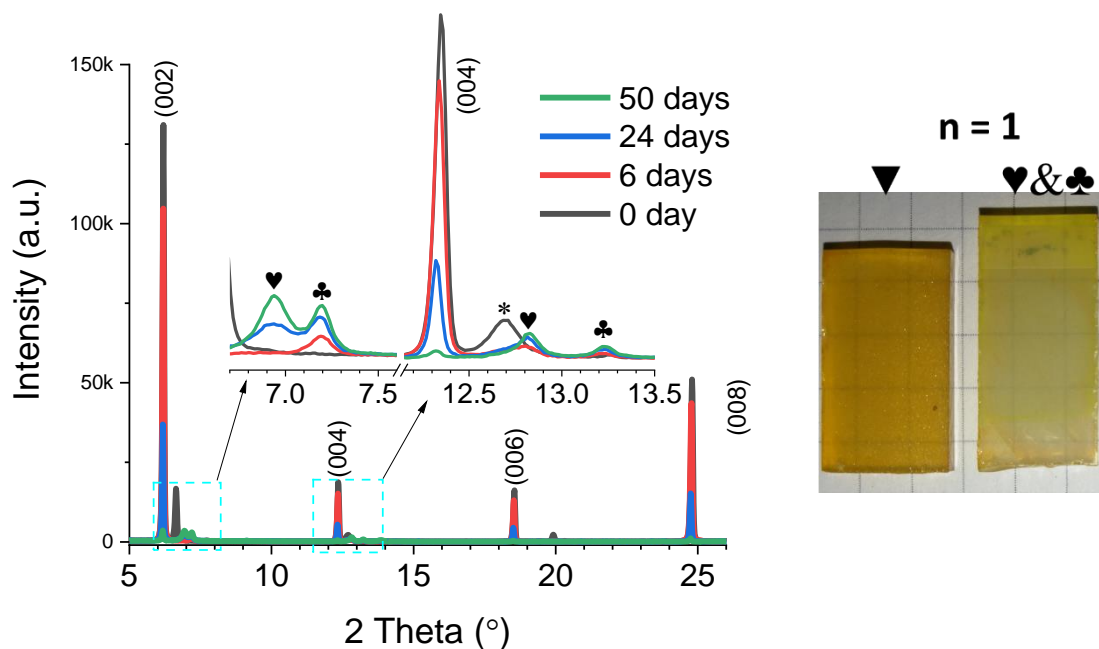


**Figure V. 13** Variation of XRD patterns with the aging time for the stoichiometric  $n = 1$  sample. The inset is a zoom of specific area. \* is  $PbI_2$ , ▼ is normal 2D peak, ♥ and ♣ are 2 kinds of new phases.

gradually transformed into another new phase ♣ after 26-days aging in ambient (Figure V.14 red one). The phase ♣ should be a stable phase at room temperature. This conclusion can also stand from the other XRD aging patterns of 2D/3D samples as shown in Figure V.7. However, the ♣ phase was quickly transformed to ♥ phase, and normal 2D phase ▼ further decomposed slightly after annealing the aged  $n = 1$  sample at  $125^\circ\text{C}$  for 5 min as shown in Figure 14b. The ♣ phase should be a hydrate.

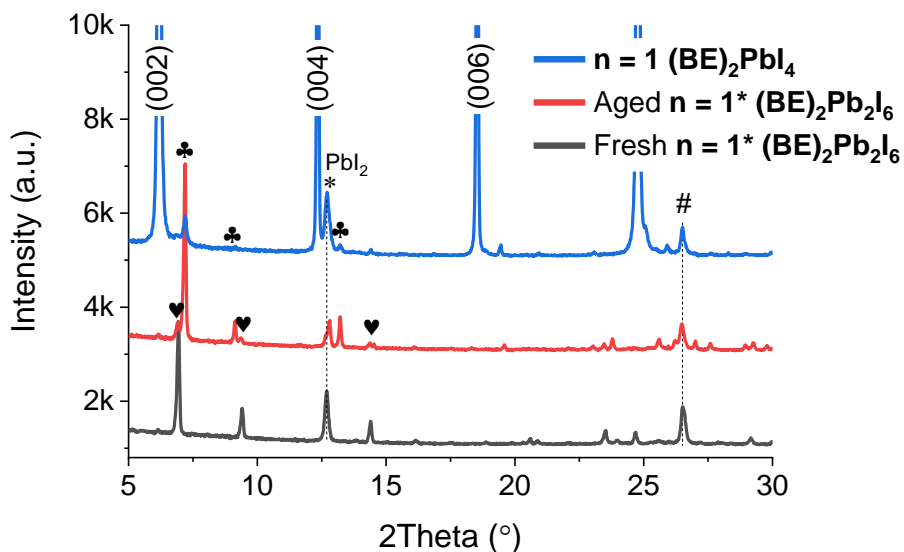


**Figure V. 14** XRD patterns of stoichiometric sample  $n = 1$  (blue), and sample  $n = 1^*$  with excess  $\text{PbI}_2$  in fresh (black) and aged (red) situations.

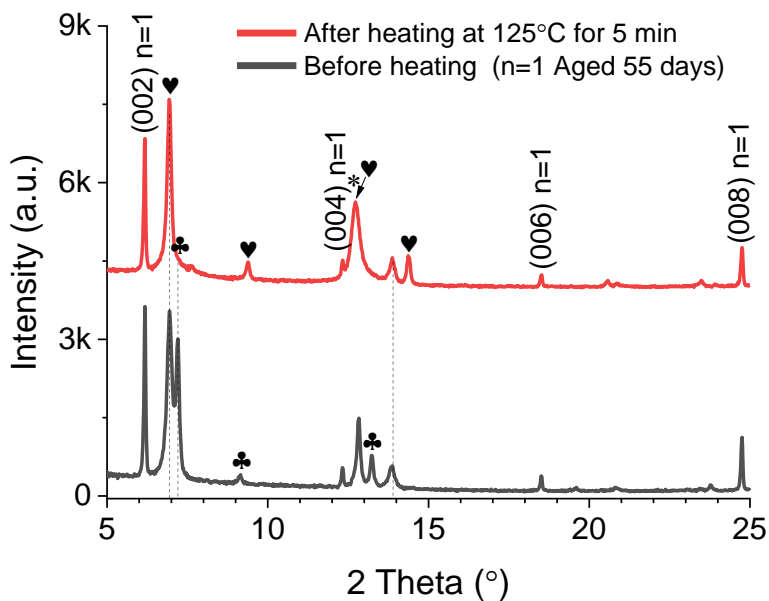


**Figure V.14b** XRD patterns of aged  $n = 1$  sample before and after annealing at  $125^\circ\text{C}$  for 5 min.

## UV-Vis absorbance and steady-state PL spectra

The absorbance and steady-state PL spectra are shown in Figure V.15. The absorption edge and PL peak of sample 1\* with excess  $\text{PbI}_2$  has a blue shift compared to the stoichiometric sample  $n = 1$ . A small absorption edge of stoichiometric  $n = 1$  crystal are observed in  $n = 1^*$  sample as shown in the differential absorbance curve (up and red curve) while no such a phase is observed in the corresponding XRD pattern (Figure V.14).

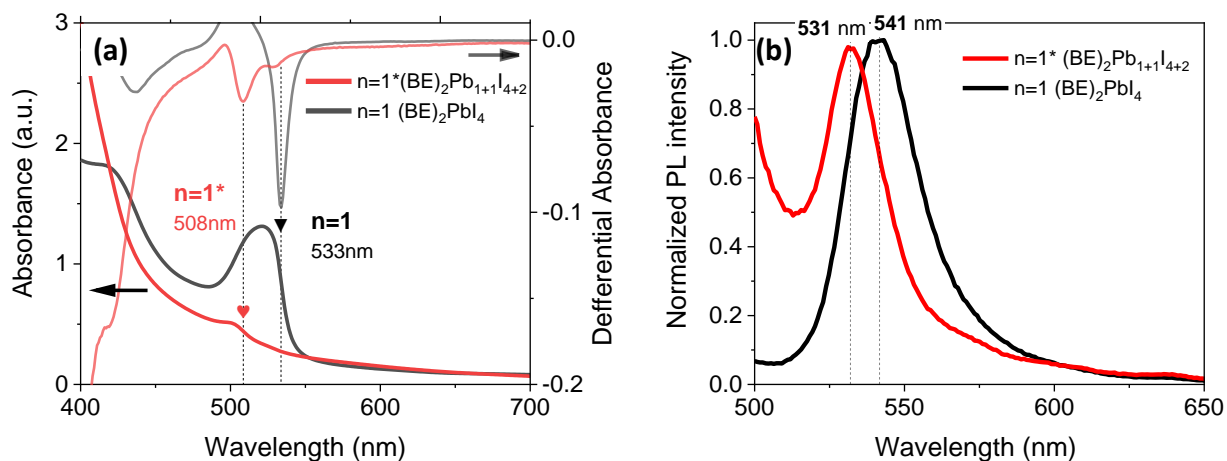


**Figure V. 15** Stoichiometry  $n = 1$  and  $n = 1^*$  with excess  $\text{PbI}_2$ : (a) absorbance at left Y axis and differential absorbance at right Y-axis. (b) Normalized steady-state PL spectra.

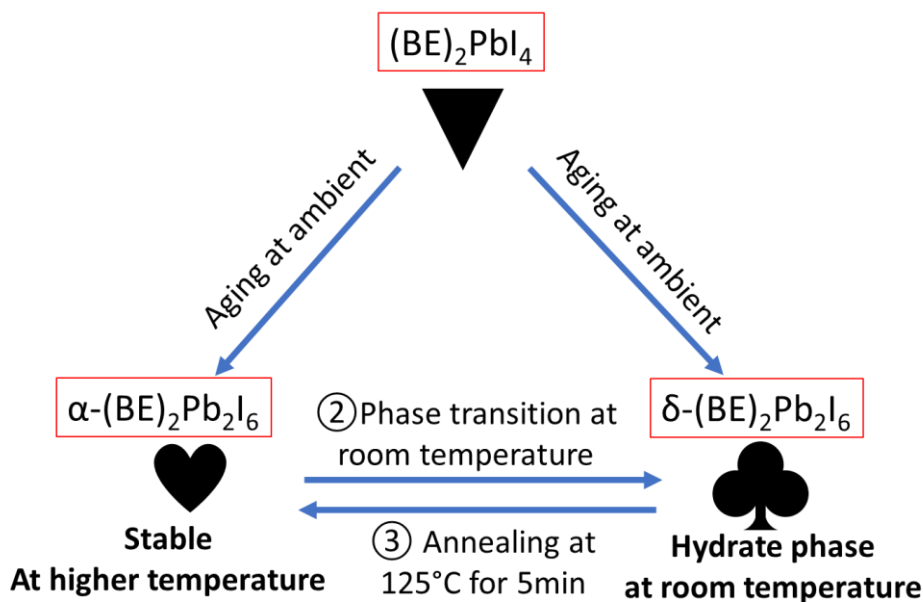


**Figure V. 16** The observed transitions among the  $\blacktriangledown$ ,  $\heartsuit$  and  $\clubsuit$  phase for  $(\text{BE})_2\text{Pb}_{1+x}\text{I}_{4+2x}$  sample.

The relationship between the three phases ( $\blacktriangledown$ ,  $\heartsuit$  and  $\clubsuit$ ) is summarized in Figure V.16. 2D perovskite  $(BE)_2PbI_4$  ( $n = 1$ ) should be stable under the condition of no excess  $PbI_2$  and inert gas. But in a realistic situation, excess  $PbI_2$  inevitably exist in defective places in the film, which will trigger the reaction to form the  $\heartsuit$  and  $\clubsuit$  phase. The morphologies of these three phases were characterized by SEM and they are quite different as shown in Figure V.17 and in Annex-V (Figure A.V.5). The three phases between  $n = 1$  and  $n = 1^*$  have a similar bandgap of 2.33 eV-2.44 eV (Figure V.15) but different absorbance coefficient. It remains a question that if the phase transitions would affect the solar cells photovoltaic properties.

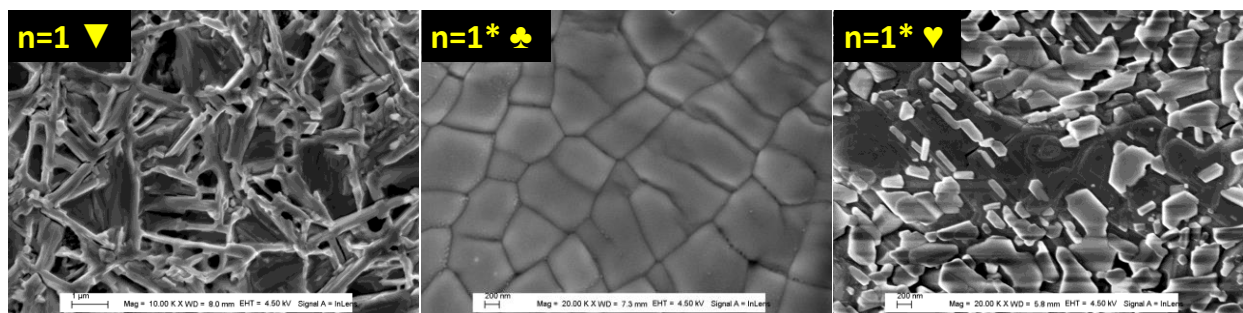


**Figure V. 17** Morphologies of these three phases were characterized by SEM.

## V.5 Conclusions

In summary, BEI based 2D/3D perovskite films and PV devices were systematically studied. We fabricated a series of RP perovskite films with molecular formula of  $BE_2FA_{n-1}Pb_nI_{3n+1}$  ( $n = 1, 2, 3, 5, 9,$  and  $\infty$ ). Then the films were first characterized by XRD, UV-absorbance spectroscopy, and steady-state PL spectroscopy, to analyze the phase composition. The results showed that the quasi-2D perovskite films ( $n \leq 5$ ) were composed of mixed 2D phases, which belong to  $n = 2, n = 3, n = 4, \dots$  and so on. The 2D phases with smaller  $n$  values tend to form at the bottom of the film, which caused the 3D perovskite cannot be well protected. The larger the  $n$  values, the more homogeneous the 2D/3D perovskite films. The morphology of the 2D/3D perovskite films changed from porous structures with dendritic crystals to dense films with cubic crystals as the  $n$  values increasing. The corresponding 2D/3D PSCs were made, and their efficiencies also increased with the  $n$  values. After optimization of the fabrication process, the quasi-3D PSCs and quasi-2D PSCs produced best efficiencies of 19.6% and 17.3%, respectively.

The  $n = 5$  and  $n = 9$  films were the most stable in this series according to the stability test. The 2D/3D perovskite films with more hydrophobic 2D materials in the structure did not present better stability, according to the aging test of these films in ambient. This result confirmed our prediction that the bottom 2D/3D perovskite phases with lower  $n$  values would not effectively protect the perovskite films. The homogeneous 2D/3D perovskite films with suitable  $n$  values can possibly make solar cells with high efficiency and stability. Then, the stability of  $n = 5$  and  $n = 9$  devices were tested in high-humidity and ambient conditions, respectively. Device  $n = 9$  presented better stability in high-humidity condition within 50h while it did not show advantages in a longer time stability test of 27 days in the ambient condition. But the device aspect was stable than that of 3D perovskite. Unfortunately, device  $n = 9$  presented bad stability either, under continuous 1 sun shining. We speculated that the 2D parts  $(\text{BE})_2\text{PbI}_4$  in the films was unstable. Two another non-perovskite phases ( $\heartsuit$  and  $\clubsuit$ ) related to BEI and  $\text{PbI}_2$  were proved to exist in the  $n = 1$  films. The work is still in progress.

This research has given rise to further developments that are leading to a patent pending.

## References

1. Stoumpos, C. C. *et al.* Ruddlesden–Popper hybrid lead iodide perovskite 2D homologous semiconductors. *Chem. Mater.* **28**, 2852–2867 (2016).
2. Mao, L. *et al.* Hybrid Dion–Jacobson 2D lead iodide perovskites. *J. Am. Chem. Soc.* **140**, 3775–3783 (2018).
3. Quan, L. N. *et al.* Ligand-Stabilized Reduced-Dimensionality Perovskites. *J. Am. Chem. Soc.* **138**, 2649–2655 (2016).
4. Wu, G. *et al.* Fine Multi-Phase Alignments in 2D Perovskite Solar Cells with Efficiency over 17% via Slow Post-Annealing. *Adv. Mater.* **31**, 1903889 (2019).
5. Luo, T. *et al.* Compositional Control in 2D Perovskites with Alternating Cations in the Interlayer Space for Photovoltaics with Efficiency over 18%. *Adv. Mater.* **31**, 1903848 (2019).
6. Qing, J. *et al.* Aligned and Graded Type-II Ruddlesden–Popper Perovskite Films for Efficient Solar Cells. *Adv. Energy Mater.* **8**, 1800185 (2018).
7. Cao, D. H., Stoumpos, C. C., Farha, O. K., Hupp, J. T. & Kanatzidis, M. G. 2D Homologous Perovskites as Light-Absorbing Materials for Solar Cell Applications. *J. Am. Chem. Soc.* **137**, 7843–7850 (2015).

8. Li, Y. *et al.* Bifunctional Organic Spacers for Formamidinium-Based Hybrid Dion–Jacobson Two-Dimensional Perovskite Solar Cells. *Nano Lett.* **19**, 150–157 (2019).
9. Lin, Y. *et al.* Unveiling the operation mechanism of layered perovskite solar cells. *Nat. Commun.* **10**, 1008 (2019).
10. Zheng, H. *et al.* The Effect of Hydrophobicity of Ammonium Salts on Stability of Quasi-2D Perovskite Materials in Moist Condition. *Adv. Energy Mater.* **8**, 1800051 (2018).
11. Mao, L. *et al.* Role of Organic Counterion in Lead- and Tin-Based Two-Dimensional Semiconducting Iodide Perovskites and Application in Planar Solar Cells. *Chem. Mater.* **28**, 7781–7792 (2016).
12. Lee, J.-W. *et al.* 2D perovskite stabilized phase-pure formamidinium perovskite solar cells. *Nat. Commun.* **9**, 3021 (2018).
13. Shi, J. *et al.* Fluorinated Low-Dimensional Ruddlesden–Popper Perovskite Solar Cells with over 17% Power Conversion Efficiency and Improved Stability. *Adv. Mater.* **31**, 1901673 (2019).
14. Kim, M. *et al.* Methylammonium Chloride Induces Intermediate Phase Stabilization for Efficient Perovskite Solar Cells. *Joule* **3**, 2179–2192 (2019).
15. Rolston, N. *et al.* Engineering Stress in Perovskite Solar Cells to Improve Stability. *Adv. Energy Mater.* **8**, 1802139 (2018).



## General Conclusion and Perspectives

### General conclusion

The serious energy shortage and environmental pollution problems urge the development of renewable energies. Photovoltaic technologies as one of the most promising strategy have attracted extensive attention since the middle of the 20<sup>th</sup> century. Nowadays, the most advanced solar cells can produce a power conversion efficiency (PCE, from light energy to electricity) greater than 40% while these devices are extremely expensive. The high cost inhibits large-scale production. Perovskite solar cells are leading the next-generation photovoltaic devices due to their superior photovoltaic properties and low cost. The certified record efficiencies for single junction PSC and 2-terminal perovskite/Si tandem device have already reached 25.5% and 29.1% in the past 10 years.

In this thesis, we have improved the photovoltaic properties of PSCs in terms of interface control and perovskite composition engineering. In Chapter I, basic semiconductor knowledges, such as doping, energy band level, crystals, and so on, were given firstly to favor the understanding to the results and discussion in the thesis. Then the working principles of main photovoltaic devices are illustrated. The fundamental theory is the photoelectric effect. The evolution of PSCs was introduced through reviewing the classic papers. Besides, we also provided a brief introduction to ultra-violet (UV) photodetectors (PDs) and explained the important parameters for UV PDs.

In Chapter II, we studied the effect of modifying TiO<sub>2</sub> layers by various organic acid molecules with a dipole moment varying in a large range. The adsorption of the acid modifiers was then thoroughly investigated by a combined experimental and theoretical approach. A bridging bidentate mode was determined as the binding methods of carboxylate group onto TiO<sub>2</sub> surface. The theoretical FTIR spectra have been found in good agreement with the experimental ones and clearly show the binding of the molecular dipole onto the oxide surface. The surface work functions (WFs) of these samples are characterized by Kelvin probe and UV photoelectron spectroscopy (UPS). A linear relationship between the WF values and the dipole moments of the adsorbed modifiers has been determined. We have then designed and fabricated a solid-state nanostructured UV-A photodetector based on the TiO<sub>2</sub>/Spiro-OMeTAD p-n heterojunction. Reliable study of the effect of interfacial acid modifiers on the PD response was provided in this Chapter. The NBA modifier has permitted to boost the responsivity of the device by 70% compared to the pristine p-n junction. The higher responsivity of the NBA-modified PD has been then

explained by the better and faster electron charge transfer towards the electrical contact on TiO<sub>2</sub>. The measured response time was very fast, below 3 ms. In addition, the photocurrent in an NBA modified UV PD was almost unchanged after 156 days of storage in ambient condition. The long-term stability of the devices was important for the practical application.

In Chapter III, we have demonstrated that the engineering of the interface between perovskite and titania is important to get highly efficient perovskite solar cells. By using this strategy, we have been able to prepare PSCs reaching a PCE of 21.3%. We have shown that in high efficiency triple cation PSCs, the chloride-functionalized benzoic acid molecule provides a significant beneficial effect. CBA forms a SAM at the TiO<sub>2</sub> surface and is attached in a bridging bidentate mode as we discussed in Chapter II. Our experimental and theoretical investigations emphasized that CBA SAM at the oxide/perovskite interface is beneficial for the structural continuity, the trap state reduction and for the global quality of the perovskite. We showed that the presence of a halogen substituent on the ligand (Cl in the case of CBA) is a significant requirement to establish a stable bonding with the perovskite. By modeling, fast charge injection (24 fs) and efficient electronic charge transfer (99.94%) were calculated for the TiO<sub>2</sub>/CBA/MAPI system.

In Chapter IV, we developed the use of methyl ammonium chloride as an additive at rather low concentration mixed organic cation precursor solutions. MA<sub>2</sub>Cl is shown to mediate the growth of the layers. The resulting films were uniform, compact, with no pinholes and made of remarkably large size perovskite crystal grains. By this technique, a small amount of MA cation was incorporated in FAPbI<sub>3</sub>, stabilizing the pure  $\alpha$ -phase. The exact composition with FA<sub>0.94</sub>MA<sub>0.06</sub>PbI<sub>3</sub> molecular formula was determined by liquid <sup>1</sup>H-NMR. The excess MA<sub>2</sub>Cl was removed by sublimation and degradation. The presented growth technique is reliable, robust and gives devices efficient over a large range of additive concentration (40 m%-55 m%). To further increase the PCE of the solar cells, a treatment with a PEAI solution was implemented. This treatment, without any thermal annealing step, leads to the spontaneous formation of a (PEA)<sub>2</sub>PbI<sub>4</sub> perovskite layer at the surface. This buffer layer has been shown to favor a fast transfer of the holes towards the HTL and to reduce the recombination at the perovskite/HTL interface. Overall, the optimized devices had a stabilized PCE of 22.1%. A comprehensive investigation of the systems by impedance spectroscopy was carried out. The power output of the produced devices was

remarkably stable. These PSCs were proved resistant to electrical stresses, to light irradiation and to moisture.

In Chapter V, BEI based mixed-dimensional (MD) OIHPs were employed as a light absorber layer due to their excellent stability against moisture. We have systematically studied the properties of the so-called MD-OIHP solar cells. A series of perovskite films with molecular formula of  $\text{BE}_2\text{FA}_{n-1}\text{Pb}_n\text{I}_{3n+1}$  ( $n = 1, 2, 3, 5, 9, \text{ and } \infty$ ) were fabricated. The result showed that the quasi-2D perovskite films ( $2 \leq n \leq 5$ ) were composed of multiple 2D phases, which belongs to  $n = 2, n = 3, n = 4, \dots$  and so on. The 2D phases with smaller  $n$  values tend to form at the bottom of the film and cannot efficiently protect the perovskite layer. The larger the  $n$  values, the more homogeneous the 2D/3D perovskite films. Films for  $n = 5$  and  $n = 9$  were the most stable in this series after the stability test. This indicates that suitable  $n$  values can possibly make solar cell with high efficiency and stability. In this experiment, we have obtained highly stable  $n = 9$  perovskite films. However, the corresponding solar cells had a serious light instability problem. We speculate that this is related to the fact that the poor interface and  $(\text{BE})_2\text{PbI}_4$  can easily produce a hydrate phase ♣. This process needs more  $\text{PbI}_2$  participating, which might take from the 3D perovskite structure.

## Perspectives

Nowadays, perovskite solar cell is still a hot research topic. We propose several perspectives according to the studies in this thesis:

**1. Interface engineering:** Defects are easy to appear at the interface, which limits the  $V_{\text{OC}}$  in the devices. In Chapter II, we introduced Cl-terminated benzoic acid to bridge  $\text{TiO}_2$  and perovskite. It successfully improved the charge injection and reduced the defects. However, we did not find improvement for the  $V_{\text{OC}}$  and the stability. And the slightly increased hysteresis was another disconcerting factor. On the other hand,  $\text{NO}_2$ -terminated benzoic acid damaged the cells efficiency, but it remarkably improved the cells stability (Figure III.13 and 17). This indicates that the stability can be improved, even though the modifier layer locates at the bottom.  $\beta$ -alanine is also worth noting because it possibly passivates the shallow traps of  $\text{TiO}_2$  layer according to its UPS curve in Figure II.6 and it did not increase the cells hysteresis. Comprehensively, fluorine-terminated benzoic acids or linear alkyl acids could be considered as the new SAMs. The anchoring group of carboxyl can be retained due to their passivation to the defects on  $\text{TiO}_2$ .

On the other hand, the efficiency loss at the perovskite/HTM interface occupied a big part and were possibly reduced. PEAI treatment was proved to improve the cells efficiency by the passivation to the defects on the perovskite surface. We need to distinguish the functions from PEAI itself and/or the in-situ formed 2D perovskite layer. It will help us to find better 2D materials for the post-treatment. PEAI post-treatment could apparently improve the cells efficiency while it is not working on the device stability improvement. Strong hydrophobic 2D materials, such as pentafluorophenylethylammonium (4F-PEAI) and p-methoxyphenethylammonium iodide (CH<sub>3</sub>O-PEAI) are interesting. 2D perovskites with higher formation energy (1-naphthylmethylamine iodide) are considered with better stability, whatever considering from the functions of 2D materials itself or the formed 2D perovskites. On the other hand, it is also important to design the post-treatment materials based on the HTM structure, especially in terms of improving the contacts between the perovskite and HTM.

**2. Perovskite composition engineering:** FAPbI<sub>3</sub> perovskite has a suitable bandgap and higher thermal stability. FA<sup>+</sup> cation is suggested keeping in the structure. For inhibiting its  $\delta$ -phase transform and improving its stability, inorganic alkali metal cations, such as K<sup>+</sup>, Rb<sup>+</sup>, Cs<sup>+</sup>, can be considered. To make high-quality perovskite films, the suitable additives in the precursor solutions are very important, which determined the devices photovoltaic properties. To the best of knowledge, the Cl<sup>-</sup> ion is a good candidate.

**3. Low-cost HTM:** The commonly used spiro-OMeTAD and poly(triarylamine) (PTAA) are quite expensive. Their conductivities depend on doping engineering, which sacrifice their stability. Inorganic HTM materials and polymer HTM materials are noteworthy, such as nickel oxide (NiO), poly(3-hexylthiophene-2-5-diyl) (P3HT), and so on.

## Annex II-Chapter II

### II.3 Computational Details

All calculations were carried out with the ab initio CRYSTAL17 code,<sup>[1]</sup> which is based on a linear combination of atom-centered Gaussian orbitals and solves self-consistently Hartree-Fock and Kohn-Sham equations.

The (101) surface of the anatase phase of TiO<sub>2</sub> was considered for the adsorption of the ligands since this surface is well-known to be highly stable and reactive (Q8\_Rev#3).<sup>[2-4]</sup> A two-dimensional periodic slab with 4-Ti layers was cut out from the TiO<sub>2</sub> anatase bulk system (I4<sub>1</sub>/amd space group) with the following PBE0-D3 optimized cell parameters: 3.7578 Å (a), 9.7039 Å (c). The slab obtained here is used as a starting point for the adsorption, and a rectangular (2x1) supercell was considered in order to avoid artificial interaction between adsorbates from one cell to the other due to the 2D periodicity of the model. The *a* and *b* lattice parameters for this supercell slab model are 7.4906 Å and 5.5442 Å, respectively, corresponding to a surface coverage of one ligand molecule per 3.9 nm<sup>2</sup>. Sampling of the irreducible Brillouin zone was done with 7 k points for this system. Numerical DFT integration was performed considering 75 radial points and 974 angular points, ensuring an error on the integrated electron density lower than 10<sup>-5</sup> |e<sup>-</sup>| per unit cell. The Coulomb and exchange series were truncated with threshold values of 10<sup>-7</sup>, 10<sup>-7</sup>, 10<sup>-7</sup>, 10<sup>-7</sup>, and 10<sup>-18</sup>.

Organic ligands were described using all electron basis sets with (621/21/1), (7311/311/1), (8411/411/1), (511/1) and (86311/6311) for C, N, O, H and Cl atoms, respectively. Durand and Barthelat large core pseudopotentials with (1/1/41) and (31/31) contractions were used for Ti and O atoms of the TiO<sub>2</sub> substrate, respectively.<sup>[5,6]</sup>

Exchange and correlation energies were described using the global hybrid PBE0 functional,<sup>[7]</sup> with 25% of HF exchange. Additional D3 dispersion corrections were also included.<sup>[8]</sup>

To simulate the experimental environment, the solvent, methanol, was added to the models, considering a molecular binding mode to the TiO<sub>2</sub> surface. As described in the manuscript, this allows to limit the tilting of the different ligands adsorbed on the surface.

For adsorption energies ( $E_{\text{ads}}$ ), total adsorption energies of ligand and methanol ( $E_{\text{ads-total}}$ ) were first computed, as the difference between the total energies ( $E_{\text{adsorbate-surface}}$ ) of the combined adsorbate/substrate system and the sum of the relaxed energies of a TiO<sub>2</sub> surface with a H<sup>+</sup> ( $E_{\text{surface+H}}$ ) and a negatively charged adsorbate molecule in the gas phase ( $E_{\text{ligand-}}$ ), and a methanol molecule in the gas phase ( $E_{\text{CH3OH}}$ ) as:

$$E_{\text{ads-total}} = E_{\text{adsorbate-surface}} - (E_{\text{surface+H}} + E_{\text{ligand-}} + E_{\text{CH3OH}})$$

The adsorption energy of methanol  $E_{\text{ads-methanol}}$  was calculated with the following formula:

$$E_{\text{ads-methanol}} = E_{\text{CH3OH-surface}} - (E_{\text{surface}} + E_{\text{CH3OH}})$$

with  $E_{\text{CH3OH-surface}}$  corresponding to the difference of the total energy of the CH<sub>3</sub>OH/TiO<sub>2</sub> system and the sum of the relaxed energies of a bare TiO<sub>2</sub> surface and the CH<sub>3</sub>OH molecule. Finally, the adsorption energies of the ligands ( $E_{\text{ads-ligand-}}$ ) were computed as the difference between  $E_{\text{ads-total}}$  and  $E_{\text{ads-methanol}}$ :

$$E_{\text{ads-ligand-}} = E_{\text{ads-total}} - E_{\text{ads-methanol}}$$

A negative value of  $E_{\text{ads-ligand-}}$  corresponds a thermodynamically favored adsorption process.

During geometry optimization, only atomic positions were allowed to relax, while lattice parameters were constrained to those of the supercell mentioned above. Numerical harmonic frequency calculations were performed at the  $\Gamma$ -point on the optimized structures in order to compute the IR spectra of the adsorbed molecules. To limit computational cost, only the first TiO<sub>2</sub> layer and the adsorbed ligand and methanol

molecule were included in the Hessian construction. Test calculations including more TiO<sub>2</sub> layers showed negligible differences with values discussed here.

**Table A.II.1** Molecular structure and atom labelling of (a) CBA, (b) NBA, (c) MBA and (d)  $\beta$ -ALA. Selected geometrical parameters (Angles in deg; Distances in Å) for isolated and adsorbed molecular systems and corresponding adsorption energies (in kcal/mol) and tilt angle to the surface normal ( $\theta_a$ ).

	(a)	(b)	(c)	(d)	
	CBA	NBA	MBA	Beta-alanine	
Distance(Å)	CBA	CBA@TiO <sub>2</sub>	Distance(Å)	NBA	NBA@TiO <sub>2</sub>
$d_{O_1C_7}/d_{O_2C_7}$	1.35/1.21	1.26/1.27	$d_{O_1C_7}/d_{O_2C_7}$	1.35/1.21	1.26/1.27
$d_{C_1C_7}/d_{C_4Cl}$	1.48/1.79	1.48/1.79	$d_{C_1C_7}/d_{C_4N}$	1.49/1.47	1.49/1.48
$d_{H_2C_5}/d_{H_3C_3}$	1.09/1.09	1.09/1.09	$d_{H_2C_5}/d_{H_3C_3}$	1.09/1.08	1.08/1.08
$d_{H_4C_6}/d_{H_5C_2}$	1.09/1.09	1.08/1.09	$d_{H_4C_6}/d_{H_5C_2}$	1.09/1.09	1.08/1.09
$d_{O_1Ti}/d_{O_2Ti}$	-	2.15/2.06	$d_{O_3N}/d_{O_4N}$	1.22/1.22	1.22/1.22
$\Theta_a$		30.3°	$d_{O_1Ti}/d_{O_2Ti}$	-	2.16/2.05
$E_{ads-ligand}$		-20.73	$\Theta_a$		31.6°
			$E_{ads-ligand}$		-11.33
Distance(Å)	MBA	MBA@TiO <sub>2</sub>		Beta-ALA	Beta-ALA@TiO <sub>2</sub>
$d_{O_1C_7}/d_{O_2C_7}$	1.35/1.21	1.27/1.27	$d_{O_1C_1}/d_{O_2C_1}$	1.35/1.21	1.26/1.27
$d_{C_1C_7}/d_{C_4O}$	1.47/1.36	1.48/1.35	$d_{C_1C_2}/d_{C_2C_3}$	1.51/1.54	1.51/1.52
$d_{H_2C_5}/d_{H_3C_3}$	1.09/1.09	1.09/1.08	$d_{C_3N_1}$	1.46	1.46
$d_{H_4C_6}/d_{H_5C_2}$	1.09/1.09	1.08/1.09	$d_{H_2C_2}/d_{H_3C_2}$	1.10/1.09	1.10/1.10
$d_{OC_8}/d_{H_{6-8}C_8}$	1.41/1.10	1.35/1.10	$d_{C_3H_4}/d_{C_3H_5}$	1.10/1.10	1.10/1.09
$d_{O_1Ti}/d_{O_2Ti}$	-	2.16/2.04	$d_{NH_6}/d_{NH_7}$	1.02/1.01	1.02/1.01
$\Theta_a$		31.6°	$d_{O_1Ti}/d_{O_2Ti}$	-	2.13/2.08
$E_{ads-ligand}$		-30.62	$\Theta_a$		13.4°
			$E_{ads-ligand}$		-20.20

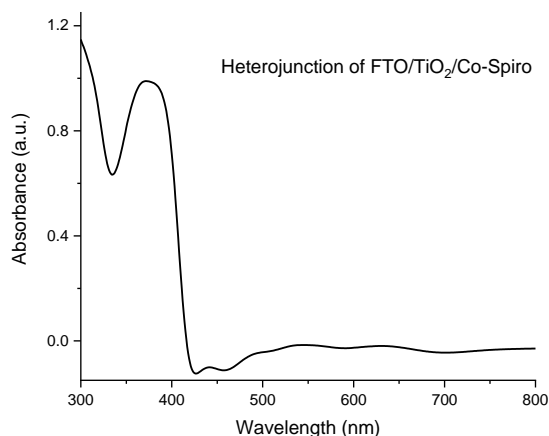


**Figure A.II.1** UV-vis absorbance of the heterojunction based Co doped spiro-OMeTAD.

**Table A.II.2a** Photovoltaic parameters in fresh pure spiro system.

	<i>V<sub>oc</sub></i> /V	<i>J<sub>sc</sub></i> mA/cm <sup>2</sup>	<i>FF</i> /%	<i>PCE</i> /%
Solvent	0.737	0.67	33.87	0.16
CBA	0.588	1.19	32.38	0.22
MBA	0.707	0.63	15.97	0.07
β-ALA	0.817	0.93	35.34	0.27
NBA	0.429	1.25	25.75	0.14

**Table A.II.2b** Photovoltaic parameters in **matured pure** spiro system. (aging 4 weeks in air)

	<i>V<sub>oc</sub></i> /V	<i>J<sub>sc</sub></i> mA/cm <sup>2</sup>	<i>FF</i> /%	<i>PCE</i> /%
Solvent	0.651	0.83	39.75	0.22
CBA	0.575	1.24	46.03	0.33
MBA	0.714	0.75	43.49	0.23
β-ALA	0.796	0.765	45.91	0.28
NBA	0.466	1.51	31.80	0.22

**Table A.II.3a** Photovoltaic parameters in **fresh Co-doped** spiro system.

	<i>V<sub>oc</sub></i> /V	<i>J<sub>sc</sub></i> mA/cm <sup>2</sup>	<i>FF</i> /%	<i>PCE</i> /%
Solvent	0.545	0.56	44.23	0.13
CBA	0.470	0.71	50.35	0.16
MBA	0.545	0.50	44.39	0.11
NBA	0.441	0.62	44.24	0.12
β-ALA	0.632	0.55	39.87	0.14

**Table A.II.3b** Photovoltaic parameters in **matured Co-doped** spiro based PDs. (aging 2 weeks in air)

	<i>V<sub>oc</sub></i> /V	<i>J<sub>sc</sub></i> mA/cm <sup>2</sup>	<i>FF</i> /%	<i>PCE</i> /%
Solvent	0.569	0.56	47.27	0.15
CBA	0.479	0.70	51.43	0.17
MBA	0.551	0.52	41.90	0.12
NBA	0.453	0.67	47.41	0.14
β-ALA	0.640	0.54	45.36	0.16

**Table A.II.4a** Photovoltaic parameters in **Li&Co doped** spiro system.

	<b>Voc /V</b>	<b>Jsc mA/cm<sup>2</sup></b>	<b>FF /%</b>	<b>PCE /%</b>
Solvent	0.723	0.15	57.91	0.06
CBA	0.717	0.22	57.28	0.09
MBA	0.735	0.22	61.34	0.10
NBA	0.685	0.31	58.77	0.12
$\beta$ -ALA	0.758	0.16	60.58	0.07

## References

1. Barnard, P. Zapol, *Phys. Rev. B* **2004**, 70, 235403.
2. A. Barnard, P. Zapol, L. Curtiss, *Surf. Sci.* **2005**, 582, 173.
3. C. Arrouvel, M. Digne, M. Breyse, H. Toulhoat, P. Raybaud, *J. Catal.* **2004**, 222, 152.
4. J. Berthelat, P. Durand, *Gazzetta Chimica Italiana* **1978**, 108, 225.
5. J. Barthelat, P. Durand, A. Serafini, *Molecular Physics* **1977**, 33, 159.
6. C. Adamo, V. Barone, *J. Chem. Phys.* **1999**, 110, 6158.
7. S. Grimme, S. Ehrlich, L. Goerigk, *J. Comput. Chem.* **2011**, 32, 1456.

## Annex III-Chapter III

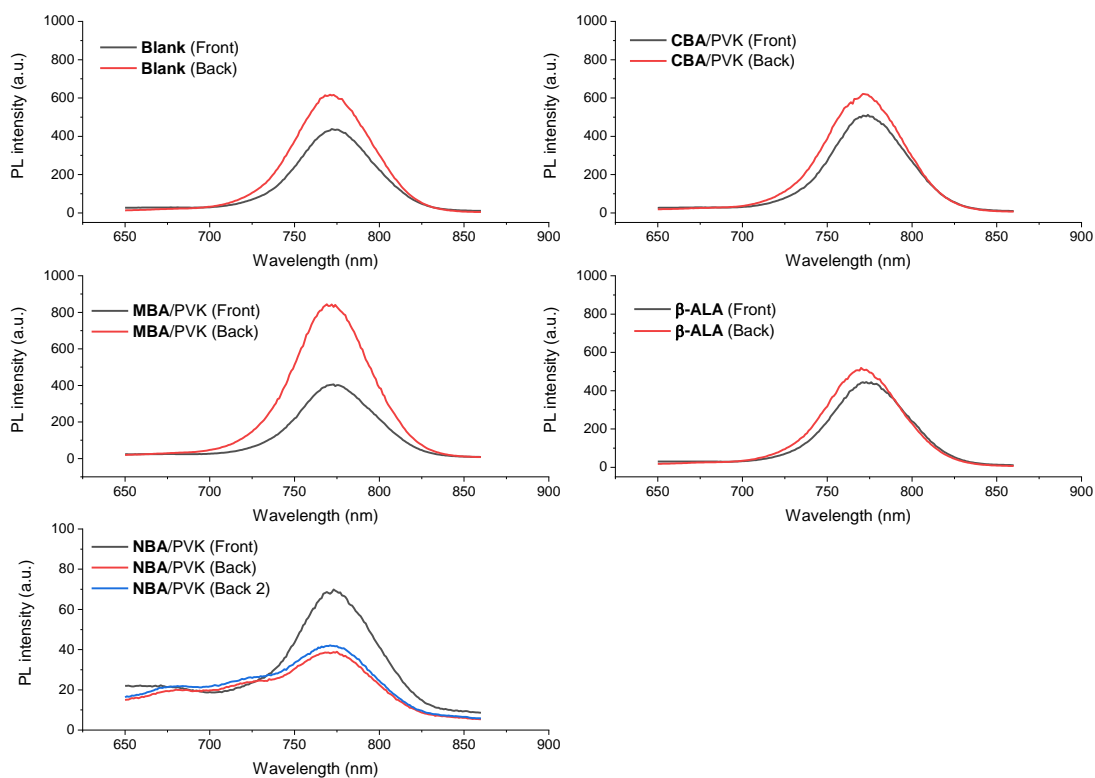


**Figure A.III.1** Steady-state PL spectra of Cs8FAMA layer on SAMs measuring from front and back side after 4 days.

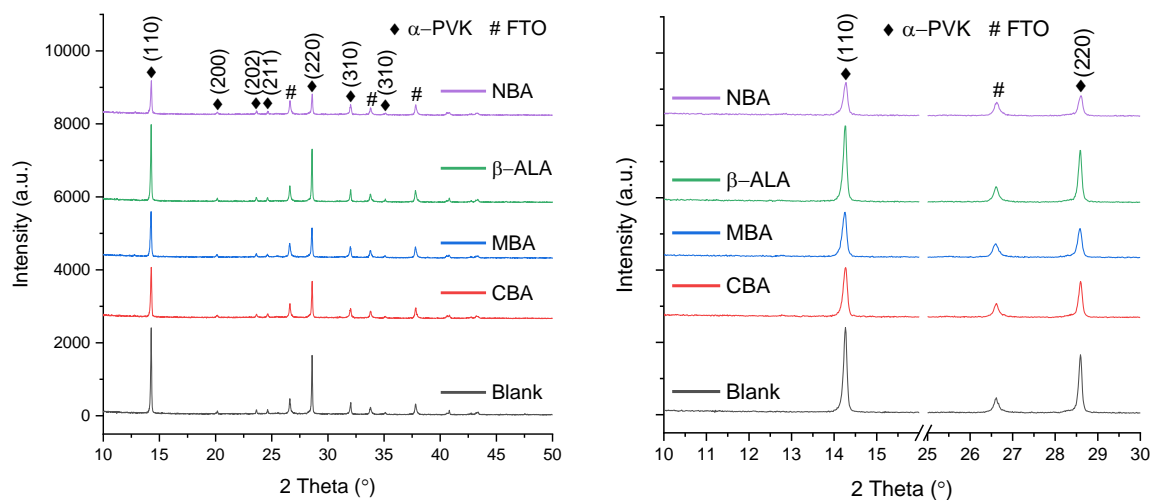


**Figure A.III.2** (a) The XRD patterns of MAPI layer on CBA, MBA, Beta-alanine and NBA modified  $\text{TiO}_2$ ; (b) The peaks marked with black square means perovskite  $\alpha$  phase and no  $\text{PbI}_2$  phase was found.

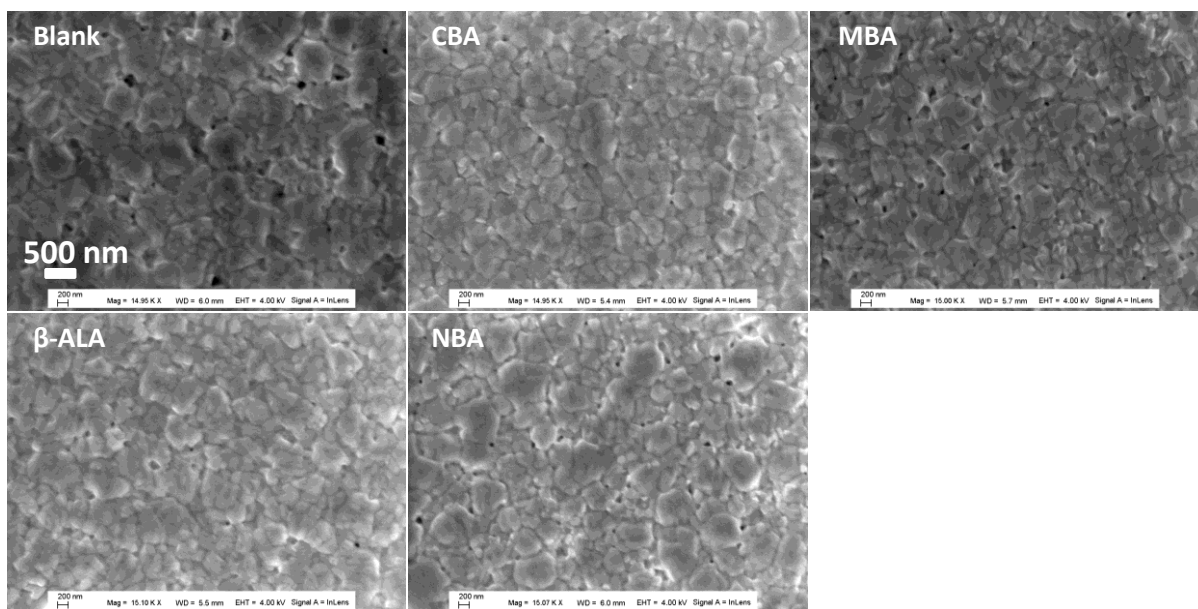


**Figure A.III.3** Top-view SEM images of the MAPbI<sub>3</sub> film deposited on SAMs modified *mp*-TiO<sub>2</sub>.

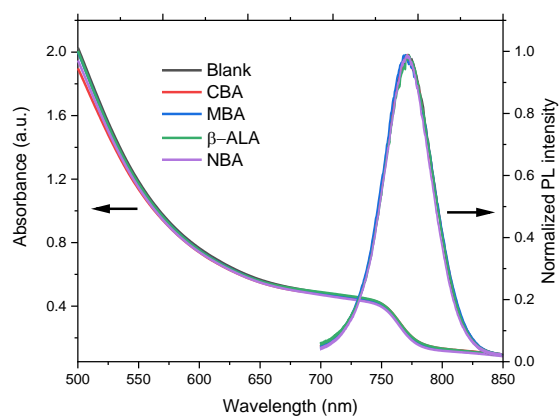


**Figure A.III.4** UV-visible absorbance and normalized PL spectrum of MAPI on SAMs modified TiO<sub>2</sub>.

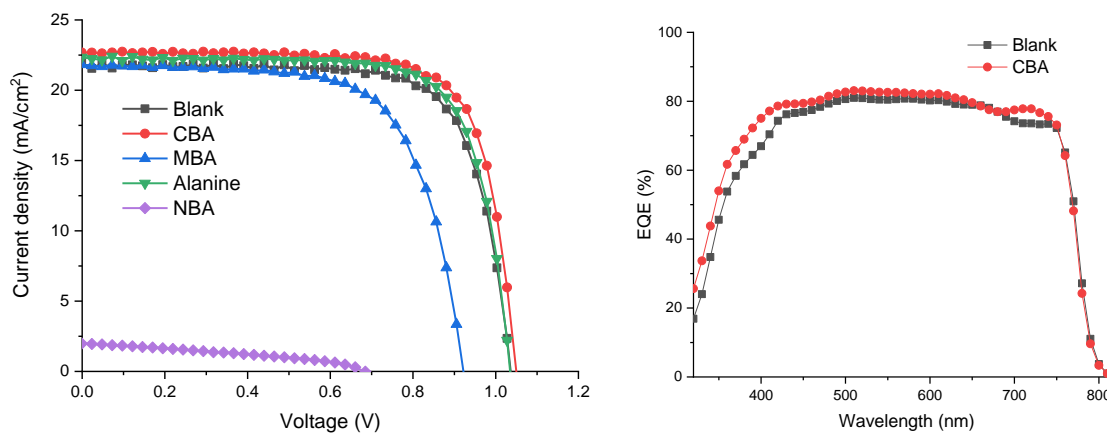


**Figure A.III.5** *J*-*V* and IPCE curves of MAPI cells basing different SAMs.

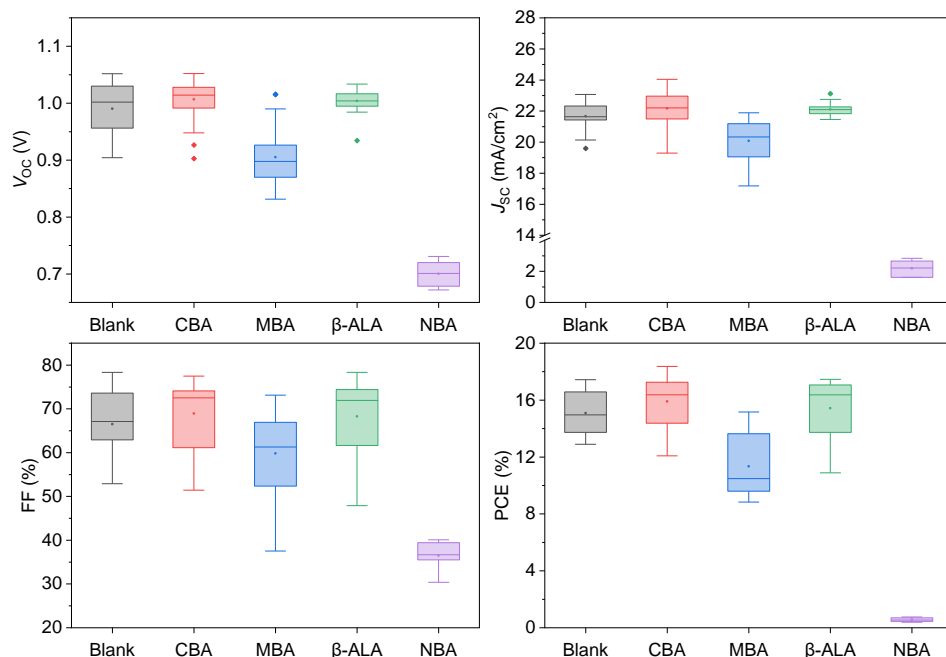


**Figure A.III.6** Device statistics in MAPI system: 4 times experiment with totally 51 pieces cells and 3-4 results were recorded for one cell including reverse scan and forward scan.

### Analysis of the model of the interface

Starting from converged surface models of the oxide and MAPI, a MAPI/CBA/TiO<sub>2</sub> interface was built. For the oxide part, the building block is a (2x2) supercell model of the anatase TiO<sub>2</sub> most stable(101) surface with a thickness of 8 slabs layers (8 O-Ti-O trilayers), accounting for 96 atoms with lattice parameters  $a=14.981 \text{ \AA}$ ,  $b=11.088 \text{ \AA}$  and  $\gamma=109.7^\circ$ . For MAPI, a (110) surface orientation, MAI-terminated, was considered as this surface is known to be stable<sup>1</sup> and the MAI termination can be expected to bind more easily with a functionalized oxide surface than the PbI<sub>2</sub> termination. A slab with 3-PbI<sub>2</sub> layers was cut out from the MAPbI<sub>3</sub> bulk system (space group I4/mcm), with  $a$ ,  $b$  and  $\gamma$  lattice parameters of  $12.343 \text{ \AA}$ ,  $12.555 \text{ \AA}$  and  $90.0^\circ$ , resulting in a rather large cell parameter mismatch between the TiO<sub>2</sub> and MAPI lattices. The interface was created by using CBA as a linker: the carboxylate part was used to bind to TiO<sub>2</sub> in a bridging bidentate mode, while Cl atoms were oriented towards the Pb atoms of MAPI close to the TiO<sub>2</sub> substrate, and Pb-Cl bonds were created by substituting all I<sup>-</sup> of the last layer of the MAPI surface with Cl atoms. To ensure charge neutrality of the resulting unit cell, H<sup>+</sup> of the last layer of MA moieties of MAPI were then removed. Finally, cell parameters matching was ensured by modifying the MAPI lattice to match the cell parameters of the TiO<sub>2</sub> supercell. The resulting interface model had P1 symmetry, with 328 atoms and 3876 atomic orbitals. The lattice was then fully-relaxed, and all atoms were allowed to relax except for the 6 bottom layers of the TiO<sub>2</sub> substrate which were kept fixed to their relaxed positions in the clean supercell.

**Table A.III.1** EDX measurement for perovskite layer (Atoms ratio)

PVK	Measurement	Pb (M-series)	Cs (Cs/Pb) (L-series)	I (L-series)	Br (L-series)	(I+Br)/(Pb) At.%
Cs8FAMA	1	10.65	0.45 (4%)	28.59	4.13	3.07
	2	10.51	0.82 (8%)	28.53	3.41	3.04

### Reference

- 1 Haruyama, J.; Sodeyama, K.; Han, L.; Tateyama, Y. Termination Dependence of Tetragonal CH<sub>3</sub>NH<sub>3</sub>PbI<sub>3</sub> Surfaces for Perovskite Solar Cells. *J. Phys. Chem. Lett.* **2014**, *5*, 2903–2909.

## Annex IV-Chapter IV

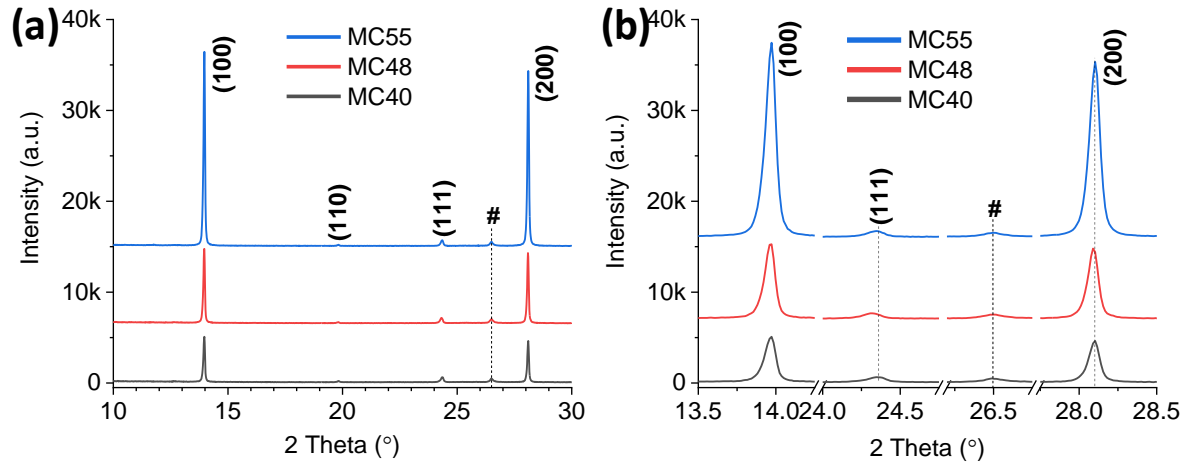
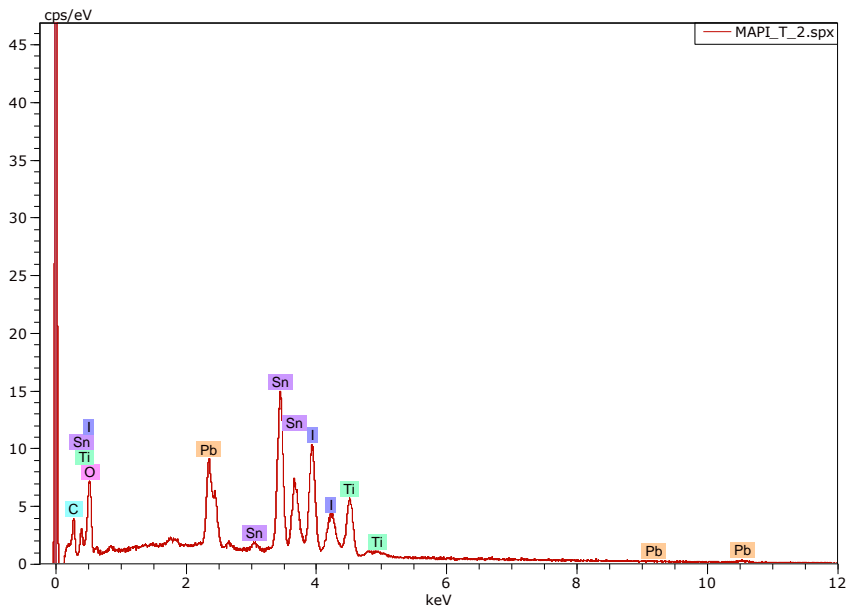


Figure A.IV.1 XRD patterns of MC40, MC48 and MC55.

### MAPI

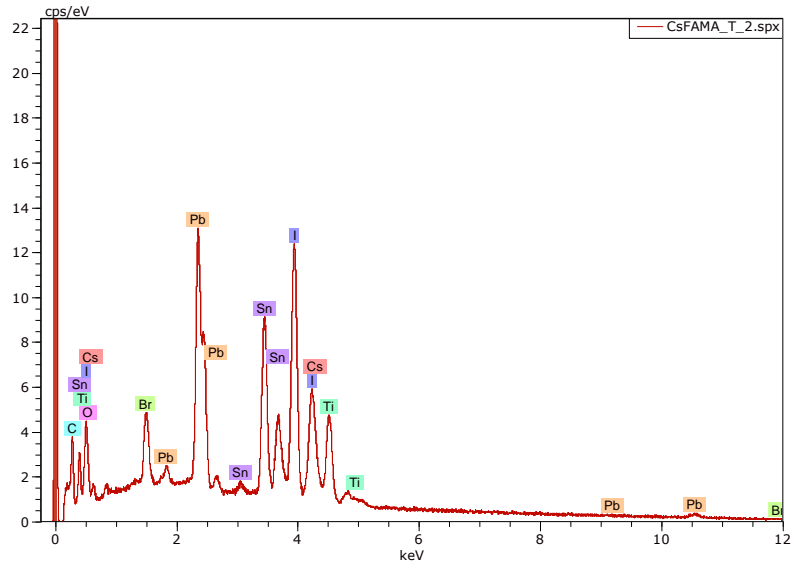


Spectrum: MAPI\_T\_2.spx

Element	Series	unn. C [wt.%]	norm. C [wt.%]	Atom. C [at.%]	Error (3 Sigma) [wt.%]
carbone	K-series	2.63	3.10	17.90	1.35
oxygène	K-series	5.23	6.17	26.76	2.34
plomb	M-series	13.05	15.39	5.15	1.48
titane	K-series	7.18	8.47	12.27	0.73
étain	L-series	30.92	36.49	21.32	2.87
iode	L-series	25.74	30.38	16.60	2.35
Total:		84.75	100.00	100.00	

# Cs8FAMA

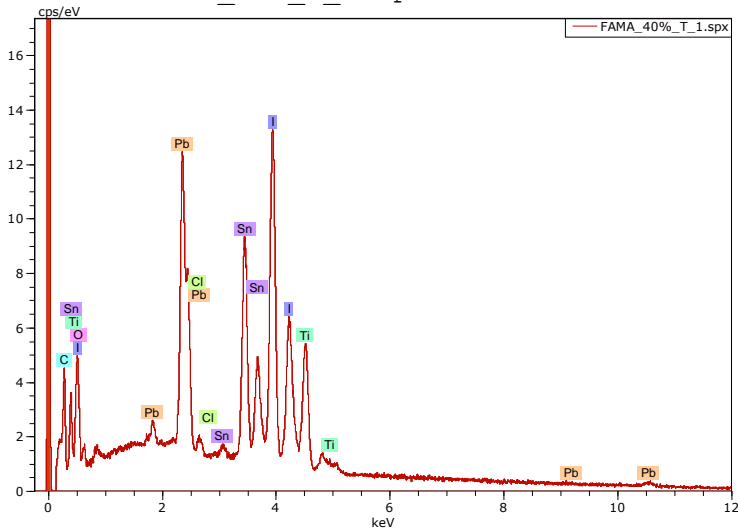
Spectrum: CsFAMA\_T\_2.spx



Element	Series	unn. C [wt.%]	norm. C [wt.%]	Atom. C [at.%]	Error (3 Sigma) [wt.%]
carbone	K-series	2.95	3.04	22.86	1.39
oxygène	K-series	1.26	1.30	7.33	0.71
titane	K-series	4.90	5.06	9.54	0.52
étain	L-series	21.11	21.78	16.57	1.98
iode	L-series	38.86	40.10	28.53	3.48
plomb	M-series	23.36	24.11	10.51	2.55
brome	L-series	3.30	3.41	3.85	0.55
césium	L-series	1.17	1.21	0.82	0.20
Total:		96.91	100.00	100.00	

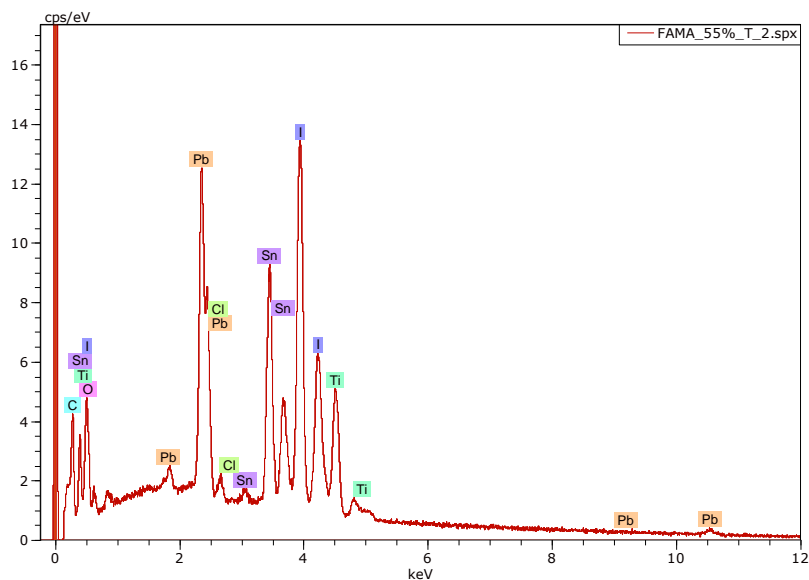
# MC40

Spectrum: FAMA\_40%\_T\_1.spx



Element	Series	unn. C [wt.%]	norm. C [wt.%]	Atom. C [at.%]	Error (3 Sigma) [wt.%]
carbone	K-series	3.01	3.12	22.84	1.37
oxygène	K-series	1.66	1.73	9.49	0.86
titane	K-series	5.84	6.06	11.12	0.60
étain	L-series	21.10	21.92	16.22	1.98
iode	L-series	41.80	43.42	30.06	3.74
plomb	M-series	22.77	23.65	10.03	2.49
chlore	K-series	0.09	0.09	0.23	0.09
Total:		96.27	100.00	100.00	

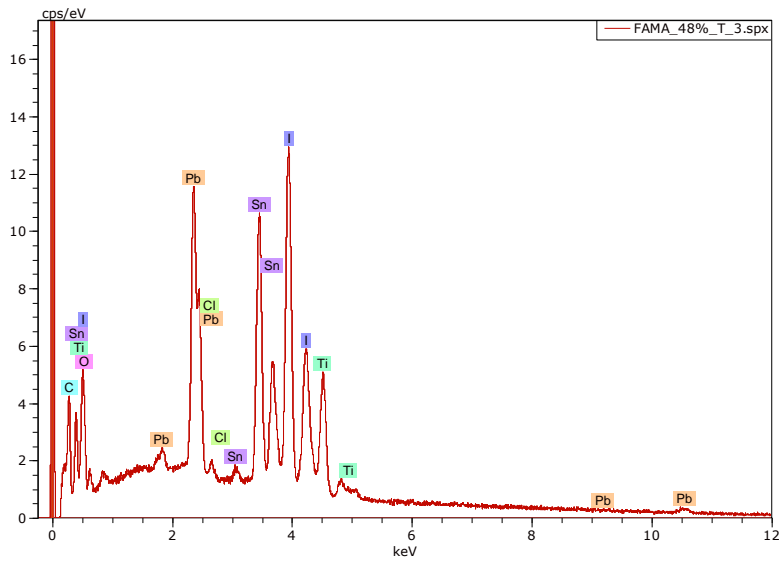
### MC55



Spectrum: FAMA\_55%\_T\_2.spx

Element	Series	unn. C [wt.%]	norm. C [wt.%]	Atom. C [at.%]	Error (3 Sigma) [wt.%]
carbone	K-series	2.96	3.03	22.80	1.36
oxygène	K-series	1.41	1.44	8.13	0.76
titane	K-series	5.32	5.44	10.26	0.55
étain	L-series	21.27	21.77	16.55	2.00
iode	L-series	43.25	44.25	31.48	3.86
plomb	M-series	23.38	23.92	10.42	2.56
chlore	K-series	0.14	0.14	0.35	0.10
Total:		97.73	100.00	100.00	

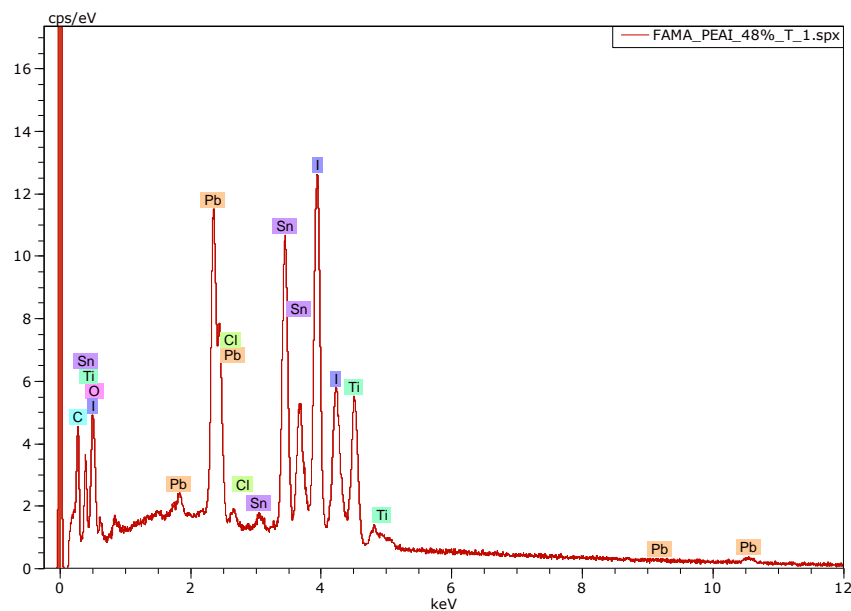
### MC48



Spectrum: FAMA\_48%\_T\_3.spx

Element	Series	unn. C [wt.%]	norm. C [wt.%]	Atom. C [at.%]	Error (3 Sigma) [wt.%]
carbone	K-series	2.91	3.09	22.34	1.34
oxygène	K-series	1.95	2.07	11.22	0.97
titane	K-series	5.02	5.33	9.67	0.53
étain	L-series	24.36	25.84	18.92	2.27
iode	L-series	39.51	41.91	28.70	3.54
plomb	M-series	20.50	21.75	9.12	2.25
chlore	K-series	0.02	0.02	0.04	0.08
Total:		94.27	100.00	100.00	

### MC48-PEAI



Spectrum: FAMA\_PEA1\_48%\_T\_1.spx

Element	Series	unn. C [wt.%]	norm. C [wt.%]	Atom. C [at.%]	Error (3 Sigma) [wt.%]
carbone	K-series	3.27	3.39	23.54	1.47
oxygène	K-series	2.15	2.22	11.59	1.05
titane	K-series	6.34	6.57	11.45	0.64
étain	L-series	24.50	25.37	17.83	2.29
iode	L-series	39.26	40.67	26.74	3.52
plomb	M-series	20.98	21.73	8.75	2.30
chlore	K-series	0.04	0.04	0.10	0.08
Total:		96.54	100.00	100.00	

## NMR

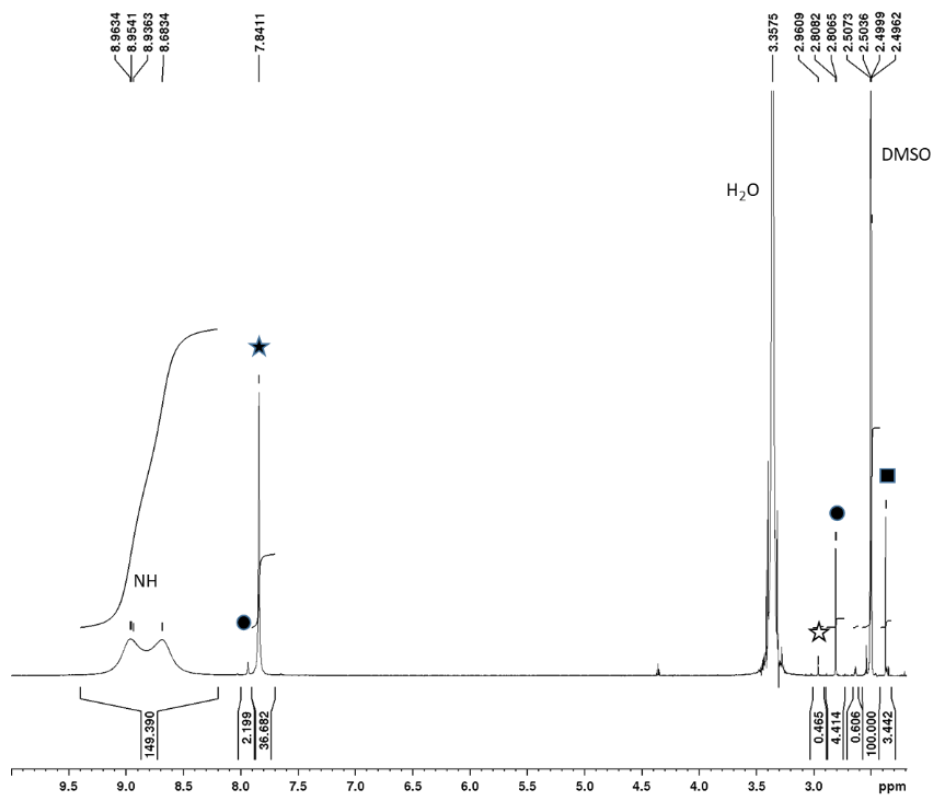


**Figure A.IV.1a:** <sup>1</sup>H NMR spectrum of the **MC48 film**. ★: Formamidinium; ■: Methylamonium, ●: N-methyl formamidinium; ☆: N, N'-dimethyl formamidinium

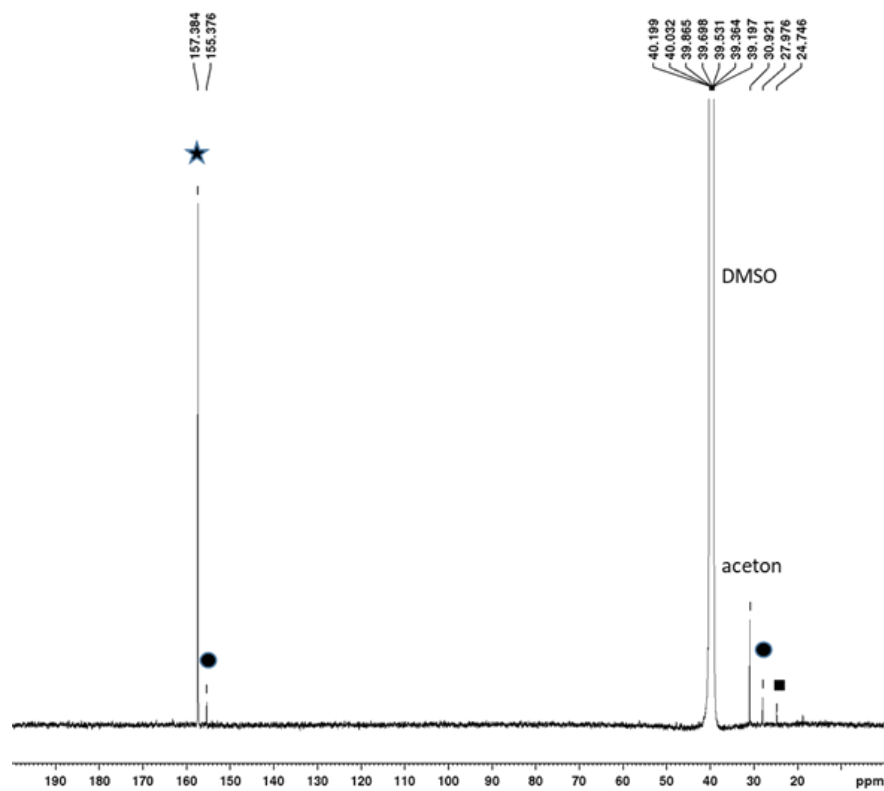


**Figure A.IV.1b:**  $^{13}\text{C}$  NMR spectrum of the **MC48 film**. ★: Formamidinium; ■ : Methylamonium, ●: N-methyl formamidinium.

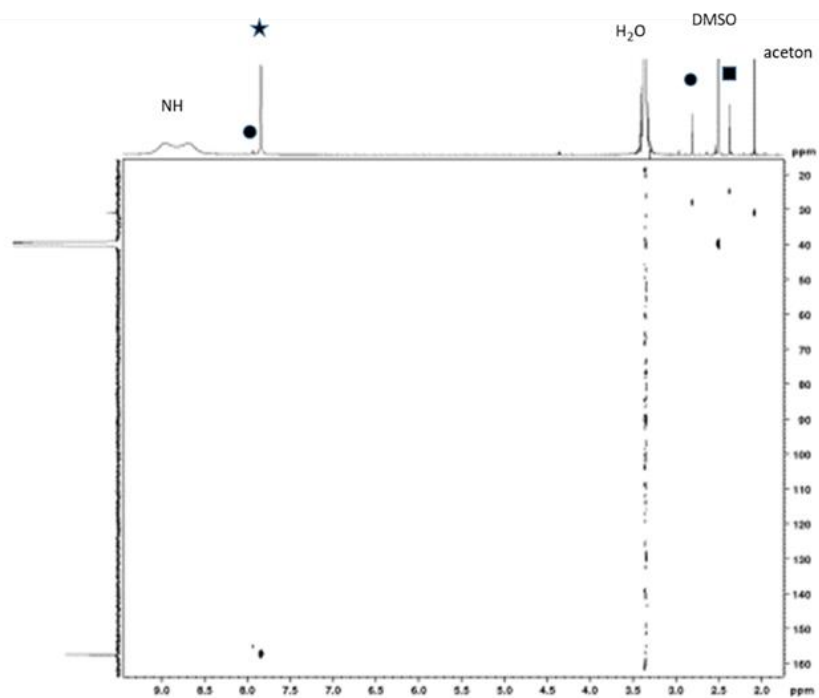


**Figure A.IV.1c:**  $^1\text{H}$ - $^{13}\text{C}$  HSQC NMR spectrum of **MC48 film**. ★: Formamidinium; ■ : Methylamonium, ●: N-methyl formamidinium.

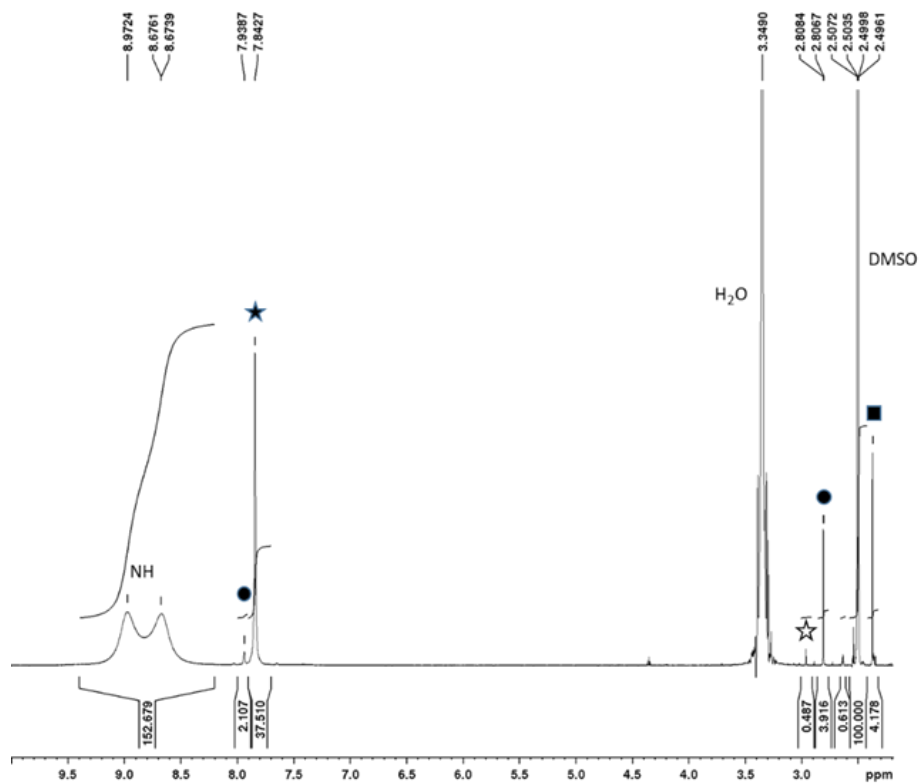


**Figure A.IV.1d:**  $^1\text{H}$  NMR spectrum of the MC40 film. ★: Formamidinium; ■ : Methylamonium, ●: N-methyl formamidinium; ☆: N, N'-dimethyl formamidinium.

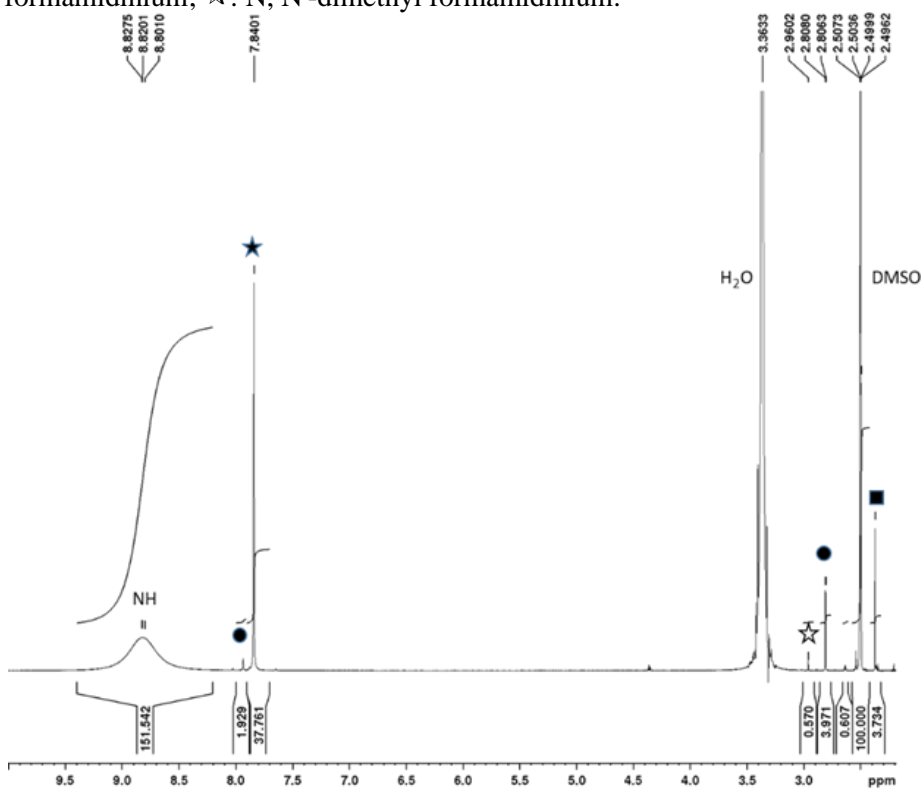


**Figure A.IV.1e:**  $^1\text{H}$  NMR spectrum of the MC55 film. ★: Formamidinium; ■ : Methylamonium, ●: N-methyl formamidinium; ☆: N, N'-dimethyl formamidinium.

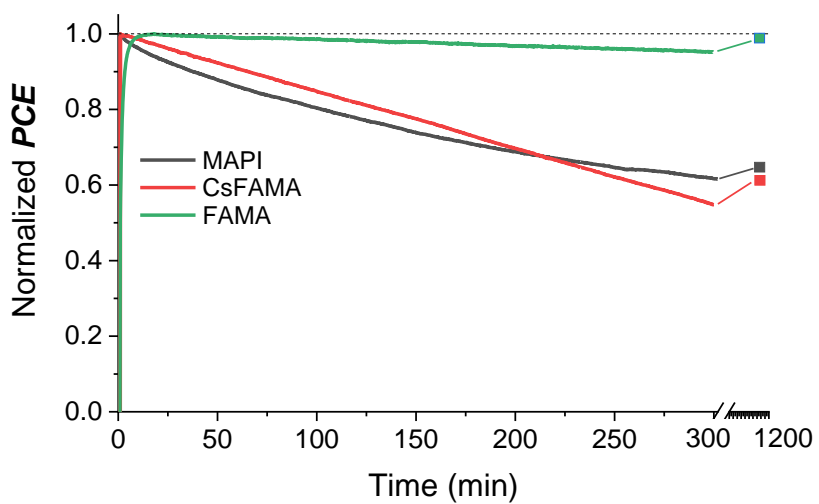


**Figure A.IV2.** MPP tracking for 5h and measuring again after 1-night recover. CsFAMA treated with PEAI and TEAI

## Annex V-Chapter V

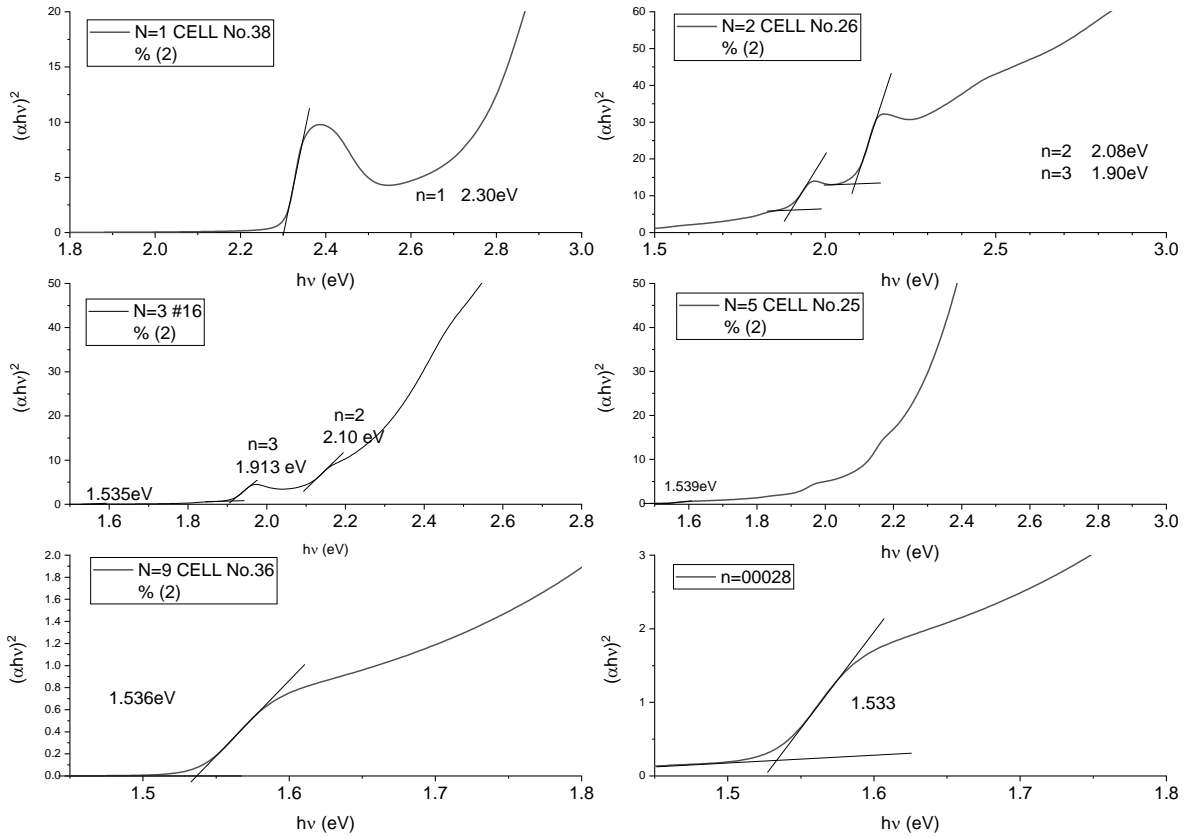
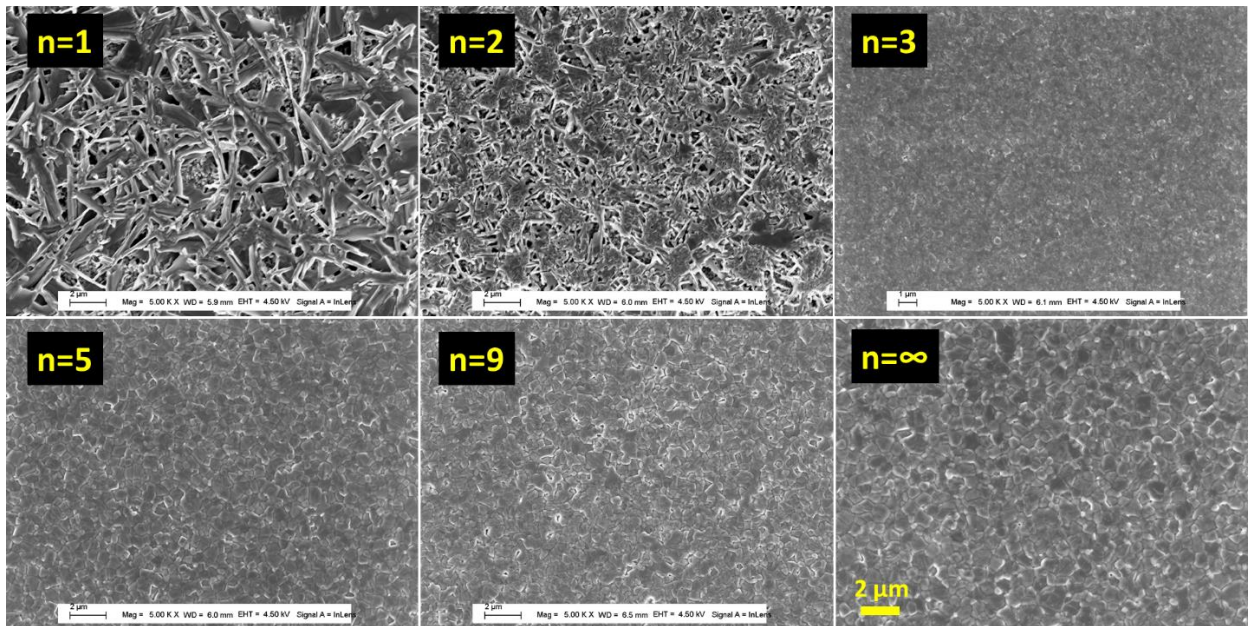
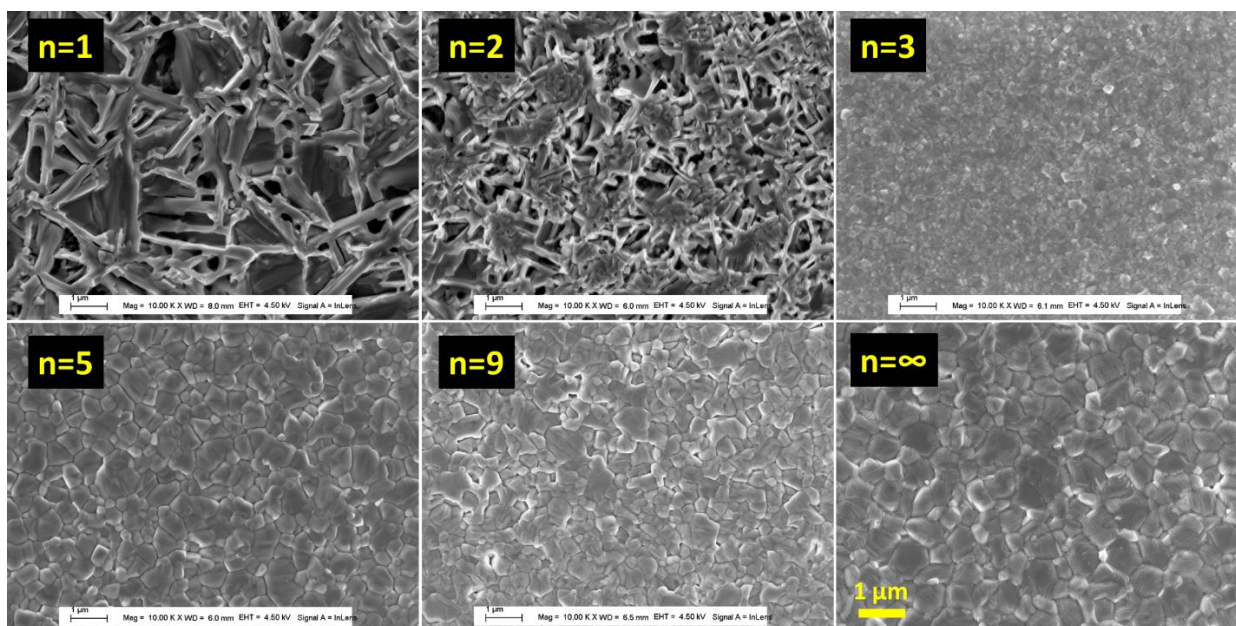
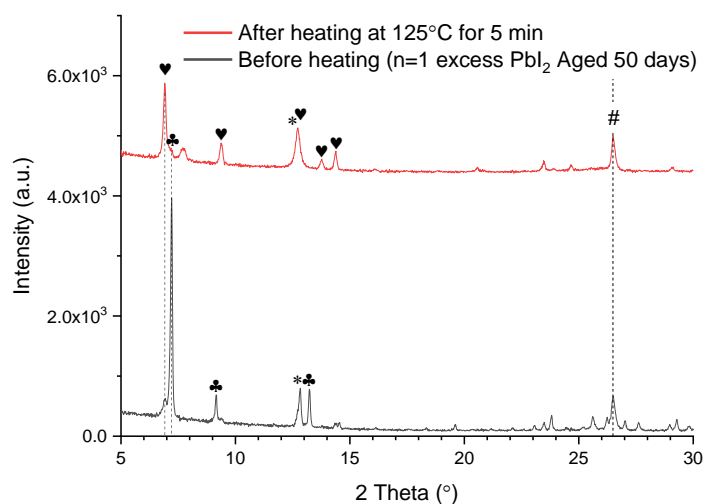


Figure V.A. 1 Band gaps of various 2D/3D perovskite





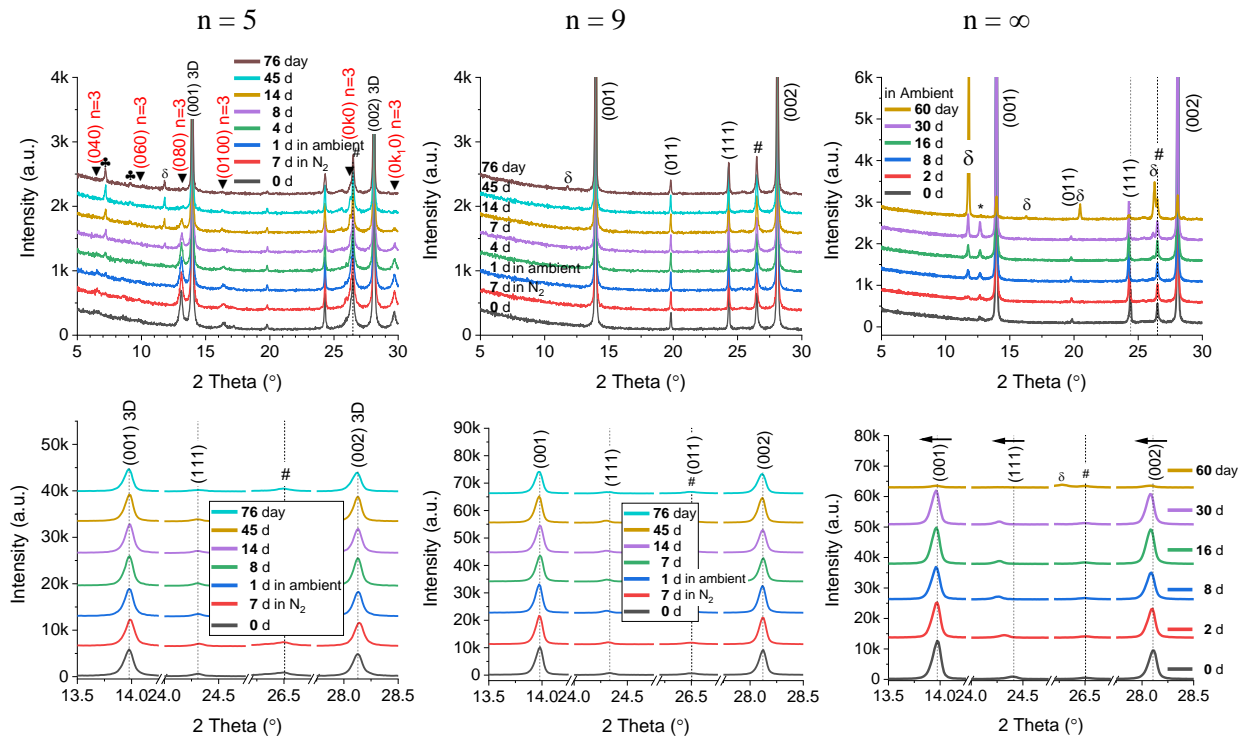
**Figure V.A. 2** SEM of various 2D/3D perovskite films (magnification of 5k and 10k).



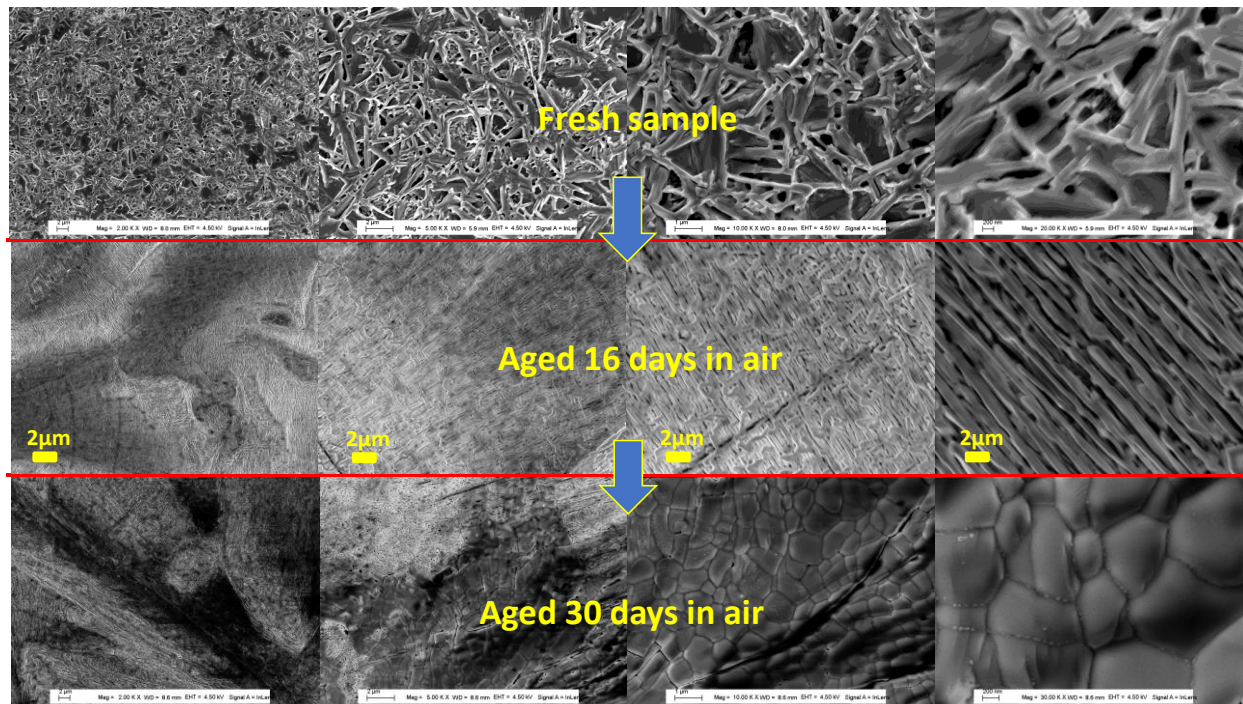
**Figure V.A. 3** XRD of  $n = 1^*$  with excess 1time molar of  $PbI_2$  before and after annealing.

**Table V.A.1** Typical  $J$ - $V$  curve parameters of 2D/3D PSCs. (The forward  $J$ - $V$  curves were not measured for the low efficiency cells.)

Cell	Scan direction	$V_{oc}$ /V	$J_{sc}$ mA/cm <sup>2</sup>	FF /%	PCE /%	HI/ %
36%MACl n=9	Reverse	0.960	23.18	69.35	15.43	38%
	Forward	0.915	23.03	45.32	9.55	
n=20	Reverse	0.877	25.60	78.45	17.62	27.2
	Forward	0.879	25.16	58.00	12.83	



**Figure V.A. 4** The zoom view of 2D/3D peaks for  $n = 5$ ,  $n = 9$  and  $n = \infty$ .



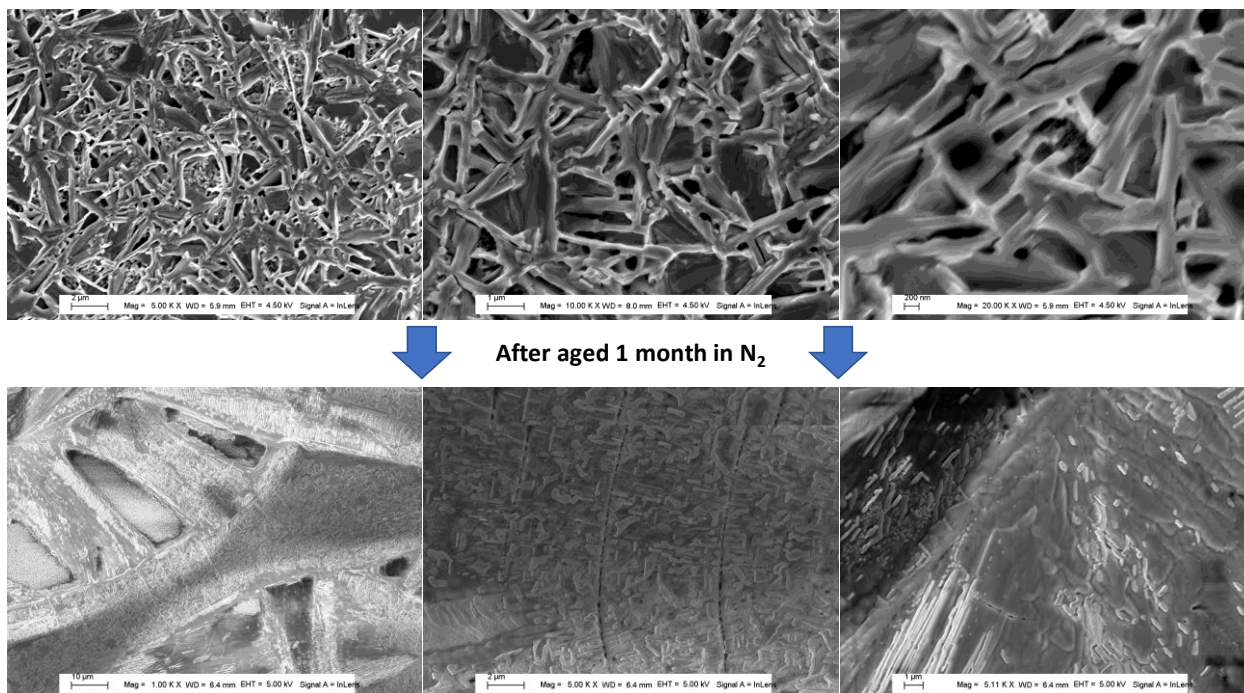


Figure V.A. 5 Morphology evolution of n = 1 sample aging in the N<sub>2</sub> and air.

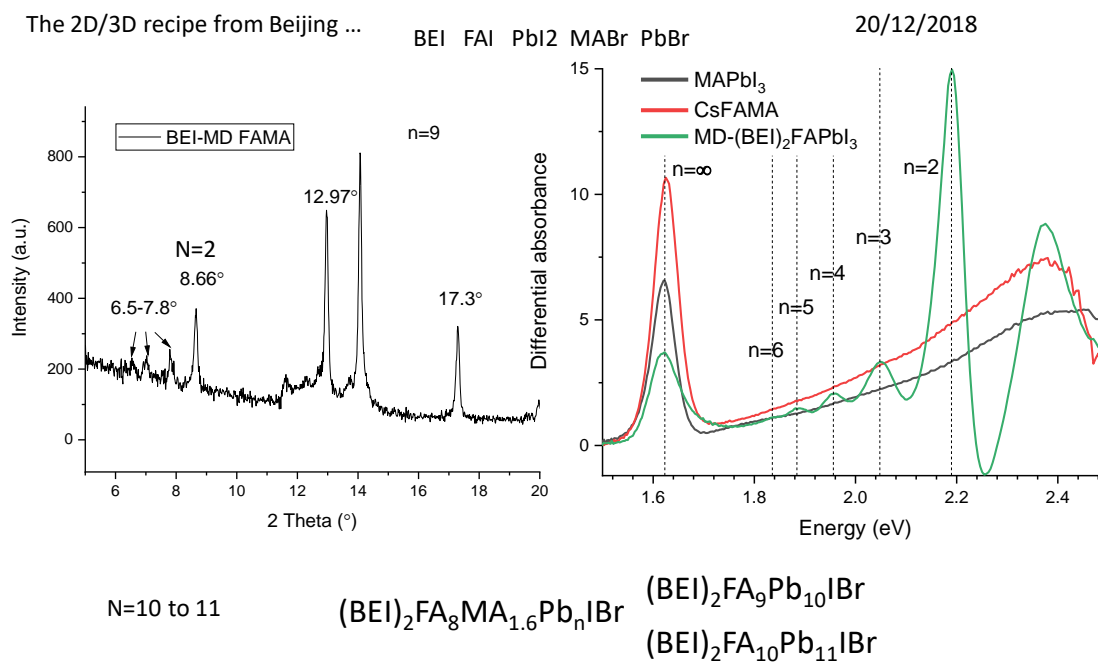


Figure V.A. 6 XRD and deferential absorbance for (BE)FA<sub>n-1</sub>Pb<sub>n</sub>IBr (n = 10 to 11).

## List of publications and presentations

### Published Articles

- [1] **T. Zhu**, D. Zheng, M.-N. Rager, Th. Pauporté\*, Actual Organic Cations Composition Determination in Perovskite Thin Films. Application to Formamidinium Lead Iodide Stabilization for High Efficiency Solar Cell. *Solar RRL* (2020) 200348.
- [2] **T. Zhu**, D. Zheng, J. Liu, L. Coolen, Th. Pauporté\*, Electrical Response of High Efficiency and Stable Solar Cells Based on MACl Mediated Grown  $\text{FA}_{0.94}\text{MA}_{0.06}\text{PbI}_3$  Perovskite. *ACS Appl. Mater Interfaces* 12 (2020) 37197.
- [3] **T. Zhu**, J. Su, F. Labat, I. Ciofini, Th. Pauporté\*, Interfacial Engineering through Chloride-Functionalized Self-Assembled Monolayer for High Efficiency Perovskite Solar Cells. *ACS Appl. Mater Interfaces* 12 (2020) 744-752.
- [4] **T. Zhu**, J. Su, J. Alvarez, G. Lefèvre, F. Labat, I. Ciofini, Th. Pauporté\*, Response Enhancement of Self-Powered Visible-Blind UV Photodetectors by Nanostructured Heterointerface Engineering. *Adv. Funct. Mater.* 29 (2019) 1903981.
- [5] D. Zheng,‡ **T. Zhu**,‡ Th. Pauporté\*, Using Monovalent- to Trivalent-Cation Hybrid Perovskites for Producing High-Efficiency Solar Cells: Electrical Response, Impedance, and Stability. *ACS Appl. Energy Mater.* 3 (2020) 10349-10361.
- [6] J. Su, **T. Zhu**, Th Pauporté, I. Ciofini, F. Labat, Improving the Heterointerface in Hybrid Organic-Inorganic Perovskite Solar Cells by Surface Engineering: Insights from Periodic Hybrid Density Functional Theory Calculations. *J. Comput. Chem.* (2020) DOI: 10.1002/jcc.26215.

### Submitted Articles

- [7] D. Zheng, **T. Zhu**, Th. Pauporté\*, Synergistic Effects of Chloride-Additives on the Growth of Methylammonium-Free Perovskite Films for Efficient, Hysteresis-Free, Highly Stable Solar Cells. *Adv. Funct. Mater.* Under review.

### Oral communications (presenting author is underlined)

- [1] **T. Zhu**, Th. Pauporté, J. Su, F. Labat, I. Ciofini, J. Alvarez, "Interfacial modification by dipolar molecules for the improvement of photovoltaic devices." 47th IUPAC World Chemistry Congress, July 5-12th 2019, Paris, France.
- [2] J. Su, **T. Zhu**, Th. Pauporté, F. Labat, I. Ciofini "A periodic DFT investigation of the MAPI-ligand-TiO<sub>2</sub> interface for perovskite solar cell application: Role of the ligand." 18<sup>th</sup> International Conference on Density-Functional Theory and its Applications. July 22-26, 2019. Alicante, Spain.

- [3] A. Leblanc, N. Mercier, M. Allain, J. Dittmer, V. Fernandez, Th. Pauporté, **T. Zhu**, M. Kepenekian, C. Katan, F. Boucher, 18th ECASIA meeting, will be held from September 15th to 20th, 2019 in Dresden, Germany.
- [4] Th. Pauporté, M. Ulfa, **T. Zhu**, D. Zheng, "Impedance Spectroscopy Study of Perovskite Solar Cells." 5ème Journées Pérovskites Halogénées, March 27-29th 2019, Limoges, France.

**Poster communications** (presenting author is underlined)

- [1] Th. Pauporté, **T. Zhu**, D. Zheng, "Electrical Impedance Spectroscopy Study of Mesoscopic Perovskite Solar Cells- From Selective Contact Optimizing to the Puzzling Capacitive Behaviors." 47th IUPAC World Chemistry Congress, July 5-12th 2019, Paris, France.
- [2] J. Su, **T. Zhu**, Th. Pauporté, F. Labat, I. Ciofini. 9e édition des "Journées nationales du Photovoltaïque, JNPV19, December 3-6th, 2019, Dourdan, France.
- [3] J. Su, **T. Zhu**, Th. Pauporté, F. Labat and I. Ciofini. "A periodic DFT investigation of the hybrid perovskite solar cell interface: From structural features to electron injection through ligand's connection." 2nd Quantum International Frontiers. Nov. 18-22, 2019. Shanghai, China.
- [4] T. Pauporté, **T. Zhu** and D. Zheng, "The Electrical Response of Mesoscopic Perovskite Solar Cells." EMN Meeting on Nanoparticles June 10-14th 2019, Prague, Czech Republic.
- [5] M. Ulfa, **T. Zhu**, T. Pauporté, "Impedance Spectroscopy Study of Perovskite Solar Cells", Workshop "Spectroscopy tools for halide perovskites", Paris, November 22th, 2018.

## RÉSUMÉ

---

Au cours des dix dernières années, les cellules solaires à pérovskite (CSP) se sont révélées la technologie la plus prometteuse en photovoltaïque. Dans cette thèse, nous avons développé des stratégies pour obtenir des cellules solaires très performantes et stables grâce à de l'ingénierie d'interface et à de l'ingénierie sur la composition de la pérovskite. Le chapitre I présente le contexte de cette recherche, développe les matériaux semiconducteurs et pérovskites, leur utilisation en optoélectronique et l'énergie solaire. Le chapitre II présente la modification d'interface par des monocouches auto-assemblées (MAA) et son application dans les photo-détecteurs UV. Le chapitre III montre l'application des MAA aux CSP ce qui a permis d'atteindre un rendement de 21,35%. Au chapitre IV, nous étudions des pérovskites à bande interdite étroite basées sur le formamidinium (FAPbI<sub>3</sub> stabilisé par le méthyle d'ammonium). Par utilisation d'additifs dans les solutions de précurseur et passivation interfaciale, le dispositif champion a atteint un rendement stabilisé de 22,1%. Dans le chapitre V, nous nous intéressons à l'amélioration de la stabilité des CSP. Des pérovskites 2D/3D à base de benzyle ammonium ont été systématiquement étudiées. Nous avons obtenu des films et ces cellules solaires remarquablement stables.

## MOTS CLÉS

---

Cellules solaires à pérovskite, Photodétecteurs UV, Monocouches auto-assemblées, Passivation de l'interface, Pérovskites à dimensions mixtes.

## ABSTRACT

---

In the past ten years, perovskite solar cells (PSCs) have emerged as the most promising next-generation photovoltaic technology. In this thesis, we have developed strategies to get highly efficient and stable PSCs through interface engineering of the devices and composition engineering of the perovskite. Chapter I presents the context of this research, develop semiconductors and perovskite materials and the solar energy. In Chapter II, we have developed interfacial modifications by self-assembled monolayers (SAMs) and their application to UV photodetectors. The SAMs applied in PSCs are investigated in Chapter III and, in this work, the highest efficiency has reached 21.35%. In Chapter IV, we have investigated narrow bandgap formamidinium perovskites (FAPbI<sub>3</sub> stabilized by methylammonium). Through additive engineering and interfacial passivation, the champion device reached a stabilized efficiency of 22.1%. In Chapter V, strategies to improve the stability of PSCs have been implemented by playing on their dimensionality. 2D/3D perovskites based on benzylammonium have been systematically studied. We have prepared films and solar cells with remarkably improved stability.

## KEYWORDS

---

Perovskite solar cells, UV Photodetectors, Self-assembled monolayer, Interface passivation, Mixed dimensional perovskite.